

9-5-2013

# Uranium-series isotope constraints on magma generation and differentiation in the central Oregon Cascades

Euan Mitchell

Follow this and additional works at: [https://digitalrepository.unm.edu/eps\\_etds](https://digitalrepository.unm.edu/eps_etds)

---

## Recommended Citation

Mitchell, Euan. "Uranium-series isotope constraints on magma generation and differentiation in the central Oregon Cascades." (2013). [https://digitalrepository.unm.edu/eps\\_etds/54](https://digitalrepository.unm.edu/eps_etds/54)

This Dissertation is brought to you for free and open access by the Electronic Theses and Dissertations at UNM Digital Repository. It has been accepted for inclusion in Earth and Planetary Sciences ETDs by an authorized administrator of UNM Digital Repository. For more information, please contact [disc@unm.edu](mailto:disc@unm.edu).

**Euan C. Mitchell**

*Candidate*

---

**Earth and Planetary Sciences**

*Department*

---

This dissertation is approved, and it is acceptable in quality and form for publication:

*Approved by the Dissertation Committee:*

Yemane Asmerom, Chairperson

---

Carl Agee

---

David Draper

---

Tobias Fischer

---

Jane Selverstone

---

---

---

---

---

---

**URANIUM-SERIES ISOTOPE CONSTRAINTS ON MAGMA  
GENERATION AND DIFFERENTIATION IN THE CENTRAL  
OREGON CASCADES**

**by**

**EUAN C. MITCHELL**

M.E.Sci., Geology, University of Liverpool, 2005  
M.S., Earth and Planetary Sciences, University of New Mexico, 2007

DISSERTATION

Submitted in Partial Fulfillment of the  
Requirements for the Degree of

**Doctor of Philosophy  
Earth and Planetary Sciences**

The University of New Mexico  
Albuquerque, New Mexico

**July, 2013**

## ACKNOWLEDGEMENTS

This study was supported by National Science Foundation grant EAR-0948703 to Yemane Asmerom, Department of Earth and Planetary Sciences, University of New Mexico. Graduate student scholarships distributed by the Department of Earth and Planetary Sciences on behalf of many generous supporters of the department are gratefully acknowledged.

This dissertation would not have been possible without the training, guidance, and support of Victor Polyak in all aspects of the laboratory work. Mehdi Ali provided access to the Analytical Chemistry Laboratory in E&PS for sample preparation, and provided valuable assistance with the XRF analyses. Tim DeBey and the staff of the U.S. Geological Survey TRIGA reactor facility in Denver, CO, are thanked for their efforts in producing the Pa spikes.

I would like to thank my committee chair and advisor Yemane Asmerom for giving me the opportunity to work on this project, and his input at every stage of the process. I also would like to acknowledge my other committee members: Carl Agee, Tobias Fischer, and Jane Selverstone at UNM, and Dave Draper at NASA.

The support and friendship of the faculty, staff, and students of the Department of Earth and Planetary Sciences over the last eight years has been essential. Lastly, I would not be where I am today without the love and support of my family, who have always encouraged me in pursuit of my goals, even when that has taken me so far from home for so long.

**URANIUM-SERIES ISOTOPE CONSTRAINTS ON MAGMA GENERATION  
AND DIFFERENTIATION IN THE CENTRAL OREGON CASCADES**

by

**Euan C. Mitchell**

**M.E.Sci., Geology, University of Liverpool, 2005**

**M.S., Earth and Planetary Sciences, University of New Mexico, 2007**

**Ph.D., Earth and Planetary Sciences, University of New Mexico, 2013**

**ABSTRACT**

The Cascade volcanic arc, extending for ~ 1250 km from northern California, USA, to southern British Columbia, Canada, is the surface expression of NE-directed subduction of the Juan de Fuca microplate beneath North America. Slow subduction of young, hot oceanic lithosphere creates an unusually warm subduction environment at depth. Fore-arc rotation and impingement of Basin and Range faulting create an extensional environment within much of the arc. The combination of these factors has been postulated as a cause of the wide variety of primitive basaltic compositions erupted within the arc. Within central Oregon, where intra-arc extension is highly focused, young mafic volcanism is particularly abundant, and eruption of true rhyolite is unusually common also. This dissertation seeks to address the generation and differentiation of young (< 20 ka) magmas in the central Oregon Cascades through application of uranium-series (U-series) isotope data, in conjunction with elemental and Sr-Nd isotope data.

Trace element and isotopic ( $^{87}\text{Sr}/^{86}\text{Sr}$ ,  $^{143}\text{Nd}/^{144}\text{Nd}$ ) data for the most primitive lavas suggest derivation by < 10% partial melting of a garnet-bearing mantle source. This source is interpreted to have experienced relatively minor modification by a slab-derived component, most likely via addition of a partial melt of subducted sediments. The  $^{238}\text{U}$ -

$^{230}\text{Th}$ - $^{226}\text{Ra}$  U-series data are consistent with this interpretation. However, as a result of the minor ( $^{230}\text{Th}/^{238}\text{U}$ ) disequilibrium created in the mantle wedge as a consequence of fluid addition, the data cannot resolve whether fluid modification of the source initiated melting or was an earlier ( $> 350$  k.y. prior) event.

( $^{231}\text{Pa}/^{235}\text{U}$ ) data for these samples, the first such data from the Cascades, are two to four times higher than any U-Pa data previously measured in lavas from any tectonic setting. The data cannot be reproduced from a secular equilibrium or U-enriched source with reasonable model parameters, implying significant pre-melting source  $^{231}\text{Pa}$ -enrichment. This source enrichment is interpreted to result from addition of a subducted sediment partial melt, generated in the presence of an allanite/monazite-free residue as a consequence of the hot conditions within the subducting slab. This implies melt addition to the sub-arc mantle  $\ll 150$  k.y. prior to melting.

The majority of the mafic lavas erupted in the study area have been modified from mantle-derived compositions by passage through the  $\sim 45$  km thick overlying arc crust. Modification of mantle-derived magmas in the Three Sisters appears to have been dominated by interaction with a lower crustal component, likely a partial melt of mafic lower crust and/or a residual liquid from fractional crystallization of hydrous basalt. Crustal interaction at Newberry, in contrast, is dominated by assimilation of a felsic upper crustal component, similar in composition to obsidians erupted within the central caldera. Magma differentiation in the Three Sisters region leads to both decreases and increases in U-series isotope activity ratios, while at Newberry activity ratios are lowered by assimilation of felsic crust.

Eruption of true rhyolite is unusually common around South Sister in comparison with the arc axis elsewhere. Newberry is a bimodal basalt-rhyolite volcanic field similar to other rear-arc volcanoes in the Cascades, with abundant true rhyolite also. Three compositionally very similar South Sister rhyolites are interpreted as 15 to 20% partial melts of lower crustal mafic amphibolite, modified slightly by AFC processes in the same shallow magma chamber prior to eruption. Two Newberry obsidians display slightly greater compositional variability, including U-series variations, and are interpreted as separate melts of upper crustal granitic rocks, which are themselves interpreted to ultimately result from lower crustal melting.

A recurrent theme throughout this dissertation is the strong control exerted on magmatism in the study area by local tectonic factors. In the Three Sisters region, where intra-arc extension is highly focused and the study area lies within the High Cascades graben, primitive magmas are relatively common. Furthermore, lower crustal processes are the dominant influence on differentiation of primitive magmas as well as generation of felsic magmas, with minor upper crustal interaction. In contrast, primitive compositions are rare or absent at Newberry, where a large volcanic edifice has developed since at least 0.5 Ma. Melts from the mantle or lower crust are intercepted beneath the central caldera, where only felsic lavas generated by re-melting of shallow granitic intrusions are erupted. Evolved mafic magmas, carrying a signature of upper crustal interaction, are confined to flank eruptions along rift zones.

## TABLE OF CONTENTS

LIST OF FIGURES .....	x
LIST OF TABLES .....	xiii
Chapter 1: Introduction .....	1
1.1. Scope of the Dissertation .....	1
1.2. The Cascades .....	1
1.2.1. Tectonic Setting .....	1
1.2.2. High Cascades Magmatism.....	6
1.2.3. Field Area and Samples .....	9
1.3. Uranium-Series Isotope Systematics .....	11
1.4. U-series isotope systematics of mafic magmas from central Oregon: Implications for fluid involvement and melting processes in the Cascade arc (Chapter 2) .....	17
1.5. Extreme <sup>231</sup> Pa-enrichment in young Cascade arc lavas - signature of sediment melting in a warm arc? (Chapter 3) .....	17
1.6. Crustal modification of mantle-derived U-series isotope signatures: A case study from the central Oregon Cascades (Chapter 4).....	18
1.7. <sup>238</sup> U- <sup>230</sup> Th- <sup>226</sup> Ra and <sup>235</sup> U- <sup>231</sup> Pa constraints on rhyolite generation at South Sister and Newberry volcanoes, central Oregon Cascades (Chapter 5).....	20
References .....	22
Appendix A1 .....	33
References .....	36
Chapter 2: U-series isotope systematics of mafic magmas from central Oregon: Implications for fluid involvement and melting processes in the Cascade arc.....	38
Abstract .....	38
2.1. Introduction.....	40
2.2. Geologic Setting and Background .....	41
2.3. Materials and Methods.....	45
2.4. Results.....	52
2.4.1. Major and Trace Elements .....	52
2.4.2. Sr and Nd Isotopes .....	53

2.4.3. U-Series Isotopes .....	55
2.5. Discussion .....	58
2.5.1. Comparison with Existing Cascade Lava Types .....	59
2.5.2. Crustal Processing.....	60
2.5.3. Mantle Sources and Slab Components .....	62
2.5.4. U-Series Isotopes and Mantle Melting .....	69
2.6. Conclusions.....	75
Acknowledgements.....	76
References.....	77
Chapter 3: Extreme <sup>231</sup> Pa-enrichment in young Cascade arc lavas - signature of sediment melting in a warm arc?.....	88
Abstract.....	88
3.1. Introduction.....	89
3.2. Samples and Results .....	90
3.3. Discussion and Conclusions .....	91
Acknowledgements.....	98
References.....	99
Appendix A3.....	103
A3.1. Materials and Methods.....	104
A3.1.1 Samples .....	104
A3.1.2 Methods.....	105
A3.2. Supplementary Text .....	108
A3.2.1. The Melting Model .....	108
A3.2.2. Accessory Phases in Subducted Sediments and Crust.....	110
A3.2.3. The Slab Component, Source Modification, and Melting.....	114
A3.2.4. Trace Element Constraints.....	116
References.....	121
Chapter 4: Crustal modification of mantle-derived U-series isotope signatures: A case study from the central Oregon Cascades .....	126
Abstract.....	126
4.1. Introduction.....	128

4.2. Background .....	131
4.3. Samples and Methods .....	135
4.3.1. Samples .....	135
4.3.2. Methods.....	138
4.4. Results.....	146
4.4.1. Major and Trace Elements .....	146
4.4.2. U-series, Sr, and Nd Isotopes.....	154
4.5. Discussion .....	160
4.5.1. Identification of Primitive Magmas and Parental Compositions .....	160
4.5.2. Previous Studies.....	162
4.5.3. Origin of the Newberry Group Trend .....	163
4.5.4. Origin of the Nash Crater and Belknap Group Trends .....	168
4.5.5. Implications for Arc Magmatism and Cascades U-Series Data.....	177
4.6. Conclusions.....	179
Acknowledgements.....	180
References.....	181
Appendix A4.....	192
A4.1. Silicate U-Th-Ra-Sr-Nd Chemistry Procedure .....	193
Chapter 5: $^{238}\text{U}$ - $^{230}\text{Th}$ - $^{226}\text{Ra}$ and $^{235}\text{U}$ - $^{231}\text{Pa}$ constraints on rhyolite generation at South Sister and Newberry volcanoes, central Oregon Cascades .....	197
Abstract.....	197
5.1. Introduction.....	198
5.2. Samples and Methods .....	201
5.3. Results.....	203
5.4. Discussion and Conclusions .....	206
Acknowledgements.....	216
References.....	217
Appendix A5.....	225
A5.1. U-Series Analytical Methods .....	226
A5.2. Major Element Constraints on Crustal Melting Scenarios.....	229
References.....	232

## LIST OF FIGURES

<b>Figure 1.1:</b> Tectonic setting of the central and southern Cascadia margin. ....	2
<b>Figure 1.2:</b> Shaded relief map of the study area in central Oregon. ....	5
<b>Figure 1.3:</b> Schematic illustration of the three uranium-series decay chains.....	12
<b>Figure 1.4:</b> U-series isotope activity ratio diagrams, showing fields for arc lavas, mid-ocean ridge basalts (MORB), and ocean-island basalts (OIB). ....	15
<b>Figure 2.1:</b> Shaded relief map of the study area in central Oregon. ....	42
<b>Figure 2.2:</b> Various major element, trace element, and isotopic data for central Oregon lavas. ....	53
<b>Figure 2.3:</b> Trace element data for central Oregon lavas. ....	54
<b>Figure 2.4:</b> U-series isotope data for central Oregon lavas.....	58
<b>Figure 2.5:</b> Crustal contamination modeling for central Oregon lavas.....	61
<b>Figure 2.6:</b> La/Yb vs. Tb/Yb modeling plot for central Oregon lavas.....	64
<b>Figure 2.7:</b> Slab component modeling plot for central Oregon lavas. ....	67
<b>Figure 2.8:</b> U-series isotope modeling plots for central Oregon lavas.....	71
<b>Figure 3.1:</b> ( $^{230}\text{Th}/^{238}\text{U}$ ) vs. ( $^{231}\text{Pa}/^{235}\text{U}$ ) <sub>i</sub> data for young, mafic lavas from the central Oregon Cascades.....	91
<b>Figure 3.2:</b> Results of combined U-Th-Pa modeling of sediment melt-modified mantle sources.....	96
<b>Figure A3.1:</b> Results of combining a single $^{231}\text{Pa}/^{233}\text{Pa}$ determination for the Ryan standard with multiple uranium isotope ( $^{235}\text{U}/^{233}\text{U}$ ) analyses, each of a separate batch of powder.....	107

<b>Figure A3.2:</b> U-Th-Ra-Pa results of modeling a secular equilibrium ( $(^{231}\text{Pa}/^{235}\text{U}) = 1$ ) source. ....	110
<b>Figure A3.3:</b> Primitive mantle-normalized sediment melt compositions. ....	117
<b>Figure A3.4:</b> Trace element and isotope mixing/melting plots calculated using the sediment melt composition shown in Fig. A3.3a, run C-1868. ....	118
<b>Figure 4.1:</b> Shaded relief map of the study area in central Oregon. ....	134
<b>Figure 4.2:</b> SiO <sub>2</sub> vs. alkali element plots for central Oregon lavas. ....	147
<b>Figure 4.3:</b> Harker-type major element variation diagrams for central Oregon lavas plotted against MgO. ....	149
<b>Figure 4.4:</b> Harker-type trace element variation diagrams for central Oregon lavas plotted against MgO. ....	151
<b>Figure 4.5:</b> Primitive mantle-normalized incompatible element ‘spidergrams’ (panel a) and chondrite-normalized REE profiles (panel b) for central Oregon lavas plotted by geographic groupings identified in Figure 4.1. ....	153
<b>Figure 4.6:</b> Isotopic data for central Oregon lavas. ....	159
<b>Figure 4.7:</b> MgO vs. ( $^{230}\text{Th}/^{238}\text{U}$ ) and ( $^{226}\text{Ra}/^{230}\text{Th}$ ) <sub>i</sub> plots for central Oregon lavas, symbols as Figure 4.4. ....	160
<b>Figure 4.8:</b> Trace element ‘spidergram’ mixing plots for Newberry group samples. ....	165
<b>Figure 4.9:</b> REE mixing plots for Newberry group samples. ....	166
<b>Figure 4.10:</b> H vs. H/M plots for central Oregon lavas. ....	169
<b>Figure 4.11:</b> Plots of various trace element ratios vs. ( $^{230}\text{Th}/^{238}\text{U}$ ) for central Oregon lavas. ....	171

<b>Figure 4.12:</b> Trace element ‘spidergram’ and REE profiles for the average Nash Crater and Belknap crustal melt end members. ....	175
<b>Figure 5.1:</b> Trace element data for Holocene felsic rocks from South Sister and Newberry and fields for regional mafic rocks. ....	205
<b>Figure 5.2:</b> U-Th-Pa-Sr-Nd isotope data for Holocene felsic rocks from South Sister and Newberry.....	207
<b>Figure 5.3:</b> Results of lower crustal partial melting models for South Sister and Newberry.....	209
<b>Figure 5.4:</b> ( $^{231}\text{Pa}/^{235}\text{U}$ ) and ( $^{230}\text{Th}/^{238}\text{U}$ ) modeling plots for South Sister and Newberry Holocene felsic rocks .....	211
<b>Figure A5.1:</b> Location maps of the study area in central Oregon. ....	226
<b>Figure A5.2:</b> Harker variation diagrams for Holocene felsic rocks from South Sister and Newberry.....	227
<b>Figure A5.3:</b> Plots of $\text{SiO}_2$ vs. $\text{Al}_2\text{O}_3$ , $\text{FeO}$ , $\text{CaO}$ , and $\text{MgO}$ for South Sister and Newberry Holocene rhyolites and the fields for experimentally produced glasses.....	230
<b>Figure A5.4:</b> Qtz-Ab-Or ternary plot for Holocene felsic rocks from South Sister and Newberry.....	231

## LIST OF TABLES

<b>Table A1.1</b> Sample age and location information.....	34
<b>Table 2.1</b> Major and trace element data for central Oregon lavas .....	47
<b>Table 2.2</b> U-Th-Ra-Sr-Nd isotope data for central Oregon lavas .....	56
<b>Table 2.3</b> Composition of mantle sources and slab components, and partition coefficients, used in modeling .....	65
<b>Table 3.1</b> U-Th-Pa isotope and trace element data for central Oregon lavas.....	92
<b>Table A3.1</b> Mantle sources, slab components, and partition coefficients used in trace element modeling.....	120
<b>Table 4.1</b> Major and trace element data for central Oregon lavas .....	139
<b>Table 4.2</b> U-Th-Ra-Pa-Sr-Nd isotope data for central Oregon lavas.....	155
<b>Table 4.3</b> Estimated composition of crustal melt components beneath the Three Sisters .....	173
<b>Table A4.1</b> U-Th-Ra-Sr-Nd column separation procedure .....	195
<b>Table A4.2</b> Pa column separation procedure .....	196
<b>Table 5.1</b> Major and trace element data for South Sister and Newberry rhyolites .....	204
<b>Table 5.2</b> U-Th-Ra-Pa-Sr-Nd isotope data for South Sister and Newberry rhyolites....	206

## **Chapter 1: Introduction**

### **1.1. Scope of the Dissertation**

The Oregon segment of the Cascade volcanic arc, including the rear-arc Newberry Volcanic Field, contains a truly remarkable density of Quaternary volcanoes, with at least 1500 vents in a volcanic belt 25 to 50 km wide, which extends along the crest of the Cascades for 340 km south of Mount Hood (Guffanti and Weaver, 1988; Hildreth, 2007). Within the Oregon segment, the Sisters reach (named for the Three Sisters volcanoes) contains more postglacial mafic eruptive units than any other region in the Cascades. Furthermore, eruption of true rhyolite, some of it postglacial as well, is unusually common in this reach also (Hildreth, 2007).

This dissertation seeks to take advantage of the profusion of young volcanic rocks in the Sisters reach of the Oregon Cascades through the application of uranium-series (U-series) isotope data to issues of magma generation and differentiation within the arc. Three broad themes will be addressed in the chapters to follow: (i) the slab and mantle processes, and associated timescales, that generate primary mantle-derived melts beneath the arc; (ii) the processes and timescales of crustal differentiation of those mantle melts; and (iii) the apparent connection between the abundant mafic and felsic volcanism in the region.

### **1.2. The Cascades**

#### *1.2.1. Tectonic Setting*

The Cascade arc is the surface expression of oblique, NE-directed subduction of the Juan de Fuca plate beneath North America (Fig. 1.1). The young slab (< 10 Ma at the trench)

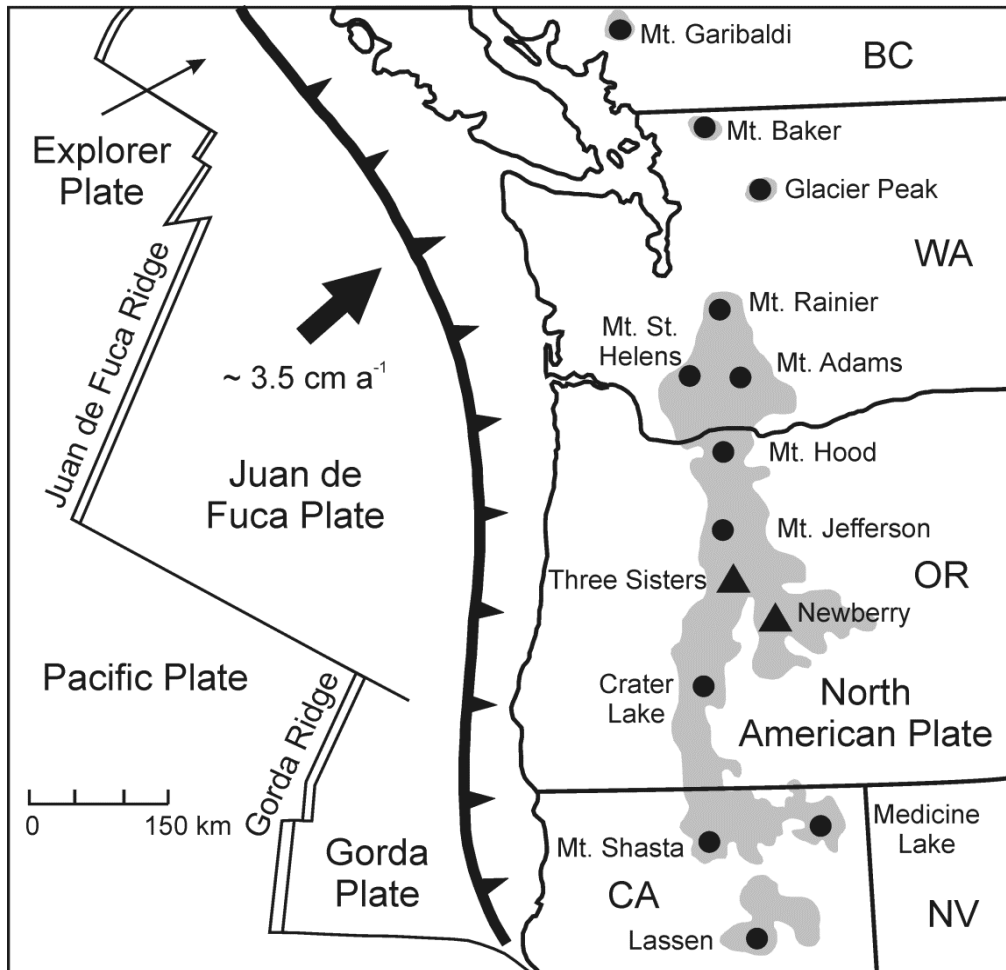


**Figure 1.1:** Tectonic setting of the central and southern Cascadia margin (after Luedke & Smith, 1982). The Juan de Fuca microplate is subducting to the NE beneath North America at  $\sim 3.5 \text{ cm a}^{-1}$ . Thick black line is the trench, teeth on overriding plate. Double and single lines along the Juan de Fuca plate boundary mark spreading centers and transform faults respectively. Shaded area shows the extent of the Quaternary High Cascades. Prominent volcanoes are indicated with circles and labeled. The study area lies in central Oregon in the vicinity of the Three Sisters volcanoes and Newberry Volcanic Field, marked with triangles.

is subducting to the NE at  $\sim 3.5 \text{ cm a}^{-1}$ , resulting in an anomalously warm subduction environment (Hyndman and Wang, 1993; Wilson, 2002). As such, the Cascadia subduction zone represents a hot slab end member in the global suite of convergent margins, with a slab thermal parameter of  $\sim 1.5$  to  $2.2 \text{ km}$  (Wada and Wang, 2009).

Thermal models predict slab surface temperatures of 850 to 950°C (Syracuse et al., 2010), up to 300°C hotter than in cooler subduction zones with older subducting slabs (Peacock, 2003). A lower thermal gradient within the subducting basaltic crust and lithospheric mantle (i.e. higher internal slab temperature) is predicted also by such models (van Keken et al., 2002). Elevated temperatures are indicated also by compositional proxies for slab surface temperature (Ruscitto et al., 2010; Cooper et al., 2012).

Such anomalously warm conditions are expected to result in shallow dehydration of the slab, which in this region of the arc lies at a depth of ~ 70 to 100 km (McCrorry et al., 2006; Obrebski et al., 2010) and dips ~ 50°E (Xue and Allen, 2007; Roth et al., 2008). This should lead to extensive serpentinization of the fore-arc mantle wedge, consistent with geochemical and geophysical observations (e.g., Bostock et al., 2002; Brocher et al., 2003; Hurwitz et al., 2005; Leeman et al., 2005; Rondenay et al., 2008). Extensive, early dehydration should result also in a reduced volatile flux to the sub-arc mantle wedge, as suggested by geochemical data (e.g., Green and Harry, 1999; Harry and Green, 1999; Leeman et al., 2005). Furthermore, the mantle wedge temperature is predicted to be unusually high, with transient temperatures near the base of the crust as high as 1300 to 1450°C beneath the northern California segment of the arc (Elkins Tanton et al., 2001), and similar inferred temperatures beneath northern Oregon and southern Washington (Leeman et al., 2005).

A number of tectonic factors strongly control volcanism in central Oregon. A combination of oblique convergence between North America and the Juan de Fuca microplate (Wilson, 2002), dextral shear between the Pacific and North American plates

(Atwater, 1970), and impingement of Basin and Range extension (Lawrence, 1976; Jones et al., 1996), has resulted in clockwise rotation of the Oregon fore-arc block and east-west intra-arc extension since at least 5 Ma (Wells et al., 1998; Hildreth, 2007; McCaffrey et al., 2007). The surface expression of this intra-arc extension in central Oregon has been the formation and subsequent northward propagation of the High Cascades graben, marked by the western Horse Creek and eastern Green Ridge fault zones, and numerous north-south vent alignments (Sherrod and Smith, 1990; Conrey et al., 2002; Hildreth, 2007). Graben width and vent density both reach a maximum in the Three Sisters region (Guffanti and Weaver, 1988), probably as a result of intersection with the arc of the Basin and Range-related Brother's fault zone.

The Quaternary arc, which extends from Mt. Meager, in British Columbia, to Mt. Lassen, in northern California, a distance of ~ 1250 km, is defined by the location of large, andesitic and dacitic stratovolcanoes (e.g., Mt. Baker, Mt. Rainier, Mt. Hood, Mt. Jefferson, Mt. Shasta) (Hildreth, 2007). Volumetrically, however, the arc output is dominated by small, mafic, monogenetic vents and shield volcanoes (Hildreth, 2007). This is especially true in the Sisters reach of the Oregon segment, the locus of the most voluminous episode of postglacial mafic volcanism (Hildreth, 2007). The study area lies within the High Cascades graben in the vicinity of the Three Sisters, between the stratovolcanoes of Three-Fingered Jack and Mt. Bachelor, and extends also to the rear-arc Newberry Volcanic Field (Fig. 1.2). The Newberry edifice appears to occupy a unique tectonic niche, where the southeast trending Sisters fault zone, a continuation of the eastern graben-defining Green Ridge fault zone, merges with the Brothers fault zone, which extends across eastern Oregon into the Basin and Range province (Jordan et al.,

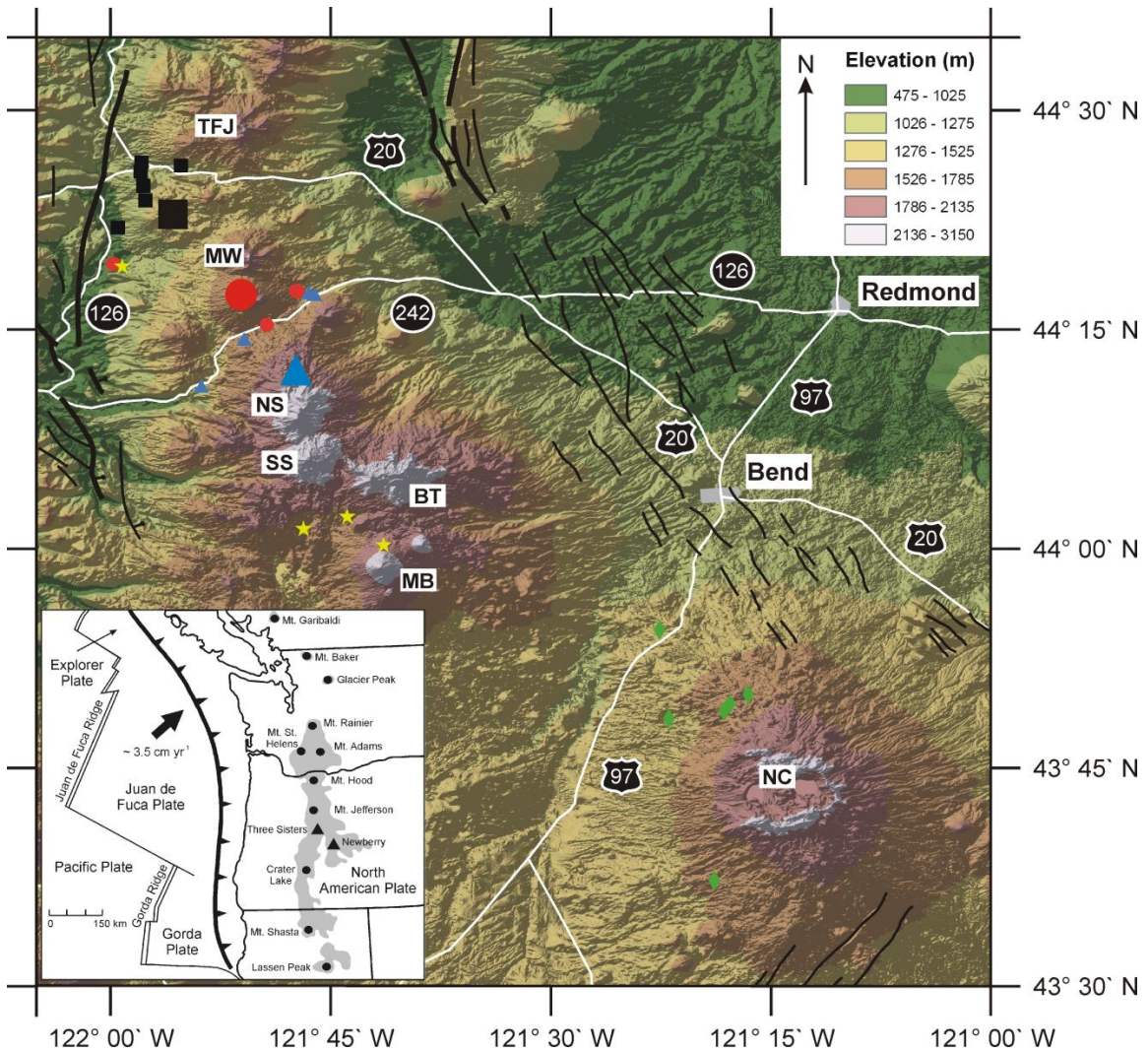


**Figure 1.2:** Shaded relief map of the study area in central Oregon. Prominent volcanoes are labeled: TFJ = Three Fingered Jack, MW = Mt. Washington, NS = North Sister, SS = South Sister, BT = Broken Top, MB = Mt. Bachelor, and NC = Newberry caldera. Mafic sample localities are shown with white circles and felsic sample localities are shown with white squares. Black lines are faults, ball and bar on downthrown side. Thin lines show faults with < 300 m displacement and thick lines show faults with > 300 m displacement (Sherrod et al., 2004). Major towns and roads in the area are marked also.

2004; Sherrod et al., 2004). The Three Sisters/Newberry region lies at the leading northwestern edge of a crustal-melting anomaly that has propagated across the High Lava

Plains of southeastern Oregon since the middle Miocene (10-15 Ma), generating a bimodal basalt-rhyolite volcanic field (MacLeod et al., 1975; Jordan et al., 2004).

The arc crust is interpreted to be ~ 40 to 45 km thick in central Oregon (Stanley et al., 1990; Eagar et al., 2011), consisting of mafic amphibolites and granulites in the middle and lower crust respectively (Stanley et al., 1990; Conrey et al., 2001). Underplating of voluminous quantities of mafic magma to the base of the crust is responsible in part for the presence of mafic granulite in the lower crust (Conrey et al., 2001).

### *1.2.2. High Cascades Magmatism*

The Cascade arc has been active since ~ 40 Ma (Lux, 1982; Phillips et al., 1986) and in the Oregon segment is divided into two geographic provinces, the Western Cascades (40-10 Ma) and the High Cascades (10-0 Ma). Magmatism in the central Oregon High Cascades has been especially voluminous since initiation of intra-arc rifting ~ 5 Ma (Sherrod and Smith, 1990; Conrey et al., 2002). The compositional diversity of basalts erupted in Oregon encompasses much of the diversity observed within the broader arc.

At least five distinct basaltic compositions have been recognized in the Oregon Cascades, distinguished largely on the basis of trace element concentrations (Hughes and Taylor, 1986; Bacon, 1990; Hughes, 1990; Leeman et al., 1990; 2005; Bacon et al., 1994; 1997; Conrey et al., 1997; 2001; Schmidt et al., 2008; Rowe et al., 2009). These compositions are commonly referred to as low-K tholeiitic basalt (LKT, also called high-alumina olivine tholeiite (HAOT) or MORB-like basalt), ocean island-like basalt (OIB, also called high field strength element (HFSE)-enriched or intraplate basalt), calc-alkaline basalt (CAB), shoshonitic basalt (SHO, including absarokite), and high-Mg

basaltic andesite (BA). LKTs and intraplate basalts are commonly grouped together because they appear to have been derived from a mantle source little modified by a subduction component, and were labeled Group I basalts by Leeman et al. (2005). CABs, SHOs, and high-Mg BAs are interpreted as products of a source more extensively fluxed by slab-derived fluids, and were designated Group II basalts by Leeman et al. (2005).

LKT basalts are compositionally similar to E-MORB, but with slight Sr and Ba enrichments (Leeman et al., 2005). LKT REE patterns are flat and lack HREE depletion, suggesting shallow final equilibration in the uppermost mantle (Hildreth, 2007), consistent with phase equilibria, which imply final equilibration with spinel lherzolite at ~ 1300°C and ~ 11 to 15 kb (Bartels et al., 1991; Baker et al., 1994; Elkins-Tanton et al., 2001). Intraplate basalts resemble OIB-lavas in their enrichment of high field strength elements, notably Nb and Ta, and are nepheline- or hypersthene-normative (Hildreth, 2007). In addition to distinctive trace element concentrations, Group I lavas have low water contents (Anderson, 1973; Sisson and Grove, 1993; Le Voyer et al., 2010), MORB-like  $\delta^7\text{Li}$  (Leeman et al., 2004), and generally lower  $^{87}\text{Sr}/^{86}\text{Sr}$  than CABs from the same region (Schmidt et al., 2008). LKTs are found almost exclusively in parts of the arc undergoing lithospheric extension, while intraplate basalts are most common in southern Washington, rare in northern and central Oregon, and unknown in southern Oregon and northern California (Hildreth, 2007). Group I lavas are most commonly interpreted as high temperature, anhydrous decompression melts of relatively fertile, essentially MORB-like (LKT) and more enriched (intraplate) mantle sources.

CABs are the dominant Group II variant and are found throughout the arc. They were described by Hildreth (2007) as “the paradigmatic arc suite” (p. 79) due to their

enrichment in large ion lithophile elements (LILE) and light rare earth elements (LREE), and depletion in high field strength elements (HFSE) and heavy rare earth elements (HREE). Fractionated REE profiles suggest derivation from a deeper, garnet-bearing, source than Group I lavas. Group II lavas also have higher water contents and  $^{87}\text{Sr}/^{86}\text{Sr}$  than Group I lavas (Anderson, 1979; Sisson and Grove, 1993; Grove et al., 2002; Schmidt et al., 2008; Le Voyer et al., 2010; Ruscitto et al., 2010), more variable  $\delta^7\text{Li}$  (Magna et al., 2006), and are more oxidized (Righter, 2000). The high-Mg BAs and shoshonites are interpreted as high and low degree melts, respectively, of extensively fluxed mantle sources (Hildreth, 2007). In general, Group II lavas are usually interpreted to represent the standard paradigm of fluid-fluxed melting of a more refractory mantle wedge. However, Leeman et al. (2005) interpreted Group II lavas to be decompression melts of relatively shallow, previously metasomatized mantle sources, while Reiners et al. (2000) suggested that both Group I and II lavas are the products of flux melting.

Clearly there are unanswered questions about magma generation in the Cascade arc, particularly concerning the role of slab-derived fluids, the timing of addition of slab-derived fluids to the mantle wedge in relation to initiation of melting, and the depth/mineralogy of the mantle source(s). Uranium-series isotope fractionation is sensitive to the magnitude and timing of fluid addition, as well as residual mineralogy during melting, thus U-series isotopes are an ideal tool with which to attempt to resolve some of these issues. The details of U-series isotope systematics are more fully addressed in Section 1.3.

### *1.2.3. Field Area and Samples*

The field area for this study largely lies within the Mt. Jefferson, Mt. Washington, and Three Sisters Wilderness areas, as well as the Newberry National Volcanic Monument, which are protected by the Deschutes and Willamette National Forests, near Bend, Oregon. Access to the Three Sisters region is possible from numerous trailheads along Cascade Lakes Highway/Century Drive (Hwy 46) south of the Three Sisters, McKenzie Pass Highway (Hwy 242) north of the Three Sisters, and Santiam Pass Highway (Hwy 20) north of Mt. Washington (Fig. 1.2). Numerous Forest Service roads criss-cross the flanks of Newberry volcano.

There is a long history of geological and volcanological work in this region, starting with that of Hodge (1925) and Williams (1944) in the Three Sisters region, and Williams (1935) at Newberry. The Three Sisters field area lies within the Bend 30- x 60-Minute Quadrangle (Sherrod et al., 2004) and the central part is included in a more recent map of the Three Sisters volcanic cluster (Hildreth et al., 2012). The most recent geologic map of Newberry is that of MacLeod et al. (1995). Hildreth (2007) presented an overview of the entire Quaternary Cascade arc.

The Three Sisters volcanoes (North, Middle, and South) are surrounded by an older, early Pleistocene mafic platform (McBirney et al., 1974; Hughes and Taylor, 1986; Hughes, 1990; Taylor, 1990). North Sister is the oldest and most mafic of the Three Sisters, and has erupted a compositionally monotonous basaltic andesite since ~ 120 ka (Schmidt and Grunder, 2009). South Sister repeatedly, and alternately, erupted rhyolitic and intermediate magmas between 50 and 2 ka (Fierstein et al., 2011). Middle Sister is a basaltic to dacitic volcano active mostly between 25 and 18 ka (Hildreth et al., 2012).

Newberry is a large shield volcano, capped by a late Pleistocene caldera, which was active as early as 0.6 Ma (MacLeod et al., 1995). Volcanic activity at Newberry has been distinctly bimodal, with a central rhyolite-rich core and extensive mafic flank eruptions (Hildreth, 2007).

Numerous postglacial mafic eruptions have occurred around the periphery of the Three Sisters, from Egan Cone on the flank of Mt. Bachelor in the south, to the Sand Mountain and Nash Crater fields in the north (Sherrod et al., 2004). Postglacial activity in the immediate vicinity of the Three Sisters volcanoes includes eruptions from Collier Cone, Four-in-One Cone, and Yapoah Crater, all to the north of North Sister, as well as from Cayuse and Le Conte Craters around South Sister, among others (Hildreth et al., 2012). A brief pulse of rhyolitic activity occurred on the flanks of South Sister around 2.3 to 2.0 ka (Scott, 1987). Holocene activity at Newberry has continued the pronounced bimodal association there, with mafic eruptions on the flanks, mostly concentrated along the northwest rift zone (Linneman, 1990; McKay et al., 2009), and rhyolitic activity restricted to the central caldera (Linneman, 1990).

A total of twenty nine samples were collected from the Three Sisters/Newberry area in Fall 2007 and Summer 2008 (Appendix A1). Of these twenty nine samples, eighteen were collected from mafic flows in the Three Sisters region and a further six were collected from mafic flows on the flanks of Newberry volcano. The remaining five samples are from rhyolitic units, three from the south flank of South Sister and two from Newberry caldera. All twenty nine samples were analyzed for major and trace elements, U-Th-Ra, and Sr-Nd isotopes. Additionally, U-Pa data were obtained for twenty four of these samples.

These samples represent nearly every Holocene flow in the Three Sisters area and the majority of the large flows from the northwest rift zone eruption at Newberry. Road closure along a significant stretch of Highway 242 in the vicinity of McKenzie Pass in the Summer of 2008 prevented planned sample collection from the Twin Craters and Sims Butte flows, as well as further sample collection from the Four-in-One Cone flow near the vent.

Two samples have been re-assigned to different flows since collection. The sample locality for 07-NC-01 is within the ‘Northwest Nash Crater Flow’ unit of Sherrod et al. (2004), but geochemical and isotopic data (Chapter 4) suggest it may belong to the adjacent un-named Sand Mountain flow to the east. Sample 08-WIC-01 was believed to have been collected from the westernmost inlier of unit Qybic from Inaccessible Cone (Sherrod et al., 2004), although the porphyritic nature and secular equilibrium ( $^{226}\text{Ra}/^{230}\text{Th}$ ) value suggest it actually belongs to the adjacent Pleistocene unit.

### **1.3. Uranium-Series Isotope Systematics**

The uranium-series (U-series) decay chains consist of the intermediate nuclides produced by the decay of  $^{238}\text{U}$  to  $^{206}\text{Pb}$  and  $^{235}\text{U}$  to  $^{207}\text{Pb}$  (as well as  $^{232}\text{Th}$  to  $^{208}\text{Pb}$ ) (Fig. 1.3). The first publication of a radioactive decay chain, a “uranium-series”, occurred in 1903 (Rutherford, 1903), only a few short years after the discovery of radioactivity (Becquerel, 1896; Curie, 1898). The recognition that the same element could take different forms, with different masses and half-lives, led Soddy to coin the term “isotope” (Soddy, 1913a), leading, exactly 100 years ago, to the first U-series decay chains plotted as a function of mass against atomic number (Fajans, 1913; Soddy, 1913b). The first application of the  $^{238}\text{U}$ - $^{230}\text{Th}$  dating method, to marine sediments, was published by

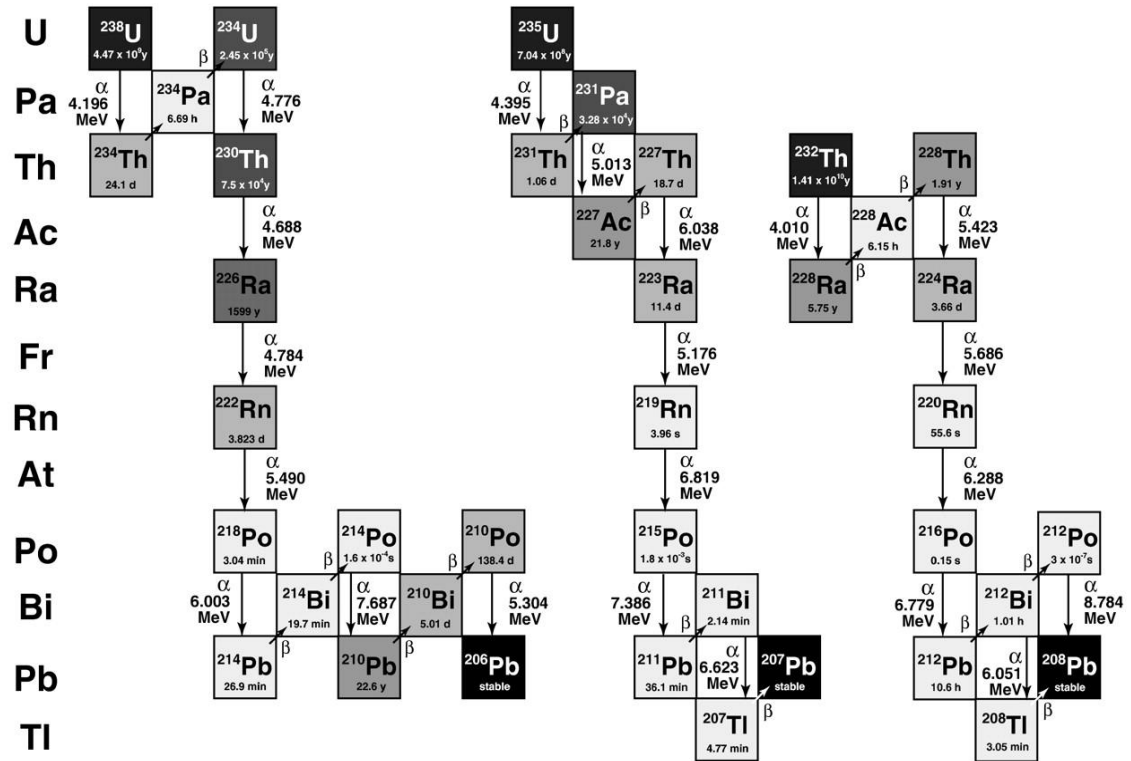


**Figure 1.3:** Schematic illustration of the three uranium-series decay chains (Bourdon et al., 2003a). Shading of each nuclide is proportional to half-life, with longer half-life nuclides shown in darker tones. Of interest in this study are the  $^{238}\text{U}$ - $^{230}\text{Th}$ - $^{226}\text{Ra}$  and  $^{235}\text{U}$ - $^{231}\text{Pa}$  systems.

Piggott and Urry (1942), although it was not until the development of alpha spectrometry a decade and a half later that measurement of  $^{230}\text{Th}$  became routine. Further significant advances occurred in the late 1980s with the development of thermal ionization mass spectrometry (TIMS) techniques, and more recently with the development of multi-collector inductively coupled plasma mass spectrometry (MC-ICPMS) and the introduction of actinide-specific resins for enhanced chemical separation (Goldstein and Stirling, 2003).

The  $^{238}\text{U}$  decay chain is the one applied most commonly to geological problems.  $^{238}\text{U}$  (half-life ( $t_{1/2}$ )  $\sim 4.47 \times 10^9$  yr) decays to  $^{234}\text{U}$  ( $t_{1/2} \sim 2.45 \times 10^5$  yr) via the very short-lived nuclides  $^{234}\text{Th}$  and  $^{234}\text{Pa}$ . Subsequent decay of  $^{234}\text{U}$  (which should not be fractionated from  $^{238}\text{U}$  by magmatic processes) produces the two most commonly utilized nuclides in petrologic studies,  $^{230}\text{Th}$  ( $t_{1/2} \sim 7.5 \times 10^4$  yr) and its daughter,  $^{226}\text{Ra}$  ( $t_{1/2} = 1599$  yr). Within the last decade or so, the  $^{235}\text{U}$  decay chain, starting with decay of  $^{235}\text{U}$  ( $t_{1/2} \sim 7.04 \times 10^8$  yr) via the very short-lived nuclide  $^{231}\text{Th}$  to  $^{231}\text{Pa}$  ( $t_{1/2} \sim 3.28 \times 10^4$  yr), has started to receive considerable interest too.

The application of measured disequilibrium between any two U-series nuclides to problems of geologic interest is predicated on the knowledge that, regardless of the initial degree of disequilibrium, the steady-state condition of secular equilibrium, where the activity ratio of the two nuclides is equal to one, will be re-attained after  $\sim 5$  to 7 half-lives of the shorter-lived nuclide (the daughter in all cases). The activity of any nuclide is defined as the number of atoms multiplied by the decay constant,  $\lambda$  ( $\lambda = \ln 2/t_{1/2}$ ). The nuclides  $^{230}\text{Th}$ ,  $^{231}\text{Pa}$ , and  $^{226}\text{Ra}$  are useful tools for investigating geologic processes because their half-lives are similar to the timescales of many geologic processes, and because they are fractionated from one another, and from their parent U nuclides, by a variety of different geological processes, such as partial melting and fractional crystallization.

The most widely measured U-series nuclide pair in volcanic rocks is  $^{238}\text{U}$ - $^{230}\text{Th}$ . Uranium is a fluid mobile element, while thorium is assumed to be largely immobile in fluids (e.g., Cochran and Masque, 2003; Goldstein and Stirling, 2003; Porcelli and Swarzenski, 2003), thus dehydration of subducting slabs should produce fluids with

elevated U/Th ratios, and therefore  $^{238}\text{U}$ -excesses (i.e.  $(^{230}\text{Th}/^{238}\text{U}) < 1$ , where parentheses indicate activity ratios). While both elements are, in general, highly incompatible in most mantle minerals (e.g., olivine, clinopyroxene, orthopyroxene, spinel, and garnet; Blundy and Wood, 2003), uranium is slightly more compatible than thorium ( $D_{\text{U}}/D_{\text{Th}} > 1$ ) in some important minerals, notably garnet and aluminous clinopyroxene (e.g., Beattie, 1993; LaTourette et al., 1993; Wood et al., 1999). Therefore, partial melting at depths  $> \sim 60$  km should generate a melt with excess  $^{230}\text{Th}$  (i.e.  $(^{230}\text{Th}/^{238}\text{U}) > 1$ ). These contrasting chemical properties explain the observation that arc lavas typically have  $(^{230}\text{Th}/^{238}\text{U}) < 1$ , due to addition of U-rich fluids to the mantle wedge, while MORB and OIB lavas have  $(^{230}\text{Th}/^{238}\text{U}) > 1$  (e.g., Lundstrom, 2003; Turner et al., 2003) (Fig. 1.4).

Radium is both more fluid mobile, and more incompatible, than its parent thorium, and as a result arc, MORB, and OIB lavas almost exclusively have  $(^{226}\text{Ra}/^{230}\text{Th}) > 1$ , although arc lava excesses can extend to much higher values (Fig. 1.4). Protactinium is expected to behave in a similar fashion to thorium, as both are fluid immobile and more incompatible than the parent uranium (e.g., Guillaumont et al., 1986; Blundy and Wood, 2003; Goldstein and Stirling, 2003). However, arc lavas generally have  $(^{231}\text{Pa}/^{235}\text{U}) > 1$  (e.g., Turner et al., 2003) (Fig. 1.4), which is interpreted to reflect the dominant role of melting, rather than fluid addition, in controlling  $^{235}\text{U}$ - $^{231}\text{Pa}$  systematics (e.g., Bourdon et al., 1999; 2003b; Thomas et al., 2002; Dosseto et al., 2003; Turner et al., 2006).

It has been recognized recently that a number of accessory phases (e.g., allanite, apatite, monazite, rutile, and zircon) have partition coefficients for one or more of the U-series elements that are orders of magnitude larger than in typical mantle phases (e.g.,

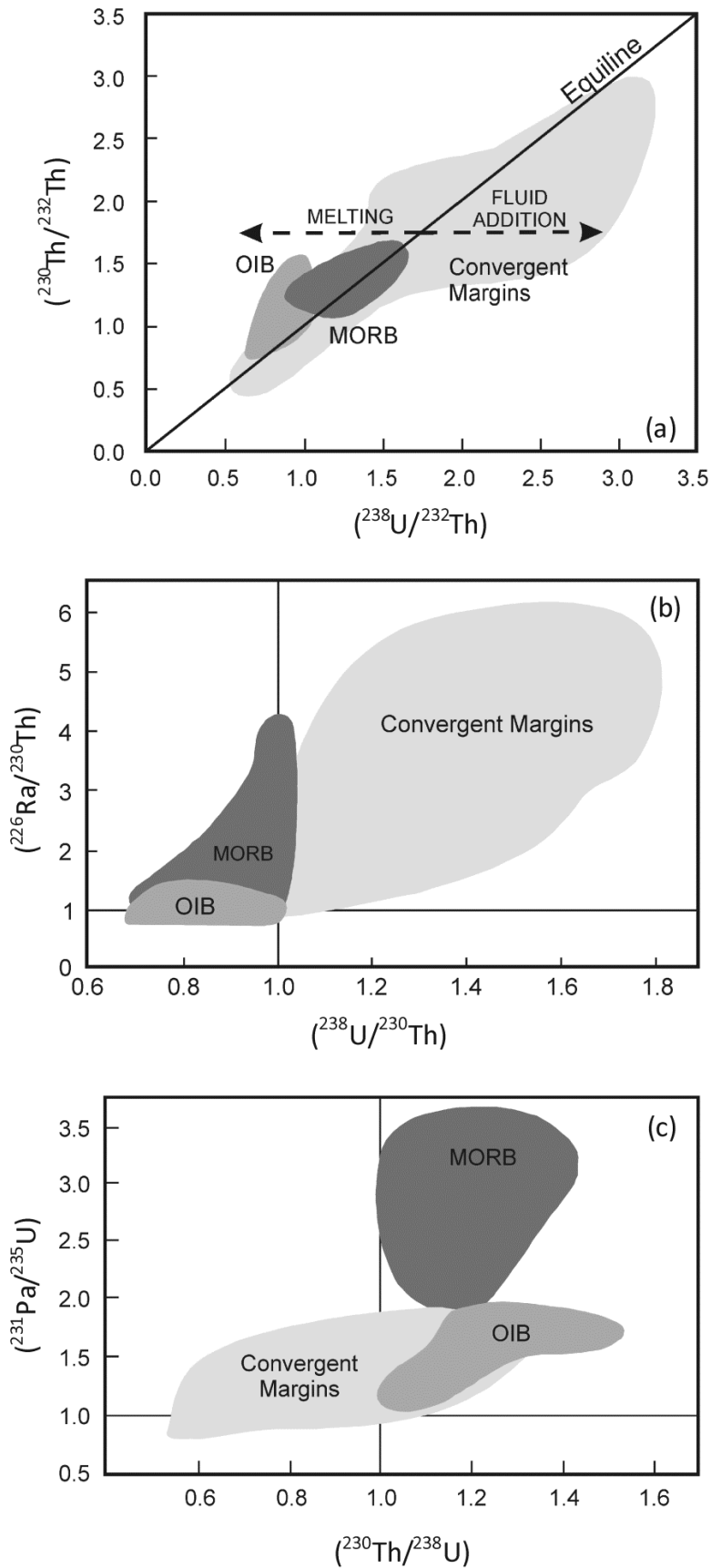


**Figure 1.4:** U-series isotope activity ratio diagrams, showing fields for arc lavas, mid-ocean ridge basalts (MORB), and ocean-island basalts (OIB) (after Lundstrom, 2003). Panel (a):  $(^{238}\text{U}/^{232}\text{Th})$  vs.  $(^{230}\text{Th}/^{232}\text{Th})$  plot. Diagonal line is the secular equilibrium 'equiline'. Panel (b):  $(^{238}\text{U}/^{230}\text{Th})$  vs.  $(^{226}\text{Ra}/^{230}\text{Th})$ . Panel (c):  $(^{230}\text{Th}/^{238}\text{U})$  vs.  $(^{231}\text{Pa}/^{235}\text{U})$ .

Hermann, 2002; Klemme et al., 2005; Prowatke and Klemme, 2006; Schmitt, 2007; Stepanov et al., 2012; Nardi et al., 2013). Therefore, the presence of these phases, for example during dehydration and/or melting of subducted oceanic crust and/or sediments, or in felsic liquids, will exert a strong control on the generation of U-series disequilibria.

Further constraints can be placed on the generation of U-series disequilibria during mantle melting with the application of numerical models that explicitly include the duration of the melting process. A number of such 'ingrowth' models have been developed (e.g., McKenzie, 1985; Williams and Gill, 1989; Spiegelman and Elliott, 1993). In all these models melt and solid phases coexist but move independently, creating different 'effective velocities', and therefore different residence times in the melting column, for elements with different D values. In the simplest such 'dynamic melting' models (McKenzie, 1985; Williams and Gill, 1989), residence time differences are created during the initial stages of melting as the more incompatible element preferentially partitions into the melt phase once some critical porosity is reached, and thereafter melt transport is treated as instantaneous. In more complex 'equilibrium transport' models, chemical equilibrium during transport and/or the melt ascent time are explicitly accounted for (Spiegelman and Elliott, 1993). All else being equal, these equilibrium transport models generate greater disequilibrium than dynamic melting models (Lundstrom, 2003). Most recently, flux melting models, in which addition of slab-derived fluids initiates melting of the mantle wedge, have been developed. These models include the amount and rate of fluid addition, which influences the degree of melting, as well as the solubility of nuclides of interest in the slab fluids (e.g., Thomas et al., 2002; Bourdon et al., 2003b).

#### **1.4. U-series isotope systematics of mafic magmas from central Oregon: Implications for fluid involvement and melting processes in the Cascade arc (Chapter 2)**

This chapter focuses on the elemental and isotopic ( $^{87}\text{Sr}/^{86}\text{Sr}$ ,  $^{143}\text{Nd}/^{144}\text{Nd}$ ,  $^{238}\text{U}$ - $^{230}\text{Th}$ - $^{226}\text{Ra}$ ) composition of the most primitive samples in the suite to address the source and amount of fluid added to the sub-arc mantle wedge, the composition of that mantle source, and the nature, extent, and timing of melting of that mantle source. The trace element and long-lived isotope data indicate < 10% melting following minimal (~ 1%) addition of a fluid derived from subducting sediments to an enriched, garnet-bearing mantle source. The U-series data are consistent with dynamic melting of such a source, although the small degree of fluid addition required does not permit distinction between scenarios where fluid addition was the trigger for melting, and ones in which it was an older event, unrelated to initiation of melting.

This chapter was published in Earth and Planetary Science Letters (Mitchell and Asmerom, 2011). The analytical work, interpretations, and writing are all my own. My co-author and advisor, Yemane Asmerom, assisted with initial sample collection and contributed feedback on earlier versions of the manuscript.

#### **1.5. Extreme $^{231}\text{Pa}$ -enrichment in young Cascade arc lavas - signature of sediment melting in a warm arc? (Chapter 3)**

This chapter builds upon the data presented in Chapter 2 by presenting the first ( $^{231}\text{Pa}/^{235}\text{U}$ ) data for lavas from the Cascade arc. The ( $^{231}\text{Pa}/^{235}\text{U}$ ) data are two to four times higher than any data previously reported in arc lavas, or in lavas from any other

tectonic setting, and cannot have been generated solely by partial melting processes in the mantle wedge.

It is proposed that the unusually hot conditions in the subducting Juan de Fuca slab beneath the arc, a result of both the slow subduction and young age of the slab, control the accessory phase assemblage present. In particular, the temperature within the subducting slab during sediment melting is inferred to exceed that at which phases normally present in cooler slabs, such as allanite, monazite, and zircon, are exhausted from the residue, generating a highly  $^{231}\text{Pa}$ -enriched melt component.

These conclusions differ significantly from standard interpretations of arc lava ( $^{231}\text{Pa}/^{235}\text{U}$ ) disequilibria, which are usually attributed to Pa ingrowth during partial melting overprinting the effects of U-rich fluid addition. If correct, the interpretation presented in this chapter constrains the timing of fluid addition to the mantle wedge beneath the arc to  $\ll 150$  k.y. prior to the onset of melting, conclusively resolving this issue in central Oregon. An alternative interpretation of the data questions the entire prevailing paradigm of arc magma generation.

This chapter is in preparation for submission to Science. The analytical work, interpretations, and writing are all my own. My co-author and advisor, Yemane Asmerom, contributed feedback on earlier versions of the manuscript.

#### **1.6. Crustal modification of mantle-derived U-series isotope signatures: A case study from the central Oregon Cascades (Chapter 4)**

Primary melt compositions are unknown in the Cascades, and primitive magmas are rare. The majority of erupted lavas have been modified from their parental melt composition

during passage through, and residence in, the ~ 45 km thick overlying arc crust. The aim of this chapter is to use the same dataset presented in Chapters 2 and 3 to identify the processes responsible for differentiation of mantle-derived melts in central Oregon, and the effects of these processes on U-series isotope activity ratios. The conclusions have implications for the use of U-series and melt inclusion data, especially from continental margins, in evaluating source processes.

The data indicate that different processes, occurring at different levels within the crust as a result of local tectonic factors, are controlling magma evolution in the Three Sisters region and at Newberry. In the Three Sisters region, mantle-derived melts are interacting with a mafic, lower crustal component, likely a partial melt of mafic granulite and/or the residual liquid from incomplete fractional crystallization of earlier intruded mafic melts. This lower crustal component is chemically and isotopically similar to the erupted lavas, making the signature of crustal interaction especially cryptic. Linear trends in U-series activity ratios are an effective indicator of this subtle crustal interaction. At Newberry, in contrast, evolution of mantle-derived melts appears to be controlled dominantly by assimilation of felsic upper crust.

These contrasting processes have different effects on U-series activity ratios, with bulk assimilation at Newberry driving activity ratios closer to one (i.e. secular equilibrium), while beneath the Three Sisters interaction with a non-equilibrium component can both decrease and increase mantle-derived activity ratios. This runs counter to the normal assumption that differentiation serves only to lower activity ratios.

The analytical work, interpretations, and writing are all my own. My co-author and advisor, Yemane Asmerom, contributed feedback on earlier versions of the manuscript.

### **1.7. $^{238}\text{U}$ - $^{230}\text{Th}$ - $^{226}\text{Ra}$ and $^{235}\text{U}$ - $^{231}\text{Pa}$ constraints on rhyolite generation at South Sister and Newberry volcanoes, central Oregon Cascades (Chapter 5)**

The central Oregon Cascades are the locus of the most voluminous episode of postglacial mafic magmatism in the arc, but the region is also unusual for the amount of true rhyolite (> 72 wt.%  $\text{SiO}_2$ ) erupted along the axis of the arc. It seems likely that these two unusual characteristics are related in some fashion. This chapter investigates the elemental and isotopic characteristics of two sets of Holocene felsic magmas, the Devils Hill/Rock Mesa rhyolites of South Sister, and the intracaldera obsidians of Newberry volcano, in an attempt to understand the details of the relationship between mafic and felsic volcanism.

The two sets of lavas have similar, but subtly distinct, major element compositions, and these distinctions become more apparent when considering the trace element and isotopic data. The South Sister lavas are most consistent with an origin via partial melting of mafic amphibolite in the lower crust, with minor assimilation and fractional crystallization at shallower depths prior to eruption. The Newberry lavas are interpreted as melts of upper crustal granitic intrusions, likely emplaced during the late Pleistocene and likely originating ultimately as lower crustal melts also. The U-series data are able to place further constraints on these processes than is possible from consideration of the trace element data alone.

Chapters 4 and 5 both reach similar conclusions regarding the dominant depth in the crust beneath the Three Sisters and Newberry at which magma differentiation and generation processes are occurring. This is suggested to result from local tectonic factors,

where extension, and intra-arc graben faults, around the Three Sisters facilitate rapid ascent and eruption of magma from the lower crust, with minimal upper crustal interaction. At Newberry, in contrast, mantle and/or lower crustal melts are interpreted to be prevented from reaching the surface within the caldera, where only re-melted upper crust can be erupted, with mafic melts restricted to flank eruptions along rift zones.

This chapter is in preparation for submission to *Geophysical Research Letters*. The analytical work, interpretations, and writing are all my own. My co-author and advisor, Yemane Asmerom, contributed feedback on earlier versions of the manuscript.

## References

- Anderson, A. (1973). The before-eruption water content of some high-alumina magmas. *Bulletin of Volcanology* **37**, 530-552.
- Anderson, A. (1979). Water in some hypersthenic magmas. *Journal of Geology* **87**, 509-531.
- Atwater, T. (1970). Implications of plate tectonics for the Cenozoic evolution of western North America. *Geological Society of America Bulletin* **81**, 3513-3536.
- Bacon, C. R. (1990). Calc-alkaline, shosonitic, and primitive tholeiitic lavas from monogenetic volcanoes near Crater Lake, Oregon. *Journal of Petrology* **31**, 135-166.
- Bacon, C. R., Gunn, S. H., Lanphere, M. A. & Wooden, J. L. (1994). Multiple isotopic components in Quaternary volcanic rocks of the Cascade arc near Crater Lake, Oregon. *Journal of Petrology* **35**, 1521-1556.
- Bacon, C. R., Bruggman, P. E., Christiansen, R. L., Clynne, M. A., Donnelly-Nolan, J. M. & Hildreth, W. (1997). Primitive magmas at five Cascade volcanic fields; melts from hot, heterogeneous sub-arc mantle. *The Canadian Mineralogist* **35**, 397-423.
- Baker, M. B., Grove, T. L. & Price, R. (1994). Primitive basalts and andesites from the Mt. Shasta region, N. California: products of varying melt fraction and water content. *Contributions To Mineralogy and Petrology* **118**, 111-129.
- Bartels, K., Kinzler, R. & Grove, T. (1991). High pressure phase relations of primitive high-alumina basalts from Medicine Lake volcano, northern California. *Contributions To Mineralogy and Petrology* **108**, 253-270.
- Beattie, P. (1993). Uranium-thorium disequilibria and partitioning on melting of garnet peridotite. *Nature* **363**, 63-65.
- Becquerel, A. H. (1896). On the invisible rays emitted by phosphorescent bodies. *Comptes Rendus de Seances de l'Academie de Sciences* **122**, 501-503.
- Blundy, J. & Wood, B. (2003). Mineral-melt partitioning of uranium, thorium and their daughters. *Reviews in Mineralogy and Geochemistry* **52**, 59-123.

- Bourdon, B., Turner, S. & Allegre, C. J. (1999). Melting dynamics beneath the Tonga-Kermadec island arc inferred from  $^{231}\text{Pa}$ - $^{235}\text{U}$  systematics. *Science* **286**, 2491-2493.
- Bourdon, B., Turner, S., Henderson, G. M. & Lundstrom, C. C. (2003a) Introduction to U-series geochemistry. *Reviews in Mineralogy and Geochemistry* **52**, 1-21.
- Bourdon, B., Turner, S. & Dosseto, A. (2003b). Dehydration and partial melting in subduction zones: Constraints from U-series disequilibria. *Journal of Geophysical Research* **108**, doi:10.1029/2002JB001839.
- Bostock, M. G., Hyndman, R. D., Rondenay, S. & Peacock, S. M. (2002). An inverted continental Moho and serpentinization of the forearc mantle. *Nature* **417**, 536-538.
- Brocher, T. M., Parsons, T., Trehu, A. M., Snelson, C. M. & Fisher, M. A. (2003). Seismic evidence for widespread serpentinized forearc upper mantle along the Cascadia margin. *Geology* **31**, 267-270.
- Cochran, J. K. & Masqué, P. (2003). Short-lived U/Th-series radionuclides in the ocean: Tracers for scavenging rates, export fluxes and particle dynamics. *Reviews in Mineralogy and Geochemistry* **52**, 461-492.
- Conrey, R. M., Sherrod, D. R., Hooper, P. R. & Swanson, D. A. (1997). Diverse primitive magmas in the Cascade Arc, northern Oregon and southern Washington. *The Canadian Mineralogist* **35**, 367-396.
- Conrey, R. M., Hooper, P. R., Larson, P. B., Chesley, J. & Ruiz, J. (2001). Trace element and isotopic evidence for two types of crustal melting beneath a High Cascade volcanic center, Mt. Jefferson, Oregon. *Contributions to Mineralogy and Petrology* **141**, 710-732.
- Conrey, R. M., Taylor, E. M., Donnelly-Nolan, J. M. & Sherrod, D. (2002). North-Central Oregon Cascades: Exploring petrologic and tectonic intimacy in a propagating intra-arc rift. In: Moore, G. (Ed.) Field Guide to Geologic Processes in Cascadia. *Oregon Department of Geology & Mineral Industries Special Paper* **36**, 47-90.
- Cooper, L. B., Ruscitto, D. M., Plank, T., Wallace, P. J., Syracuse, E. M. & Manning, C. E. (2012). Global variations in  $\text{H}_2\text{O}/\text{Ce}$ : 1. Slab surface temperatures beneath

- volcanic arcs. *Geochemistry Geophysics Geosystems* **13**,  
doi:10.1029/2011GC003902.
- Curie, M. (1898). Rays emitted by compounds of uranium and thorium. *Comptes Rendus de Seances de l'Academie de Sciences* **126**, 1101-1103.
- Dosseto, A., Bourdon, B., Joron, J. L. & Dupre, B. (2003). U-Th-Pa-Ra study of the Kamchatka arc: new constraints on the genesis of arc lavas. *Geochimica et Cosmochimica Acta* **67**, 2857-2877.
- Eagar, K. C., Fouch, M. J., James, D. E. & Carlson, R. W. (2011). Crustal structure beneath the High Lava Plains of eastern Oregon and surrounding regions from receiver function analysis. *Journal of Geophysical Research* **116**,  
doi:10.1029/2010JB007795.
- Elkins Tanton, L. T., Grove, T. L. & Donnelly-Nolan, J. (2001) Hot, shallow mantle melting under the Cascades volcanic arc. *Geology* **29**, 631-634.
- Fajans, K. (1913). Radioactive transformations and the periodic system of the elements. *Berichte der Deutschen Chemischen Gesellschaft* **46**, 422-439.
- Fierstein, J., Hildreth, W. & Calvert, A. T. (2011). Eruptive history of South Sister, Oregon Cascades. *Journal of Volcanology and Geothermal Research* **207**, 145-179.
- Goldstein, S. J. & Stirling, C. H. (2003). Techniques for measuring uranium-series nuclides: 1992-2002. *Reviews in Mineralogy and Geochemistry* **52**, 23-57.
- Green, N. L. & Harry, D. L. (1999). On the relationship between subducted slab age and arc basalt petrogenesis, Cascadia subduction system, North America. *Earth and Planetary Science Letters* **171**, 367-381.
- Grove, T. L., Parman, S. W., Bowring, S. A., Price, R. C. & Baker, M. B. (2002). The role of an H<sub>2</sub>O-rich fluid in the generation of primitive basaltic andesites and andesites from the Mount Shasta region, N. California. *Contributions to Mineralogy and Petrology* **142**, 375-396.

- Guffanti, M. & Weaver, C. S. (1988). Distribution of Late Cenozoic volcanic vents in the Cascade Range: volcanic arc segmentation and regional tectonic considerations. *Journal of Geophysical Research* **93**, 6513-6529.
- Guillaumont, R., Bouissières, G. & Muxart, Y. (1968). Protactinium chemistry. 1. Aqueous solutions for penta- and tetravalent protactinium. *Actinides Reviews* **1**, 135-163.
- Harry, D. L. & Green, N. L. (1999). Slab dehydration and basalt petrogenesis in subduction systems involving very young oceanic lithosphere. *Chemical Geology* **160**, 309-333.
- Hermann, J. (2002). Allanite: thorium and light rare earth element carrier in subducted crust. *Chemical Geology* **192**, 289-306.
- Hildreth, W. (2007). Quaternary Magmatism in the Cascades - Geologic Perspectives. *U.S. Geological Survey Professional Paper* **1744**.
- Hildreth, W., Fierstein, J. & Calvert, A. T. (2012). Geologic map of Three Sisters volcanic cluster, Cascade Range, Oregon. *U.S. Geological Survey Scientific Investigations Map* **3186**, scale 1:24,000.
- Hodge, E. T. (1925). Mount Multnomah, ancient ancestor of the Three Sisters. *University of Oregon Publications* **2**.
- Hughes, S. S. (1990). Mafic magmatism and associated tectonism of the Central High Cascade range, Oregon. *Journal of Geophysical Research* **95**, 19,623-19,638.
- Hughes, S. S. & Taylor, E. M. (1986). Geochemistry, petrogenesis, and tectonic implications of central High Cascade mafic platform lavas. *Geological Society of America Bulletin* **97**, 1024-1036.
- Hurwitz, S., Mariner, R. H., Fehn, U. & Snyder, G. T. (2005). Systematics of halogen elements and their radioisotopes in thermal springs of the Cascade Range, Central Oregon, Western USA. *Earth and Planetary Science Letters* **235**, 700-714.

- Hyndman, R. D., & Wang, K., (1993). Thermal constraints on the zone of major thrust earthquake failure: the Cascadia subduction zone. *Journal of Geophysical Research* **98**, 2029-2060.
- Jones, C. H., Unruh, J. R. & Sonder, L. J. (1996). The role of gravitational potential energy in active deformation in the southwestern United States. *Nature* **381**, 37-41.
- Jordan, B. T., Grunder, A. L., Duncan, R. A. & Deino, A. L. (2004). Geochronology of age-progressive volcanism of the Oregon High Lava Plains: Implications for the plume interpretation of Yellowstone. *Journal of Geophysical Research* **109**, doi:10.1029/2003JB002776.
- Klemme, S., Prowatke, S., Hametner, K. & Gunther, D. (2005). Partitioning of trace elements between rutile and silicate melts: Implications for subduction zones. *Geochimica et Cosmochimica Acta* **69**, 2361-2371.
- LaTourette, T. Z., Kennedy, A. K. & Wasserburg, G. J. (1993). Thorium-uranium fractionation by garnet; evidence for a deep source and rapid rise of oceanic basalts. *Science* **261**, 739-742.
- Lawrence, R. D. (1976). Strike-slip faulting terminates the Basin and Range province in Oregon. *Geological Society of America Bulletin* **87**, 846-850.
- Leeman, W. P., Smith, D. R., Hildreth, W., Palacz, Z. & Rogers, N. (1990). Compositional diversity of Late Cenozoic basalts in a transect across the southern Washington Cascades: Implications for subduction zone magmatism. *Journal of Geophysical Research* **95**, 19,561-19,582.
- Leeman, W. P., Tonarini, S., Chan, L. H. & Borg, L. E. (2004). Boron and lithium isotopic variations in a hot subduction zone-the southern Washington Cascades. *Chemical Geology* **212**, 101-124.
- Leeman, W. P., Lewis, J. F., Evarts, R. C., Conrey, R. M. & Streck, M. J. (2005). Petrologic constraints on the thermal structure of the Cascades arc. *Journal of Volcanology and Geothermal Research* **140**, 67-105.

- Le Voyer, M., Rose-Koga, E. F., Shimizu, N., Grove, T. L. & Schiano, P. (2010). Two contrasting H<sub>2</sub>O-rich components in primary melt inclusions from Mount Shasta. *Journal of Petrology* **51**, 1571-1595.
- Linneman, S. R. (1990). The petrologic evolution of the Holocene magmatic system of Newberry Volcano, central Oregon. *Ph.D. Dissertation*, University of Wyoming.
- Luedke, R. G. & Smith, R. L. (1982). Map showing distribution, composition, and age of Late Cenozoic volcanic centers in Oregon and Washington. *U.S. Geological Survey Miscellaneous Investigations Series I-1091 D*, scale 1:500,000.
- Lundstrom, C. C. (2003). Uranium-series disequilibria in mid-ocean ridge basalts: Observations and models of basalt genesis. *Reviews in Mineralogy and Geochemistry* **52**, 175-214.
- Lux, D. R. (1982). K-Ar and <sup>40</sup>Ar-<sup>39</sup>Ar ages of mid-Tertiary rocks from the Western Cascade Range, Oregon. *Isochron/West* **33**, 27-32.
- MacLeod, N. S., Walker, G. W. & McKee, E. H. (1975). Geothermal significance of eastward increase in age of Upper Cenozoic rhyolitic domes in southeastern Oregon. *U.S. Geological Survey Open-File Report* **75-348**.
- MacLeod, N. S., Sherrod, D. R., Chitwood, L. A. & Jensen, R. A. (1995). Geologic map of Newberry volcano, Deschutes, Klamath, and Lake Counties, Oregon. *U.S. Geological Survey Miscellaneous Investigations Series I-2455*, scale 1:62,500.
- Magna, T., Wiechert, U., Grove, T. L. & Halliday, A. N. (2006). Lithium isotope fractionation in the southern Cascadia subduction zone. *Earth and Planetary Science Letters* **250**, 428-443.
- McBirney, A. R., Sutter, J. F., Naslund, H. R., Sutton, K. G. & White, C. M. (1974). Episodic volcanism in the central Oregon Cascade Range. *Geology* **2**, 585-589.
- McCaffrey, R., Qamar, A. I., King, R. W., Wells, R., Khazaradze, G., Williams, C. A., Stevens, C. W., Vollick, J. J. & Zwick, P. C. (2007). Fault locking, block rotation and crustal deformation in the Pacific Northwest. *Geophysical Journal International* **169**, 1315-1340.

- McCrorry, P. A., Blair, J. L., Oppenheimer, D. H. & Walter, S. R. (2006). Depth to the Juan de Fuca slab beneath the Cascadia subduction margin - A 3-D model for sorting earthquakes. *U. S. Geological Survey Data Series* **91**, Version 1.2.
- McKay, D., Donnelly-Nolan, J. M., Jensen, R. A. & Champion, D. E. (2009). The post-Mazama northwest rift zone eruption at Newberry Volcano, Oregon. In: O'Connor, J. E., Dorsey, R. J. & Madin, I. P. (Eds.) *Volcanoes to Vineyards: Geologic Field Trips through the Dynamic Landscape of the Pacific Northwest. Geological Society of America Field Guide* **15**, 91-110.
- McKenzie, D. (1985).  $^{230}\text{Th}$ - $^{238}\text{U}$  disequilibrium and the melting processes beneath ridge axes. *Earth and Planetary Science Letters* **72**, 149-157.
- Mitchell, E. C. & Asmerom, Y. (2011) U-series isotope systematics of mafic magmas from central Oregon: Implications for fluid involvement and melting processes in the Cascade arc. *Earth and Planetary Science Letters* **312**, 378-389.
- Nardi, L. V. S., Formoso, M. L. L., Muller, I. F., Fontana, E., Jarvis, K. & Lamarao, C. (2013). Zircon/rock partition coefficients of REEs, Y, Th, U, Nb, and Ta in granitic rocks: Uses for provenance and mineral exploration purposes. *Chemical Geology* **335**, 1-7.
- Obrebski, M., Allen, R. M., Xue, M. & Hung, S.-H. (2010). Slab-plume interaction beneath the Pacific Northwest. *Geophysical Research Letters* **37**, L14305, doi: 10.1029/2010gl043489.
- Peacock, S. M. (2003). Thermal structure and metamorphic evolution of subducting slabs. In: Eiler, J. (Ed.), *Inside the Subduction Factory. American Geophysical Union Geophysical Monograph* **138**, 7-22.
- Phillips, W. M., Korosec, M. A., Schasse, H. W., Anderson, J. L. & Hagen, R. A. (1986). K-Ar ages of volcanic rocks in southwest Washington. *Isochron/West* **47**, 18-24.
- Piggott, C. S. & Urry, W. D. (1942). Time relations in ocean sediments. *Geological Society of America Bulletin* **53**, 1187-1210.
- Porcelli, D. & Swarzenski, P. W. (2003). The behavior of U- and Th-series nuclides in groundwater. *Reviews in Mineralogy and Geochemistry* **52**, 317-361.

- Prowatke, S. & Klemme, S. (2006). Trace element partitioning between apatite and silicate melts. *Geochimica et Cosmochimica Acta* **70**, 4513-4527.
- Reiners, P. W., Hammond, P. E., McKenna, J. M. & Duncan, R. A. (2000). Young basalts of the central Washington Cascades, flux melting of the mantle, and trace element signatures of primary arc magmas. *Contributions to Mineralogy and Petrology* **138**, 249-264.
- Righter, K. (2000). A comparison of basaltic volcanism in the Cascades and western Mexico: Compositional diversity in continental arcs. *Tectonophysics* **318**, 99-117.
- Rondenay, S., Abers, G. A. & van Keken, P. E. (2008). Seismic imaging of subduction zone metamorphism. *Geology* **36**, 275-278.
- Roth, J. B., Fouch, M. J., James, D. E. & Carlson, R. W. (2008). Three-dimensional seismic velocity structure of the northwestern United States. *Geophysical Research Letters* **35**, L15304, doi:10.1029/2008GL034669.
- Rowe, M. C., Kent, A. J. R. & Nielsen, R. L. (2009). Subduction influence on oxygen fugacity and trace and volatile elements in basalts across the Cascade volcanic arc. *Journal of Petrology* **50**, 61-91.
- Ruscitto, D. M., Wallace, P. J., Johnson, E. R., Kent, A. J. R. & Bindeman, I. N. (2010). Volatile contents of mafic magmas from cinder cones in the Central Oregon High Cascades: Implications for magma formation and mantle conditions in a hot arc. *Earth and Planetary Science Letters* **298**, 153-161.
- Rutherford, E. (1903). Radioactive change. *Philosophical Magazine* **5**, 576-591.
- Schmidt, M. E., Grunder, A. L. & Rowe, M. C. (2008). Segmentation of the Cascade Arc as indicated by Sr and Nd isotopic variation among diverse primitive basalts. *Earth and Planetary Science Letters* **266**, 166-181.
- Schmidt, M. E. & Grunder, A. L. (2009). The evolution of North Sister: A volcano shaped by extension and ice in the central Oregon Cascade Arc. *Geological Society of America Bulletin* **121**, 643-662.

- Schmitt, A. K. (2007). Ion microprobe analysis of ( $^{231}\text{Pa}$ )/( $^{235}\text{U}$ ) and an appraisal of protactinium partitioning in igneous zircon. *American Mineralogist* **92**, 691-694.
- Scott, W. E. (1987). Holocene rhyodacite eruptions on the flanks of South Sister volcano, Oregon. In: Fink, J. H. (Ed.) The Emplacement of Silicic Domes and Lava Flows. *Geological Society of America Special Paper* **212**, 35-53.
- Sherrod, D. R. & Smith, J. G. (1990). Quaternary extrusion rates of the Cascade Range, northwestern United States and southern British Columbia. *Journal of Geophysical Research* **95**, 19,465-19,474.
- Sherrod, D. R., Taylor, E. M., Ferns, M. L., Scott, W. E., Conrey, R. M. & Smith, G. A. (2004). Geologic map of the Bend 30- x 60-minute quadrangle, central Oregon. *U.S. Geological Survey Geologic Investigations Series I-2683*, scale 1:100,000.
- Sisson, T. W. & Grove, T. L. (1993). Temperatures and H<sub>2</sub>O contents of low-MgO high-alumina basalts. *Contributions to Mineralogy and Petrology* **113**, 167-184.
- Soddy, F. (1913a). Radioactivity. In: *Annual Reports on the Progress of Chemistry*. The Chemical Society, 262-288.
- Soddy, F. (1913b). The radio-elements and the periodic law. *Chemical News* **107**, 97-99.
- Spiegelman, M. & Elliott, T. (1993). Consequences of melt transport for uranium-series disequilibrium in young lavas. *Earth and Planetary Science Letters* **118**, 1-20.
- Stanley, W. D., Mooney, W. D. & Fuis, G. S. (1990). Deep crustal structure of the Cascade Range and surrounding regions from seismic refraction and magnetotelluric data. *Journal of Geophysical Research* **95**, 19,419-19,438.
- Stepanov, A. S., Hermann, J., Rubatto, D. & Rapp, R. P. (2012). Experimental study of monazite/melt partitioning with implications for the REE, Th and U geochemistry of crustal rocks. *Chemical Geology* **300-301**, 200-220.
- Syracuse, E. M., van Keken, P. E., Abers, G. A., Suetsugu, D., Bina, C., Inoue, T., Wiens, D. & Jellinek, M. (2010). The global range of subduction zone thermal models. *Physics of the Earth and Planetary Interiors* **183**, 73-90.

- Taylor, E. M. (1990). Volcanic history and tectonic development of the central High Cascade Range, Oregon. *Journal of Geophysical Research* **95**, 19,611-19,622.
- Thomas, R. B., Hirschmann, M. M., Cheng, H., Reagan, M. K. & Edwards, R. L. (2002). ( $^{231}\text{Pa}/^{235}\text{U}$ )-( $^{230}\text{Th}/^{238}\text{U}$ ) of young mafic volcanic rocks from Nicaragua and Costa Rica and the influence of flux melting on U-series systematics of arc lavas. *Geochimica et Cosmochimica Acta* **66**, 4287-4309.
- Turner, S., Bourdon, B. & Gill, J. (2003). Insights into magma genesis at convergent margins from U-series isotopes. *Reviews in Mineralogy and Geochemistry* **52**, 255-315.
- Turner, S., Regelous, M., Hawkesworth, C. & Rostami, K. (2006). Partial melting processes above subducting plates: Constraints from  $^{231}\text{Pa}$ - $^{235}\text{U}$  disequilibria. *Geochimica et Cosmochimica Acta* **70**, 480-503.
- van Keken, P. E., Kiefer, B. & Peacock, S. M. (2002). High-resolution models of subduction zones: Implications for mineral dehydration reactions and the transport of water into the deep mantle. *Geochemistry Geophysics Geosystems* **3**, doi:10.1029/2001GC000256.
- Wada, I. & Wang, K. (2009). Common depth of slab-mantle decoupling: Reconciling diversity and uniformity of subduction zones. *Geochemistry Geophysics Geosystems* **10**, doi:10.1029/2009GC002570.
- Wells, R. E., Weaver, C. S. & Blakely, R. J. (1998). Fore-arc migration in Cascadia and its neotectonic significance. *Geology* **26**, 759-762.
- Williams, H. (1935). Newberry volcano of central Oregon. *Geological Society of America Bulletin* **46**, 253-304.
- Williams, H. (1944). Volcanoes of the Three Sisters region, Oregon Cascades. *University of California Publications, Bulletin of the Department of Geological Sciences* **27**, 37-84.
- Williams, R. W. & Gill, J. B. (1989). Effects of partial melting on the uranium decay series. *Geochimica et Cosmochimica Acta* **53**, 1607-1619.

- Wilson, D. S. (2002). The Juan de Fuca plate and slab - isochron structure and Cenozoic plate motions. *U.S. Geological Survey Open-File Report 02-328*, 9-12.
- Wood, B. J., Blundy, J. D. & Robinson, J. A. C. (1999). The role of clinopyroxene in generating U-series disequilibrium during mantle melting. *Geochimica et Cosmochimica Acta* **63**, 1613-1620.
- Xue, M. & Allen, R. M. (2007). The fate of the Juan de Fuca plate: Implications for a Yellowstone plume head. *Earth and Planetary Science Letters* **264**, 266-276.

## **Appendix A1**

This appendix contains:

Table A1.1 - Sample age and location information.

References

**Table A1.1**

Sample age and location information.

Sample ID	Latitude (N)	Longitude (W)	Age <sup>‡</sup> ( <sup>14</sup> C yr B.P.)	Age (Calendar yr before 2010)	Age Reference
<i>Mafic Samples</i>					
08-LL-01	44° 26.259'	121° 54.924'	1950 ± 150	1938 <sup>+174</sup> <sub>-167</sub>	1, 2
07-LN-01	44° 26.474'	121° 57.589'	< 2590 ± 150	< 2808 <sup>+101</sup> <sub>-279</sub>	3
08-NCSW-01	44° 24.869'	121° 57.457'		2850 ± 50	4
08-SM-01	44° 23.867'	121° 57.318'		2850 ± 50	4
08-SMCL-01	44° 22.014'	121° 59.179'		2850 ± 50	4
07-NC-01	44° 25.842'	121° 57.648'		2850 ± 50	4
08-WBB-01	44° 19.526'	121° 59.506'	1400 ± 100	1356 <sup>+59</sup> <sub>-36</sub>	1, 5
07-LB-01	44° 15.337'	121° 49.101'	2883 ± 175	3035 <sup>+287</sup> <sub>-195</sub>	1, 2, 6
07-BCB-01	44° 17.675'	121° 47.108'	> 2883 ± 175	> 3035 <sup>+287</sup> <sub>-195</sub>	1, 3, 5
07-BCB-02	44° 17.620'	121° 46.963'	> 2883 ± 175	> 3035 <sup>+287</sup> <sub>-195</sub>	1, 3, 5
07-FCA-01	44° 14.389'	121° 50.622'	1980 ± 160	1970 <sup>+213</sup> <sub>-190</sub>	7
07-YC-01	44° 17.569'	121° 46.251'	< 2883 ± 175 > 1980 ± 160	< 3035 <sup>+287</sup> <sub>-195</sub> > 1970 <sup>+213</sup> <sub>-190</sub>	3
07-YC-02	44° 17.431'	121° 45.835'	< 2883 ± 175 > 1980 ± 160	< 3035 <sup>+287</sup> <sub>-195</sub> > 1970 <sup>+213</sup> <sub>-190</sub>	3
07-CC-01	44° 11.167'	121° 53.529'	1600 ± 100	1571 <sup>+58</sup> <sub>-157</sub>	7
08-SPBF-01	43° 48.360'	121° 21.820'	5870 ± 60	6780 ± 80	8
08-FRF-01	43° 49.375'	121° 17.681'	5960 ± 100	6860 ± 100	9
08-LCFF-01	43° 48.856'	121° 18.085'	6320 ± 110	7300 ± 70	9
08-SF-01	43° 37.275'	121° 18.748'	6030 ± 90	7010 ± 190	9, 10
08-LBF-01	43° 54.416'	121° 22.466'	6160 ± 70	7130 ± 110	8, 11
08-MBF-02	43° 50.017'	121° 16.447'		6900 ± 200	
08-WIC-01	44° 19.368'	121° 58.871'		> 7650	3
08-CYC-01	44° 02.224'	121° 43.638'		> 7650	3, 12, 13
08-EC-01	44° 00.280'	121° 41.157'		> 7650	3, 12
08-LC-01	44° 01.400'	121° 46.598'		> 7650	3
<i>Felsic Samples</i>					
07-DH-01	44° 01.978'	121° 45.340'	2150 ± 150	2150 ± 150	13
08-NF-01	44° 04.363'	121° 43.947'	2150 ± 150	2150 ± 150	13
08-RM-01	44° 03.520'	121° 47.298'	2150 ± 150	2150 ± 150	13
08-BOF-01	43° 42.371'	121° 14.278'		1300 ± 200	14, 15
08-ELO-01	43° 43.024'	121° 11.998'		3500 ± 200	14, 15

**Table A1.1**

Continued.

Sample ID	Group*	Map Unit <sup>†</sup>	Map Unit Name	Flow Unit
<i>Mafic Samples</i>				
08-LL-01	Nash Crater	Qybl	Basalt of Lost Lake	
07-LN-01	Nash Crater	Qybln	Basaltic andesite of Little Nash Crater	
08-NCSW-01	Nash Crater	Qybn	Basaltic andesite of Nash Crater	Un-named flow SW of crater
08-SM-01	Sand Mountain	Qybsm	Basalt of Sand Mountain	Un-named flow north of Clear Lake Flow
08-SMCL-01	Sand Mountain	Qybsm	Basalt of Sand Mountain	Clear Lake Flow
07-NC-01	Sand Mountain	Qybn	Basaltic andesite of Nash Crater	NW Nash Crater Flow
08-WBB-01	Belknap	Qybk	Basalt and basaltic andesite of Belknap Crater	Un-named basalt flow on western flank
07-LB-01	Belknap	Qyblk	Basaltic andesite of Little Belknap	
07-BCB-01	Belknap	Qybk	Basalt and basaltic andesite of Belknap Crater	Un-named basalt flow on eastern flank
07-BCB-02	Belknap	Qybk	Basalt and basaltic andesite of Belknap Crater	Un-named basalt flow on eastern flank
07-FCA-01	Yapoah	Qya	Andesite of Four In One Cone	
07-YC-01	Yapoah	Qyby	Basaltic andesite of Yapoah Crater	
07-YC-02	Yapoah	Qyby	Basaltic andesite of Yapoah Crater	
07-CC-01	Yapoah	Qybc	Basaltic andesite and andesite of Collier Cone	
08-SPBF-01	Newberry	Qyb6	Young basaltic andesite	Sugar Pine Butte Flow
08-FRF-01	Newberry	Qyb7	Young basaltic andesite	Forest Road Flow
08-LCFF-01	Newberry	Qyb8	Young basaltic andesite	Lava Cast Forest Flow
08-SF-01	Newberry	Qyb15	Young basaltic andesite	Surveyor Flow
08-LBF-01	Newberry	Qyb1	Young basaltic andesite	Lava Butte Flow
08-MBF-02	Newberry	Qyb3	Young basaltic andesite	Mokst Butte Flow
08-WIC-01	pre-Mazama	Qb		
08-CYC-01	pre-Mazama	Qbcy	Basalt of Cayuse Crater	
08-EC-01	pre-Mazama	Qbec	Basalt of Egan Cone	
08-LC-01	pre-Mazama	Qbal	Basaltic andesite of Le Conte Crater	
<i>Felsic Samples</i>				
07-DH-01		Qrrm	Rhyolite of Rock Mesa and Devils Hill	Devils Hill Flow
08-NF-01		Qrrm	Rhyolite of Rock Mesa and Devils Hill	Newberry Flow
08-RM-01		Qrrm	Rhyolite of Rock Mesa and Devils Hill	Rock Mesa Flow
08-BOF-01		Qyo	Young obsidian flows	Big Obsidian Flow
08-ELO-01		Qyo	Young obsidian flows	East Lake Obsidian Flow

<sup>‡</sup>Where possible ages are <sup>14</sup>C ages from the sources listed. Calibrated ages (before 1950) from those sources have been adjusted to calendar years before 2010. Age for sample 08-MBF-02 is an estimate based on the ages of other Newberry northwest rift zone lavas. Ages for Newberry felsic rocks are hydration-rind ages. Age references: 1 - Chatters, 1968; 2 - Taylor, 1968; 3 - Sherrod et al., 2004; 4 - N. Deligne, pers. comm., 2011; 5 - Taylor, 1965; 6 - Taylor, 1990; 7 - Scott, 1990; 8 - Robinson and Trimble, 1981; 9 - Peterson and Groh, 1969; 10 - Swanberg et al., 1988; 11 - Chitwood et al., 1977; 12 - Scott and Gardner, 1992; 13 - Scott, 1987; 14 - Friedman, 1977; 15 - Friedman and Obradovich, 1981. \*Groups are those identified in Chapter 2 and revised slightly in Chapter 4.

<sup>†</sup>Map units are those of Sherrod et al. (2004) for the Three Sisters samples and MacLeod et al. (1995) for the Newberry samples. Flow unit names for the Nash Crater, Sand Mountain, and Belknap samples are in general informal descriptions based on un-named subdivisions of map units.

## References

- Chatters, R. M. (1968). Washington State University natural radiocarbon measurements, I. *Radiocarbon* **10**, 479-498.
- Chitwood, L. A., Jensen, R. A. & Groh, E. A. (1977). The age of Lava Butte. *The Ore Bin* **39**, 157-164.
- Friedman, I. (1977). Hydration dating of volcanism at Newberry Crater, Oregon. *U.S. Geological Survey Journal of Research* **5**, 337-342.
- Friedman, I. & Obradovich, J. (1981). Obsidian hydration dating of volcanic events. *Quaternary Research* **16**, 37-47.
- MacLeod, N. S., Sherrod, D. R., Chitwood, L. A. & Jensen, R. A. (1995). Geologic map of Newberry volcano, Deschutes, Klamath, and Lake Counties, Oregon. *U.S. Geological Survey Miscellaneous Investigations Series I-2455*, scale 1:62,500.
- Peterson, N. V. & Groh, E. A. (1969). The ages of some Holocene volcanic eruptions in the Newberry volcano area, Oregon. *The Ore Bin* **31**, 73-87.
- Robinson, S. W. & Trimble, D. A. (1981). U.S. Geological Survey, Menlo Park, California, radiocarbon measurements II. *Radiocarbon* **23**, 305-321.
- Scott, W. E. (1987). Holocene rhyodacite eruptions on the flanks of South Sister volcano, Oregon. In: Fink, J. H. (Ed.) *The Emplacement of Silicic Domes and Lava Flows. Geological Society of America Special Paper* **212**, 35-53.
- Scott, W. E. (1990). Temporal relations between eruptions of the Mount Bachelor volcanic chain and fluctuations of late Quaternary glaciers. *Oregon Geology* **52**, 114-117.
- Scott, W. E. & Gardner, C. A. (1992). Geologic map of the Mount Bachelor volcanic chain and surrounding area, Cascade Range, Oregon. *U.S. Geological Survey Miscellaneous Investigations Series I-1967*, scale 1:50,000.
- Sherrod, D. R., Taylor, E. M., Ferns, M. L., Scott, W. E., Conrey, R. M. & Smith, G. A. (2004). Geologic map of the Bend 30- x 60-minute quadrangle, central Oregon. *U.S. Geological Survey Geologic Investigations Series I-2683*, scale 1:100,000.

- Swanberg, C. A., Walkey, W. C. & Combs, J. (1988). Core hole drilling and the “rain curtain” phenomenon at Newberry volcano, Oregon. *Journal of Geophysical Research* **93**, 10,163-10,173.
- Taylor, E. M. (1965). Recent volcanism between Three Fingered Jack and North Sister, Oregon Cascade Range: Part I – History of volcanic activity. *The Ore Bin* **27**, 121-147.
- Taylor, E. M. (1968) Roadside geology, Santiam and McKenzie Pass highways, Oregon. *In: Dole, H. M. (Ed.) Andesite Conference Guidebook. Oregon Department of Geology and Mineral Industries Bulletin* **62**, 3-34.
- Taylor, E. M. (1990). Sand Mountain, Oregon and Belknap, Oregon. *In: Wood, C. A. & Kienle, J. (Eds.) Volcanoes of North America. Cambridge University Press*, 180-183.

## **Chapter 2: U-series isotope systematics of mafic magmas from central Oregon: Implications for fluid involvement and melting processes in the Cascade arc.**

### **Abstract**

The Cascade arc is the warm-slab subduction zone global end member, where a broad variety of primitive magmas with highly variable slab fluid signatures have erupted in close spatial and temporal proximity. A number of petrogenetic models have been proposed to explain the occurrence of such diverse magmas, but the source(s) of these magmas and the timing of fluid addition to the sub-arc mantle remain controversial.

We present uranium-series isotope data ( $^{238}\text{U}$ - $^{230}\text{Th}$ - $^{226}\text{Ra}$ ) for eighteen mafic lavas from the Three Sisters region of the central Oregon Cascades, and for a further six lavas from the rear-arc Newberry Volcano. The majority of these samples have geochemical characteristics (e.g., Nb/Zr, Ba/Zr,  $^{87}\text{Sr}/^{86}\text{Sr}$ ) consistent with previously described calc-alkaline basalts from this region of the arc, and indicative of limited fluid involvement at some stage in their genesis. Trace element and long-lived radiogenic isotope modeling suggests that this fluid was derived from dehydration of subducting sediments, and was added to an enriched, garnet-bearing mantle wedge source. The trace element systematics of the lavas are consistent with small degree (< 10%) melts of this fluid-modified source. All samples display ( $^{230}\text{Th}/^{238}\text{U}$ ) and ( $^{226}\text{Ra}/^{230}\text{Th}$ )  $\geq 1$ , similar to values measured in fresh MORB and other parts of the arc. Results of a dynamic melting model support the interpretation that these lavas are small degree melts of an asthenospheric source, and do not allow for a lithospheric mantle source. However, the U-series data do not permit us to determine whether fluid addition was the trigger for melting, or whether the lavas were generated from a secular equilibrium source that had experienced fluid addition > 350

k.y. prior to melting. Regardless, modern fluid input is limited and melting is dominantly occurring in response to upwelling and decompression.

## 2.1. Introduction

Significant progress has been made in our understanding of magma genesis in arc settings, although a number of questions remain unanswered, including the role of slab-derived volatiles and the heterogeneity of mantle wedge source regions (e.g., Arculus, 1994; Righter, 2000). The Cascade volcanic arc results from slow ( $\sim 3.5 \text{ cm a}^{-1}$ ) subduction of the young ( $< 10 \text{ Ma}$  at the trench) Juan de Fuca plate beneath North America (Wilson, 2002). As such it represents the global end member for a warm-slab subduction zone, with a slab thermal parameter of  $\sim 1.5$  to  $2.2 \text{ km}$  (Wada and Wang, 2009). Thermal models predict temperatures at the slab-mantle interface up to  $300^\circ\text{C}$  hotter than in cooler subduction zones with older subducting slabs (Peacock, 2003). Compositional proxies for slab surface temperature also indicate elevated temperatures ( $850\text{-}950^\circ\text{C}$ ), at the upper end of the global arc range (Ruscitto et al., 2010). These warm conditions are expected to lead to shallow dehydration of the slab and extensive metasomatism of the fore-arc, consistent with geochemical and geophysical observations (e.g., Bostock et al., 2002; Brocher et al., 2003; Hurwitz et al., 2005; Leeman et al., 2005; Rondenay et al., 2008). Such extensive early dehydration should result in a reduced volatile flux to the sub-arc mantle wedge, a view supported by geochemical data (e.g., Green and Harry, 1999; Harry and Green, 1999; Leeman et al., 2005), although the degree to which the slab is dehydrated is still debated (e.g., Hildreth, 2007).

A long history of petrological and geochemical investigations in the Cascades by many workers has revealed a compositionally diverse suite of mafic magmas, which are often interpreted to be the result of the distinctive thermal state of the Cascadia margin. However, many questions still remain, especially concerning the role of fluids in

generating these magmas and the timing of addition of such fluids to the mantle wedge. Some workers argue for flux melting of the mantle wedge (e.g., Reiners et al., 2000), as is the case in most arcs, while others have suggested that fluid addition is an older feature and that melting is dominated by decompression (e.g., Leeman et al., 2005), as is the case beneath mid-ocean ridges.

This paper presents U-series isotope data for a suite of mafic magmas from central Oregon, one of the most active segments of the Cascade arc over the last ~ 1 m.y. (Guffanti and Weaver, 1988). The results support the notion of reduced volatile fluxing of the mantle wedge, and melting dominated by upwelling and decompression. However, the data are not able to unambiguously constrain the timing of fluid addition.

## **2.2. Geologic Setting and Background**

The Quaternary Cascade arc extends from Mt. Lassen in northern California to Mt. Meager in British Columbia, a distance of ~ 1250 km (Hildreth, 2007) (Fig. 2.1). The modern arc is defined by the location of large stratovolcanoes, which typically erupt andesites to dacites, although volumetrically the arc output is dominated by mafic magmatism from small monogenetic and shield vents (Hildreth, 2007). Such small volume mafic magmatism is especially abundant in the central Oregon Cascades, largely as a result of intra-arc rifting that initiated ~ 5 Ma in central Oregon and which has subsequently propagated northwards into southern Washington (Sherrod and Smith, 1990; Conrey et al., 2002). Not only is mafic magmatism abundant in this region but it extends for over 100 km from the fore-arc into the back-arc (Guffanti and Weaver, 1988) and encompasses all of the compositional diversity identified within the Cascades (Conrey et al., 1997) (see below). The study area for this work lies within the intra-arc

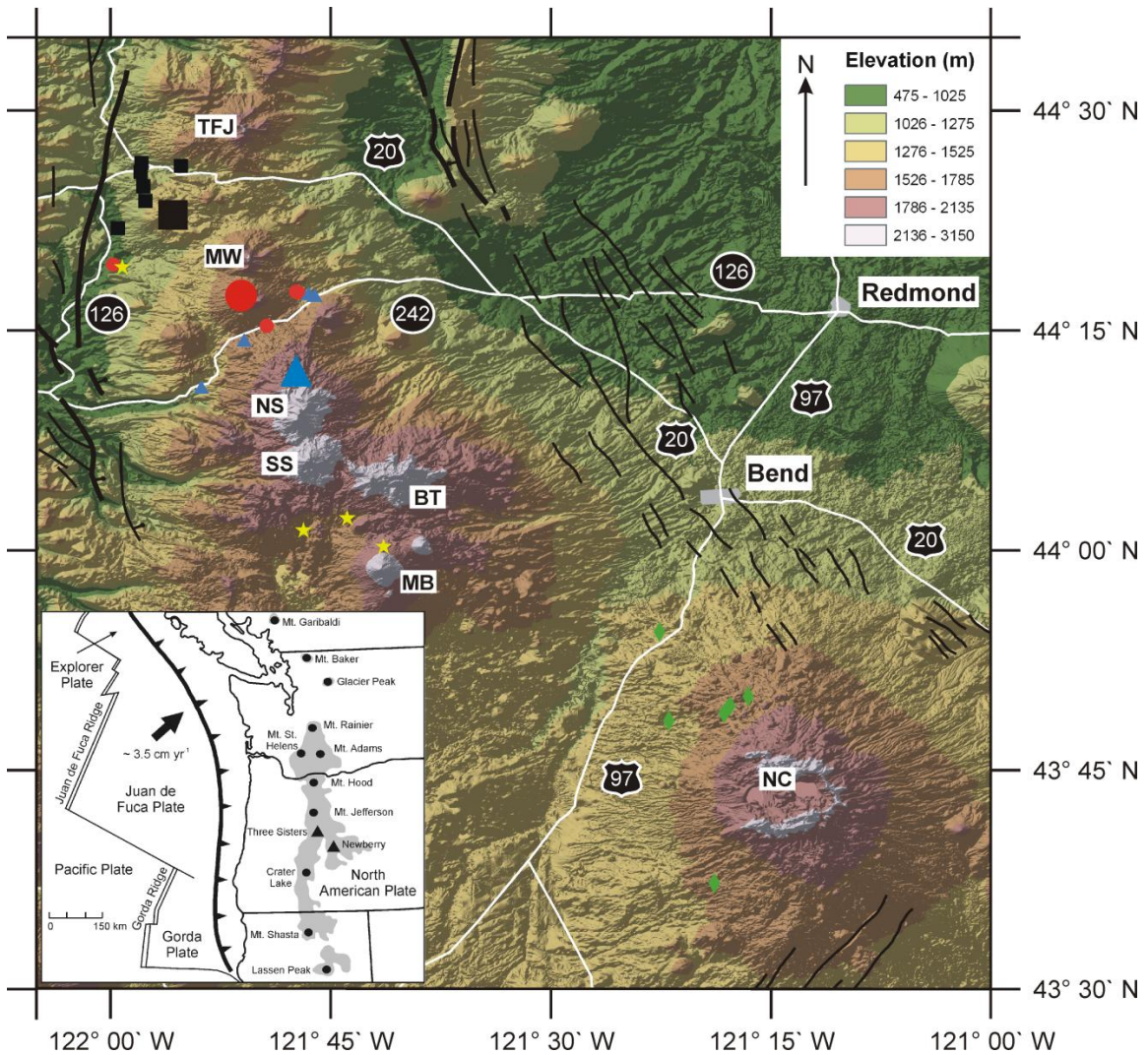


**Figure 2.1:** Shaded relief map of the study area in central Oregon. Sample localities, grouped on the basis of vent location, are indicated with small symbols. Black squares = Sand Mountain group; red circles = Belknop group; blue triangles = Yapoah group; green diamonds = Newberry group; yellow stars = pre-Mazama group. Larger symbols mark approximate vent locations for the first three groups. Prominent stratovolcanoes are labeled: TFJ = Three Fingered Jack, MW = Mt. Washington, NS = North Sister, SS = South Sister, BT = Broken Top, MB = Mt. Bachelor, NC = Newberry Caldera. Black lines are faults, ball and bar on downthrown side. Thin lines are faults with displacement < 300 m, thick lines are faults with displacement > 300 m. Major towns and roads in the area are marked. Inset shows general tectonic setting of the Cascadia margin (after Luedke & Smith, 1981). Thick black line is the trench, teeth on overriding plate. Shaded area shows the extent of the Quaternary High Cascades. Prominent volcanoes are indicated with circles and labeled. The study area lies in central Oregon in the vicinity of the Three Sisters and Newberry volcano, marked with triangles.

graben in the vicinity of the Three Sisters, between the stratovolcanoes of Mt. Bachelor and Three-Fingered Jack, and also extends to Newberry Volcano, a shield volcano located ~ 50 km east of the arc axis that has been interpreted as a rear-arc center analogous to Medicine Lake or Mt. Adams (Donnelly-Nolan et al., 2008) (Fig. 2.1). The slab in this region of the arc lies at a depth of ~ 70 to 100 km (McCroory et al., 2006; Obrebski et al., 2010) and dips ~ 50°E (Xue and Allen, 2007; Roth et al., 2008). The crust is interpreted to be ~ 40 to 45 km thick (Leaver et al., 1984; Catchings and Mooney, 1988; Stanley et al., 1990; Eagar et al., 2011).

An extensive history of previous work in the Cascades has identified, largely on the basis of trace element systematics, at least five distinct mafic compositions, all of which have been recognized in central Oregon (Hughes and Taylor, 1986; Bacon, 1990; Hughes, 1990; Bacon et al., 1997; Conrey et al., 1997; Leeman et al., 2005; Schmidt et al., 2008, Rowe et al., 2009). Leeman et al. (2005) proposed a broader classification based on the inferred degree of subduction fluid involvement in magma genesis. Group I lavas contain a weak fluid signature and are interpreted to be derived from a source little modified by a subduction component and include two sub-groups: low-K tholeiites (LKTs; also called MORB-like basalts or high-alumina olivine tholeiites (HAOT) by some workers) and intraplate type lavas (called OIB-like, or high field strength element (HFSE)-enriched, or enriched intraplate (EIB) basalts by some workers) (Leeman et al., 2005). In contrast, Group II lavas contain a stronger fluid signature and are interpreted to be derived from a source that has been more substantially modified by a subduction component and include at least three sub-groups: typical calc-alkaline arc basalts (CABs), shoshonitic lavas (SHO), and high-Mg basaltic andesites (BAs).

In addition to N-MORB or OIB-like trace element concentrations, Group I lavas have low water contents (Anderson, 1973; Sisson and Grove, 1993; Le Voyer et al., 2010), MORB-like  $\delta^7\text{Li}$  (Leeman et al., 2004) and generally lower  $^{87}\text{Sr}/^{86}\text{Sr}$  than CABs from the same region (Schmidt et al., 2008). These lavas are interpreted to be low pressure, high temperature, anhydrous decompression melts of a little modified source, a view supported by petrologic studies and high-pressure phase relations (Bartels et al., 1991; Elkins-Tanton et al., 2001). The LKT source is inferred to be essentially MORB-like, whereas the intraplate lavas are interpreted to require a distinct, more enriched mantle source present only locally along the arc (e.g., Leeman et al., 1990; Conrey et al., 1997; Leeman et al., 2005; Schmidt et al., 2008).

CABs are the dominant Group II lava and are found throughout the arc. They have been described as “the paradigmatic arc suite” (Hildreth, 2007, pg. 79) and display trace element characteristics typical of arc lavas globally, such as enrichments in large ion lithophile elements (LILE) and light rare earth elements (LREE), as well as HFSE, notably Nb and Ta, depletions (Bacon et al., 1997; Borg et al. 1997; Conrey et al., 1997; Leeman et al., 2005; Reiners et al., 2000; Rowe et al., 2009). Fractionated REE profiles suggest that these lavas originated within the garnet stability field. Water contents and  $^{87}\text{Sr}/^{86}\text{Sr}$  are higher than Group I lavas (Anderson, 1979; Sisson and Grove, 1993; Grove et al., 2002; Schmidt et al., 2008; Le Voyer et al., 2010; Ruscitto et al., 2010),  $\delta^7\text{Li}$  values are more variable (Magna et al., 2006) and the lavas are more oxidized (Righter, 2000). These characteristics are usually interpreted to reflect a flux melting origin for such lavas.  $^{87}\text{Sr}/^{86}\text{Sr}$  and  $^{143}\text{Nd}/^{144}\text{Nd}$  data for CABs from central and southern Oregon are consistent

with derivation from the same mantle source as LKTs, with only modest fluid input (Schmidt et al., 2008).

Despite this extensive body of prior work important questions remain. For example, the timing of fluid addition and style of melting that generated the Group II lavas is uncertain, with Leeman et al. (2005) suggesting that these lavas may result from decompression melting of a source containing a metasomatic component inherited from earlier stages of subduction. In contrast, Reiners et al. (2000) suggested that both groups could be derived by flux melting alone. The depth of generation of CABs is also debated, with conflicting evidence for lithospheric and asthenospheric sources (e.g., Baker et al., 1994; Borg et al., 1997; Conrey et al., 1997; Reiners et al., 2000; Borg et al., 2002; Leeman et al., 2005; Hildreth, 2007). The time sensitive nature of uranium-series isotopes makes them ideally suited to differentiate between flux melting of the mantle and decompression melting of a previously metasomatized source. Furthermore, to a first order U-Th fractionation is controlled by source mineralogy, and thus depth of melting, enabling the delineation of lithospheric from asthenospheric sources.

### **2.3. Materials and Methods**

A total of eighteen samples were collected from sixteen separate mafic flows in the Three Sisters region of the Oregon Cascades, and a further six samples from six separate flows were collected from the flanks of Newberry Volcano (Fig. 2.1). The Three Sisters samples are divided into four groups on the basis of vent location (Sand Mountain, Belknap, and Yapoah groups), with four older samples grouped separately (pre-Mazama group). The Newberry samples comprise a fifth group (Fig. 2.1).

Whole-rock major and trace element concentrations were determined by X-ray fluorescence (XRF) and inductively coupled plasma mass spectrometry (ICP-MS) at the University of New Mexico. XRF analyses were conducted in the Analytical Chemistry Laboratory on fused glass disks comprised of a 9:1  $\text{Li}_2\text{B}_4\text{O}_7$  flux:sample mixture, using a Rigaku ZSX Primus II wavelength dispersive spectrometer. Analytical accuracy, based on analysis of known standards (Table 2.1), is estimated at  $\pm \leq 1\%$  for most elements. ICP-MS analyses were conducted in the Radiogenic Isotope Laboratory using a Thermo X-Series II quadrupole instrument. A known amount ( $\sim 0.25$  g) of powder was thoroughly mixed with  $\sim 1.25$ g of ultra pure  $\text{LiBO}_2$  flux, fused for 10 minutes at  $1100^\circ\text{C}$ , poured directly into  $\sim 150$  mL of 3%  $\text{HNO}_3$  containing a 10 ppb In internal standard and stirred continuously with a magnetic stirrer until complete dissolution had been achieved (typically  $< 10$  minutes). A  $\sim 1$  g aliquot of this solution was subsequently diluted a further 100x for analysis of high concentration trace elements (e.g., Sr, Ba, Zr, V, Cr, Ni). Analytical accuracy, based on analysis of known standards (Table 2.1), is estimated at  $\pm \leq 3\%$  for most elements.

U-Th-Ra-Sr-Nd isotope analyses were performed at the Radiogenic Isotope Laboratory, University of New Mexico, on a single powder batch following the dissolution and U-Th separation procedure described in Asmerom and Edwards (1995) and Asmerom (1999). Elemental separation and purification of Ra-Sr-Nd followed a procedure modified from Chabaux et al. (1994) and Turner et al. (2000). Approximately 200 to 250 mg of whole rock powder was weighed into a PVA bomb containing an HF- $\text{HNO}_3$  mixture and dissolved at  $110^\circ\text{C}$  for  $\sim 48$  hours. Following dissolution the solution was transferred to a 30 mL PFA beaker containing  $\sim 1$  g of a mixed  $^{228}\text{Ra}$ - $^{229}\text{Th}$ - $^{233}\text{U}$ - $^{236}\text{U}$

**Table 2.1**

Major and trace element data for central Oregon lavas.

Sample ID	08-LL-01	07-LN-01	08-NCSW-01	08-SM-01	08-SMCL-01	07-NC-01	08-WBB-01
Latitude (N)	44° 26.259'	44° 26.474'	44° 24.869'	44° 23.867'	44° 22.014'	44° 25.842'	44° 19.526'
Longitude (W)	121° 54.924'	121° 57.589'	121° 57.457'	121° 57.318'	121° 59.179'	121° 57.648'	121° 59.506'
Group	Nash Crater	Nash Crater	Nash Crater	Sand Mtn.	Sand Mtn.	Sand Mtn.	Belknap
SiO <sub>2</sub>	49.56	52.30	52.60	51.60	52.87	53.21	51.02
Al <sub>2</sub> O <sub>3</sub>	16.58	17.52	17.76	16.86	17.34	17.88	16.72
Fe <sub>2</sub> O <sub>3T</sub>	9.83	9.18	8.91	8.91	8.50	8.28	9.59
MgO	8.99	6.25	5.70	6.99	6.00	5.57	8.09
CaO	9.33	8.44	8.52	9.56	9.07	8.75	8.66
Na <sub>2</sub> O	3.13	3.70	3.86	3.27	3.58	3.80	3.43
K <sub>2</sub> O	0.75	0.80	0.83	0.99	0.86	0.82	0.70
TiO <sub>2</sub>	1.37	1.27	1.28	1.32	1.27	1.22	1.34
P <sub>2</sub> O <sub>5</sub>	0.31	0.39	0.39	0.37	0.37	0.35	0.30
MnO	0.15	0.14	0.13	0.14	0.13	0.13	0.15
Measured Total	99.98	99.77	100.00	99.88	99.64	99.00	100.33
Mg#	63.23	55.97	54.36	59.50	56.87	55.67	61.27
Sc	27.03	24.88	19.88	27.05	22.87	23.62	23.73
V	195.2	173.0	170.0	186.7	170.0	166.7	195.1
Cr	356.5	124.5	101.0	192.4	133.5	92.86	302.60
Co	90.89	36.40	33.48	67.63	54.87	30.57	47.82
Ni	206.3	150.5	102.4	121.6	100.7	118.4	180.8
Cu	58.46	55.38	51.50	58.98	56.81	55.24	67.99
Zn	74.25	83.54	80.90	74.47	76.82	76.78	77.28
Rb	8.76	9.59	9.70	9.88	9.21	8.32	10.13
Sr	648.5	722.1	761.5	1002	1046	982.1	508.1
Y	22.75	23.59	23.24	23.65	22.50	20.68	23.09
Zr	136.6	177.2	173.6	164.8	168.3	162.5	135.8
Nb	10.62	12.60	12.20	12.51	11.11	10.47	12.48
Cs	0.18	0.22	0.22	0.20	0.20	0.17	0.22
Ba	288.9	326.0	326.9	381.4	332.5	314.6	246.0
La	14.03	17.69	18.00	19.04	20.41	18.46	13.83
Ce	33.39	42.02	43.03	45.56	48.05	43.13	31.65
Pr	4.45	5.45	5.61	5.89	6.14	5.51	4.14
Nd	19.81	23.83	24.53	25.31	26.09	23.57	18.06
Sm	4.44	5.05	5.18	5.12	5.25	4.80	4.37
Eu	1.34	1.49	1.50	1.52	1.53	1.43	1.23
Gd	4.01	4.53	4.64	4.50	4.57	4.21	4.52
Tb	0.685	0.749	0.750	0.723	0.726	0.679	0.745
Dy	3.90	4.08	4.19	4.05	3.97	3.66	4.24
Ho	0.832	0.824	0.834	0.852	0.802	0.752	0.905
Er	2.27	2.30	2.36	2.37	2.27	2.08	2.45
Tm	0.318	0.315	0.325	0.329	0.306	0.282	0.343
Yb	2.12	2.12	2.16	2.21	2.12	1.90	2.28
Lu	0.313	0.311	0.317	0.328	0.308	0.281	0.336
Hf	2.69	3.32	3.31	3.27	3.33	3.20	3.01
Ta	0.60	0.66	0.67	0.69	0.59	0.57	0.73
Th	1.29	1.15	1.24	1.41	1.41	1.36	1.15
U	0.43	0.44	0.46	0.48	0.48	0.46	0.45

**Table 2.1**

Continued.

Sample ID	07-LB-01	07-BCB-01	07-BCB-02	07-FCA-01	07-YC-01	07-YC-02	07-CC-01
Latitude (N)	44° 15.337'	44° 17.675'	44° 17.620'	44° 14.389'	44° 17.569'	44° 17.431'	44° 11.167'
Longitude (W)	121° 49.101'	121° 47.108'	121° 46.963'	121° 50.622'	121° 46.251'	121° 45.835'	121° 53.529'
Group	Belknap	Belknap	Belknap	Yapoah	Yapoah	Yapoah	Yapoah
SiO <sub>2</sub>	53.22	53.43	53.37	53.45	55.66	55.96	58.55
Al <sub>2</sub> O <sub>3</sub>	17.94	17.95	17.91	16.86	18.90	18.80	17.43
Fe <sub>2</sub> O <sub>3T</sub>	8.47	8.40	8.45	9.17	6.83	6.71	7.48
MgO	5.30	4.86	4.91	6.22	4.78	4.60	3.22
CaO	8.81	8.82	8.88	7.86	8.22	8.15	6.48
Na <sub>2</sub> O	3.73	3.90	3.83	3.65	3.66	3.80	4.41
K <sub>2</sub> O	0.81	0.86	0.86	1.02	0.92	0.95	1.14
TiO <sub>2</sub>	1.22	1.27	1.28	1.32	0.77	0.77	1.04
P <sub>2</sub> O <sub>5</sub>	0.36	0.38	0.38	0.31	0.15	0.15	0.14
MnO	0.13	0.13	0.13	0.14	0.11	0.11	0.12
Measured Total	100.16	100.13	99.43	99.53	99.54	99.87	99.48
Mg#	53.89	51.87	52.01	55.83	56.78	56.24	44.39
Sc	26.34	27.38	26.49	25.46	21.27	21.44	22.22
V	179.4	180.2	179.2	171.6	142.6	143.9	190.9
Cr	88.88	81.97	77.85	172.0	71.30	68.94	22.25
Co	28.33	41.84	39.61	50.71	43.14	24.84	34.21
Ni	48.22	40.82	42.02	116.3	70.85	58.84	20.94
Cu	66.67	69.03	67.16	61.44	64.89	63.36	47.97
Zn	75.76	75.37	72.03	75.20	57.58	56.38	66.47
Rb	11.21	12.07	11.60	17.53	16.45	16.62	20.36
Sr	623.8	595.8	589.8	413.1	635.0	622.9	493.2
Y	23.42	24.01	24.53	26.84	14.06	14.62	17.99
Zr	171.0	175.0	167.6	163.6	102.1	99.31	113.9
Nb	12.52	13.00	12.30	10.57	5.19	5.09	5.34
Cs	0.26	0.28	0.25	0.47	0.54	0.55	0.66
Ba	323.0	327.5	323.3	358.9	288.5	300.5	355.2
La	17.77	17.91	18.32	15.79	10.40	10.67	11.17
Ce	40.77	41.20	42.74	36.26	22.66	23.68	25.06
Pr	5.27	5.36	5.56	4.75	2.87	3.01	3.21
Nd	22.51	22.82	23.61	20.48	12.15	12.55	13.74
Sm	5.00	5.13	5.23	4.85	2.83	2.88	3.32
Eu	1.38	1.41	1.45	1.36	0.86	0.88	1.01
Gd	5.07	5.14	5.25	5.09	2.84	2.94	3.41
Tb	0.785	0.808	0.834	0.834	0.455	0.467	0.558
Dy	4.33	4.44	4.62	4.82	2.57	2.60	3.21
Ho	0.878	0.907	0.937	0.998	0.550	0.548	0.680
Er	2.47	2.54	2.64	2.87	1.47	1.54	1.89
Tm	0.336	0.353	0.361	0.405	0.215	0.218	0.266
Yb	2.26	2.36	2.43	2.72	1.45	1.48	1.80
Lu	0.334	0.347	0.364	0.406	0.216	0.220	0.269
Hf	3.64	3.65	3.76	3.55	2.31	2.45	2.82
Ta	0.72	0.74	0.75	0.66	0.34	0.36	0.37
Th	1.22	1.28	1.30	1.81	1.63	1.69	2.09
U	0.48	0.51	0.51	0.69	0.63	0.66	0.87

**Table 2.1**

Continued.

Sample ID	08-SPBF-01	08-FRF-01	08-LCFF-01	08-SF-01	08-LBF-01	08-MBF-02	08-WIC-01
Latitude (N)	43° 48.360'	43° 49.375'	43° 48.856'	43° 37.275'	43° 54.416'	43° 50.017'	44° 19.368'
Longitude (W)	121° 21.820'	121° 17.681'	121° 18.085'	121° 18.748'	121° 22.466'	121° 16.447'	121° 58.871'
Group	Newberry	Newberry	Newberry	Newberry	Newberry	Newberry	Pre-Mazama
SiO <sub>2</sub>	52.12	53.35	53.62	54.66	55.55	57.74	49.55
Al <sub>2</sub> O <sub>3</sub>	16.83	17.05	16.96	16.75	16.95	15.73	16.98
Fe <sub>2</sub> O <sub>3T</sub>	9.60	8.96	8.90	8.49	7.89	8.31	10.17
MgO	5.74	5.40	5.26	5.15	5.02	4.01	8.00
CaO	9.58	9.04	8.88	8.44	8.04	6.93	9.51
Na <sub>2</sub> O	3.55	3.64	3.74	3.71	3.81	3.98	3.20
K <sub>2</sub> O	0.77	0.92	0.98	1.19	1.33	1.74	0.63
TiO <sub>2</sub>	1.37	1.24	1.23	1.19	1.06	1.20	1.47
P <sub>2</sub> O <sub>5</sub>	0.28	0.27	0.27	0.26	0.23	0.21	0.32
MnO	0.16	0.15	0.14	0.14	0.13	0.14	0.16
Measured Total	99.67	99.86	100.08	99.79	99.55	99.51	99.73
Mg#	52.77	52.97	52.47	53.07	54.25	47.16	59.64
Sc	32.36	26.45	28.00	26.85	24.03	23.69	28.60
V	228.6	210.7	206.7	180.2	171.0	185.2	216.2
Cr	113.1	109.1	101.5	106.6	103.8	40.0	272.0
Co	34.95	55.65	104.3	29.73	37.93	112.9	49.65
Ni	44.42	52.19	72.47	46.51	59.05	60.14	139.3
Cu	76.79	72.19	70.01	64.96	63.01	53.25	59.93
Zn	75.66	74.97	73.08	71.66	69.54	70.41	74.11
Rb	14.31	18.96	21.46	28.88	33.80	48.65	8.74
Sr	404.9	427.2	408.9	367.2	386.4	272.0	427.2
Y	23.14	23.02	23.04	24.51	24.33	29.70	23.99
Zr	125.9	135.8	137.8	156.3	167.0	193.2	137.9
Nb	10.30	10.04	10.06	11.44	11.03	12.48	14.25
Cs	0.45	0.65	0.74	1.01	1.17	1.73	0.21
Ba	245.0	292.2	292.1	325.7	354.4	398.1	196.1
La	11.55	12.56	12.71	13.90	14.66	16.36	12.43
Ce	26.29	28.35	28.54	30.76	32.26	35.85	28.86
Pr	3.56	3.77	3.80	4.01	4.14	4.52	3.84
Nd	15.67	16.32	16.31	17.23	17.21	18.73	16.28
Sm	3.97	4.03	4.06	4.16	4.08	4.57	4.24
Eu	1.23	1.22	1.19	1.18	1.15	1.18	1.33
Gd	4.35	4.35	4.40	4.67	4.57	5.13	4.06
Tb	0.710	0.706	0.713	0.740	0.735	0.842	0.686
Dy	4.14	4.15	4.17	4.35	4.31	5.09	4.23
Ho	0.873	0.874	0.865	0.898	0.900	1.064	0.891
Er	2.46	2.49	2.50	2.62	2.65	3.18	2.48
Tm	0.343	0.345	0.351	0.371	0.377	0.461	0.342
Yb	2.32	2.40	2.42	2.53	2.62	3.18	2.33
Lu	0.343	0.346	0.351	0.377	0.384	0.473	0.341
Hf	2.73	3.01	3.07	3.48	3.66	4.40	2.80
Ta	0.61	0.60	0.59	0.69	0.68	0.83	0.87
Th	1.55	2.06	2.17	2.89	3.16	4.68	1.14
U	0.59	0.78	0.83	1.10	1.21	1.74	0.43

**Table 2.1**

Continued.

Sample ID	08-CYC-01	08-EC-01	08-LC-01	BHVO-2 Standard (n = 6)			
Latitude (N)	44° 02.224'	44° 00.280'	44° 01.400'	Measured	St. Dev.	Certified	±
Longitude (W)	121° 43.638'	121° 41.157'	121° 46.598'				
Group	Pre-Mazama	Pre-Mazama	Pre-Mazama				
SiO <sub>2</sub>	51.19	51.96	55.44	49.71	0.026	49.9	0.6
Al <sub>2</sub> O <sub>3</sub>	16.47	17.42	16.41	13.47	0.009	13.5	0.2
Fe <sub>2</sub> O <sub>3T</sub>	9.32	10.72	8.33	12.27	0.051	12.3	0.2
MgO	8.76	5.01	5.88	7.19	0.016	7.23	0.12
CaO	9.27	8.11	7.21	11.48	0.030	11.4	0.2
Na <sub>2</sub> O	2.98	3.70	3.66	2.20	0.011	2.22	0.08
K <sub>2</sub> O	0.62	0.72	1.35	0.53	0.007	0.52	0.01
TiO <sub>2</sub>	1.03	1.64	1.28	2.72	0.006	2.73	0.04
P <sub>2</sub> O <sub>5</sub>	0.21	0.54	0.30	0.26	0.002	0.27	0.02
MnO	0.15	0.17	0.13	0.17	0.001	0.17	0.01
Measured Total	98.96	99.61	99.44				
Mg#	64.00	46.47	56.77				
Sc	27.37	21.76	20.46	30.9	0.544	32	1
V	196.3	182.9	165.8	320.9	6.709	317	11
Cr	453.2	54.53	179.8	286.7	8.540	280	19
Co	42.71	94.85	77.93	45.7	1.274	45	3
Ni	155.1	78.09	131.5	117.6	5.229	119	7
Cu	58.43	44.58	42.77	126.5	4.485	127	7
Zn	71.21	93.35	70.47	102.8	3.538	103	6
Rb	10.25	9.76	27.19	9.64	0.096	9.8	1.0
Sr	439.4	482.40	409.0	392.6	8.661	389	23
Y	18.25	32.26	22.38	25.3	0.856	26	2
Zr	101.2	148.9	178.3	177.9	2.970	172	11
Nb	6.95	9.23	12.20	18.3	0.229	18	2
Cs	0.34	0.35	0.89	0.102	0.003		
Ba	212.0	327.90	403.7	127.2	4.748	130	13
La	9.67	14.87	15.61	15.3	0.478	15	1
Ce	21.57	36.43	34.44	38.1	1.095	38	2
Pr	2.90	5.11	4.39	5.32	0.166		
Nd	12.74	23.30	18.38	24.51	0.580	25.0	1.8
Sm	3.15	5.91	4.23	6.11	0.160	6.2	0.4
Eu	1.00	1.78	1.25	1.71	0.030		
Gd	3.50	5.58	4.58	6.25	0.115	6.3	0.2
Tb	0.565	0.932	0.707	0.97	0.025	0.9	
Dy	3.31	5.68	4.06	5.21	0.123		
Ho	0.713	1.181	0.846	1.00	0.038	1.04	0.04
Er	2.01	3.31	2.41	2.54	0.047		
Tm	0.279	0.457	0.330	0.328	0.010		
Yb	1.93	3.07	2.31	2.04	0.037	2.0	0.2
Lu	0.280	0.448	0.341	0.285	0.014	0.28	0.01
Hf	2.34	3.35	3.79	4.17	0.172	4.1	0.3
Ta	0.39	0.56	0.76	1.16	0.024	1.4	
Th	1.28	1.00	2.68				
U	0.48	0.44	1.03				

Group refers to the sample groups identified in Figure 2.1 and subsequent plots. Major elements (wt.%) were determined by XRF on fused glass disks. Analyses are normalized to 100% on an anhydrous basis. Measured analytical totals are given for reference. Total Fe is reported as Fe<sub>2</sub>O<sub>3</sub>. Mg# = molar (MgO/(MgO+FeO))\*100. Trace element concentrations (ppm) were determined by ICP-MS, except Th and U concentrations which were determined from Neptune MC-ICP-MS analyses. Measured values for the USGS standard BHVO-2 are the mean of six separate analyses.

spike and fluxed with perchloric and boric acids to ensure breakdown of fluoride compounds and complete spike-sample equilibration. A co-precipitation step with iron hydroxides was employed before the sample was dissolved in 7N HNO<sub>3</sub> for element separation and purification. U and Th were isolated and purified using Biorad AG 1-X8 anion exchange resin, eluting with H<sub>2</sub>O, HBr, and HCl respectively. The load and washes from this column were dried and dissolved in 2.5N HCl and passed through Biorad AG 50W-X8 cation exchange resin to separate Ra, Sr, and the REEs. Ra was purified with further passes through cation resin and Ra-Ba separation was achieved using Eichrom Sr resin. Sr was purified with Eichrom Sr resin and Nd was separated from the REEs with Eichrom LN resin.

Ra analyses were conducted on a Micromass Sector 54 thermal ionization mass spectrometer (TIMS) equipped with a Daly ion counter and WARP energy filter. U, Th, Sr, and Nd isotope ratios were measured on a Neptune MC-ICP-MS. Sr and Nd isotopes were analyzed in Faraday cups, monitoring <sup>83</sup>Kr and <sup>85</sup>Rb for interference during Sr runs and <sup>147</sup>Sm during Nd runs. NBS-987 Sr standard and the La Jolla Nd standard were run at the beginning and end of each analytical session, yielding average values (n = 8) of 0.71026 ± 2 and 0.511830 ± 6 (2σ) respectively. Sr ratios are normalized to <sup>86</sup>Sr/<sup>88</sup>Sr = 0.1194 and Nd ratios are normalized to <sup>146</sup>Nd/<sup>144</sup>Nd = 0.7219. U and Th were analyzed in static mode using a combination of Faraday cups (<sup>229</sup>Th, <sup>232</sup>Th, <sup>233</sup>U, <sup>235</sup>U, <sup>236</sup>U and <sup>238</sup>U) with 10<sup>10</sup>-10<sup>12</sup> Ω resistors, and a secondary electron multiplier (SEM) for <sup>230</sup>Th and <sup>234</sup>U. SEM-Faraday gain was monitored using NBL-112 U standard for U and an in-house Th standard for Th. Mass fractionation was corrected for using the spike <sup>233</sup>U-<sup>236</sup>U ratio of 1.00046. Repeat analyses of spiked NBL-112 U standard yielded average δ<sup>234</sup>U = -37.16

$\pm 0.74\text{‰}$  ( $n = 9$ ) in agreement with published values (Edwards et al., 1993; Cheng et al., 2000) ( $\delta^{234}\text{U}$  is the per mil deviation of the  $^{234}\text{U}/^{238}\text{U}$  from the secular equilibrium ratio).

## 2.4. Results

### 2.4.1. Major and Trace Elements

Major and trace element data are presented in Table 2.1, and a variety of major and trace element data are plotted in Figure 2.2. The majority of samples plot within the basalt or basaltic andesite fields in a silica vs. total alkalis plot (Fig. 2.2a) and all plot within the calc-alkaline field in a plot of  $\text{SiO}_2$  vs.  $\text{K}_2\text{O}$  (Fig 2.2b). Ni concentrations vary from  $\sim 20$  to 200 ppm and MgO content ranges from  $\sim 3$  to 9 wt.% (Fig. 2.2c & 2.2d) with Mg# (molar  $\text{MgO}/(\text{MgO}+\text{FeO})\cdot 100$ ) ranging from 44 to 64. The Sand Mountain group samples are generally the most primitive, although a small number of Belknap and pre-Mazama group samples also appear equally primitive.

Primitive mantle-normalized incompatible element ‘spidergrams’, and chondrite-normalized REE profiles, are shown in Figure 2.3. Sand Mountain group samples generally have the lowest incompatible element abundances with moderate Ba and Sr spikes. More evolved samples have more pronounced K and Sr spikes and Nb-Ta troughs. One pre-Mazama group sample (08-WIC-01) has elevated Nb and Ta concentrations (Fig. 2.3), with higher Nb/Zr and lower Ba/Zr ratios (Fig. 2.2e), more typical of Group I intraplate lavas. REE profiles are relatively smooth, with LREE enrichment and moderate negative Eu anomalies in the more evolved samples.

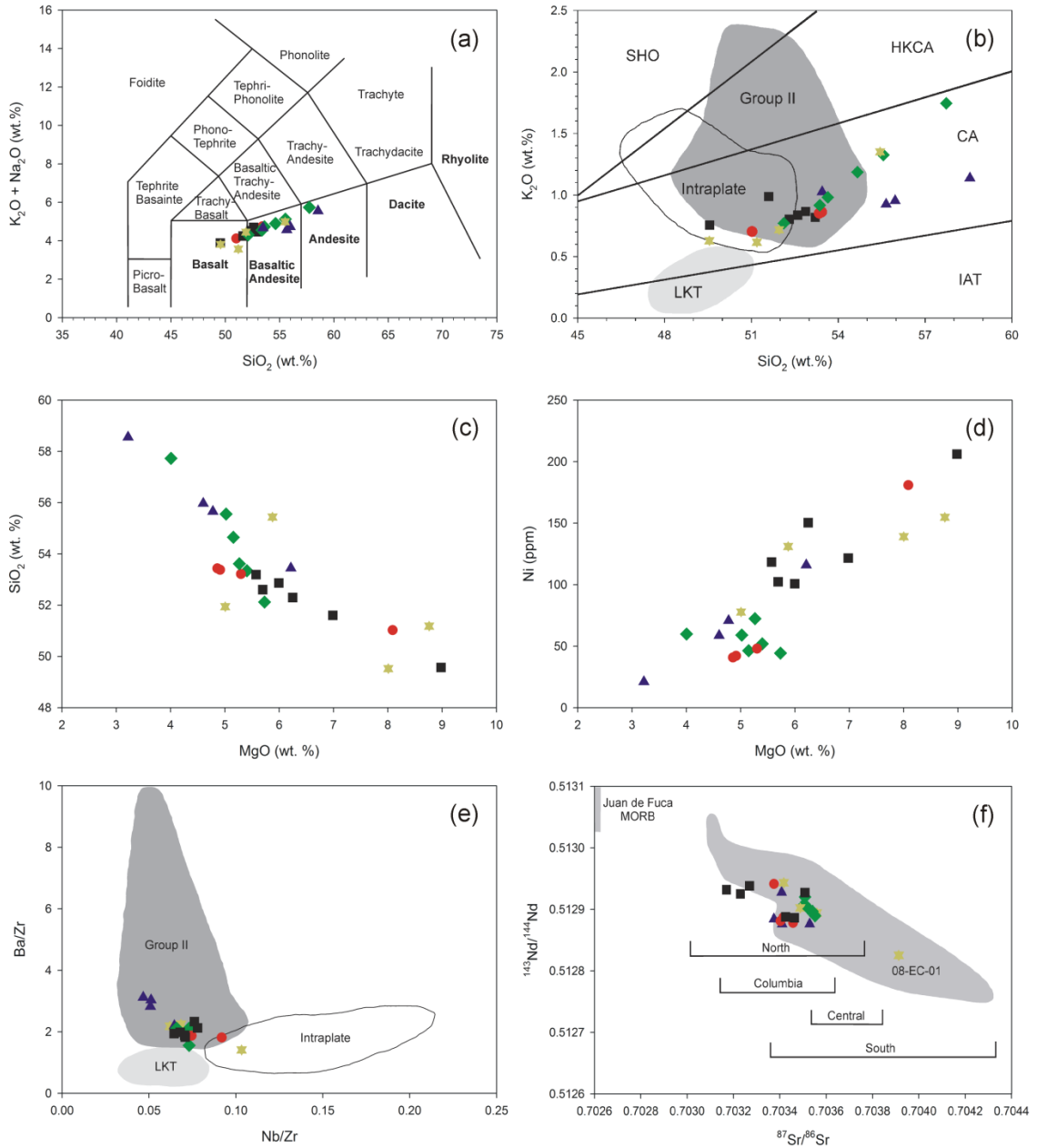


**Figure 2.2:** Various major element, trace element, and isotopic data for central Oregon lavas, symbols as Figure 2.1. Panel (a):  $\text{SiO}_2$  vs.  $(\text{K}_2\text{O} + \text{Na}_2\text{O})$  plot with IUGS classification scheme (after Le Bas et al., 1986). Panel (b):  $\text{SiO}_2$  vs.  $\text{K}_2\text{O}$  plot with fields for primitive LKT, Intraplate, and Group II lavas identified in the Cascades (after Leeman et al., 2005). Black lines are divisions between fields for island arc tholeiites (IAT), calc-alkaline basalts (CA), high-K calc-alkaline basalts (HKCA) and shoshonites (SHO). Panel (c):  $\text{MgO}$  vs.  $\text{SiO}_2$  plot. Panel (d):  $\text{MgO}$  vs.  $\text{Ni}$  plot. Panel (e):  $\text{Nb/Zr}$  vs.  $\text{Ba/Zr}$  plot with primitive LKT, Intraplate, and Group II fields as in panel (b). Panel (f):  $^{87}\text{Sr}/^{86}\text{Sr}$  vs.  $^{143}\text{Nd}/^{144}\text{Nd}$  plot. Shaded area is the field of Cascades CABs and the range of  $^{87}\text{Sr}/^{86}\text{Sr}$  is shown for each segment (after Schmidt et al., 2008). Juan de Fuca and Gorda ridge MORB field (indicated) extends to  $^{87}\text{Sr}/^{86}\text{Sr} = 0.7023$  and  $^{143}\text{Nd}/^{144}\text{Nd} = 0.51325$  (after White et al., 1987).

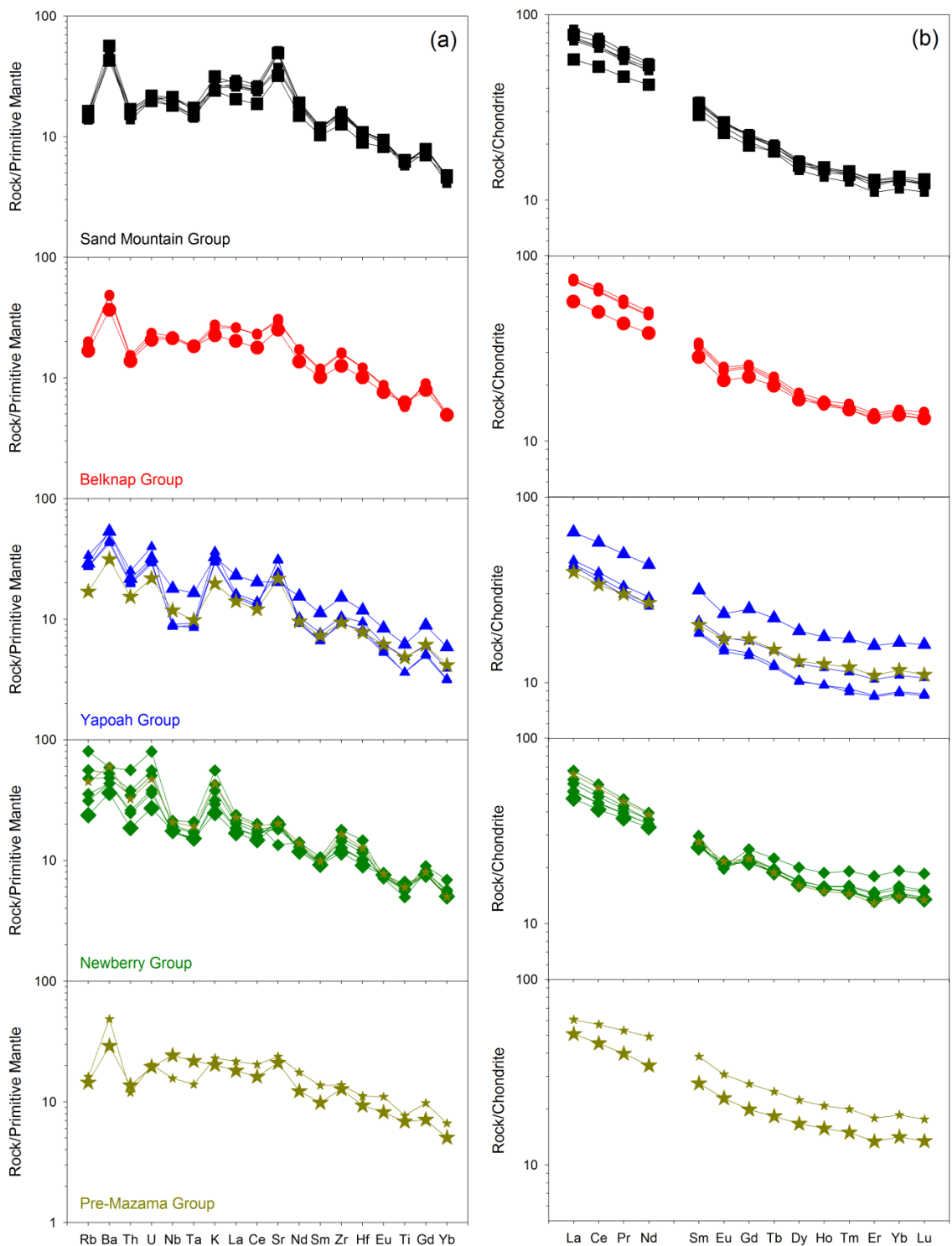


**Figure 2.3:** Trace element data for central Oregon lavas. Panel (a): Incompatible element spidergrams, normalized to primitive mantle (Palme and O’Neill, 2003). Lavas are plotted in groups as defined in Figure 2.1 and in the text. Primitive samples in each group (08-LL-01, 08-SM-01, 08-WBB-01, 07-FCA-01, 08-WIC-01 and 08-CYC-01) are plotted with larger symbols. Pre-Mazama group samples CYC and LC are shown with the

#### 2.4.2. Sr and Nd Isotopes

Sr and Nd isotope ratios exhibit little variation and, with the exception of sample 08-EC-01 ( $^{87}\text{Sr}/^{86}\text{Sr} = 0.70391$ ;  $\epsilon_{\text{Nd}} = 3.67$ ),  $^{87}\text{Sr}/^{86}\text{Sr}$  varies from 0.70317 to 0.70356 and  $\epsilon_{\text{Nd}}$  varies from 4.64 to 5.97 (Table 2.2, Fig. 2.2f). These values are, respectively, higher and lower than typical N-MORB (Su and Langmuir, 2003), and are within the range of previously published data for the Cascades (Schmidt et al., 2008). Sample 08-WIC-01 is indistinguishable from the other samples. Schmidt et al. (2008) divided the Cascade arc into four segments on the basis of Sr and Nd isotopes, putting the boundary between the Columbia and Central segments between Mt. Jefferson, just to the north of the study area, and the Three Sisters. Our Sr and Nd data indicate that the Columbia segment should be extended to the south to encompass the study area (Fig. 2.2f).

#### 2.4.3. U-Series Isotopes

All samples display  $^{230}\text{Th}$  enrichment ( $(^{230}\text{Th}/^{238}\text{U}) > 1$ ) or are in secular equilibrium ( $(^{230}\text{Th}/^{238}\text{U}) = 1$ ), with a range of non-equilibrium ( $^{230}\text{Th}/^{238}\text{U}$ ) values of 1.029 to 1.350 (3-35%  $^{230}\text{Th}$  enrichment) and ( $^{230}\text{Th}/^{232}\text{Th}$ ) values ranging from 1.191 to 1.393 (Table 2.2, Fig. 2.4a). Sand Mountain group samples have the largest  $^{230}\text{Th}$ -excesses. Enrichment in  $^{230}\text{Th}$  over  $^{238}\text{U}$  is unusual for most arc lavas, which typically show  $^{238}\text{U}$ -enrichment (Turner et al., 2003a), although  $^{230}\text{Th}$ -enrichment is the norm in the Cascades. The samples also display modest  $^{226}\text{Ra}$ -enrichment, although a greater number of samples are in Ra-Th secular equilibrium (Table 2.2). Measured non-equilibrium ( $^{226}\text{Ra}/^{230}\text{Th}$ ) values range from 1.046 to 1.197, with ( $^{226}\text{Ra}/^{230}\text{Th}$ )<sub>i</sub> values (age-corrected

---

Yapoah and Newberry groups respectively. Panel (b): Chondrite-normalized REE plots, with normalization values from Palme and Jones (2003). All samples are enriched in LREEs over HREEs and most have slight negative Eu anomalies.

**Table 2.2**

U-Th-Ra-Sr-Nd isotope data for central Oregon lavas.

Sample ID	Age ( $^{14}\text{C}$ yr B.P.)	U (ppm)	Th (ppm)	$^{232}\text{Th}/^{238}\text{U}$	$(^{230}\text{Th}/^{232}\text{Th})$	$(^{238}\text{U}/^{232}\text{Th})$	$(^{234}\text{U}/^{238}\text{U})$	$(^{230}\text{Th}/^{238}\text{U})$
<i>Three Sisters</i>								
07-BCB-01	$>2883 \pm 175$	$0.511 \pm 1$	$1.284 \pm 5$	$2.598 \pm 11$	$1.342 \pm 8$	$1.207 \pm 5$	$1.003 \pm 1$	$1.112 \pm 6$
07-BCB-02	$>2883 \pm 175$	$0.512 \pm 1$	$1.300 \pm 3$	$2.626 \pm 9$	$1.346 \pm 6$	$1.194 \pm 4$	$1.000 \pm 1$	$1.127 \pm 5$
07-CC-01	$1600 \pm 100$	$0.866 \pm 3$	$2.094 \pm 5$	$2.498 \pm 11$	$1.292 \pm 6$	$1.255 \pm 5$	$1.002 \pm 2$	$1.029 \pm 5$
07-FCA-01	$1980 \pm 160$	$0.694 \pm 2$	$1.811 \pm 5$	$2.696 \pm 15$	$1.204 \pm 6$	$1.163 \pm 5$	$1.000 \pm 2$	$1.035 \pm 5$
07-LB-01	$2883 \pm 175$	$0.483 \pm 1$	$1.236 \pm 3$	$2.646 \pm 9$	$1.329 \pm 5$	$1.185 \pm 4$	$1.001 \pm 1$	$1.121 \pm 4$
07-LN-01	$<2590 \pm 150$	$0.439 \pm 1$	$1.151 \pm 3$	$2.708 \pm 9$	$1.411 \pm 5$	$1.158 \pm 4$	$1.002 \pm 1$	$1.219 \pm 5$
07-NC-01	$<3850 \pm 215$	$0.460 \pm 1$	$1.360 \pm 3$	$3.058 \pm 10$	$1.384 \pm 6$	$1.025 \pm 3$	$1.001 \pm 1$	$1.350 \pm 5$
07-YC-01	$>1980 \pm 160$ $<2883 \pm 175$	$0.634 \pm 1$	$1.626 \pm 4$	$2.650 \pm 9$	$1.263 \pm 6$	$1.183 \pm 4$	$1.001 \pm 1$	$1.067 \pm 4$
07-YC-02	$>1980 \pm 160$ $<2883 \pm 175$	$0.650 \pm 1$	$1.660 \pm 4$	$2.639 \pm 9$	$1.278 \pm 5$	$1.188 \pm 4$	$1.004 \pm 1$	$1.076 \pm 4$
08-CYC-01	$> \text{MMA}$	$0.475 \pm 1$	$1.279 \pm 4$	$2.782 \pm 11$	$1.215 \pm 6$	$1.127 \pm 4$	$1.000 \pm 1$	$1.078 \pm 5$
08-EC-01	$> \text{MMA}$	$0.442 \pm 1$	$0.996 \pm 3$	$2.329 \pm 9$	$1.368 \pm 6$	$1.346 \pm 5$	$1.001 \pm 1$	$1.016 \pm 4$
08-LC-01	$> \text{MMA}$	$1.033 \pm 2$	$2.682 \pm 6$	$2.682 \pm 9$	$1.191 \pm 5$	$1.169 \pm 4$	$1.001 \pm 1$	$1.019 \pm 4$
08-LL-01	$1950 \pm 150$	$0.432 \pm 1$	$1.305 \pm 3$	$3.119 \pm 11$	$1.287 \pm 5$	$1.005 \pm 3$	$1.003 \pm 1$	$1.280 \pm 5$
08-NCSW-01	$<3850 \pm 215$	$0.462 \pm 1$	$1.241 \pm 3$	$2.772 \pm 10$	$1.393 \pm 6$	$1.131 \pm 4$	$1.001 \pm 1$	$1.231 \pm 5$
08-SM-01	$>2750 \pm 45$ $<3850 \pm 215$	$0.471 \pm 1$	$1.403 \pm 4$	$3.079 \pm 11$	$1.339 \pm 5$	$1.018 \pm 4$	$1.001 \pm 1$	$1.315 \pm 5$
08-SMCL-01	$<2750 \pm 45$	$0.479 \pm 1$	$1.409 \pm 4$	$3.039 \pm 11$	$1.340 \pm 6$	$1.032 \pm 4$	$0.996 \pm 1$	$1.299 \pm 5$
08-WBB-01	$1400 \pm 100$	$0.445 \pm 1$	$1.150 \pm 3$	$2.670 \pm 9$	$1.294 \pm 5$	$1.174 \pm 4$	$1.002 \pm 1$	$1.102 \pm 4$
08-WIC-01	$> \text{MMA}$	$0.425 \pm 1$	$1.142 \pm 3$	$2.780 \pm 9$	$1.322 \pm 8$	$1.128 \pm 4$	$0.998 \pm 1$	$1.172 \pm 7$
<i>Newberry</i>								
08-FRF-01	$5960 \pm 100$	$0.777 \pm 2$	$2.058 \pm 5$	$2.739 \pm 9$	$1.243 \pm 5$	$1.145 \pm 5$	$1.000 \pm 1$	$1.085 \pm 4$
08-LBF-01	$6160 \pm 70$	$1.191 \pm 3$	$3.158 \pm 8$	$2.739 \pm 9$	$1.218 \pm 5$	$1.145 \pm 5$	$1.000 \pm 1$	$1.064 \pm 4$
08-LCFF-01	$6320 \pm 110$	$0.833 \pm 2$	$2.165 \pm 5$	$2.687 \pm 9$	$1.238 \pm 5$	$1.167 \pm 4$	$1.001 \pm 1$	$1.061 \pm 4$
08-MBF-02	n.d.	$1.739 \pm 4$	$4.684 \pm 11$	$2.783 \pm 9$	$1.195 \pm 5$	$1.126 \pm 4$	$1.001 \pm 1$	$1.060 \pm 4$
08-SF-01	$6030 \pm 90$	$1.097 \pm 3$	$2.887 \pm 7$	$2.718 \pm 9$	$1.222 \pm 5$	$1.153 \pm 4$	$1.001 \pm 1$	$1.059 \pm 4$
08-SPBF-01	n.d.	$0.585 \pm 1$	$1.545 \pm 4$	$2.730 \pm 9$	$1.271 \pm 5$	$1.149 \pm 4$	$1.002 \pm 1$	$1.106 \pm 4$
Ryan Std.		$1.262 \pm 3$	$7.348 \pm 18$	$6.015 \pm 21$	$0.522 \pm 2$	$0.521 \pm 2$	$1.004 \pm 1$	$1.002 \pm 4$

**Table 2.2**

Continued.

Sample ID	$^{226}\text{Ra}$ (pg/g)	$(^{226}\text{Ra}/^{230}\text{Th})$	$(^{226}\text{Ra}/^{230}\text{Th})_i$	$^{87}\text{Sr}/^{86}\text{Sr}$	$^{143}\text{Nd}/^{144}\text{Nd}$	$\epsilon_{\text{Nd}}$
<i>Three Sisters</i>						
07-BCB-01	0.205 ± 3	1.067 ± 15	1.251 <sup>+95</sup> <sub>-70</sub>	0.703417 ± 5	0.512887 ± 4	4.86 ± 0.08
07-BCB-02	0.204 ± 2	1.047 ± 10	1.176 <sup>+67</sup> <sub>-51</sub>	0.703456 ± 4	0.512879 ± 3	4.70 ± 0.06
07-CC-01	0.301 ± 3	1.112 ± 13	1.220 <sup>+32</sup> <sub>-38</sub>	0.703529 ± 5	0.512876 ± 5	4.64 ± 0.10
07-FCA-01	0.237 ± 2	1.001 ± 10	n.d.	0.703407 ± 6	0.512927 ± 2	5.64 ± 0.04
07-LB-01	0.192 ± 3	1.050 ± 14	1.187 <sup>+86</sup> <sub>-64</sub>	0.703404 ± 5	0.512881 ± 3	4.74 ± 0.06
07-LN-01	0.199 ± 2	1.122 ± 12	1.411 <sup>+61</sup> <sub>-84</sub>	0.703463 ± 7	0.512886 ± 4	4.84 ± 0.08
07-NC-01	0.250 ± 3	1.193 ± 13	2.245 <sup>+259</sup> <sub>-229</sub>	0.70323 ± 1	0.512925 ± 2	5.60 ± 0.04
07-YC-01	0.239 ± 7	1.046 ± 30	1.135 <sup>+143</sup> <sub>-99</sub>	0.70341 ± 1	0.512876 ± 4	4.64 ± 0.08
07-YC-02	0.250 ± 8	1.059 ± 35	1.176 <sup>+169</sup> <sub>-118</sub>	0.703375 ± 8	0.512884 ± 5	4.80 ± 0.10
08-CYC-01	n.m.	n.m.	n.d.	0.703561 ± 5	0.512895 ± 4	5.01 ± 0.08
08-EC-01	n.m.	n.m.	n.d.	0.703913 ± 5	0.512826 ± 5	3.67 ± 0.10
08-LC-01	n.m.	n.m.	n.d.	0.703489 ± 4	0.512903 ± 4	5.17 ± 0.08
08-LL-01	0.224 ± 4	1.197 ± 19	1.455 <sup>+84</sup> <sub>-73</sub>	0.703509 ± 6	0.512927 ± 3	5.64 ± 0.06
08-NCSW-01	0.219 ± 2	1.138 ± 12	1.889 <sup>+206</sup> <sub>-179</sub>	0.703425 ± 6	0.512888 ± 4	4.88 ± 0.08
08-SM-01	0.240 ± 4	1.146 ± 20	1.740 <sup>+252</sup> <sub>-182</sub>	0.703271 ± 9	0.512938 ± 4	5.85 ± 0.08
08-SMCL-01	0.243 ± 3	1.155 ± 15	1.546 <sup>+82</sup> <sub>-73</sub>	0.70317 ± 2	0.512931 ± 5	5.72 ± 0.10
08-WBB-01	0.179 ± 5	1.080 ± 32	1.145 <sup>+63</sup> <sub>-59</sub>	0.703374 ± 1	0.512941 ± 4	5.91 ± 0.08
08-WIC-01	0.169 ± 2	1.004 ± 11	n.d.	0.703417 ± 9	0.512944 ± 4	5.97 ± 0.08
<i>Newberry</i>						
08-FRF-01	0.284 ± 3	0.999 ± 11	n.d.	0.703544 ± 7	0.512896 ± 4	5.03 ± 0.08
08-LBF-01	n.m.	n.m.	n.d.	0.703552 ± 7	0.512890 ± 5	4.92 ± 0.10
08-LCFF-01	n.m.	n.m.	n.d.	0.703547 ± 5	0.512893 ± 4	4.97 ± 0.08
08-MBF-02	0.631 ± 15	1.014 ± 24	n.d.	0.703505 ± 6	0.512909 ± 4	5.29 ± 0.08
08-SF-01	n.m.	n.m.	n.d.	0.703530 ± 4	0.512899 ± 4	5.09 ± 0.08
08-SPBF-01	0.214 ± 12	0.980 ± 53	n.d.	0.703509 ± 5	0.512921 ± 4	5.52 ± 0.08
Ryan Std.	0.433 ± 5	1.010 ± 13	n.d.			

Ratios in parentheses represent activity ratios (the number of atoms times the decay constant,  $\lambda$ ).Decay constants used are as follows:  $\lambda_{226} = 4.33 \times 10^{-4} \text{ yr}^{-1}$ ,  $\lambda_{230} = 9.1577 \times 10^{-6} \text{ yr}^{-1}$ ,  $\lambda_{232} =$  $4.9475 \times 10^{-11} \text{ yr}^{-1}$ ,  $\lambda_{234} = 2.8263 \times 10^{-6} \text{ yr}^{-1}$ ,  $\lambda_{238} = 1.5513 \times 10^{-10} \text{ yr}^{-1}$ . All uncertainties are  $2\sigma$ 

measurement errors. Spikes were prepared from pure metals (U and Th) and Ra was milked from NIST 3159  $^{232}\text{Th}$  Standard. An in-house secular equilibrium standard was processed and measured with each batch of samples. U standard NBL-112 was also measured during each analytical session yielding a mean  $\delta^{234}\text{U}$  value of  $-37.16 \pm 0.74\%$  ( $n = 9$ ) in agreement with published values of  $-37.1 \pm 1.2\%$  (Edwards et al., 1993) and  $-36.9 \pm 2.1\%$  (Cheng et al., 2000). ( $^{226}\text{Ra}/^{230}\text{Th}$ )<sub>i</sub> ratios are initial values corrected back to the time of eruption using calibrated ages in sidereal years based on  $^{14}\text{C}$  ages (" $> \text{MMA}$ " = older than the Mt. Mazama ash horizon, approx. 7.65 ka). Sr standard NBS-987 and the La Jolla Nd standard were analyzed at the beginning and end of each analytical session, yielding average values ( $n = 8$ ) of  $0.71026 \pm 2$  and  $0.511830 \pm 6$  ( $2\sigma$ ) respectively.

$\epsilon_{\text{Nd}} = [((^{143}\text{Nd}/^{144}\text{Nd})_{\text{sample}} - (^{143}\text{Nd}/^{144}\text{Nd})_{\text{CHUR}}) / (^{143}\text{Nd}/^{144}\text{Nd})_{\text{CHUR}}] * 10,000$ , where  $(^{143}\text{Nd}/^{144}\text{Nd})_{\text{CHUR}} = 0.512638$ , relative to  $^{146}\text{Nd}/^{144}\text{Nd} = 0.7219$ .

to the time of eruption) ranging from 1.085 to 2.245 (9-125%  $^{226}\text{Ra}$ -enrichment) (Fig. 2.4b). These ranges are consistent with typical MORB (Lundstrom, 2003) and are lower than values frequently measured in arc lavas, which range up to  $\sim 6$  (Turner et al., 2003a).

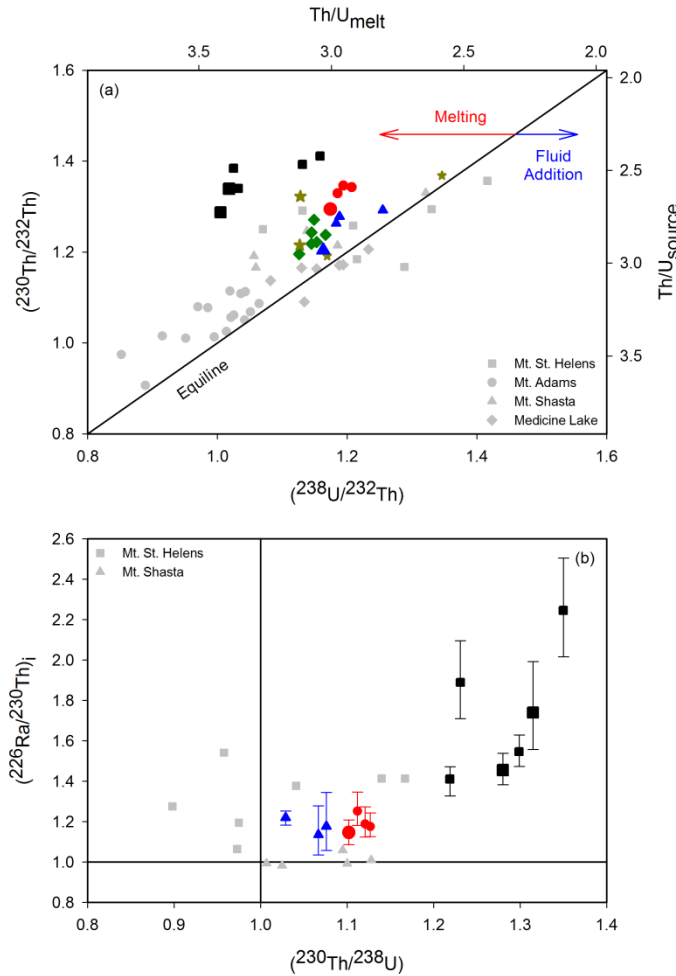


**Figure 2.4:** U-series isotope data for central Oregon lavas, symbols as Figure 2.1. Panel (a):  $(^{238}\text{U}/^{232}\text{Th})$  vs.  $(^{230}\text{Th}/^{232}\text{Th})$  ‘equiline’ plot. Error bars are smaller than symbol size. Published mass spectrometry data for other Cascades volcanoes are also shown (St Helens data: Volpe & Hammond (1991); Shasta data: Volpe (1992); Medicine Lake data: Reagan et al. (2003); Mt. Adams data: Jicha et al. (2009b)). Black line labeled ‘Equiline’ represents the steady-state condition of secular equilibrium, where  $(^{230}\text{Th}/^{238}\text{U}) = 1$ . Melting will generally move samples to the left ( $(^{230}\text{Th}/^{238}\text{U}) > 1$ ), while fluid addition will move samples to the right ( $(^{230}\text{Th}/^{238}\text{U}) < 1$ ). Aging will move samples vertically back toward the equiline. All central Oregon data, and the majority of Cascades data, plots to the

left of the equiline in the Th-enrichment field, similar to MORB and in contrast to typical arc lavas, which generally show U over Th enrichment (i.e. Lundstrom, 2003; Turner et al., 2003a). Panel (b):  $(^{230}\text{Th}/^{238}\text{U})$  vs.  $(^{226}\text{Ra}/^{230}\text{Th})_i$  plot, with other Cascades volcanoes where Ra data are available.  $(^{226}\text{Ra}/^{230}\text{Th})_i$  ratios are corrected back to the time of eruption on the basis of ages in Table 1. Newberry samples are in Ra-Th secular equilibrium and are not plotted. Error bars on Ra measurements reflect both analytical uncertainty and age uncertainties, but are dominated by the latter.

## 2.5. Discussion

### 2.5.1. Comparison with Existing Cascade Lava Types

The major, trace element, and isotopic data presented in Figures 2.2, 2.3 and 2.4 demonstrate that these samples are typical of lavas erupted in the central Cascades. On the basis of Figures 2.2b and 2.2e in particular, the majority of samples are interpreted to be Group II calc-alkaline basalts (CABs). This includes the six samples from the rear-arc Newberry Volcano, which are indistinguishable from the arc-axis Three Sisters samples. One sample (08-WIC-01) is interpreted to be a Group I intraplate basalt. The U-series data are broadly consistent with existing mass spectrometry data for the Cascades, although our data do extend the range of both ( $^{230}\text{Th}/^{238}\text{U}$ ) and ( $^{226}\text{Ra}/^{230}\text{Th}$ ) measured in Cascades lavas to higher values (Fig. 2.4).

Previous trace element and isotopic studies of the Cascades have been largely restricted to primitive lavas, defined by characteristics such as Ni > 100 ppm, Cr > 200 ppm, SiO<sub>2</sub> < 55 wt.%, MgO > 6 wt.% and Mg# > 55 (i.e. Leeman et al., 2005). Our dataset includes almost every lava in the study area young enough to be suitable for U-series work, and ranges from primitive samples with the characteristics noted above (e.g., 08-LL-01, 08-WBB-01, 08-WIC-01, 08-CYC-01) to highly evolved basaltic andesites and andesites (the majority of the Yapoah and Newberry group samples). In the following section we briefly consider the process(es) that may have generated the evolved lavas, before investigating the petrogenesis of the most primitive samples in subsequent sections.

### 2.5.2. *Crustal Processing*

The crust beneath the central Oregon Cascades is ~ 45 km thick (Leaver et al., 1984; Catchings and Mooney, 1988; Stanley et al., 1990; Eagar et al., 2011), and interaction with this crust has been identified as an important process in this region of the arc (e.g., Conrey et al., 2001; Schmidt and Grunder, 2011). Hyperbolic trends in incompatible element ratio plots (e.g., Rb/Sr vs. K/Rb, Th vs. Ba/Th, Rb vs. K/Rb), and linear trends in reciprocal plots (e.g., 1/Th vs. Ba/Th, 1/Sr vs. Rb/Sr, 1/Rb vs. K/Rb), suggest mixing plays a dominant role in the generation of the evolved lavas (Fig. 2.5). In detail, trace element behavior is complex, and offers insights into the processes operating at the crustal level. As would be expected, compatible element (i.e. Ni, Cr, Co) abundances decrease, both between and within groups, as samples become more evolved (as determined from SiO<sub>2</sub>, MgO, Mg#, etc.). Similarly, extremely incompatible element (i.e. Rb, Cs) abundances increase, between and within groups, as samples become more evolved. However, a number of elements, such as Sr, Ba, La, and Eu, show a pattern of decreasing concentrations between the most primitive sample in each group, with the Sand Mountain group having the highest concentrations followed by the Belknap group, but increasing within groups as samples become more evolved. An exception is the Newberry group, where Sr and Eu concentrations decrease as samples become more evolved.

These observations suggest that variable assimilation of a low-Sr-Ba-La-Eu component may be responsible for generating the differences between the various groups, while fractional crystallization may generate within-group differences. The characteristics of this assimilant are qualitatively consistent with partial melting of an

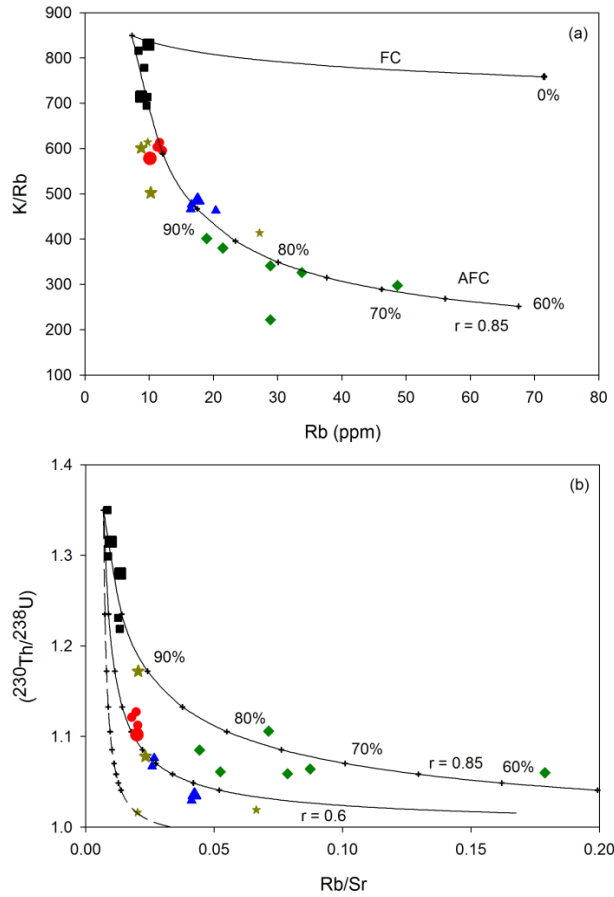


**Figure 2.5:** Crustal contamination modeling for central Oregon lavas, symbols as Figure 2.1. Panel (a): Rb vs. K/Rb plot. Line marked ‘FC’ is fractional crystallization curve for the assemblage plagioclase (60%) + olivine (20%) + clinopyroxene (20%). Initial magma has 7.3 ppm Rb and 6200 ppm K. Line marked ‘AFC’ is an assimilation-fractional crystallization trend (DePaolo, 1981) for the same initial magma and fractionating assemblage. Assimilant has 15 ppm Rb and 2500 ppm K. Assimilation to crystallization ratio ( $r$ ) is 0.85. Tick marks are the proportion of the initial magma remaining, in 5% increments, as labeled. AFC trend is insensitive to the fractionating assemblage, with a plagioclase (20%) + olivine (60%) + clinopyroxene (20%) assemblage producing nearly indistinguishable results. D values are from Claeson and Meurer (2004). Panel (b): Rb/Sr vs.  $(^{230}\text{Th}/^{238}\text{U})$  plot. Dashed line is a mixing curve between primitive lava with Rb/Sr = 0.007 and  $(^{230}\text{Th}/^{238}\text{U}) = 1.35$  and a secular equilibrium assimilant with 15 ppm Rb and 450 ppm Sr. Solid lines are AFC trends for different  $r$  values for the same assimilant and the fractionating assemblage shown in panel (a). Fractional crystallization is assumed to have no effect on  $(^{230}\text{Th}/^{238}\text{U})$ . Tick marks are the proportion of the initial magma remaining, in 5% increments, as labeled. AFC trends are again largely insensitive to the fractionating assemblage, with the higher plagioclase mode only required to produce the higher Rb/Sr values of the Newberry samples.

incompatible element depleted mafic crustal source with significant residual plagioclase. A similar component has been implicated in the generation of North Sister-type basaltic andesites (Schmidt and Grunder, 2011).

Sr concentrations increase as samples become more evolved within the Sand Mountain and Belknap groups, but decrease as Newberry group samples become more evolved. This observation suggests that plagioclase is not a significant part of the fractionating assemblage in the former groups but is in the latter group, consistent with AFC calculations (Fig. 2.5). This also implies that the negative Eu anomaly observed in the majority of samples is a feature of the assimilated melt, not a product of fractional crystallization. While it is not the purpose of this work to explain in detail the generation of the more evolved samples, these calculations demonstrate that many of the trace element differences between the more and less primitive lavas can be explained by a simple A(FC) model. The implicit assumption that a single magma is parental to all the groups will be explored further later.

### *2.5.3. Mantle Sources and Slab Components*

A point of considerable debate regarding the spectrum of basaltic lavas erupted in the Cascades is whether the various magma types (LKT, CAB, etc.) can be derived from the same source, or whether different magmas require distinct (e.g., garnet-bearing vs. garnet-free) sources (e.g., Leeman et al., 2005; Hildreth, 2007; Schmidt et al., 2008; Rowe et al., 2009). Leeman et al. (2005) noted that LKTs typically display relatively flat, unfractionated REE patterns, inconsistent with a garnet-bearing source, a conclusion supported by their inferred segregation pressures, as well as experimental results (Bartels et al., 1991). In contrast, intraplate lavas typically do exhibit fractionated REE patterns,

implying a separate, deeper source (Leeman et al., 2005), consistent with Sr and Nd isotope systematics (Schmidt et al. 2008). The role of garnet in the generation of CABs is less clear. Both Baker et al. (1994) and Reiners et al. (2000) suggested that garnet was not required to generate CABs from Mt. Shasta and central Washington respectively, while a number of studies of CABs along the length of the arc have suggested that garnet is required (Leeman et al., 1990; Bacon et al., 1997; Borg et al., 1997; Conrey et al., 1997; Borg et al., 2002; Righter et al., 2002; Green and Sinha, 2005; Jicha et al., 2009a). Leeman et al. (2005) inferred that Group II lavas have shallower segregation depths than Group I lavas, which do not have a garnet signature, a conclusion consistent with experimental data (Gaetani and Grove, 2003).

One proposed explanation of these data is that Group II lavas originated near the slab in the garnet stability field, inheriting both a garnet and fluid signature, but subsequently ‘froze’ at shallower depths. Later re-melting of these ‘pods’ of basaltic material, possibly by hot ascending Group I magmas, allowed them to be erupted (Harry and Leeman, 1995; Leeman et al., 2005). This scenario, specifically the decoupling of final melting from slab and garnet signature inheritance, is directly testable with U-series isotopes.

Figure 2.6 employs a La/Yb vs. Tb/Yb plot (Turner et al., 2003b; Jicha et al., 2009a) to investigate both source composition and mineralogy. The chosen mineralogy varies from Ol:Opx:Cpx:Grt:Spl = 62:22:14:0:2 for the garnet free source, to Ol:Opx:Cpx:Grt:Spl = 61:21:13:3:2 for the 3% garnet source, similar to previous modeling studies (e.g., Borg et al., 1997). The first salient observation is that an enriched mantle source (in this case the OIB source of Borg et al., 1997 & Jicha et al., 2009a (Table 2.3)), invoked by many workers as the source of intraplate basalts (e.g., Hildreth,

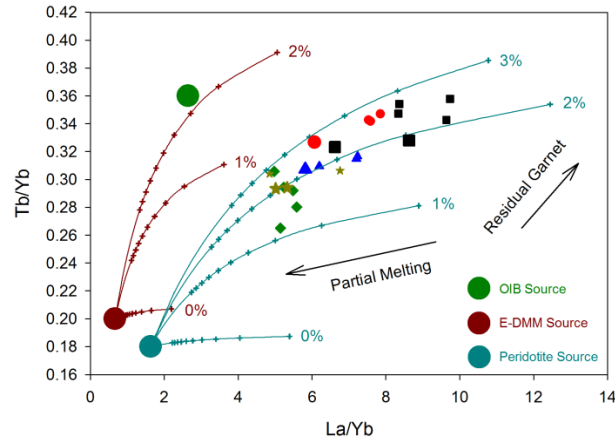


**Figure 2.6:** La/Yb vs. Tb/Yb modeling plot for central Oregon lavas, symbols as Figure 2.1. Red and blue lines are batch melting trajectories of E-DMM and peridotite sources, respectively. Amount of garnet in the source is labeled. Tick marks are 1% melting increments from 1-10%, except for peridotite 3% garnet curve, which is 2-10%. OIB source composition is also shown for reference. D values for La, Tb, and Yb range from 0.0084, 0.0487, and 0.0511 respectively for the garnet-free source to 0.0082, 0.0679, and 0.1687 respectively for the 3% garnet source. Composition of mantle sources can be found in Table 2.3.

2007), cannot be the source of any of our samples, as the OIB source Tb/Yb ratio is greater than the highest measured Tb/Yb ratio, and melting serves only to increase that ratio (Fig. 2.6). The second pertinent observation is that the enriched-depleted MORB mantle (E-DMM) source of Workman and Hart (2005) cannot generate the elevated La/Yb ratios observed in the samples. However, the peridotite source of Reiners et al. (2000), which has trace element abundances intermediate between the OIB and E-DMM sources, is able to reproduce both the La/Yb and Tb/Yb ratios of the most primitive CAB and intraplate samples through ~ 3 to 5% melting of a source containing 2 to 3% garnet. This observation suggests derivation of these lavas from a depth near the spinel/garnet transition (~ 60-90 km), consistent with our understanding of the geometry of the sub-arc

**Table 2.3**

Composition of mantle sources and slab components, and partition coefficients, used in modeling.

	DMM		E-DMM		Peridotite		OIB		AOC		Bulk Sediment		AOC Fluid		Sediment Fluid		Sediment Melt		Partition Coefficients					
	Source	Source	Source	Source	Source	Source	Source	Source	Source	Source	Source	Source	Source	Source	Source	Source	Source	Source	Ol.	Opx.	Cpx.	Grt.	Spl.	
La	0.192	0.253	0.815	1.48	3.34	21.75	3.544	13.01	12.83	0.0004	0.002	0.054	0.01	0.01										
Tb	0.070	0.076	0.09	0.20	0.72	0.80	0.00	0.00	0.00	0.0015	0.019	0.31	0.75	0.01										
Yb	0.365	0.382	0.50	0.56	2.63	2.20	0.00	0.00	0.00	0.0015	0.049	0.28	4.03	0.01										
Sr	7.664	9.718	18	28.7	142	216	261	236	538															
Nd	0.581	0.703	1.4	2.97	9.62	21.79	1.454	15.319	8.579															
Ba	0.563	1.219	9.0	13.1	12.2	746	114	718	1235	0.00011	0.0005	0.00068	0.001	0.00										
Nb	0.149	0.246	1.5	1.13	2.99	10	0.556	3.436	7.594	0.01	0.025	0.0	0.04	0.01										
Zr	5.082	6.087	25	26.4	89	146	3.61	59.8	101	0.01	0.18	0.3	0.5	0.07										
U	0.0032	0.0052	0.020	0.028	0.18	2.92	0.187	0.981	3.967	0.00006	0.0052	0.01	0.0	0.00001										
Th	0.0079	0.0157	0.070	0.160	0.14	6.63	0.064	1.656	8.696	$1.1 \times 10^{-6}$	$7.5 \times 10^{-6}$	$2.7 \times 10^{-5}$	$1 \times 10^{-7}$	0.00001										
Ra																								
La/Yb	0.526	0.662	1.630	2.643	1.270	9.886																		
Tb/Yb	0.192	0.199	0.180	0.357	0.274	0.364																		
Nb/Zr	0.029	0.040	0.060	0.043	0.034	0.068	0.154	0.057	0.075															
Ba/Zr	0.111	0.200	0.360	0.496	0.137	5.110	31.579	12.007	12.228															
$^{87}\text{Sr}/^{86}\text{Sr}$	0.7027	0.7030	0.7030	0.7030	0.7030	0.7071	0.7030	0.7071	0.7071															
$^{143}\text{Nd}/^{144}\text{Nd}$	0.51301	0.512989	0.51301	0.51253	0.51301	0.51253	0.51301	0.51253	0.51253															

DMM and E-DMM Sources: Workman and Hart (2005); Peridotite Source: Reiners et al. (2000); OIB Source: Borg et al. (1997). AOC composition from northern EPR N-MORB (Klein, 2003). Sediment composition from Plank and Langmuir (1998). Sediment Sr and Nd data from White et al., 1987. AOC fluid represents 4% dehydration using the 4 GPa, 800°C partition coefficients of Kessel et al. (2005). Sediment fluid represents 4% dehydration using the 2 GPa, 700°C partition coefficients of Johnson and Plank (1999). Sediment melt represents 12% melt using the 2 GPa, 900°C partition coefficients of Johnson and Plank (1999). REE partition coefficients from McKenzie and O'Nions (1991). Ba-Nb-Zr partition coefficients from Borg et al. (1997) Table 4. U-Th-Ra partition coefficients from Blundy and Wood (2003).

mantle in this part of the arc (McCroory et al., 2006; Obrebski et al., 2010). However, the REE data alone cannot constrain the time at which the garnet signature was acquired and are also consistent with the re-melting scenario described above. These competing hypotheses will be re-evaluated later in light of the U-series data. Interestingly, both CAB and intraplate samples require garnet in their source at some stage, suggesting that both could be derived from the same general source region.

Next we use  $^{87}\text{Sr}/^{86}\text{Sr}$ ,  $^{143}\text{Nd}/^{144}\text{Nd}$ , Nb/Zr, and Ba/Zr data to investigate the extent of fluid involvement in the generation of these lavas, and the likely source of any such fluid (Fig. 2.7). Figure 2.7a shows mixing curves between various slab components and sources with E-DMM Sr and Nd concentrations (Table 2.3) ( $^{87}\text{Sr}/^{86}\text{Sr}$  and  $^{143}\text{Nd}/^{144}\text{Nd} = 0.7027$  and  $0.51301$  respectively) and peridotite Sr and Nd concentrations (Table 2.3) ( $^{87}\text{Sr}/^{86}\text{Sr}$  and  $^{143}\text{Nd}/^{144}\text{Nd} = 0.703$  and  $0.512989$  respectively). The  $^{87}\text{Sr}/^{86}\text{Sr}$  and  $^{143}\text{Nd}/^{144}\text{Nd}$  ratios of the most primitive CABs and intraplate lavas can be modeled by addition of  $\sim 0.7$  to  $1\%$  of a sediment-derived fluid to the E-DMM source or  $\sim 0.8$  to  $1.5\%$  of the same fluid to the peridotite source. Adding an AOC component to the fluid has little impact on the mixing trajectory, but requires a larger fluid contribution ( $\sim 1.5$ - $2\%$  for both sources).

The Nb/Zr vs. Ba/Zr plot has commonly been used to illustrate the differences between the various primitive magmas erupted in the Cascades (e.g., Leeman et al., 1990) and we use such a plot to further investigate the composition of mantle sources and slab fluids (Fig. 2.7b). The Ba and Nb concentration estimates of the peridotite source are too high to match the central Oregon CAB data, although addition of  $1$  to  $2\%$  of the same sediment-derived fluid and  $8$  to  $9\%$  melting can reproduce the intraplate sample. Addition

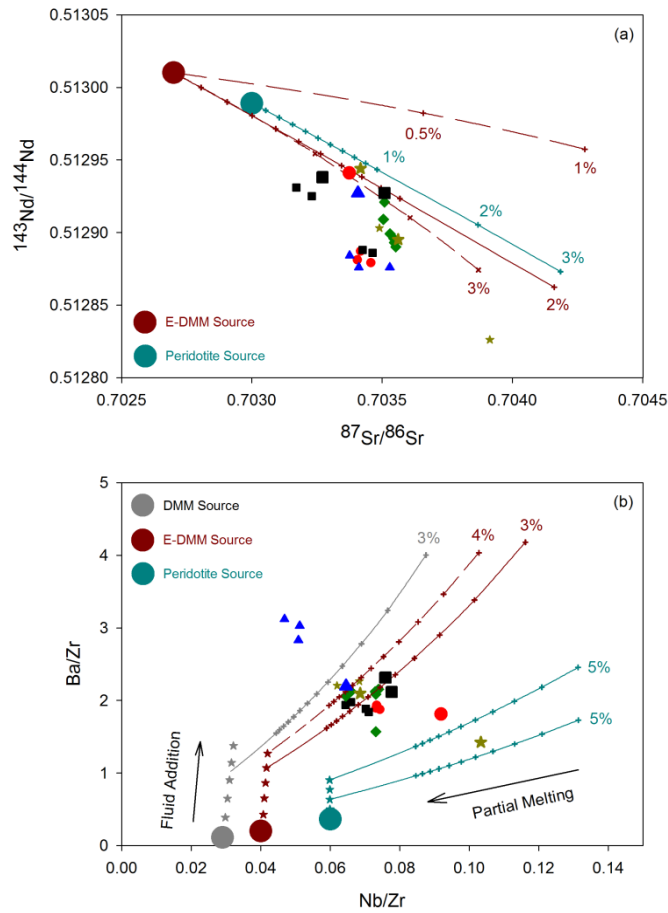


**Figure 2.7:** Slab component modeling plot for central Oregon lavas, symbols as Figure 2.1. Panel (a):  $^{87}\text{Sr}/^{86}\text{Sr}$  vs.  $^{143}\text{Nd}/^{144}\text{Nd}$  plot. Red and blue circles represent E-DMM and peridotite source compositions respectively. Solid lines are mixing curves with a sediment-derived fluid. Ticks marks are 0.1% increments to 1%, then as labeled. Long dashed line is a mixing curve with a sediment partial melt, with % melt indicated. Short dashed line is a mixing curve with a fluid derived from the altered oceanic crust (AOC) and sediment in the ratio 40:60, ticks at 1%, 2% and 3% fluid. Panel (b): Nb/Zr vs. Ba/Zr plot. Stars are mixing curves between the respective source and sediment-derived fluid in 0.2% increments to 1% for DMM sources, and in 0.5% increments to 2% for peridotite source. Solid lines are melting trajectories of sources modified by sediment-derived fluid. Dashed line is melting trajectory of E-DMM source modified by addition of 1.5% of the same 40:60 AOC/sediment-derived fluid shown in panel (a). Ticks are 1% melting increments from the labeled value to 15% melting.  $D_{\text{Ba}}$ ,  $D_{\text{Nb}}$  and  $D_{\text{Zr}}$  are 0.000277, 0.01295 and 0.0912 respectively. Composition of mantle sources and slab components can be found in Table 2.3.

of 0.8% sediment-derived fluid to the E-DMM source, and ~ 7 to 10% melting, can reproduce the primitive CAB sample characteristics. The trace element data are more consistent with a minimal AOC contribution to the fluid component. The most primitive Belknap sample (08-WBB-01) is intermediate between the intraplate and the remainder of the CAB samples in this plot, and could be reproduced by greater fluid addition to the peridotite source or lesser fluid addition to the E-DMM source, consistent with slightly more mantle-like Sr and Nd isotope ratios (Fig. 2.7a).

This model only considers a slab component derived from AOC or sediment dehydration, although at the elevated temperatures expected in the sub-arc Cascade mantle, melting of the subducting sediments and/or slab must be considered. Using the sediment melt partition coefficients of Johnson and Plank (1999), addition of a sediment melt is inconsistent with the  $^{87}\text{Sr}/^{86}\text{Sr}$  and  $^{143}\text{Nd}/^{144}\text{Nd}$  data (Fig. 2.7a). Furthermore, the primitive lavas do not possess the elevated Sr/Y, La/Yb, or Tb/Yb of western Aleutian lavas, regarded by Yogodzinski and Kelemen (1998) and Kelemen et al. (2003) as characteristic of the involvement of a slab partial melt.

In summary, the Sr-Nd, trace element, and REE systematics of the most primitive CAB and intraplate lavas can be modeled as small degree (< 10%) melts of a garnet-bearing mantle with a composition similar to the peridotite source of Reiners et al. (2000), or intermediate between this source and the E-DMM source of Workman and Hart (2005).  $^{87}\text{Sr}/^{86}\text{Sr}$ ,  $^{143}\text{Nd}/^{144}\text{Nd}$  and trace element data require modification of this source by a slab-derived component. Addition of ~ 1% of a fluid derived by 4% dehydration of bulk subducting sediment is the best match for this slab component. Minimal fluid involvement is consistent with recent olivine-hosted melt inclusion volatile

measurements made on a number of the same samples studied here, which show H<sub>2</sub>O concentrations elevated relative to MORB, but low when compared to other arcs and the southern Cascades (Ruscitto et al., 2010). The generation of both CAB and intraplate lavas by similar degrees of melting and fluid addition is consistent with the close spatial existence of veins or ‘pods’ of more and less depleted mantle (Hildreth, 2007), explaining how both groups can be generated in close spatial and temporal proximity. The characteristics of sample 08-WBB-01 suggest a continuum of variably fluid-modified sources may exist beneath the central Oregon Cascades.

#### *2.5.4. U-Series Isotopes and Mantle Melting*

The model presented above can be extended to include the behavior of U-series isotopes to provide further constraints on magma generation, and specifically, to address the outstanding issue of whether the slab component identified in these lavas (and commonly observed throughout the Cascades) is a modern slab-derived fluid, the addition of which initiates flux melting of the mantle wedge (e.g., Reiners et al., 2000), or whether these are decompression melts of a mantle source containing a ‘stored’ component from some earlier episode of Cascadia subduction (e.g., Leeman et al., 2005). In this latter scenario “earlier” is constrained by the half-life of <sup>230</sup>Th only to be > ~ 350 k.y. (~ 5 half-lives). The U-series data also permit us to distinguish between shallower garnet-free (lithospheric) and deeper garnet-bearing (asthenospheric) sources (e.g., Asmerom and Edwards, 1995; Asmerom, 1999; Asmerom et al., 2000). Re-melting of shallow material, while still preserving a garnet REE signature, would generate <sup>238</sup>U-excesses due to the absence of garnet and the presence of aluminum-poor clinopyroxene with D<sub>U</sub>/D<sub>Th</sub> < 1 (e.g., Lundstrom, 2003 and references therein). It should be noted that D<sub>U</sub>/D<sub>Th</sub> for

aluminum-rich clinopyroxene becomes greater than 1 at  $\sim 1.5$  GPa, meaning that Th-excesses can be generated below this depth in the absence of garnet (Wood et al., 1999; Landwehr et al., 2001; Salters et al., 2002; McDade et al., 2003). However, the degree of U/Th fractionation is less in cpx than in garnet, so correspondingly smaller degrees of disequilibria are created, all else being equal.

The results of simple batch and fractional melting models of the same fluid-modified peridotite source used earlier are shown in Figure 2.8a. This plot clearly shows that such time-independent models cannot generate the observed  $^{230}\text{Th}$ -excesses. These results suggest that more complex ingrowth models, incorporating the time-dependency of U-series nuclides, and accounting for the duration of melting, are necessary. This requirement for time-dependent melting, whether dynamic (e.g., McKenzie, 1985; Williams and Gill, 1989) or equilibrium transport (Spiegelman and Elliott, 1993) models, would seem to cast doubt on static melting of a lithospheric source as a viable explanation.

Below we investigate the results of the Williams and Gill (1989) model, an expanded version of the dynamic melting model of McKenzie (1985). The primary variables in such a model are the maximum degree of melting ( $F$ ), the solid mantle upwelling velocity ( $V_o$ ) and porosity ( $\phi$ ). The degree of melting is constrained by trace element variations, especially the REEs (Fig. 2.6). Mantle upwelling velocity is harder to estimate, but constraints can be inferred from the velocity of the subducting slab if it is assumed that corner flow in the mantle wedge is responsible for mantle upwelling beneath the arc (e.g., Furukawa, 1993; Currie et al., 2004). Given a convergence rate of  $\sim 4 \text{ cm yr}^{-1}$  (Wilson, 2002) a range of upwelling velocities of 1 to  $5 \text{ cm yr}^{-1}$  seems reasonable. However,

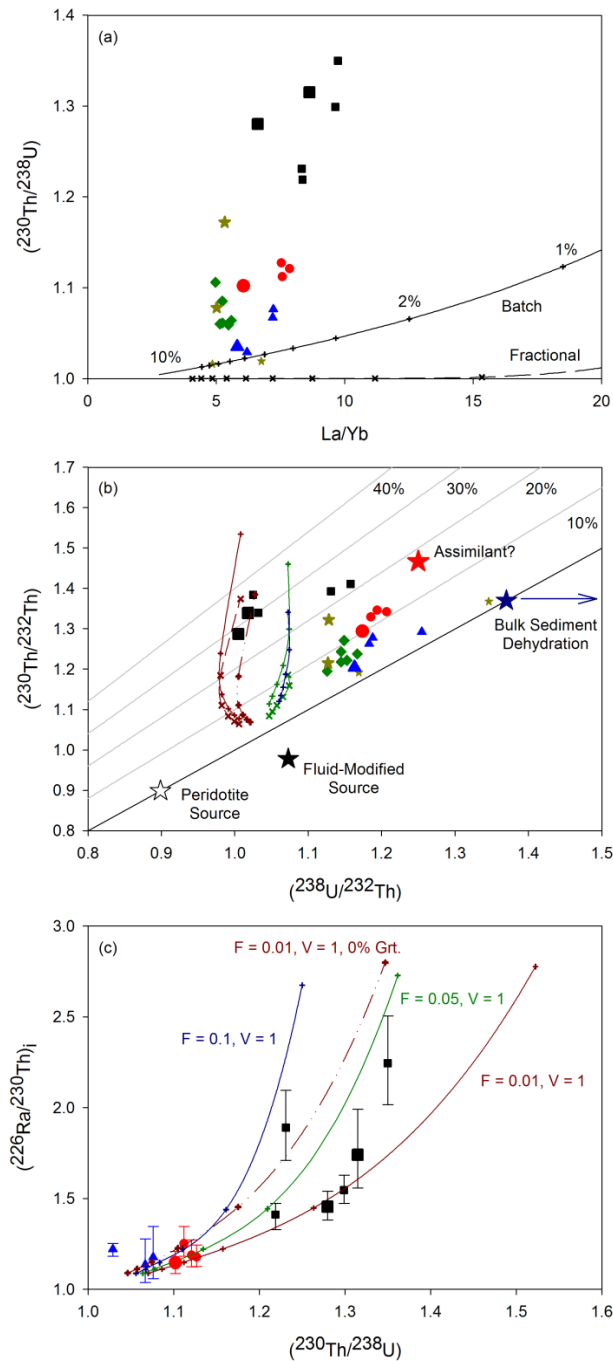


**Figure 2.8:** U-series isotope modeling plots for central Oregon lavas, symbols as Figure 2.1. Panel (a):  $\text{La}/\text{Yb}$  vs.  $(^{230}\text{Th}/^{238}\text{U})$  plot. Solid and dashed lines represent batch and fractional melting models of the peridotite source modified by addition of 1% of the sediment-derived fluid used previously (addition of the fluid component has very minimal impact on  $\text{La}/\text{Yb}$  ratio). Source contains 3% modal garnet. Tick marks are 1% melting increments.  $D_{\text{La}}$  and  $D_{\text{Yb}}$  as in Figure 2.6,  $D_{\text{U}}$  and  $D_{\text{Th}}$  given below. Panel (b):  $(^{230}\text{Th}/^{232}\text{Th})$  vs.  $(^{238}\text{U}/^{232}\text{Th})$  plot showing results of the dynamic melting model of Williams and Gill (1989). Black line is the equiline, grey lines are Th excess lines. The model assumes a 45 km long melting column, starting at 90 km depth. Densities of the solid and melt are  $3300$  and  $2900 \text{ kg m}^{-3}$  respectively. Upwelling velocities of  $1, 5,$  and  $10 \text{ cm yr}^{-1}$  correspond to melting rates of  $7.33 \times 10^{-6}, 3.67 \times 10^{-5},$  and  $7.33 \times 10^{-5}$  respectively.  $D_{\text{U}}$  and  $D_{\text{Th}}$  values are  $0.00303$  and  $0.00159$  respectively for a source containing 3% garnet. The pre-melting peridotite source has been modified by addition of 1% of a sediment-derived fluid as discussed in the text. Red, green and blue lines represent 1, 5, and 10% melting respectively ( $F = 0.01, 0.05, 0.1$ ). Solid lines with pluses, and dashed lines with crosses, represent upwelling velocities (V) of 1 and 5  $\text{cm yr}^{-1}$  respectively. Pluses/crosses indicate porosities of 0.1, 0.4, 0.8, 1.2, 1.6 and 2.0%. Smaller porosities result in greater degrees of disequilibrium. The dash-dot line is for a garnet-free source at  $F = 0.01, V = 1$  ( $D_{\text{U}} = 0.00258, D_{\text{Th}} = 0.00161$ ). Panel (c):  $(^{230}\text{Th}/^{238}\text{U})$  vs.  $(^{226}\text{Ra}/^{230}\text{Th})_i$  plot showing results of the same models shown in panel (b). All lines and symbols as in panel (b). All lines represent melting of a secular equilibrium source containing 3% garnet as discussed in the text unless labeled otherwise.  $D_{\text{Ra}} = 5.8 \times 10^{-6}$  for a 3% garnet source and  $6.1 \times 10^{-6}$  for a 0% garnet source.

Currie et al. (2004) suggested that such a model of ‘forced convection’ was unable to account for the high heat flow observed in Cascadia, and that a component of thermally driven free convection was required. This is easier to reconcile with the requirement that melting begins in the garnet stability field, but makes placing constraints on upwelling velocity more difficult. Constraining porosity is even more problematic, and we use a range of values from 0.1 to 2%, consistent with other studies (Lundstrom, 2003; Turner et al., 2003a).

The peridotite mantle source and bulk subducting sediment have calculated ( $^{238}\text{U}/^{232}\text{Th}$ ) ratios of 0.889 and 1.370 respectively, and are plotted in Figure 2.8b assuming they are in secular equilibrium before fluid addition or dehydration. Instantaneous addition of 1% of a sediment-derived fluid would result in a mantle source with ( $^{238}\text{U}/^{232}\text{Th}$ ) = 1.073, ( $^{230}\text{Th}/^{232}\text{Th}$ ) = 0.978, and ( $^{230}\text{Th}/^{238}\text{U}$ ) = 0.911 (Fig. 2.8b). The results of melting this source using the model of Williams and Gill (1989) are shown in Figure 2.8b. This model is able to replicate the ( $^{238}\text{U}/^{232}\text{Th}$ ) and ( $^{230}\text{Th}/^{232}\text{Th}$ ) ratios of the most primitive Sand Mountain samples with a reasonable range of parameters ( $F = 1\text{-}5\%$ ,  $V_o = 1\text{-}5 \text{ cm yr}^{-1}$ ,  $\phi \leq 0.5\%$ ). Furthermore, the degree of melting inferred from these results (1-5%) is in good agreement with the results of the trace element modeling (< 10%). Melting with a garnet-free source is capable of reproducing the U-Th data of the most primitive lavas only under a very narrow range of conditions ( $F \leq 1\%$ ,  $V_o \leq 1 \text{ cm yr}^{-1}$ ,  $\phi \leq 0.2\%$ ) (Fig. 2.8b).

Figure 2.8c shows the same model extended to include the ( $^{226}\text{Ra}/^{230}\text{Th}$ ) pair. Without information on the Ra concentration of the mantle source or slab components this model assumes the source is in ( $^{226}\text{Ra}/^{230}\text{Th}$ ) secular equilibrium, although this has minimal

effect on model output. Additional consideration of the ( $^{226}\text{Ra}/^{230}\text{Th}$ ) data generally confirms the U-Th modeling, although smaller extents of melting are required. If the  $^{226}\text{Ra}$ -excesses are mantle melting signatures then effectively instantaneous transport through the crust is required to preserve those excesses. However, it is important to note that  $^{226}\text{Ra}$ -excesses can also be generated within the crust and may not be related to mantle metasomatism or melting (e.g., Saal and Van Orman, 2004; Dufek and Cooper, 2005; Van Orman et al., 2006; Huang et al., 2011).

It is interesting to note that the most primitive samples from different groups do not cluster together on the equiline diagram, suggesting that differences exist in the combination of mantle source/slab fluid/melting process that gave rise to each group. This is supported by closer consideration of the ( $^{238}\text{U}/^{232}\text{Th}$ ) and ( $^{230}\text{Th}/^{232}\text{Th}$ ) data, which shows that trends from the most to least primitive samples within each group appear to converge at a common point, marked with a red star in Figure 2.8b. This point has a lower kappa (K)-value (atomic  $^{232}\text{Th}/^{238}\text{U}$ ) than the samples, closer to the MORB value of  $\sim 2.5$ , and a ( $^{230}\text{Th}/^{238}\text{U}$ ) value of  $\sim 1.15$  to  $1.20$  (15-20% Th-excess). A small degree partial melt of garnet-bearing mafic lower crust, similar to the component invoked by Jicha et al. (2009b) at Mt. Adams, is consistent with these requirements and the assimilant used to model the trace element variations between primitive and evolved lavas (Section 2.5.2). The vertical trend within the Newberry group as samples become more evolved is consistent with differentiation dominated by fractional crystallization and/or bulk assimilation.

The U-series modeling confirms the interpretation, based on the REE data, that the high ( $^{230}\text{Th}/^{238}\text{U}$ ) samples require dynamic melting of a garnet-bearing source. Static

melting, or a garnet-free (lithospheric) source, are unable to generate large  $^{230}\text{Th}$ -excesses (Asmerom, 1999; Asmerom et al., 2000). This interpretation implies that the garnet signatures observed in the REE and U-series data were obtained at the same time in an asthenospheric source, and cannot be reconciled with the suggestion (Leeman et al., 2005) that Group II lavas could represent re-melting of shallow lithospheric mantle containing a garnet signature inherited from earlier, deeper melting.

While the U-series data can effectively rule out re-melting of a lithospheric source, the necessarily small degree of fluid involvement implied by the long-lived isotope and trace element data, and the correspondingly small  $^{238}\text{U}$ -excess generated in the pre-melting mantle, do not permit us to distinguish between scenarios where limited fluid addition to the mantle wedge was the trigger for melting, as proposed at most arcs and by some workers in the Cascades (e.g., Reiners et al., 2000), and scenarios where melting occurs solely in response to mantle upwelling and decompression, and the fluid signature is inherited  $> 350$  k.y. prior to the onset of melting (e.g., Leeman et al., 2005). However, Beier et al. (2010) recently proposed a model for the Manus Basin in which addition and storage of a subduction component in the mantle wedge results in elevated oxygen fugacity, and a corresponding change in  $D_{\text{U}}$ , such that  $D_{\text{U}} \ll D_{\text{Th}}$ , and therefore dynamic melting leads not to  $^{230}\text{Th}$ -excesses but  $^{238}\text{U}$ -excesses. If this model is applicable to the Cascades then it could provide evidence in favor of recent fluid addition and flux melting.

Regardless of the timing of fluid addition, the U-series data rule out substantial modification of the central Oregon sub-arc mantle source by any slab-derived component. Despite the evidence for greater fluid involvement in the southern Cascades, no

significant along-arc differences are obvious in the growing body of U-series isotope data (Fig. 2.4a), suggesting that any along-arc variation in modern slab-input is similarly limited. This would seem to indicate that the majority of the fluid signature observed in southern Cascade lavas must be inherited from earlier subduction and/or added to the shallow mantle wedge > 350 k.y. prior to melting.

## **2.6. Conclusions**

Mafic magmas from the central Oregon Cascades display elemental and isotopic characteristics consistent with previously described Group II calc-alkaline basalts (CABs). One sample shares characteristics with Group I intraplate basalts. Trace element data suggests that the most primitive CABs can be derived by < 10% melting of a garnet-bearing enriched-mantle source that has been modified by addition of ~ 1% of a fluid derived from subducting sediments. The intraplate basalt can be derived by similar degrees of melting of a slightly more enriched source that has been modified by a similar amount and composition of fluid. Uranium-series data ( $^{238}\text{U}$ - $^{230}\text{Th}$ - $^{226}\text{Ra}$ ) are consistent with dynamic melting of such a fluid-modified source, although the data do not permit us to constrain the timing of fluid addition relative to melting. However, the amount of fluid involvement is minimal and melting is dominantly occurring in response to decompression. Limited along-arc variation in U-series isotopes suggests modern fluid involvement elsewhere in the arc is also limited. REE and U-series data require ~ 2 to 3% garnet in the source, implying that these lavas are asthenospheric melts, not melts of metasomatized subcontinental lithospheric mantle or 'frozen' basaltic 'pods' within the lithosphere. Trace element and U-series data indicate assimilation of a lower crustal melt of mafic (LKT-like) material in the generation of evolved basaltic andesite lavas.

## **Acknowledgements**

Victor Polyak provided valuable guidance and assistance in the laboratory and with the TIMS and ICP-MS analyses. Thoughtful reviews of an earlier draft of the manuscript by R. Conrey, B. Jicha, S. Turner, and editor R. Carlson resulted in significant improvements. Funding was provided by the National Science Foundation (EAR-0948703 to YA).

## References

- Anderson, A. (1973). The before-eruption water content of some high-alumina magmas. *Bulletin of Volcanology* **37**, 530-552.
- Anderson, A. (1979). Water in some hypersthenic magmas. *Journal of Geology* **87**, 509-531.
- Arculus, R. J. (1994). Aspects of magma genesis in arcs. *Lithos* **33**, 189-208.
- Asmerom, Y. (1999). Th-U fractionation and mantle structure. *Earth and Planetary Science Letters* **166**, 163-175.
- Asmerom, Y. & Edwards, R. L. (1995). U-series isotope evidence for the origin of continental basalts. *Earth and Planetary Science Letters* **134**, 1-7.
- Asmerom, Y., Cheng, H., Thomas, R., Hirschmann, M. & Edwards, R. L. (2000). Melting of the Earth's lithospheric mantle inferred from protactinium-thorium-uranium isotopic data. *Nature* **406**, 293-296.
- Bacon, C. R. (1990). Calc-alkaline, shosonitic, and primitive tholeiitic lavas from monogenetic volcanoes near Crater Lake, Oregon. *Journal of Petrology* **31**, 135-166.
- Bacon, C. R., Bruggman, P. E., Christiansen, R. L., Clynne, M. A., Donnelly-Nolan, J. M. & Hildreth, W. (1997). Primitive magmas at five Cascade volcanic fields; melts from hot, heterogeneous sub-arc mantle. *The Canadian Mineralogist* **35**, 397-423.
- Baker, M. B., Grove, T. L. & Price, R. (1994). Primitive basalts and andesites from the Mt. Shasta region, N. California: products of varying melt fraction and water content. *Contributions to Mineralogy and Petrology* **118**, 111-129.
- Bartels, K., Kinzler, R. & Grove, T. (1991). High pressure phase relations of primitive high-alumina basalts from Medicine Lake volcano, northern California. *Contributions to Mineralogy and Petrology* **108**, 253-270.
- Beier, C., Turner, S. P., Sinton, J. M. & Gill, J. B. (2010). Influence of subducted components on back-arc melting dynamics in the Manus Basin. *Geochemistry Geophysics Geosystems* **11**, doi:10.1029/2010GC003037.

- Blundy, J. & Wood, B. (2003). Mineral-melt partitioning of uranium, thorium and their daughters. *Reviews in Mineralogy and Geochemistry* **52**, 59-123.
- Borg, L. E., Clynne, M. A. & Bullen, T. D. (1997). The variable role of slab-derived fluids in the generation of a suite of primitive calc-alkaline lavas from the southernmost Cascades, California. *The Canadian Mineralogist* **35**, 425-452.
- Borg, L. E., Brandon, A. D., Clynne, M. A. & Walker, R. J. (2000). Re-Os isotopic systematics of primitive lavas from the Lassen region of the Cascade arc, California. *Earth and Planetary Science Letters* **177**, 301-317.
- Bostock, M. G., Hyndman, R. D., Rondenay, S. & Peacock, S. M. (2002). An inverted continental Moho and serpentinization of the forearc mantle. *Nature* **417**, 536-538.
- Brocher, T. M., Parsons, T., Trehu, A. M., Snelson, C. M. & Fisher, M. A. (2003). Seismic evidence for widespread serpentinized forearc upper mantle along the Cascadia margin. *Geology* **31**, 267-270.
- Catchings, R. D. & Mooney, W. D. (1988). Crustal structure of East Central Oregon: Relation between Newberry Volcano and regional crustal structure. *Journal of Geophysical Research* **93**, 10,081-10,094.
- Chabaux, F., Othman, D. B. & Birck, J. L. (1994). A new Ra-Ba chromatographic separation and its application to Ra mass-spectrometric measurement in volcanic rocks. *Chemical Geology* **114**, 191-197.
- Cheng, H., Edwards, R. L., Hoff, J., Gallup, C. D., Richards, D. A. & Asmerom, Y. (2000). The half lives of uranium-234 and thorium-230. *Chemical Geology* **169**, 17-33.
- Claeson, D. T. & Meurer, W. P. (2004). Fractional crystallization of hydrous basaltic "arc-type" magmas and the formation of amphibole-bearing gabbroic cumulates. *Contributions to Mineralogy and Petrology* **147**, 288-304.
- Conrey, R. M., Sherrod, D. R., Hooper, P. R. & Swanson, D. A. (1997). Diverse primitive magmas in the Cascade Arc, northern Oregon and southern Washington. *The Canadian Mineralogist* **35**, 367-396.

- Conrey, R. M., Hooper, P. R., Larson, P. B., Chesley, J. & Ruiz, J. (2001). Trace element and isotopic evidence for two types of crustal melting beneath a High Cascade volcanic center, Mt. Jefferson, Oregon. *Contributions to Mineralogy and Petrology* **141**, 710-732.
- Conrey, R. M., Taylor, E. M., Donnelly-Nolan, J. J. & Sherrod, D. (2002). North-Central Oregon Cascades: exploring petrologic and tectonic intimacy in a propagating intra-arc rift. In: Moore, G. (Ed.) Field Guide to Geologic Processes in Cascadia, *Oregon Department of Geology and Mineral Industries Special Paper* **36**, 47-90.
- Currie, C. A., Wang, K., Hyndman, R. D. & He, J. (2004). The thermal effects of steady-state slab-driven mantle flow above a subducting plate: the Cascadia subduction zone and backarc. *Earth and Planetary Science Letters* **223**, 35-48.
- DePaolo, D. J. (1981). Trace element and isotopic effects of combined wallrock assimilation and fractional crystallization. *Earth and Planetary Science Letters* **53**, 189-202.
- Donnelly-Nolan, J. M., Grove, T. L., Lanphere, M. A., Champion, D. E. & Ramsey, D. W. (2008). Eruptive history and tectonic setting of Medicine Lake Volcano, a large rear-arc volcano in the southern Cascades. *Journal of Volcanology and Geothermal Research* **177**, 313-328.
- Dufek, J. & Cooper, K. M. (2005).  $^{226}\text{Ra}/^{230}\text{Th}$  excess generated in the lower crust: Implications for magma transport and storage time scales. *Geology* **33**, 833-836.
- Eagar, K. C., Fouch, M. J., James, D. E. & Carlson, R. W. (2011). Crustal structure beneath the High Lava Plains of eastern Oregon and surrounding regions from receiver function analysis. *Journal of Geophysical Research* **116**, B02313, doi:10.1029/2010JB007795.
- Edwards, R. L., Beck, J. W., Burr, G. S., Donahue, D. J., Chapell, J. M. A., Bloom, A. L., Druffel, E. R. M. & Taylor, F. W. (1993). A large drop in atmospheric  $^{14}\text{C}/^{12}\text{C}$  and reduced melting in the Younger Dryas documented with  $^{230}\text{Th}$  ages of corals. *Science* **260**, 962-968.

- Elkins-Tanton, L. T., Grove, T. L. & Donnelly-Nolan, J. (2001). Hot, shallow mantle melting under the Cascades volcanic arc. *Geology* **29**, 631-634.
- Furukawa, Y. (1993). Magmatic processes under arcs and the formation of the volcanic front. *Journal of Geophysical Research* **98**, 8309-8319.
- Gaetani, G. A. & Grove, T. L. (2003). Experimental constraints on melt generation in the mantle wedge. In: Eiler, J. (Ed.), Inside the Subduction Factory. *American Geophysical Union Geophysical Monograph* **138**, 107-134.
- Green, N. L. & Harry, D. L. (1999). On the relationship between subducted slab age and arc basalt petrogenesis, Cascadia subduction system, North America. *Earth and Planetary Science Letters* **171**, 367-381.
- Green, N. L. & Sinha, A. K. (2005). Consequences of varied slab age and thermal structure on enrichment processes in the sub-arc mantle of the northern Cascadia subduction system. *Journal of Volcanology and Geothermal Research* **140**, 107-132.
- Grove, T. L., Parman, S. W., Bowring, S. A., Price, R. C. & Baker, M. B. (2002). The role of an H<sub>2</sub>O-rich fluid in the generation of primitive basaltic andesites and andesites from the Mount Shasta region, N. California. *Contributions to Mineralogy and Petrology* **142**, 375-396.
- Guffanti, M. & Weaver, C. S. (1988). Distribution of Late Cenozoic volcanic vents in the Cascade Range: volcanic arc segmentation and regional tectonic considerations. *Journal of Geophysical Research* **93**, 6513-6529.
- Harry, D. L. & Green, N. L. (1999). Slab dehydration and basalt petrogenesis in subduction systems involving very young oceanic lithosphere. *Chemical Geology* **160**, 309-333.
- Harry, D. L. & Leeman, W. P. (1995). Partial melting of melt metasomatized subcontinental mantle and the magma source potential of the lower lithosphere. *Journal of Geophysical Research* **100**, 10,255-10,269.
- Hildreth, W. (2007). Quaternary Magmatism in the Cascades - Geologic Perspectives. *U.S. Geological Survey Professional Paper* **1744**.

- Huang, F., Lundstrom, C. C., Sigurdsson, H. & Zhang, Z. (2011). U-series disequilibria in Kick'em Jenny submarine volcano lavas: A new view of time-scales of magmatism in convergent margins. *Geochimica et Cosmochimica Acta* **75**, 195-212.
- Hughes, S. S. (1990). Mafic magmatism and associated tectonism of the Central High Cascade range, Oregon. *Journal of Geophysical Research* **95**, 19,623-19,638.
- Hughes, S. S. & Taylor, E. M. (1986). Geochemistry, petrogenesis, and tectonic implications of central High Cascade mafic platform lavas. *Geological Society of America Bulletin* **97**, 1024-1036.
- Hurwitz, S., Mariner, R. H., Fehn, U. & Snyder, G. T. (2005). Systematics of halogen elements and their radioisotopes in thermal springs of the Cascade Range, Central Oregon, Western USA. *Earth and Planetary Science Letters* **235**, 700–714.
- Jicha, B., Hart, G., Johnson, C., Hildreth, W., Beard, B., Shirey, S. & Valley, J. (2009a). Isotopic and trace element constraints on the petrogenesis of lavas from the Mount Adams volcanic field, Washington. *Contributions to Mineralogy and Petrology* **157**, 189-207.
- Jicha, B. R., Johnson, C. M., Hildreth, W., Beard, B. L., Hart, G. L., Shirey, S. B. & Singer, B. S. (2009b). Discriminating assimilants and decoupling deep- vs. shallow-level crystal records at Mount Adams using  $^{238}\text{U}$ - $^{230}\text{Th}$  disequilibria and Os isotopes. *Earth and Planetary Science Letters* **277**, 38-49.
- Johnson, M. C. & Plank, T. (1999). Dehydration and melting experiments constrain the fate of subducted sediments. *Geochemistry Geophysics Geosystems* **1**, doi:10.1029/1999GC000014.
- Kelemen, P. B., Yogodzinski, G. M. & Scholl, D. W. (2003). Along-strike variation in the Aleutian island arc: Genesis of high Mg# andesite and implications for continental crust. In: Eiler, J. (Ed.), Inside the Subduction Factory. *American Geophysical Union Geophysical Monograph* **138**, 223-276.
- Kessel, R., Schmidt, M. W., Ulmer, P. & Pettke, T. (2005). Trace element signature of subduction-zone fluids, melts and supercritical liquids at 120-180 km depth. *Nature* **437**, 724-727.

- Klein, E. M. (2003). Geochemistry of the igneous oceanic crust. *In*: Rudnick, R. L. (Ed.), *The Crust. Treatise on Geochemistry* **3**, Elsevier-Pergamon, 433-463.
- Landwehr, D., Blundy, J., Chamorro-Perez, E. M., Hill, E. & Wood, B. (2001). U-series disequilibria generated by partial melting of spinel lherzolite. *Earth and Planetary Science Letters* **188**, 329-348.
- Leaver, D. S., Mooney, W. D. & Kohler, W. M. (1984). A seismic refraction study of the Oregon Cascades. *Journal of Geophysical Research* **89**, 3121-3134.
- Le Bas, M. J., LeMaitre, R. W., Streckeisen, A. L. & Zanettin, B. (1986). A chemical classification of volcanic rocks based on the total alkali-silica diagram. *Journal of Petrology* **27**, 745-750.
- Leeman, W. P., Smith, D. R., Hildreth, W., Palacz, Z. & Rogers, N. (1990). Compositional diversity of Late Cenozoic basalts in a transect across the southern Washington Cascades: Implications for subduction zone magmatism. *Journal of Geophysical Research* **95**, 19,561-19,582.
- Leeman, W. P., Tonarini, S., Chan, L. H. & Borg, L. E. (2004). Boron and lithium isotopic variations in a hot subduction zone-the southern Washington Cascades. *Chemical Geology* **212**, 101-124.
- Leeman, W. P., Lewis, J. F., Evarts, R. C., Conrey, R. M. & Streck, M. J. (2005). Petrologic constraints on the thermal structure of the Cascades arc. *Journal of Volcanology and Geothermal Research* **140**, 67-105.
- Le Voyer, M., Rose-Koga, E. F., Shimizu, N., Grove, T. L. & Schiano, P. (2010). Two contrasting H<sub>2</sub>O-rich components in primary melt inclusions from Mount Shasta. *Journal of Petrology* **51**, 1571-1595.
- Luedke, R. G. & Smith, R. L. (1982). Map showing distribution, composition, and age of Late Cenozoic volcanic centers in Oregon and Washington. *U.S. Geological Survey Miscellaneous Investigations Series I-1091 D*, scale 1:500,000.
- Lundstrom, C. C. (2003). Uranium-series disequilibria in mid-ocean ridge basalts: Observations and models of basalt genesis. *Reviews in Mineralogy and Geochemistry* **52**, 175-214.

- MacLeod, N. S., Sherrod, D. R., Chitwood, L. A. & Jensen, R. A. (1995). Geologic map of Newberry volcano, Deschutes, Klamath, and Lake Counties, Oregon. *U.S. Geological Survey Miscellaneous Investigations Series I-2455*, scale 1:62,500.
- Magna, T., Wiechert, U., Grove, T. L. & Halliday, A. N. (2006). Lithium isotope fractionation in the southern Cascadia subduction zone. *Earth and Planetary Science Letters* **250**, 428-443.
- McCrory, P. A., Blair, J. L., Oppenheimer, D. H. & Walter, S. R. (2006). Depth to the Juan de Fuca slab beneath the Cascadia subduction margin-A 3-D model for sorting earthquakes. *U.S. Geological Survey Data Series 91*, Version 1.2.
- McDade, P., Blundy, J. D. & Wood, B. (2003). Trace element partitioning on the Tinaquillo Lherzolite solidus at 1.5 GPa. *Physics of the Earth and Planetary Interiors* **139**, 129-147.
- McKenzie, D. (1985).  $^{230}\text{Th}$ - $^{238}\text{U}$  disequilibrium and the melting processes beneath ridge axes. *Earth and Planetary Science Letters* **72**, 149-157.
- McKenzie, D. & O'Nions, R. K. (1991). Partial melt distributions from inversion of rare earth element concentrations. *Journal of Petrology* **32**, 1021-1091.
- Obrebski, M., Allen, R. M., Xue, M. & Hung, S.-H. (2010). Slab-plume interaction beneath the Pacific Northwest. *Geophysical Research Letters* **37**, L14305, doi: 10.1029/2010gl043489.
- Palme, H. & Jones, A. (2003). Solar system abundances of the elements. In: Davis, A. M. (Ed.), Meteorites, Comets, and Planets. *Treatise on Geochemistry* **1**, Elsevier-Pergamon, 41-61.
- Palme, H. & O'Neill, H. S. C. (2003). Cosmochemical estimates of mantle composition. In: Carlson, R. W. (Ed.), The Mantle and Core. *Treatise on Geochemistry* **2**, Elsevier-Pergamon, 1-38.
- Peacock, S. M. (2003). Thermal structure and metamorphic evolution of subducting slabs. In: Eiler, J. (Ed.), Inside the Subduction Factory. *American Geophysical Union Geophysical Monograph* **138**, 7-22.

- Plank, T. & Langmuir, C. H. (1998). The chemical composition of subducting sediment and its consequences for the crust and mantle. *Chemical Geology* **145**, 325-394.
- Reagan, M. K., Sims, K. W. W., Erich, J., Thomas, R. B., Cheng, H., Edwards, R. L., Layne, G. & Ball, L. (2003). Time-scales of differentiation from mafic parents to rhyolite in North American continental arcs. *Journal of Petrology* **44**, 1703-1726.
- Reiners, P. W., Hammond, P. E., McKenna, J. M. & Duncan, R. A. (2000). Young basalts of the central Washington Cascades, flux melting of the mantle, and trace element signatures of primary arc magmas. *Contributions to Mineralogy and Petrology* **138**, 249-264.
- Righter, K. (2000). A comparison of basaltic volcanism in the Cascades and western Mexico: Compositional diversity in continental arcs. *Tectonophysics* **318**, 99-117.
- Righter, K., Chesley, J. T. & Ruiz, J. (2002). Genesis of primitive, arc-type basalt: Constraints from Re, Os, and Cl on the depth of melting and role of fluids. *Geology* **30**, 619-622.
- Rondenay, S., Abers, G. A. & van Keken, P. E. (2008). Seismic imaging of subduction zone metamorphism. *Geology* **36**, 275-278.
- Roth, J. B., Fouch, M. J., James, D. E. & Carlson, R. W. (2008). Three-dimensional seismic velocity structure of the northwestern United States. *Geophysical Research Letters* **35**, L15304, doi:10.1029/2008GL034669.
- Rowe, M. C., Kent, A. J. R. & Nielsen, R. L. (2009). Subduction influence on oxygen fugacity and trace and volatile elements in basalts across the Cascade volcanic arc. *Journal of Petrology* **50**, 61-91.
- Ruscitto, D. M., Wallace, P. J., Johnson, E. R., Kent, A. J. R. & Bindeman, I. N. (2010). Volatile contents of mafic magmas from cinder cones in the Central Oregon High Cascades: Implications for magma formation and mantle conditions in a hot arc. *Earth and Planetary Science Letters* **298**, 153-161.
- Saal, A. E. & Van Orman, J. A. (2004). The  $^{226}\text{Ra}$  enrichment in oceanic basalts: Evidence for melt-cumulate diffusive interaction processes within the oceanic lithosphere. *Geochemistry Geophysics Geosystems* **5**, doi:10.1029/2003GC000620.

- Salters, V. J. M., Longhi, J. E. & Bizimis, M. (2002). Near mantle solidus trace element partitioning at pressures up to 3.4 GPa. *Geochemistry Geophysics Geosystems* **3**, doi:10.1029/2001GC000148.
- Schmidt, M. E., Grunder, A. L. & Rowe, M. C. (2008). Segmentation of the Cascade Arc as indicated by Sr and Nd isotopic variation among diverse primitive basalts. *Earth and Planetary Science Letters* **266**, 166-181.
- Schmidt, M. E. & Grunder, A. L. (2011). Deep mafic roots to arc volcanoes: Mafic recharge and differentiation of basaltic andesite at North Sister volcano, Oregon Cascades. *Journal of Petrology* **52**, 603-641.
- Sherrod, D. R. & Smith, J. G. (1990). Quaternary extrusion rates of the Cascade Range, northwestern United States and southern British Columbia. *Journal of Geophysical Research* **95**, 19,465-19,474.
- Sherrod, D. R., Taylor, E. M., Ferns, M. L., Scott, W. E., Conrey, R. M. & Smith, G. A. (2004). Geologic map of the Bend 30- x 60-minute quadrangle, central Oregon. *U.S. Geological Survey Geologic Investigations Series I-2683*, scale 1:100,000.
- Sisson, T. W. & Grove, T. L. (1993). Temperatures and H<sub>2</sub>O contents of low-MgO high-alumina basalts. *Contributions to Mineralogy and Petrology* **113**, 167-184.
- Spiegelman, M. & Elliott, T. (1993). Consequences of melt transport for uranium-series disequilibrium in young lavas. *Earth and Planetary Science Letters* **118**, 1-20.
- Stanley, W. D., Mooney, W. D. & Fuis, G. S. (1990). Deep crustal structure of the Cascade Range and surrounding regions from seismic refraction and magnetotelluric data. *Journal of Geophysical Research* **95**, 19,419-19,438.
- Su, Y. & Langmuir, C. H. (2003). Global MORB chemistry compilation at the segment scale. *M.S. Thesis*, Columbia University.
- Turner, S., Bourdon, B., Hawkesworth, C. & Evans, P. (2000). <sup>226</sup>Ra-<sup>230</sup>Th evidence for multiple dehydration events, rapid melt ascent and the time scales of differentiation beneath the Tonga-Kermadec island arc. *Earth and Planetary Science Letters* **179**, 581-593.

- Turner, S., Bourdon, B. & Gill, J. (2003a). Insights into magma genesis at convergent margins from U-series isotopes. *Reviews in Mineralogy and Geochemistry* **52**, 255-315.
- Turner, S., Foden, J., George, R., Evans, P., Varne, R., Elburg, M. & Jenner, G. (2003b). Rates and processes of potassic magma evolution beneath Sangeang Api volcano, east Sunda arc, Indonesia. *Journal of Petrology* **44**, 491-515.
- Van Orman, J. A., Saal, A. E., Bourdon, B. & Hauri, E. H. (2006). Diffusive fractionation of U-series radionuclides during mantle melting and shallow-level melt-cumulate interaction. *Geochimica et Cosmochimica Acta* **70**, 4797-4812.
- Volpe, A. M. (1992).  $^{238}\text{U}$ - $^{230}\text{Th}$ - $^{226}\text{Ra}$  disequilibrium in young Mt. Shasta andesites and dacites. *Journal of Volcanology and Geothermal Research* **53**, 227-238.
- Volpe, A. M. & Hammond, P. E. (1991).  $^{238}\text{U}$ - $^{230}\text{Th}$ - $^{226}\text{Ra}$  disequilibria in young Mount St. Helens rocks: time constraint for magma formation and crystallization. *Earth and Planetary Science Letters* **107**, 475-486.
- Wada, I. & Wang, K. (2009). Common depth of slab-mantle decoupling: Reconciling diversity and uniformity of subduction zones. *Geochemistry Geophysics Geosystems* **10**, doi:10.1029/2009GC002570.
- White, W. M., Hofmann, A. W. & Puchelt, H. (1987). Isotope geochemistry of Pacific mid-ocean ridge basalt. *Journal of Geophysical Research* **92**, 4881-4893.
- Williams, R. W. & Gill, J. B. (1989). Effects of partial melting on the uranium decay series. *Geochimica et Cosmochimica Acta* **53**, 1607-1619.
- Wilson, D. S. (2002). The Juan de Fuca plate and slab - isochron structure and Cenozoic plate motions. *U.S. Geological Survey Open-File Report* **02-328**, 9-12.
- Wood, B. J., Blundy, J. D. & Robinson, A. C. (1999). The role of clinopyroxene in generating U-series disequilibrium during mantle melting. *Geochimica et Cosmochimica Acta* **63**, 1613-1620.
- Workman, R. K. & Hart, S. R. (2005). Major and trace element composition of the depleted MORB mantle (DMM). *Earth and Planetary Science Letters* **231**, 53-72.

Xue, M. & Allen, R. M. (2007). The fate of the Juan de Fuca plate: Implications for a Yellowstone plume head. *Earth and Planetary Science Letters* **264**, 266-276.

Yogodzinski, G. M. & Kelemen, P. B. (1998). Slab melting in the Aleutians: Implications of an ion probe study of clinopyroxene in primitive adakite and basalt. *Earth and Planetary Science Letters* **158**, 53-65.

### **Chapter 3: Extreme $^{231}\text{Pa}$ -enrichment in young Cascade arc lavas - signature of sediment melting in a warm arc?**

#### **Abstract**

The Cascade volcanic arc formed above an unusually warm subduction zone environment, and the impacts of this on the delivery of slab-derived components to the mantle wedge, and the style of mantle melting within that wedge, have long been debated. Here we report the first ( $^{231}\text{Pa}/^{235}\text{U}$ ) data for young, mafic lavas from the Cascade arc. These ratios are two to four times higher than any data previously reported from any tectonic setting. It is suggested that the unusually high temperatures in the young subducting plate control the assemblage of accessory minerals present during melting of subducted sediments, generating highly  $^{231}\text{Pa}$ -enriched melts. The ( $^{231}\text{Pa}/^{235}\text{U}$ ) ratios of erupted lavas preserve the signature of this slab component, rather than melting processes in the mantle as has long been assumed. An alternative interpretation of the data provides evidence for a new physico-chemical framework for subduction zone magmatism with implications for many convergent margin processes.

### 3.1. Introduction

Magmas erupted in volcanic arcs are interpreted as the products of melting of the asthenospheric mantle in response to the addition of fluids from the subducting oceanic lithosphere (e.g., McBirney, 1969; Tatsumi et al., 1983; 1986; Hawkesworth et al., 1993; Arculus, 1994). The Cascade volcanic arc, formed by the slow ( $\sim 3.5 \text{ cm a}^{-1}$ ) subduction of the young ( $< 10 \text{ Ma}$  at the trench) Juan de Fuca plate (Wilson, 2002), is the global end member, hot-slab subduction zone (Wada and Wang, 2009). Subduction zone thermal models predict slab surface temperatures beneath the volcanic arc of  $\sim 850$  to  $950^\circ\text{C}$  (Syracuse et al., 2010). Such a warm sub-arc environment is expected to lead to shallow dehydration of the slab (Rondenay et al., 2008), and has been invoked as one potential cause of the unusually broad range of geochemically distinct mafic lavas erupted within the Cascade arc (Leeman et al., 2005). However, the exact nature, amount, and timing of fluid addition to the sub-arc mantle, and therefore the style of mantle melting, remain controversial (e.g., Bacon et al., 1997; Conrey et al., 1997; Reiners et al., 2000; Leeman et al., 2005).

Uranium-series (U-series) isotopes have become an increasingly common tool for investigating both the timing of fluid addition to, and melting processes within, the sub-arc mantle (e.g., Turner et al., 2003). Geochemical and isotopic data (including  $^{238}\text{U}$ - $^{230}\text{Th}$ - $^{226}\text{Ra}$  data) for young, mafic lavas from the central Oregon segment of the Cascade arc are consistent with limited involvement of fluids derived from the subducting slab, and melting occurring primarily in response to asthenospheric mantle upwelling and decompression (Mitchell and Asmerom, 2011). However, this dataset cannot resolve conclusively whether addition of this fluid is ‘modern’ (within the last  $\sim 350 \text{ k.y.}$ ) or not.

Among the commonly applied U-series decay systems, the  $^{235}\text{U}$ - $^{231}\text{Pa}$  pair appears uniquely sensitive to the effects of partial melting, due to the strong incompatibility of Pa in mantle phases (Bourdon et al., 1999; 2003; Thomas et al., 2002; Turner et al., 2006). Here we present ( $^{231}\text{Pa}/^{235}\text{U}$ ) data for these same samples from central Oregon, the first such data for the Cascades, in an effort to constrain further the magnitude and timing of fluid involvement, and therefore the style of mantle melting, in this warm arc. Measured  $^{231}\text{Pa}$ -excesses are ~ three to four times larger than any previously reported arc data, and it is proposed that the hot nature of the Juan de Fuca plate controls the accessory mineral assemblage in subducted sediments, generating the extreme  $^{231}\text{Pa}$ -enrichment observed.

### **3.2. Samples and Results**

The 19 samples reported here are a representative sub-set of samples for which elemental and isotopic data were previously published (Mitchell and Asmerom, 2011; Appendix A3). The samples are dominantly basalts and basaltic andesites, ranging from 49.6 to 57.7 wt.%  $\text{SiO}_2$  (Mg# 63-47). Samples from restricted geographic areas generally define trends from least to most evolved lava consistent with interaction with arc crust (Mitchell and Asmerom, 2011; Chapter 4). The focus here is on the most primitive samples (49.6-52.1 wt.%  $\text{SiO}_2$ ; Mg# 63-53; Appendix A3), which are least-modified from representative mantle melts. In contrast to most arc lavas, but typical for the Cascades, all samples have  $^{230}\text{Th}$ -excesses, up to a maximum of 35% (Table 3.1 and Fig. 3.1) (Mitchell and Asmerom, 2011). All samples also have  $^{231}\text{Pa}$ -excesses, with age-corrected ( $^{231}\text{Pa}/^{235}\text{U}$ )<sub>i</sub> ratios ranging from 1.178 to 9.143 (Table 3.1 and Fig. 3.1; Appendix A3; Fig. A3.1). The five most primitive samples have ( $^{231}\text{Pa}/^{235}\text{U}$ )<sub>i</sub> ranging from 5.016 to 8.058. These values are significantly higher than any previously reported global data, which extend to

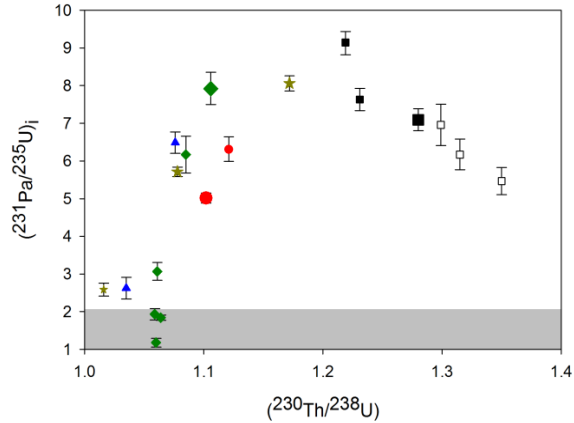


**Figure 3.1:**  $(^{230}\text{Th}/^{238}\text{U})$  vs.  $(^{231}\text{Pa}/^{235}\text{U})_i$  data for young, mafic lavas from the central Oregon Cascades. Symbols represent sample groups identified in Mitchell and Asmerom (2011). Larger symbols depict the five samples identified as being the most primitive. Grey shading is the approximate range in  $(^{231}\text{Pa}/^{235}\text{U})$  previously reported for arc lavas.

maximum  $(^{231}\text{Pa}/^{235}\text{U})_i$  values of  $\sim 2$  in arc lavas and ocean island basalts (Lundstrom, 2003; Turner et al., 2003; Avanzinelli et al., 2012), and  $\sim 2.5$  to 3.5 in continental and mid-ocean ridge basalts (e.g., Asmerom et al., 2000; Lundstrom, 2003). It is worth highlighting that the samples with the largest  $^{230}\text{Th}$ -excesses do not have the largest  $^{231}\text{Pa}$ -excesses, suggesting at least partial decoupling of the processes responsible for generating  $(^{230}\text{Th}/^{238}\text{U})$  and  $(^{231}\text{Pa}/^{235}\text{U})$  disequilibria.

### 3.3. Discussion and Conclusions

We employ a time-dependent dynamic melting simulation (after McKenzie, 1985; Williams and Gill, 1989) to model the measured data (Appendix A3). Using as a starting point the parameters of Mitchell and Asmerom (2011), and a pre-melting mantle source in  $(^{231}\text{Pa}/^{235}\text{U})$  secular equilibrium or with  $^{235}\text{U}$ -enrichment, it is possible to reproduce the  $(^{231}\text{Pa}/^{235}\text{U})$  data only if the mantle porosity is reduced to  $\sim 0.06$  to 0.02% (Fig. A3.2a),

**Table 3.1**

U-Th-Pa isotope and trace element data for central Oregon lavas.

Sample ID	Age ( <sup>14</sup> C yr B.P.)	U (ppm)	Th ( <sup>230</sup> Th/ <sup>232</sup> Th)	<sup>230</sup> Th/ <sup>238</sup> U	<sup>231</sup> Pa (pg/g)	( <sup>231</sup> Pa/ <sup>235</sup> U)	( <sup>231</sup> Pa/ <sup>235</sup> U) <sub>i</sub>	Zr	Nb	Ba	La	Dy	Yb
08-LL-01	1950 ± 150	0.432	1.305	1.287 ± 5	0.974 ± 37	6.85 ± 26	7.09 <sup>+30</sup>	136.6	10.62	288.9	14.03	3.90	2.12
07-LN-01	<2590 ± 150	0.439	1.151	1.411 ± 5	1.254 ± 37	8.67 ± 26	9.14 <sup>+29</sup>	177.2	12.60	326.0	17.69	4.08	2.12
08-NCSW-01	2850 ± 50	0.462	1.241	1.393 ± 6	1.098 ± 42	7.24 ± 28	7.63 <sup>+30</sup>	173.6	12.20	326.9	18.00	4.19	2.16
08-SM-01	2850 ± 50	0.471	1.403	1.339 ± 5	0.911 ± 58	5.87 ± 38	6.17 <sup>+41</sup>	164.8	12.51	381.4	19.04	4.05	2.21
08-SMCL-01	2850 ± 50	0.479	1.409	1.340 ± 6	1.039 ± 80	6.61 ± 51	6.96 <sup>+55</sup>	168.3	11.11	332.5	20.41	3.97	2.12
08-SMCL-01					<i>1.002 ± 103</i>	<i>6.37 ± 65</i>	<i>6.71<sup>+70</sup></i>						
07-NC-01	2850 ± 50	0.460	1.360	1.384 ± 6	1.350 ± 5	0.787 ± 51	5.21 ± 34	162.5	10.47	314.6	18.46	3.66	1.90
07-NC-01						<i>0.946 ± 105</i>	<i>6.26 ± 70</i>						
08-WBB-01	1400 ± 100	0.445	1.150	1.294 ± 5	0.716 ± 18	4.90 ± 12	5.02 <sup>+13</sup>	135.8	12.48	246.0	13.83	4.24	2.28
07-LB-01	2883 ± 175	0.483	1.236	1.329 ± 5	1.121 ± 4	0.946 ± 44	6.31 <sup>+33</sup>	171.0	12.52	323.0	17.77	4.33	2.26
07-FCA-01	1980 ± 160	0.694	1.811	1.204 ± 6	1.035 ± 5	0.558 ± 59	2.62 <sup>+29</sup>	163.6	10.57	358.9	15.79	4.82	2.72
07-YC-02	>1980 ± 160	0.650	1.660	1.278 ± 5	1.076 ± 4	1.325 ± 45	6.21 ± 21	99.31	5.09	300.5	10.67	2.60	1.48
08-SPBF-01	<2883 ± 175												
08-SPBF-01	5870 ± 60	0.585	1.545	1.271 ± 5	1.106 ± 4	1.348 ± 68	7.92 <sup>+43</sup>	125.9	10.30	245.0	11.55	4.14	2.32
08-SPBF-01						<i>1.249 ± 108</i>	<i>6.73 ± 58</i>						
08-FRE-01	5960 ± 100	0.777	2.058	1.243 ± 5	1.085 ± 4	1.345 ± 101	5.48 ± 41	135.8	10.04	292.2	12.56	4.15	2.40
08-LCFF-01	6320 ± 110	0.833	2.165	1.238 ± 5	1.061 ± 4	0.730 ± 52	3.07 <sup>+24</sup>	137.8	10.06	292.1	12.71	4.17	2.42
08-LCFF-01						<i>0.710 ± 65</i>	<i>2.71 ± 25</i>						
08-SF-01	6030 ± 90	1.097	2.887	1.222 ± 5	1.059 ± 4	0.624 ± 45	1.81 ± 13	156.3	11.44	325.7	13.90	4.35	2.53
08-LBF-01	6160 ± 70	1.191	3.158	1.218 ± 5	1.064 ± 4	0.671 ± 22	1.73 ± 6	167.0	11.03	354.4	14.66	4.31	2.62
08-LBF-01						<i>0.604 ± 18</i>	<i>1.55 ± 5</i>						
08-MBF-02	n.d.	1.739	4.684	1.195 ± 5	1.060 ± 4	0.655 ± 55	1.15 ± 10	193.2	12.48	398.1	16.36	5.09	3.18
08-WIC-01	> MMA	0.425	1.142	1.322 ± 8	1.172 ± 7	0.976 ± 24	7.00 ± 17	137.9	14.25	196.1	12.43	4.23	2.33
08-CYC-01	> MMA	0.475	1.279	1.215 ± 6	1.078 ± 5	0.775 ± 17	5.00 ± 11	101.2	6.95	212.0	9.67	3.31	1.93
08-EC-01	> MMA	0.442	0.996	1.368 ± 6	1.016 ± 4	0.329 ± 20	2.35 ± 14	148.9	9.23	327.9	14.87	5.68	3.07
Ryan Std.		1.261	7.196	0.530 ± 2	0.996 ± 2	0.426 ± 21	1.04 ± 5	n.d.					
TML-2 Std.		10.730	29.42	1.037 ± 4	0.937 ± 2	3.539 ± 166	1.01 ± 5	n.d.					
TML-3 Std.		n.m.	n.m.	n.m.	n.m.	3.641 ± 186	1.04 ± 5	n.d.					

Refer to Mitchell and Asmerom (2011) for complete U-Th data and details on analytical procedures. Ratios in parentheses represent activity ratios (the number of atoms times the decay constant, λ). Values in italics are replicate Pa analyses. Decay constants used are as follows:  $\lambda_{230} = 9.1577 \times 10^{-6} \text{ yr}^{-1}$ ,  $\lambda_{231} = 2.1158 \times 10^{-5} \text{ yr}^{-1}$ ,  $\lambda_{232} = 4.9475 \times 10^{-11} \text{ yr}^{-1}$ ,  $\lambda_{233} = 9.386925 \text{ yr}^{-1}$ ,  $\lambda_{234} = 2.8263 \times 10^{-6} \text{ yr}^{-1}$ ,  $\lambda_{235} = 9.8574 \times 10^{-10} \text{ yr}^{-1}$ ,  $\lambda_{238} = 1.5513 \times 10^{-10} \text{ yr}^{-1}$ . All uncertainties are 2σ measurement errors. <sup>233</sup>Pa spike was produced by neutron irradiation of NIST 3159 <sup>232</sup>Th Standard. A secular equilibrium standard (TML or Ryan) was processed and measured with each batch of samples. (<sup>231</sup>Pa/<sup>235</sup>U) ratios are initial values corrected back to the time of eruption using calibrated ages in sidereal years based on <sup>14</sup>C ages (> MMA" = older than the Mt. Mazama ash horizon, approx. 7.65 ka). n.m. = not measured, n.d. = not determined. Trace element data in ppm from Mitchell and Asmerom (2011).

an order of magnitude lower than is typically assumed in such models (e.g., Lundstrom, 2003). The alternative is to assume a pre-melting mantle source that is strongly enriched in  $^{231}\text{Pa}$ , such that this source enrichment is preserved through the melting process to be recorded in the erupted lavas. This implies that the  $^{235}\text{U}$ - $^{231}\text{Pa}$  system, interpreted to be the U-series pair most sensitive to partial melting, is in fact reflecting the nature of the slab component, with melting processes playing a secondary role.

Slab-derived aqueous fluids are usually considered to be enriched in U over both Th and Pa, as a result of the expected low fluid mobility of Th and Pa (Brennan et al., 1995; Bourdon et al., 1999), as well as the mobility of  $\text{U}^{6+}$  under the oxidizing conditions expected in subduction zones (Ballhaus et al., 1990; Wood et al., 1990). Until recently, only aqueous fluids have been considered as agents for introducing U-series disequilibria into the mantle source of arc lavas (Avanzinelli et al., 2012; Appendix A3). However, sediment melts (and potentially slab melts also) must be considered when interpreting arc lava U-series disequilibria (Avanzinelli et al., 2012). This is especially important given the low solute concentrations in aqueous fluids (Spandler et al., 2003; Spandler et al., 2007; Klimm et al., 2008) and the much higher concentrations in both bulk sediments and hydrous melts (Klimm et al., 2008; Hermann and Rubatto, 2009; Skora and Blundy, 2010).

Furthermore, it has been recognized recently that accessory phases (e.g., allanite, apatite, monazite, rutile, and zircon) host virtually the entire budget of many important trace elements in subducted oceanic crust and sediments (Hermann, 2002; Klemme et al., 2005; Klimm et al., 2008; Hermann and Rubatto, 2009; Skora and Blundy, 2010; Appendix A3). While bulk sediment composition undoubtedly plays a role (especially in

the case of allanite and apatite), the presence or absence of such phases is largely a function of temperature and degree of melting, and thus H<sub>2</sub>O content (Hermann and Rubatto, 2009; Skora and Blundy, 2010). Rutile and apatite are present at 4.5 GPa and 1050°C (Hermann and Rubatto, 2009), while allanite, monazite, and zircon are stable to between 800 and 900°C, depending on the H<sub>2</sub>O content of the system and thus degree of melting (Hermann and Rubatto, 2009; Skora and Blundy, 2010). As a result, all these phases may potentially be present in the residue of sediments undergoing melting at the conditions found at the slab surface beneath most arcs (Syracuse et al., 2010; Cooper et al., 2012), and will therefore control the budget of all but the most fluid-mobile elements. Indeed, the trace element signatures of sediment melts in equilibrium with these phases display many of the characteristics of the arc lava ‘slab component’ (Hermann and Rubatto, 2009; Skora and Blundy, 2010). However, the temperatures at which allanite, monazite, and zircon are eliminated from melting sediments (800-900°C) are similar to estimates of the slab surface temperature beneath the Cascade arc (850-950°C; Syracuse et al., 2010). It should be noted here that the recently developed H<sub>2</sub>O/Ce thermometer predicts slab-surface temperatures beneath Cascadia of 809°C (Plank et al., 2009; Cooper et al., 2012). However, this method is critically dependent upon the assumption that slab fluids are saturated with allanite and/or monazite.

Consequentially, the elevated temperatures found within the Cascadia margin could potentially leave rutile ( $\pm$  apatite) as the only accessory phase(s) present during partial melting of sediments. Partition coefficients have been measured recently for U and Th in rutile for the first time, with  $D_U$  ranging from  $\sim 0.2$  to 4 and  $D_U \gg D_{Th}$  (Klemme et al., 2005). The geochemistry of Pa precludes direct measurement of its partition coefficient,

but  $D_{\text{Pa}}$  is estimated to be  $\ll 0.0001$ , based on extrapolation of data for other pentavalent elements (Nb, Ta, V) (Klemme et al., 2005). Melts generated in the presence of residual rutile, but without allanite, monazite, or zircon, will therefore have  $(^{230}\text{Th}/^{238}\text{U})$  and  $(^{231}\text{Pa}/^{235}\text{U}) \gg 1$ . If apatite is also present then  $D_{\text{U}} \approx D_{\text{Th}}$  and  $(^{230}\text{Th}/^{238}\text{U}) \approx 1$ , but  $(^{231}\text{Pa}/^{235}\text{U})$  could still be significantly greater than unity if Pa is incompatible in apatite, potentially generating considerable disequilibrium in the mantle source (Appendix A3). Although  $D_{\text{Pa}}$  values in other accessory phases are generally not known, the modest  $^{231}\text{Pa}$ -excesses that characterize arcs globally argues for a phase, likely allanite/monazite or zircon, in which Pa is relatively compatible, thus retaining it in the slab.

Figure 3.2 illustrates the results of modeling the partial melting of a mantle source that has been modified by addition of a sediment melt (Appendix A3). Figure 3.2a illustrates that the U-Th data requires melting of at least two different sources, one with 0.2% melt added (Sand Mtn. samples) and the other with 0.4% melt added. Other model parameters are consistent with those in Mitchell and Asmerom (2011), including  $F = 1$  to 5%,  $V_o = 0.1$  to 5  $\text{cm a}^{-1}$ , and  $\phi = 0.1$  to 1.2%. Figures 3.2b to 3.2d illustrate U-Th-Pa modeling results for sources with variable pre-melting  $(^{231}\text{Pa}/^{235}\text{U})$  and the same ranges in  $F$  and  $V_o$ , and  $\phi$  from 0.1 to 2%. The results illustrate that the  $(^{231}\text{Pa}/^{235}\text{U})$  data can be reproduced with the same model parameters used in the  $^{238}\text{U}$ - $^{230}\text{Th}$  modeling if the pre-melting source has  $(^{231}\text{Pa}/^{235}\text{U}) \geq 10$ , and more likely in the range 25 to 50. Higher source  $(^{231}\text{Pa}/^{235}\text{U})$  values permit generation of the observed  $(^{231}\text{Pa}/^{235}\text{U})$  data from a broader range of model parameters.

In all of these models the unmodified mantle source contains 0.02 and 0.07 ppm U and Th respectively. To generate source  $(^{231}\text{Pa}/^{235}\text{U})$  values of 10, 25, and 50 through addition

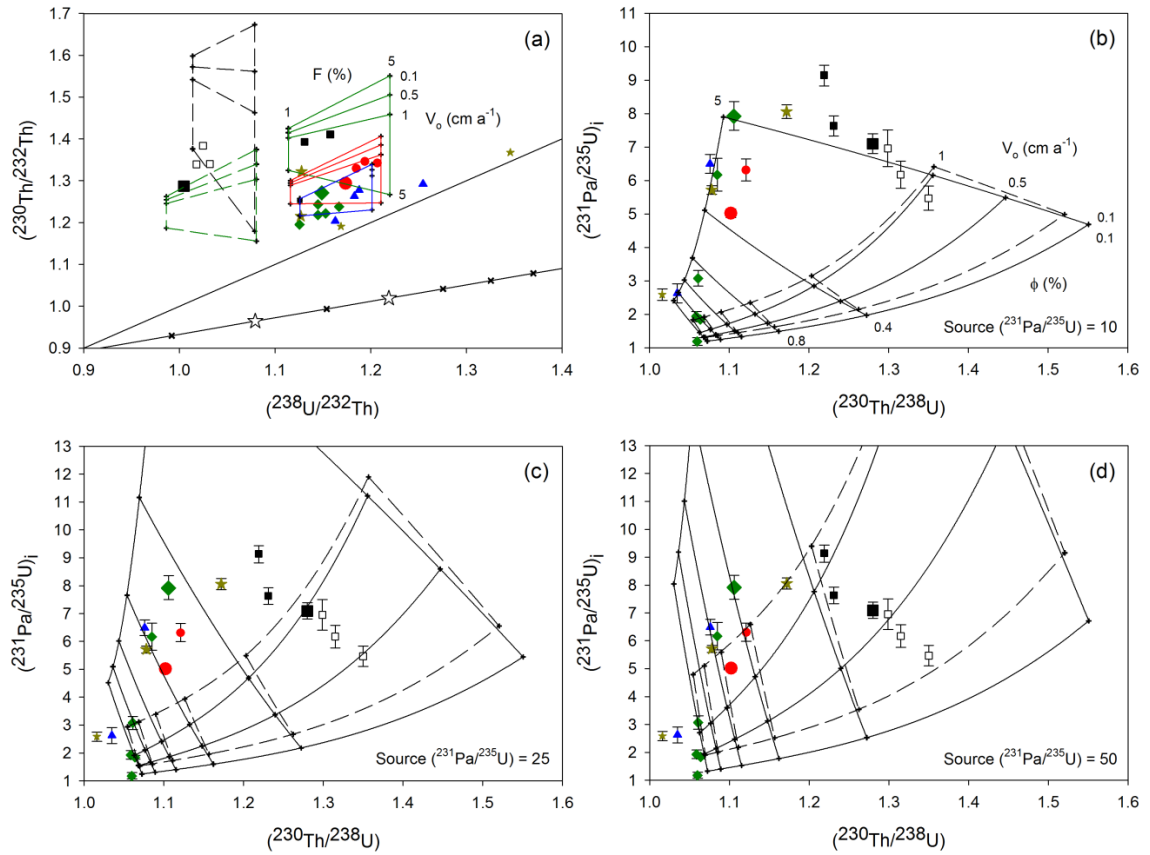


**Figure 3.2:** Results of combined U-Th-Pa modeling of sediment melt-modified mantle sources. Panel (a): U-Th modeling of mantle source modified by 0.2% (dashed lines) and 0.4% (solid lines) sediment melt. Degree of melting ( $F$ , 1-5%) and solid mantle upwelling velocity ( $V_o$ , 0.1-5  $\text{cm a}^{-1}$ ) are labeled. Black, green, red, and blue lines correspond to porosities of 0.1, 0.4, 0.8, and 1.2% respectively. Panel (b): U-Th-Pa modeling of a mantle source with pre-melting  $(^{231}\text{Pa}/^{235}\text{U}) = 10$ . Solid lines correspond to 5% melting and dashed lines to 1% melting. Upwelling velocity and mantle porosity (0.1, 0.4, 0.8, 1.2, 1.6, and 2.0 %) are labeled. Panels (c) and (d): U-Th-Pa modeling for sources with  $(^{231}\text{Pa}/^{235}\text{U}) = 25$  and 50 respectively. Modeling grids as in panel (b).

of 0.2% sediment melt requires effective bulk sediment-melt  $D_{\text{Pa}}$  values of 0.022, 0.00836, and 0.00412, respectively. It should be noted that these  $D$  values could be higher if a time-dependent model for sediment melting was employed, allowing time for  $^{231}\text{Pa}$  ingrowth during melting, thereby generating a higher ‘effective’ or ‘time-

integrated' sediment Pa concentration. This is essentially a flux-melting model (e.g., Thomas et al., 2002; Bourdon et al., 2003; Dosseto et al., 2003) with the assumption that the slab component that triggers melting is dominantly a sediment melt not an aqueous fluid. A two-step source-modification, dynamic melting model is preferred here because it allows clearer delineation of the role of slab component-inherited disequilibria from melting-induced disequilibria. Generation of source ( $^{231}\text{Pa}/^{235}\text{U}$ ) disequilibrium via melt addition requires that this melt was added to the mantle wedge shortly ( $\ll \sim 150$  k.y.) before melting, with the implication that even in this unusually warm subduction environment slab dehydration (which is required for sediment melting) likely is the trigger for initiating partial melting of the mantle wedge.

An alternative to generating, and subsequently melting, a non-equilibrium source is to produce a melt directly from a rutile- ( $\pm$  apatite) bearing source. This could be achieved if mechanical mixtures of oceanic crust, subducted sediments, and peridotitic mantle form along the slab-mantle interface, subsequently rising as buoyant diapirs into the overlying mantle wedge, where they melt to generate arc magmas (Marschall and Schumacher, 2012). Fieldwork in high-pressure mélangé zones demonstrates that this process has the potential to create rocks with bulk compositions and mineralogies that have no surface equivalent. These new compositions frequently contain the same range of accessory minerals found in subducted sediments experiencing metamorphism and partial melting - allanite, apatite, monazite, rutile, and zircon, among others (Marschall and Schumacher, 2012). If these mélangé diapirs exist beneath the Cascades and reach temperatures comparable to, or higher than, those at the slab surface interface, rutile ( $\pm$  apatite) would likely be the accessory phase(s) controlling the partitioning of U, Th, and Pa, thus

generating melts with  $^{230}\text{Th}$ - and  $^{231}\text{Pa}$ -excesses. In contrast, in cooler subduction zones any or all of allanite, monazite, and zircon would likely be present to control U-Th-Pa fractionation. If correct, this alternative framework for subduction zone magmatism has consequences for many commonly accepted interpretations (Marschall and Schumacher, 2012).

In either scenario, it is proposed here that the unusually warm conditions within the Cascadia subduction zone result in a different assemblage of accessory phases present during melting (of either subducted sediments or mélangé rocks) than occurs in cooler subduction zones. It is these accessory phases, and their fractionation of U-series nuclides during melting, that exert the primary control over the U-series disequilibria observed in erupted lavas. If the standard arc paradigm of partial melting of the metasomatized peridotitic mantle wedge is correct, then this partial melting process may not be the primary mechanism for generating arc lava U-series disequilibria, and ( $^{231}\text{Pa}/^{235}\text{U}$ ) especially may not be the sensitive tracer of melting as commonly thought. Preservation of large  $^{231}\text{Pa}$ -excesses in erupted lavas as a consequence of source metasomatism conclusively resolves this issue in the Oregon Cascades in favor of a modern slab input. Finally, similarly large  $^{231}\text{Pa}$ -excesses may be expected in arc lavas from other warm subduction zones, with equally young, hot slabs, such as the SW Japan (Nankai) margin.

### **Acknowledgements**

Victor Polyak provided assistance with the lab work and sample analysis. Tim Debey and the staff of the USGS reactor facility in Denver, CO, are thanked for their assistance in producing the  $^{233}\text{Pa}$  spikes. Funding was provided by the National Science Foundation (EAR-0948703 to YA).

## References

- Arculus, R. J. (1994). Aspects of magma genesis in arcs. *Lithos* **33**, 189-208.
- Asmerom, Y., Cheng, H., Thomas, R., Hirschmann, M. & Edwards, R. L. (2000). Melting of the Earth's lithospheric mantle inferred from protactinium-thorium-uranium isotopic data. *Nature* **406**, 293-296.
- Avanzinelli, R., Prytulak, J., Skora, S., Heumann, A., Koetsier, G. & Elliott, T. (2012). Combined  $^{238}\text{U}$ - $^{230}\text{Th}$  and  $^{235}\text{U}$ - $^{231}\text{Pa}$  constraints on the transport of slab-derived material beneath the Mariana Islands. *Geochimica et Cosmochimica Acta* **92**, 308-328.
- Bacon, C. R., Bruggman, P. E., Christiansen, R. L., Clynne, M. A., Donnelly-Nolan, J. M. & Hildreth, W. (1997). Primitive magmas at five Cascade volcanic fields; melts from hot, heterogeneous sub-arc mantle. *The Canadian Mineralogist* **35**, 397-423.
- Ballhaus, C., Berry, R. F. & Green, D. H. (1990). Oxygen fugacity controls in the Earth's upper mantle. *Nature* **348**, 437-440.
- Bourdon, B., Turner, S. & Allegre, C. J. (1999). Melting dynamics beneath the Tonga-Kermadec island arc inferred from  $^{231}\text{Pa}$ - $^{235}\text{U}$  systematics. *Science* **286**, 2491-2493.
- Bourdon, B., Turner, S. & Dosseto, A. (2003). Dehydration and partial melting in subduction zones: Constraints from U-series disequilibria. *Journal of Geophysical Research* **108**, doi:10.1029/2002JB001839.
- Brenan, J. M., Shaw, H. F., Ryerson, F. J. & Phinney, D. L. (1995). Mineral-aqueous fluid partitioning of trace elements at 900°C and 2.0 GPa: Constraints on the trace element chemistry of mantle and deep crustal fluids. *Geochimica et Cosmochimica Acta* **59**, 3331-3350.
- Conrey, R. M., Sherrod, D. R., Hooper, P. R. & Swanson, D. A. (1997). Diverse primitive magmas in the Cascade Arc, northern Oregon and southern Washington. *The Canadian Mineralogist* **35**, 367-396.

- Cooper, L. B., Ruscitto, D. M., Plank, T., Wallace, P. J., Syracuse, E. M. & Manning, C. E. (2012). Global variations in H<sub>2</sub>O/Ce: 1. Slab surface temperatures beneath volcanic arcs. *Geochemistry Geophysics Geosystems* **13**, doi:10.1029/2011gc003902.
- Hawkesworth, C. J., Gallagher, K., Hergt, J. M. & McDermott, F. (1993). Mantle and slab contributions in arc magmas. *Annual Review of Earth and Planetary Sciences* **21**, 175-204.
- Hermann, J. (2002). Allanite: thorium and light rare earth element carrier in subducted crust. *Chemical Geology* **192**, 289-306.
- Hermann, J. & Rubatto, D. (2009). Accessory phase control on the trace element signature of sediment melts in subduction zones. *Chemical Geology* **265**, 512-526.
- Klemme, S., Prowatke, S., Hametner, K. & Gunther, D. (2005). Partitioning of trace elements between rutile and silicate melts: Implications for subduction zones. *Geochimica et Cosmochimica Acta* **69**, 2361-2371.
- Klimm, K., Blundy, J. D. & Green, T. H. (2008). Trace element partitioning and accessory phase saturation during H<sub>2</sub>O-saturated melting of basalt with implications for subduction zone chemical fluxes. *Journal of Petrology* **49**, 523-553.
- Leeman, W. P., Lewis, J. F., Evarts, R. C., Conrey, R. M. & Streck, M. J. (2005). Petrologic constraints on the thermal structure of the Cascades arc. *Journal of Volcanology and Geothermal Research* **140**, 67-105.
- Lundstrom, C. C. (2003). Uranium-series disequilibria in mid-ocean ridge basalts: Observations and models of basalt genesis. *Reviews in Mineralogy and Geochemistry* **52**, 175-214.
- Marschall, H. R. & Schumacher, J. C. (2012). Arc magmas sourced from mélange diapirs in subduction zones. *Nature Geoscience* **5**, 862-867.
- McBirney, A. R. (1969). Andesitic and rhyolitic volcanism of orogenic belts. In: Hart, P. J. (Ed.), The Earth's Crust and Upper Mantle. *American Geophysical Union Geophysical Monograph* **13**, 501-506.

- McKenzie, D. (1985).  $^{230}\text{Th}$ - $^{238}\text{U}$  disequilibrium and the melting processes beneath ridge axes. *Earth and Planetary Science Letters* **72**, 149-157.
- Mitchell, E. C. & Asmerom, Y. (2011). U-series isotope systematics of mafic magmas from central Oregon: Implications for fluid involvement and melting processes in the Cascade arc. *Earth and Planetary Science Letters* **312**, 378-389.
- Plank, T., Cooper, L. B. & Manning, C. E. (2009). Emerging geothermometers for estimating slab surface temperatures. *Nature Geoscience* **2**, 611-615.
- Reiners, P. W., Hammond, P. E., McKenna, J. M. & Duncan, R. A. (2000). Young basalts of the central Washington Cascades, flux melting of the mantle, and trace element signatures of primary arc magmas. *Contributions to Mineralogy and Petrology* **138**, 249-264.
- Rondenay, S., Abers, G. A. & van Keken, P. E. (2008). Seismic imaging of subduction zone metamorphism. *Geology* **36**, 275-278.
- Skora, S. & Blundy, J. (2010). High-pressure hydrous phase relations of radiolarian clay and implications for the involvement of subducted sediment in arc magmatism. *Journal of Petrology* **51**, 2211-2243.
- Spandler, C., Hermann, J., Arculus, R. & Mavrogenes, J. (2003). Redistribution of trace elements during prograde metamorphism from lawsonite blueschist to eclogite facies; Implications for deep subduction-zone processes. *Contributions to Mineralogy and Petrology* **146**, 205-222.
- Spandler, C., Mavrogenes, J. & Hermann, J. (2007). Experimental constraints on element mobility from subducted sediments using high-P synthetic fluid/melt inclusions. *Chemical Geology* **239**, 228-249.
- Syracuse, E. M., van Keken, P. E., Abers, G. A., Suetsugu, D., Bina, C., Inoue, T., Wiens, D. & Jellinek, M. (2010). The global range of subduction zone thermal models. *Physics of the Earth and Planetary Interiors* **183**, 73-90.
- Tatsumi, Y., Sakuyama, M., Fukuyama, H. & Kushiro, I. (1983). Generation of arc basalt magmas and thermal structure of mantle wedge in subduction zones. *Journal of Geophysical Research* **88**, 5815-5825.

- Tatsumi, Y., Hamilton, D. L. & Nesbitt, R. W. (1986). Chemical characteristics of fluid phase released from a subducted lithosphere and origin of arc magmas: Evidence from high pressure experiments and natural rocks. *Journal of Volcanology and Geothermal Research* **29**, 293-309.
- Thomas, R. B., Hirschmann, M. M., Cheng, H., Reagan, M. K. & Edwards, R. L. (2002). ( $^{231}\text{Pa}/^{235}\text{U}$ )-( $^{230}\text{Th}/^{238}\text{U}$ ) of young mafic volcanic rocks from Nicaragua and Costa Rica and the influence of flux melting on U-series systematics of arc lavas. *Geochimica et Cosmochimica Acta* **66**, 4287-4309.
- Turner, S., Bourdon, B. & Gill, J. (2003). Insights into magma genesis at convergent margins from U-series isotopes. *Reviews in Mineralogy and Geochemistry* **52**, 255-315.
- Turner, S., Regelous, M., Hawkesworth, C. & Rostami, K. (2006). Partial melting processes above subducting plates: Constraints from  $^{231}\text{Pa}$ - $^{235}\text{U}$  disequilibria. *Geochimica et Cosmochimica Acta* **70**, 480-503.
- Wada, I. & Wang, K. (2009). Common depth of slab-mantle decoupling: Reconciling diversity and uniformity of subduction zones. *Geochemistry Geophysics Geosystems* **10**, doi:10.1029/2009GC002570.
- Williams, R. W. & Gill, J. B. (1989). Effects of partial melting on the uranium decay series. *Geochimica et Cosmochimica Acta* **53**, 1607-1619.
- Wilson, D. S. (2002). The Juan de Fuca plate and slab - isochron structure and Cenozoic plate motions. *U.S. Geological Survey Open-File Report* **02-328**, 9-12.
- Wood, B. J., Bryndzia, L. T. & Johnson, K. E. (1990). Mantle oxidation state and its relationship to tectonic environment and fluid speciation. *Science* **248**, 337-345.

## Appendix A3

This appendix contains:

Appendix A3.1. Materials and Methods

Appendix A3.2. Supplementary Text

Figure A3.1: Results of combining a single  $^{231}\text{Pa}/^{233}\text{Pa}$  determination for the Ryan standard with multiple uranium isotope ( $^{235}\text{U}/^{233}\text{U}$ ) analyses, each of a separate batch of powder.

Figure A3.2: U-Th-Ra-Pa results of modeling a secular equilibrium ( $(^{231}\text{Pa}/^{235}\text{U}) = 1$ ) source.

Figure A3.3: Primitive mantle-normalized sediment melt compositions.

Figure A3.4: Trace element and isotope mixing/melting plots calculated using the sediment melt composition shown in Figure A3.3a, run C-1868.

Table A3.1 - Mantle sources, slab components, and partition coefficients used in trace element modeling.

References

### **A3.1. Materials and Methods**

#### *A3.1.1 Samples*

A total of eighteen samples were collected from sixteen separate latest Pleistocene or Holocene lava flows in the Three Sisters region of the central Oregon Cascades, between Three-Fingered Jack and Mount Bachelor, as well as a further six samples from six separate mid-Holocene flows from the flanks of Newberry volcano. The Three Sisters samples are divided into four groups on the basis of vent location and/or age, with the Newberry samples comprising a fifth group. Samples are generally porphyritic basalts and basaltic andesites with phenocrysts of plagioclase and/or olivine.

Complete major element (XRF), trace element (QICP-MS) and isotopic data (U-Th-Ra, Sr-Nd) have been published previously and can be found, along with a description of analytical methods, in Mitchell and Asmerom (2011). All samples lie within the calc-alkaline field in a plot of SiO<sub>2</sub> vs K<sub>2</sub>O, and all but one lie within the basalt or basaltic andesite fields in a silica vs. total alkalis plot. Primitive mantle-normalized trace element spidergrams, and chondrite-normalized REE profiles, are consistent with other ‘Group II’ basalts from the Cascades (Mitchell and Asmerom, 2011, and references therein), generally interpreted as melts of a subduction-modified peridotitic mantle.

The samples define limited ranges in <sup>87</sup>Sr/<sup>86</sup>Sr and <sup>143</sup>Nd/<sup>144</sup>Nd, which are higher and lower, respectively, than typical N-MORB and consistent with previously published data for the Cascades. All samples display (<sup>230</sup>Th/<sup>238</sup>U) > 1 and (<sup>226</sup>Ra/<sup>230</sup>Th)<sub>i</sub> ≥ 1. The U-Th-Ra data are broadly comparable to MORB, extend the field for Cascade samples to higher (<sup>230</sup>Th/<sup>238</sup>U), and have lower (<sup>226</sup>Ra/<sup>230</sup>Th)<sub>i</sub> than typical arc lavas.

Of the nineteen samples for which ( $^{231}\text{Pa}/^{235}\text{U}$ ) data were obtained, this paper focuses on those five that are identified as being the most primitive, and thus least modified from representative mantle-derived melts. Primitive samples are defined by the following characteristics: Ni > 100 ppm, Cr > 200 ppm, SiO<sub>2</sub> < 55 wt.%, MgO > 6 wt.%, and Mg# > 55 (Leeman et al., 2005). Four samples meet all these criteria (08-CYC-01, 08-LL-01, 08-WBB-01, 08-WIC-01) and a fifth (08-SPBF-01) is included in this group because it is the most primitive of the Newberry samples. It should be noted that it is unlikely that any of these lavas represent a primary melt composition; rather they are the most primitive identified in the study area.

#### *A3.1.2 Methods*

Protactinium isotope analyses were performed in the Radiogenic Isotope Laboratory at the University of New Mexico following the general Pa separation procedure described in Thomas et al. (2002). Approximately 450 to 500 mg of the same whole rock powder used for elemental and isotopic analysis (Mitchell and Asmerom, 2011) was weighed into a PVA bomb containing 25 drops (~ 0.5 mL) of 15N HNO<sub>3</sub>, to which 4.5 to 5 mL of concentrated HF was added. The mixture was disaggregated and dissolved at 120°C for ~ 48 hours. The resultant solution was evaporated to dryness in the presence of perchloric acid in a 30 mL PFA beaker and dissolved twice in 15N HNO<sub>3</sub> before dissolution in 6N HCl. Final dissolution and fluxing of the samples was achieved in 15 mL of 2N HCl and 0.5 mL boric acid. After fluxing, this solution was split in half by weight into two clean PFA beakers, one of which contained a  $^{233}\text{Pa}$  spike solution (the remaining half was either spiked with a mixed  $^{229}\text{Th}$ - $^{233}\text{U}$ - $^{236}\text{U}$  spike for U-Th analysis or kept for subsequent  $^{233}\text{Pa}$  spiking and replicate Pa analysis). The  $^{233}\text{Pa}$ -spiked aliquot was dried down and

subsequently re-dissolved and fluxed in 10 mL 2N HCl before pH neutralization with  $\text{NH}_4\text{OH}$  and co-precipitation with iron hydroxides. Initial Pa separation was achieved by loading in 7N  $\text{HNO}_3$  into a 1.2 mL column of Biorad AG 1-X8 anion exchange resin and eluting in 9.8N HCl + 0.05N HF after Th removal in 9.8N HCl. Further separation of Th and Pa was achieved by three passes through separate 0.5 mL columns containing Biorad AG 1-X8 anion exchange resin. Samples were loaded between thin layers of graphite in ~ 0.5 to 1  $\mu\text{L}$  of 1N  $\text{HNO}_3$  + 0.4N HF onto zone refined, sintered Re filaments within 24 hours of final Th-Pa separation.

Analyses were conducted on a VG/Micromass sector 54 thermal ionization mass spectrometer (TIMS) equipped with a Daly ion counter and WARP energy filter. Due to decay of the short-lived  $^{233}\text{Pa}$  spike isotope to  $^{233}\text{U}$  (half-life ~ 27 days), analyses were conducted as soon as possible (typically within a week) after final column separation. Additionally, slow sample warm-up and burning-off of uranium at lower temperature (~ 1700°C) is essential. Runs were started at 1800-1900°C, once the mass 238 signal was < 100 cps. A secular equilibrium standard (either Table Mountain Latite (TML) or the in-house basalt standard 'Ryan') was processed and analyzed with each of the three batches of samples.

As a result of the rapid decay of  $^{233}\text{Pa}$  to  $^{233}\text{U}$ , a mixed U-Pa spike cannot be used, therefore U and Pa analyses must be made on separate sample aliquots, potentially introducing errors via sample heterogeneity or weighing errors. To evaluate the magnitude of such potential errors the ( $^{231}\text{Pa}/^{235}\text{U}$ ) ratio of the Ryan standard was calculated from a single  $^{231}\text{Pa}/^{233}\text{Pa}$  determination combined with U isotope analyses of multiple separate batches of powder analyzed over the course of several years. The

results are displayed in Figure A3.1 and demonstrate that U and Pa ratio measurements can be made on separate aliquots without introducing significant errors into ( $^{231}\text{Pa}/^{235}\text{U}$ ).

The  $^{233}\text{Pa}$  spike was produced by neutron irradiation of a 10 mg/g  $^{232}\text{Th}$  solution (NIST 3159) in HDPE vials at the USGS TRIGA reactor facility outside Denver, CO. The irradiated vials were subsequently fluxed in 7N  $\text{HNO}_3$ , which was then dried down, treated twice with 15N  $\text{HNO}_3$ , and subjected to the same column separation procedure as the samples. A volume of  $^{232}\text{Th}$  solution sufficient to generate a 1 pg/g  $^{233}\text{Pa}$  spike solution was irradiated approximately every four months over the course of one year to produce three separate spike solutions. The  $^{233}\text{Pa}$  concentration of each spike was calibrated by at least two analyses of a high-U (~ 450 ppm) stalagmite from cave C-322 in Grand Canyon National Park, AZ, with a U-Pb age of  $0.663 \pm 0.029$  Ma (V. Polyak, pers. comm., 2013).

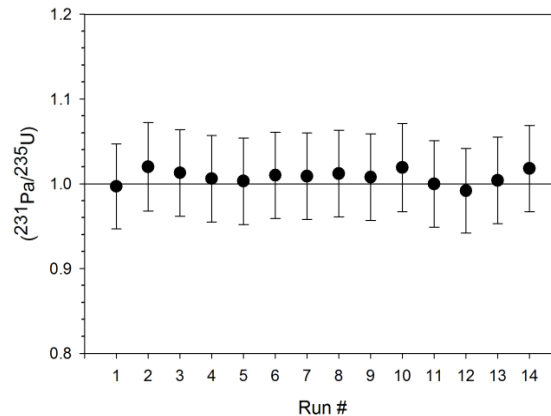


**Figure A3.1:** Results of combining a single  $^{231}\text{Pa}/^{233}\text{Pa}$  determination for the Ryan standard with multiple uranium isotope ( $^{235}\text{U}/^{233}\text{U}$ ) analyses, each of a separate batch of powder.

## A3.2. Supplementary Text

### A3.2.1. *The Melting Model*

The melting model used is the expanded Williams and Gill (1989) version of the dynamic melting model of McKenzie (1985). The model simulates upwelling, decompression, and partial melting of a parcel of solid mantle. The model accounts for the time taken for the parcel of mantle to traverse the specified melting region, thereby allowing 'ingrowth' of daughter isotopes such as  $^{230}\text{Th}$  and  $^{231}\text{Pa}$  during melting, and thus generating greater disequilibria than simple batch or fractional melting models. More complex models (e.g., Spiegelman and Elliott, 1993) that account for continuous re-equilibration between melt and solid during ascent (equilibrium transport models) can generate slightly greater disequilibria than pure dynamic melting models, but still insufficient in this case to explain the observed data. Model variables that can affect the degree of disequilibria produced include the melting column length (45 km (90 to 45 km depth) in our model), the solid mantle upwelling velocity ( $V_o$ ), the total degree of melting (F), the bulk solid-liquid partition coefficient (D;  $D_U = 0.00303$ ,  $D_{Th} = 0.00159$ ,  $D_{Pa} = 5 \times 10^{-6}$  in our model), and the threshold porosity of the solid mantle ( $\phi$ ). This last parameter specifies a critical value above which melt is extracted from the solid and instantaneously transported to the surface. If  $\phi$  is too large then no fractionation of parent and daughter isotopes occurs, and no disequilibria is generated. As a result of variations in bulk D and daughter nuclide half-life, different U-series pairs are sensitive to different variables. For example, ( $^{226}\text{Ra}/^{230}\text{Th}$ ) disequilibrium is very sensitive to  $\phi$ , while ( $^{230}\text{Th}/^{238}\text{U}$ ) disequilibrium is more sensitive to F and the ratio  $D_U/D_{Th}$ . ( $^{231}\text{Pa}/^{235}\text{U}$ ) disequilibrium is intermediate

between these two end members, being sensitive to a variety of parameters, including the solid mantle upwelling rate in instances where source  $(^{231}\text{Pa}/^{235}\text{U}) \neq 1$ .

The model allows the user to specify the source activity ratios before melting begins. Our initial modeling assumes two different initial sources - one in which the source is in secular equilibrium (i.e.  $(^{231}\text{Pa}/^{235}\text{U}) = 1$ ), representing either fluid addition more than approximately 165 k.y. prior to the initiation of melting and/or no fractionation of U from Pa during slab dehydration; and one in which the source is  $^{235}\text{U}$ -enriched (i.e.  $(^{231}\text{Pa}/^{235}\text{U}) < 1$ ), representing recent addition of a U-enriched fluid to the mantle. For example, the fluid-modified source of Mitchell and Asmerom (2011), which had  $(^{230}\text{Th}/^{238}\text{U}) = 0.911$ , would have  $(^{231}\text{Pa}/^{235}\text{U}) = 0.675$ , assuming a Pa-free fluid. Using either of these sources, the  $(^{231}\text{Pa}/^{235}\text{U})$  data can be reproduced only by lowering  $\phi$ , the threshold porosity, to be in the range 0.02 to 0.06% (Fig. A3.2a). Application of this, and similar, models to magma generation beneath mid-ocean ridges and arcs generally requires or assumes porosities in the range 0.1 to 0.5% (Lundstrom, 2003), and even these values have been criticized as being too low (Faul, 2001). Temporarily setting aside this difficulty, appealing to a sub-arc mantle that has inherently different physical properties than typical upper mantle in the absence of evidence and a priori knowledge is an unsatisfying conclusion. Furthermore, to explain the spread in measured  $(^{230}\text{Th}/^{238}\text{U})$  with this model requires that the ratio  $D_{\text{U}}/D_{\text{Th}}$  varies significantly (from  $\sim 1.1$  to 1.4) in the sub-arc mantle over very short length scales, which seems improbable, and also is considerably lower than the value of 1.91 used in Mitchell and Asmerom (2011) based on reasonable assumptions about mantle composition and known D values (Fig. A3.2b).

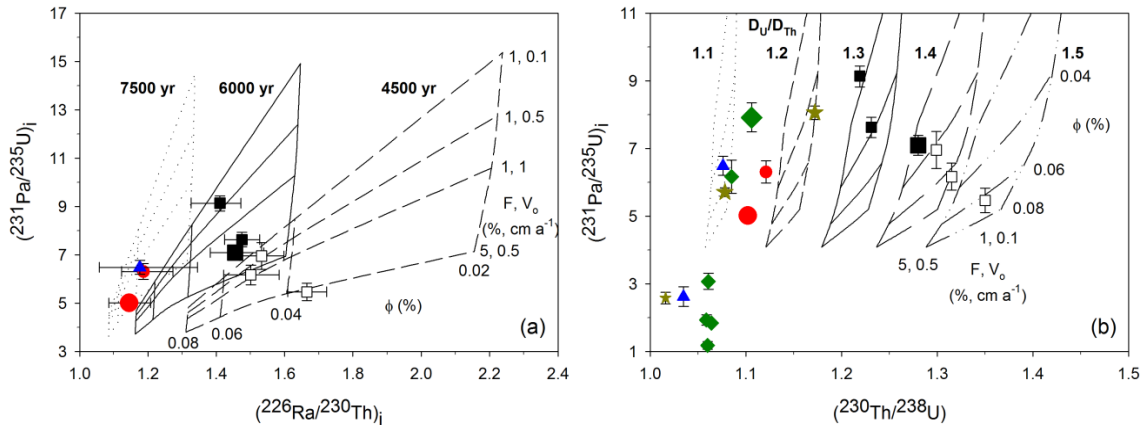


**Figure A3.2:** U-Th-Ra-Pa results of modeling a secular equilibrium ( $(^{231}\text{Pa}/^{235}\text{U}) = 1$ ) source. Panel (a):  $(^{226}\text{Ra}/^{230}\text{Th})$  vs.  $(^{231}\text{Pa}/^{235}\text{U})$  results. The  $(^{226}\text{Ra}/^{230}\text{Th})$  system is very sensitive to  $\phi$ , so the low values of  $\phi$  required in this model result in  $(^{226}\text{Ra}/^{230}\text{Th})$  values that are far higher than those measured. Aging of the melt (for example, including the time for melt to transit the crust) for 4500 (dashed lines), 6000 (solid lines), and 7500 (dotted lines) years can bring the  $(^{226}\text{Ra}/^{230}\text{Th})$  melt values into line with the data without significantly affecting  $(^{231}\text{Pa}/^{235}\text{U})$  because of the much shorter half-life of  $^{226}\text{Ra}$  (1599 years) compared to  $^{231}\text{Pa}$  ( $\sim 32,760$  years). To reproduce the data with this source requires unrealistically low values of  $\phi$ , no greater than  $\sim 0.06\%$ . Panel (b):  $(^{230}\text{Th}/^{238}\text{U})$  vs.  $(^{231}\text{Pa}/^{235}\text{U})$  results for the same model parameters. Reproducing the  $(^{230}\text{Th}/^{238}\text{U})$  data requires  $D_U/D_{Th}$  to be much lower than estimated from partitioning data, and additionally to vary significantly over short length scales in the mantle wedge.

The alternative to this model is to allow the pre-melting source to have  $(^{231}\text{Pa}/^{235}\text{U}) \gg$

1. In the following section we explore the relevant data on accessory phase stability and trace element partitioning that could generate such a source beneath the Cascades.

### A3.2.2. Accessory Phases in Subducted Sediments and Crust

Arc lavas are commonly characterized by  $^{238}\text{U}$ -excesses, in contrast to lavas generated in other tectonic settings, and this is typically interpreted to reflect metasomatism of the sub-arc mantle wedge by a U-bearing but (Pa- and) Th-free aqueous fluid phase liberated from the mafic oceanic crust (e.g., Gill, 1981; Allegre and Condomines, 1982; Newman et al., 1984; Hawkesworth et al., 1993; Elliott et al., 1997; Elliott, 2003; Turner et al.,

2003). Although it should be noted that the possibility of  $^{230}\text{Th}$ - and  $^{231}\text{Pa}$ -bearing fluids has been raised (Thomas et al., 2002; Dosseto et al., 2003). However, recent studies of natural rocks and experimental data have demonstrated that aqueous fluids driven off the subducting plate have low solute concentrations (Spandler et al., 2003; Hermann et al., 2006; Spandler et al., 2007; Klimm et al., 2008) and are likely incapable of transferring the sufficient quantities of trace elements from the slab to the mantle wedge that are necessary to generate the characteristic 'slab signature' seen in arc lavas. Subducting sediments, on the other hand, typically have trace element concentrations that can be an order of magnitude or more higher than in the basaltic slab (Plank and Langmuir, 1998; Gale et al., 2013), and likely exceed the wet pelite solidus in most arcs (Nichols et al., 1994; Vielzeuf and Schmidt, 2001; Hermann and Spandler, 2008; Syracuse et al., 2010). As a result, hydrous melts of subducted sediments, not mafic crust-derived aqueous fluids, are likely the dominant phase in which all but the most fluid mobile trace elements are transferred from the slab to the mantle wedge beneath arcs (Spandler et al., 2003; Hermann et al., 2006; Spandler et al., 2007; Hermann and Spandler, 2008; Hermann and Rubatto, 2009; Avanzinelli et al., 2012; Cooper et al., 2012). Only very recently, however, have such melts been considered when interpreting arc lava U-series disequilibria (Avanzinelli et al., 2012).

Recent experimental studies simulating hydrous melting of subducted sediment (Hermann and Rubatto, 2009; Skora and Blundy, 2010), and basalt (Klimm et al., 2008) have demonstrated that accessory phases are ubiquitously present and exert a strong control over the concentration of trace elements in the melts produced. Allanite ((Ca,Ce,La)<sub>2</sub>(Fe,Al)<sub>3</sub>O(Si<sub>2</sub>O<sub>7</sub>)(SiO<sub>4</sub>)(OH)) and/or monazite ((Ce,La,Th)PO<sub>4</sub>) are likely to

be present in both sediments and basalts, with the presence of allanite in particular depending upon bulk composition. Allanite occurs in metabasalt and CaO-rich metasediments, and in CaO-poor metasediments only at low temperature, to be replaced by monazite at higher temperatures (Hermann and Spandler, 2008; Klimm et al., 2008; Hermann and Rubatto, 2009). Temperatures of at least 850 to 900°C are required to eliminate allanite/monazite from the residue of either basalt or sediment (Klimm et al., 2008; Hermann and Rubatto, 2009; Skora and Blundy, 2010). When present, either phase will exert the dominant control over the behavior of Th and U (as well as the REE, particularly the LREE) owing to the high partition coefficients for both elements, and will preferentially retain Th in the residue (Hermann, 2002; Stepanov et al., 2012). Skora and Blundy (2010) argue on the basis of Th/La systematics that monazite is not a residual phase beneath most arcs, although this interpretation has been questioned (Hermann and Rubatto, 2009; Stepanov et al., 2012), and seem unlikely in light of recent thermal models (Syracuse et al., 2010).

Apatite ( $\text{Ca}_5(\text{PO}_4)_3(\text{F},\text{OH},\text{Cl})$ ) is another accessory phase for which the presence or absence appears sensitive to bulk composition, being absent from the low-CaO, low- $\text{P}_2\text{O}_5$  starting material experiments of Skora and Blundy (2010), but nearly ubiquitous in the high-CaO, high- $\text{P}_2\text{O}_5$  starting material experiments of Hermann and Rubatto (2009). The bulk composition of sediment subducting beneath the Cascades (Plank and Langmuir, 1998) is closer in composition to the starting material of Hermann and Rubatto (2009), so apatite may be present in the subducted sediments there. Apatite-melt partitioning data are scarce, although recent 1 GPa, 1250°C experiments with a variety of silicate melt compositions suggest  $D_{\text{U}}$  and  $D_{\text{Th}} \sim 1$  and, in general,  $D_{\text{Th}} > D_{\text{U}}$  (Prowatke and Klemme,

2006). Apatite  $D_{Pa}$  values are unknown, although other pentavalent elements, such as Nb and Ta, have D values approximately two orders of magnitude lower than U or Th (Prowatke and Klemme, 2006), suggesting that  $D_{Pa}$  may be similarly low.

Zircon ( $ZrSiO_4$ ) is the primary host for Zr and Hf in metasediments and will be an important control on U behavior if present when allanite/monazite are not, although it appears to be consumed relatively early during sediment melting (Hermann and Rubatto, 2009; Skora and Blundy, 2010). Schmitt (2007) estimated zircon-rhyolitic melt  $D_{Pa}/D_U = 0.9$  to 2.2, while  $D_U/D_{Th}$  is  $\sim 6$  (Blundy and Wood, 2003).

Rutile ( $TiO_2$ ) is the dominant host for Ti, Nb, and Ta, but is not expected to affect U or Th if allanite, monazite, or zircon are present due to the greater affinity of U and Th for these phases. Klemme et al. (2005) measured  $D_U$  to be  $\sim 0.1$  to 1, with  $D_U \gg D_{Th}$ . Extrapolation of D values for other pentavalent elements (V, Nb, Ta) leads to estimates of  $D_{Pa} \ll 0.0001$  (Klemme et al., 2005). Significantly, rutile appears to persist to higher temperatures than other accessory phases. It is present in all experimental run products with metabasalt at 750 to 900°C and 2.5 GPa (Klimm et al., 2008), all sediment-melting experiments of Hermann and Rubatto (2009) (max. 1050°C and 4.5 GPa), and all sediment-melting experiments of Skora and Blundy (2010) below 1100°C (3 GPa). Subsequently, it is proposed that rutile ( $\pm$  apatite) will be the only remaining accessory phase(s) present during high temperature ( $\geq 850$  to 900°C) melting of subducted sediments. Such high temperatures are unlikely to be encountered in most subduction zones, but may be attained in margins with hot, young slabs, such as Cascadia, and potentially Nankai, where the young ( $\sim 15$  Ma; Peacock and Wang, 1999) Philippine Sea Plate is subducting relatively slowly (30-50 mm  $a^{-1}$ ; Seno et al., 1993) beneath SW Japan.

Melts generated in the presence of residual rutile, but without allanite, monazite, or zircon, will therefore have  $(^{230}\text{Th}/^{238}\text{U})$  and  $(^{231}\text{Pa}/^{235}\text{U}) \gg 1$ . If apatite is present also then  $D_{\text{U}} \approx D_{\text{Th}}$  and  $(^{230}\text{Th}/^{238}\text{U}) \approx 1$ , but  $(^{231}\text{Pa}/^{235}\text{U})$  could still be significantly greater than unity if Pa is incompatible in apatite.

### *A3.2.3. The Slab Component, Source Modification, and Melting*

The melting model applied here uses the same initial peridotite mantle source as Mitchell and Asmerom (2011), containing 0.02 ppm U and 0.07 ppm Th, and  $(^{238}\text{U}/^{232}\text{Th}) = 0.889$ . The same bulk sediment, with 2.92 ppm U and 6.63 ppm Th ( $(^{238}\text{U}/^{232}\text{Th}) = 1.370$ ), is also used. The mantle source is assumed to be in  $(^{230}\text{Th}/^{238}\text{U})$  and  $(^{231}\text{Pa}/^{235}\text{U})$  secular equilibrium before melt addition, and the bulk sediment likewise is assumed to be in secular equilibrium before melting.

Our sediment melt component is calculated using average  $U_{\text{N}}$  and  $\text{Th}_{\text{N}}$  values from the most applicable P/T condition experiments of Hermann and Rubatto (2009) and Skora and Blundy (2010), where  $U_{\text{N}}$  and  $\text{Th}_{\text{N}}$  are the experimental melt concentrations normalized to the starting composition (i.e. 1/effective bulk D). With  $U_{\text{N}}$  and  $\text{Th}_{\text{N}}$  values of 1.5 and 0.97 ( $D_{\text{U}} = 0.67$ ,  $D_{\text{Th}} = 1.031$ ) we calculate a sediment melt component containing 4.38 ppm U and 6.46 ppm Th ( $(^{238}\text{U}/^{232}\text{Th}) = 2.11$ ). Instantaneous addition of 0.2% of this melt to our peridotitic mantle would generate the following source parameters: U = 0.02872 ppm, Th = 0.08278 ppm,  $(^{230}\text{Th}/^{232}\text{Th}) = 0.964$ ,  $(^{238}\text{U}/^{232}\text{Th}) = 1.080$ , and  $(^{230}\text{Th}/^{238}\text{U}) = 0.893$ . Instantaneous addition of 0.4% of this melt would generate the following source parameters: U = 0.03744 ppm, Th = 0.09556 ppm,  $(^{230}\text{Th}/^{232}\text{Th}) = 1.019$ ,  $(^{238}\text{U}/^{232}\text{Th}) = 1.219$ , and  $(^{230}\text{Th}/^{238}\text{U}) = 0.836$ . These modified

sources, the mantle-sediment melt mixing line, and the U-Th model results for melting of these sources, are all illustrated in Figure 3.2a.

The unmodified source, with 0.02 ppm U, and bulk sediment, with 2.92 ppm U, would have  $^{231}\text{Pa}$  concentrations at secular equilibrium of  $6.709 \times 10^{-9}$  and  $9.784 \times 10^{-7}$  ppm respectively. To generate non-equilibrium sources with  $(^{231}\text{Pa}/^{235}\text{U}) = 10, 25, \text{ and } 50$ , using a melt U concentration of 4.38 ppm and addition of 0.2% melt, requires melt  $^{231}\text{Pa}$  concentrations of  $4.48 \times 10^{-5}$ ,  $1.17 \times 10^{-4}$ , and  $2.38 \times 10^{-4}$  respectively. This in turn requires effective bulk  $D$ s of 0.022, 0.00836, and 0.00412 respectively. As noted in the main text, these  $D$  values could be higher if the timescale of sediment melting is accounted for, which seems reasonable.

Sediment melting experiments indicate that under dry conditions sediments are refractory to very high temperatures, and thus an external source of water is required (e.g., Skora and Blundy, 2010). Serpentinite dehydration in the ultramafic portion of the slab is the likely source for most of this water (e.g., Ulmer and Trommsdorff, 1995; van Keken et al., 2002), with a smaller contribution from the dehydrating altered oceanic crust, which in a hot slab like that beneath the Cascades may itself also melt (van Keken et al., 2002). A fluid phase is not considered in our modeled slab component but likely contributes relatively low concentrations of trace elements (Scambelluri et al., 2001; Spandler et al., 2003; Hermann et al., 2006; Spandler et al., 2007; Klimm et al., 2008), although a flux of dilute aqueous fluid in addition to the sediment melt presumably is still required to initiate melting in the mantle wedge. We have also considered the effects of slab and sediment dehydration on the assumption that the sediment is in secular equilibrium prior to melting. Again, the very low solute concentrations in aqueous fluids,

as a result of the presence of accessory phases with high D values for U and Th, likely severely limits U and Th (and Pa) loss, and thus any deviation from secular equilibrium. A hydrous melt of the basaltic crust could transport greater quantities of trace elements, but the presence of accessory phases such as allanite and rutile (Hermann and Green, 2001; Klimm et al., 2008), and the low trace element concentrations in mafic crust, will likely result in the sediment melt component dominating the trace element budget of the bulk slab component, especially if phases such as allanite, monazite, and zircon are not residual during sediment melting as proposed here.

Figure 3.2b-d illustrates the results of modeling melting of modified sources with  $(^{231}\text{Pa}/^{235}\text{U}) = 10, 25, \text{ and } 50$  respectively. Figure 3.2b demonstrates that a source with  $(^{231}\text{Pa}/^{235}\text{U}) = 10$  is capable of reproducing the data for the primitive samples only at the highest upwelling rates and lowest porosities. A more  $^{231}\text{Pa}$ -enriched source permits a broader range of model parameters, more consistent with the  $(^{230}\text{Th}/^{238}\text{U})$  results. The five most primitive samples can in general be explained equally well by either the  $(^{231}\text{Pa}/^{235}\text{U}) = 25$  or  $(^{231}\text{Pa}/^{235}\text{U}) = 50$  sources, especially when considering that the amount of sediment melt added is the primary factor controlling  $(^{238}\text{U}/^{232}\text{Th})$  variation.

#### *A3.2.4. Trace Element Constraints*

The presence or absence of certain accessory phases in the residue during melting exerts a control on the trace element composition of the melts produced. In this section we explore the effect of melting Cascadia sediment (Plank and Langmuir, 1998) in the presence of various accessory phase assemblages, and evaluate whether a sediment melt produced in the presence of rutile and apatite, but in the absence of allanite, monazite, and zircon, is consistent with the observed trace element systematics in the erupted lavas.

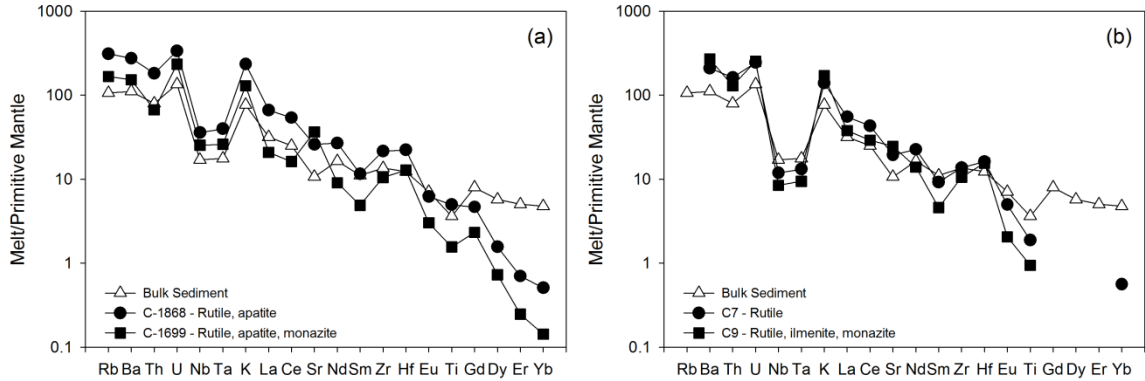


**Figure A3.3:** Primitive mantle-normalized sediment melt compositions. Panel (a): Cascadia sediment melt compositions calculated using data from samples C-1868 and C-1699 of Hermann and Rubatto (2009), conducted at 4.5 GPa/1050°C and 3.5 GPa/900°C respectively. Run products in both experiments contained garnet, quartz/coesite, clinopyroxene, and kyanite, in addition to the accessory phases indicated. Panel (b): Cascadia sediment melt compositions calculated using data from runs c7 and c9 of Skora and Blundy (2010), conducted at 3 GPa/1000°C and 3 GPa/900°C respectively. Run products in both experiments contained garnet, kyanite, and quartz/coesite, in addition to the accessory phases indicated. Bulk sediment composition (Plank and Langmuir, 1998) shown for comparison in both panels.

The composition of Cascadia sediment melts was calculated by applying the relative enrichment or depletion factors (i.e. experimental melt/starting material) from four experiments run with different starting materials and/or at different compositions (Hermann and Rubatto, 2009; Skora and Blundy, 2010). Experiments C-1699 and C-1868 of Hermann and Rubatto (2009) were conducted on a starting material with bulk composition similar to GLOSS (Plank and Langmuir, 1998), with relatively high CaO, K<sub>2</sub>O, and P<sub>2</sub>O<sub>5</sub>, at 3.5 GPa/900°C and 4.5 GPa/1050°C respectively. Run products in both experiments contained garnet, quartz/coesite, clinopyroxene, and kyanite. In addition, the lower P/T experiment (C-1699) contained rutile, apatite, phengite, and monazite, while the higher P/T experiment (C-1868) contained only rutile and apatite. Experiments c9 and c7 of Skora and Blundy (2010) were conducted on a starting material with bulk

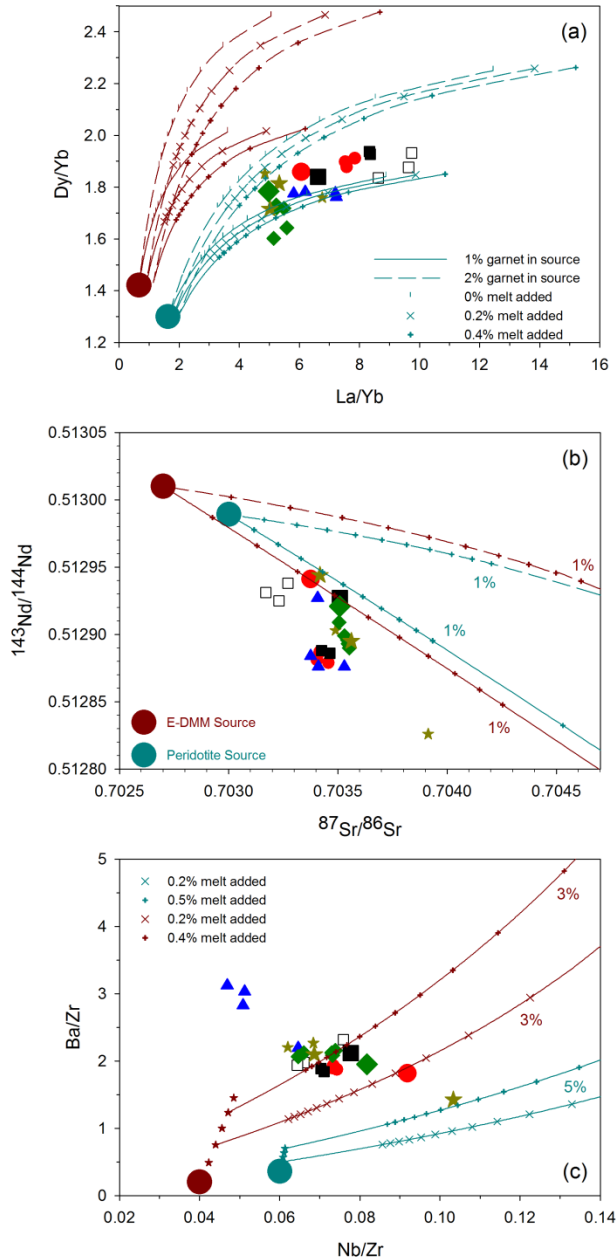


**Figure A3.4:** Trace element and isotope mixing/melting plots calculated using the sediment melt composition shown in Fig. A3.3a, run C-1868. Sample symbols are as figures in the main text. Composition of mantle sources and sediment melt component are given in Table A3.1. Panel (a): La/Yb vs. Dy/Yb plot. Melting trajectories are for two different sources containing 1 or 2% garnet, and 0, 0.2, or 0.4% sediment garnet. Ticks indicate degree of melting in 1% increments from 1 to 10%. Panel (b):  $^{87}\text{Sr}/^{86}\text{Sr}$  vs.  $^{143}\text{Nd}/^{144}\text{Nd}$  mixing plot. Solid lines are mixing curves using the sediment melt Sr and Nd concentrations from Fig. A3.3a, run C-1868; dashed lines are mixing curves using the sediment melt Sr and Nd concentrations from Fig. A3.3a, run C-1699. Ticks indicate 0 to 1% melt addition in 0.1% increments. Panel (c): Nb/Zr vs. Ba/Zr plot. Small stars represent mixing 0.5% sediment melt into the source in 0.1% increments. Melting trajectories are for sources containing 1% garnet. Ticks indicate degree of melting in 1% increments from the value indicated to 15%.

composition similar to radiolarian clay (Plank and Langmuir, 1998), having lower CaO,  $\text{K}_2\text{O}$ , and  $\text{P}_2\text{O}_5$ , at 3 GPa/900°C and 3 GPa/1000°C respectively. Run products in both of these experiments contained garnet, quartz/coesite, and kyanite. In addition, the lower T experiment (c9) contained rutile, ilmenite, and monazite, while the higher T experiment (c7) contained only rutile.

The results of applying relative enrichment or depletion factors from these experiments to bulk Cascadia sediment are illustrated in Figure A3.3. The bulk composition of Cascadia sediment is thought to be closer to the starting material of Hermann and Rubatto (2009), and the accessory phase assemblage in their high temperature experiment is the same as that inferred for the slab beneath the Cascades, so their experiments are the focus here. In general the higher temperature run has elevated trace element concentrations relative to the lower temperature run. The presence of garnet lowers HREE concentrations significantly relative to bulk sediment, and the presence of monazite at lower temperature lowers LREE and Th concentrations also. As a consequence the melt U/Th and Sr/Nd ratios are significantly higher when monazite is present.

Figure A3.4 shows the results of three modeling plots from Mitchell and Asmerom (2011) re-calculated using the sediment melt component calculated from experiment C-1868 (Table A3.1). In agreement with the interpretation based on the U and Th data, the amount of melt addition required is lowered substantially, relative to the old modeling scenario, to  $\leq 0.5\%$ . Other parameters, such as source composition, the amount of garnet in the source, and the degree of melting required are very similar to those in the original modeling. Mixing with a melt generated without residual monazite is a much better fit to the  $^{87}\text{Sr}/^{86}\text{Sr}$  and  $^{143}\text{Nd}/^{144}\text{Nd}$  data than mixing with the residual monazite melt (Fig. A3.4b).

**Table A3.1**

Mantle sources, slab components, and partition coefficients used in trace element modeling.

	DMM	E-DMM	Peridotite	Bulk	Sediment	Partition Coefficients				
	Source	Source	Source	Sediment	Melt	Ol.	Opx.	Cpx.	Grt.	Spl.
La	0.192	0.253	0.815	21.75	45.24	0.0004	0.002	0.054	0.01	0.01
Dy	0.505	0.543	0.650	4.06	1.11	0.0017	0.022	0.33	1.06	0.01
Yb	0.365	0.382	0.50	2.20	0.235	0.0015	0.049	0.28	4.03	0.01
Sr	7.664	9.718	18	216	525					
Nd	0.581	0.703	1.4	21.79	35.59					
Ba	0.563	1.219	9.0	746	1849	0.00011	0.0005	0.00068	0.001	0.00
Nb	0.149	0.246	1.5	10	21.05	0.01	0.025	0.0	0.04	0.01
Zr	5.082	6.087	25	146	232	0.01	0.18	0.3	0.5	0.07
La/Yb	0.526	0.662	1.630	9.886	192					
Dy/Yb	0.192	0.199	0.180	0.364	4.711					
Nb/Zr	0.029	0.040	0.060	0.068	0.091					
Ba/Zr	0.111	0.200	0.360	5.110	7.969					
<sup>87</sup> Sr/ <sup>86</sup> Sr		0.7027	0.7030	0.7071	0.7071					
<sup>143</sup> Nd/ <sup>144</sup> Nd		0.51301	0.512989	0.51253	0.51253					

DMM and E-DMM Sources: Workman and Hart (2005); Peridotite Source: Reiners et al. (2000). Peridotite source Dy value calculated by interpolation. Sediment composition from Plank and Langmuir (1998). Sediment Sr and Nd data from White et al., 1987. Sediment melt calculated from bulk Cascade sediment using data from Hermann and Rubatto (2009), run C-1868. REE partition coefficients from McKenzie and O'Nions (1991). Ba-Nb-Zr partition coefficients from Borg et al. (1997) Table 4.

## References

- Allegre, C. J. & Condomines, M. (1982). Basalt genesis and mantle structure studied through Th-isotopic geochemistry. *Nature* **299**, 21-24.
- Avanzinelli, R., Prytulak, J., Skora, S., Heumann, A., Koetsier, G. & Elliott, T. (2012). Combined  $^{238}\text{U}$ - $^{230}\text{Th}$  and  $^{235}\text{U}$ - $^{231}\text{Pa}$  constraints on the transport of slab-derived material beneath the Mariana Islands. *Geochimica et Cosmochimica Acta* **92**, 308-328.
- Blundy, J. & Wood, B. (2003). Mineral-melt partitioning of uranium, thorium and their daughters. *Reviews in Mineralogy and Geochemistry* **52**, 59-123.
- Cooper, L. B., Ruscitto, D. M., Plank, T., Wallace, P. J., Syracuse, E. M. & Manning, C. E. (2012). Global variations in  $\text{H}_2\text{O}/\text{Ce}$ : 1. Slab surface temperatures beneath volcanic arcs. *Geochemistry Geophysics Geosystems* **13**, doi:10.1029/2011gc003902.
- Dosseto, A., Bourdon, B., Joron, J. L. & Dupre, B. (2003). U-Th-Pa-Ra study of the Kamchatka arc: new constraints on the genesis of arc lavas. *Geochimica et Cosmochimica Acta* **67**, 2857-2877.
- Elliott, T. (2003). Tracers of the slab. In: Eiler, J. (Ed.), Inside the Subduction Factory. *American Geophysical Union Geophysical Monograph* **138**, 23-45.
- Elliott, T., Plank, T., Zindler, A., White, W. & Bourdon, B. (1997). Element transport from slab to volcanic front at the Mariana arc. *Journal of Geophysical Research* **102**, 14991-15019.
- Faul, U. H. (2001). Melt retention and segregation beneath mid-ocean ridges. *Nature* **410**, 920-923.
- Gale, A., Dalton, C. A., Langmuir, C. H., Su, Y. & Schilling, J. G. (2013). The mean composition of ocean ridge basalts. *Geochemistry, Geophysics, Geosystems* **14**, doi: 10.1029/2012GC004334.
- Gill, J. B. (1981). *Orogenic Andesites and Plate Tectonics*. Springer Verlag, Berlin, 412 pp.

- Hawkesworth, C. J., Gallagher, K., Hergt, J. M. & McDermott, F. (1993). Mantle and slab contributions in arc magmas. *Annual Review of Earth and Planetary Sciences* **21**, 175-204.
- Hermann, J. (2002). Allanite: thorium and light rare earth element carrier in subducted crust. *Chemical Geology* **192**, 289-306.
- Hermann, J. & Green, D. H. (2001). Experimental constraints on high pressure melting in subducted crust. *Earth and Planetary Science Letters* **188**, 149-168.
- Hermann, J. & Spandler, C. J. (2008). Sediment melts at sub-arc depths: an experimental study. *Journal of Petrology* **49**, 717-740.
- Hermann, J. & Rubatto, D. (2009). Accessory phase control on the trace element signature of sediment melts in subduction zones. *Chemical Geology* **265**, 512-526.
- Hermann, J., Spandler, C., Hack, A. & Korsakov, A. V. (2006). Aqueous fluids and hydrous melts in high-pressure and ultra-high pressure rocks: Implications for element transfer in subduction zones. *Lithos* **92**, 399-417.
- Klemme, S., Prowatke, S., Hametner, K. & Gunther, D. (2005). Partitioning of trace elements between rutile and silicate melts: Implications for subduction zones. *Geochimica et Cosmochimica Acta* **69**, 2361-2371.
- Klimm, K., Blundy, J. D. & Green, T. H. (2008). Trace element partitioning and accessory phase saturation during H<sub>2</sub>O-saturated melting of basalt with implications for subduction zone chemical fluxes. *Journal of Petrology* **49**, 523-553.
- Leeman, W. P., Lewis, J. F., Evarts, R. C., Conrey, R. M. & Streck, M. J. (2005). Petrologic constraints on the thermal structure of the Cascades arc. *Journal of Volcanology and Geothermal Research* **140**, 67-105.
- Lundstrom, C. C. (2003). Uranium-series disequilibria in mid-ocean ridge basalts: Observations and models of basalt genesis. *Reviews in Mineralogy and Geochemistry* **52**, 175-214.
- McKenzie, D. (1985). <sup>230</sup>Th-<sup>238</sup>U disequilibrium and the melting processes beneath ridge axes. *Earth and Planetary Science Letters* **72**, 149-157.

- Mitchell, E. C. & Asmerom, Y. (2011). U-series isotope systematics of mafic magmas from central Oregon: Implications for fluid involvement and melting processes in the Cascade arc. *Earth and Planetary Science Letters* **312**, 378-389.
- Newman, S., Macdougall, J. D. & Finkel, R. C. (1984).  $^{230}\text{Th}$ - $^{238}\text{U}$  disequilibrium in island arcs: evidence from the Aleutians and the Marianas. *Nature* **308**, 268-270.
- Nichols, G. T., Wyllie, P. J. & Stern, C. R. (1994). Subduction zone melting of pelagic sediments constrained by melting experiments. *Nature* **371**, 785-788.
- Peacock, S. M. & Wang, K. (1999). Seismic consequences of warm versus cool subduction metamorphism: Examples from southwest and northeast Japan. *Science* **286**, 937-939.
- Plank, T. & Langmuir, C. H. (1998). The chemical composition of subducting sediment and its consequences for the crust and mantle. *Chemical Geology* **145**, 325-394.
- Prowatke, S. & Klemme, S. (2006). Trace element partitioning between apatite and silicate melts. *Geochimica et Cosmochimica Acta* **70**, 4513-4527.
- Scambelluri, M., Rampone, E. & Piccardo, G. B. (2001). Fluid and element cycling in subducted serpentinite: a trace-element study of the Erro-Tobbio high-pressure ultramafites (western Alps, NW Italy). *Journal of Petrology* **42**, 55-67.
- Schmitt, A. K. (2007). Ion microprobe analysis of  $(^{231}\text{Pa})/(^{235}\text{U})$  and an appraisal of protactinium partitioning in igneous zircon. *American Mineralogist* **92**, 691-694.
- Seno, T., Stein, S. & Gripp, A. E. (1993). A model for the motion of the Philippine Sea Plate consistent with NUVEL-1 and geologic data. *Journal of Geophysical Research* **98**, 17941-17948.
- Skora, S. & Blundy, J. (2010). High-pressure hydrous phase relations of radiolarian clay and implications for the involvement of subducted sediment in arc magmatism. *Journal of Petrology* **51**, 2211-2243.
- Spandler, C., Hermann, J., Arculus, R. & Mavrogenes, J. (2003). Redistribution of trace elements during prograde metamorphism from lawsonite blueschist to eclogite

- facies; Implications for deep subduction-zone processes. *Contributions to Mineralogy and Petrology* **146**, 205-222.
- Spandler, C., Mavrogenes, J. & Hermann, J. (2007). Experimental constraints on element mobility from subducted sediments using high-P synthetic fluid/melt inclusions. *Chemical Geology* **239**, 228-249.
- Spiegelman, M. & Elliott, T. (1993). Consequences of melt transport for uranium-series disequilibrium in young lavas. *Earth and Planetary Science Letters* **118**, 1-20.
- Stepanov, A. S., Hermann, J., Rubatto, D. & Rapp, R. P. (2012). Experimental study of monazite/melt partitioning with implications for the REE, Th and U geochemistry of crustal rocks. *Chemical Geology* **300-301**, 200-220.
- Syracuse, E. M., van Keken, P. E., Abers, G. A., Suetsugu, D., Bina, C., Inoue, T., Wiens, D. & Jellinek, M. (2010). The global range of subduction zone thermal models. *Physics of the Earth and Planetary Interiors* **183**, 73-90.
- Thomas, R. B., Hirschmann, M. M., Cheng, H., Reagan, M. K. & Edwards, R. L. (2002). ( $^{231}\text{Pa}/^{235}\text{U}$ )-( $^{230}\text{Th}/^{238}\text{U}$ ) of young mafic volcanic rocks from Nicaragua and Costa Rica and the influence of flux melting on U-series systematics of arc lavas. *Geochimica et Cosmochimica Acta* **66**, 4287-4309.
- Turner, S., Bourdon, B. & Gill, J. (2003). Insights into magma genesis at convergent margins from U-series isotopes. *Reviews in Mineralogy and Geochemistry* **52**, 255-315.
- Ulmer, P. & Trommsdorff, V. (1995). Serpentine stability to mantle depths and subduction-related magmatism. *Science* **268**, 858-861.
- van Keken, P. E., Kiefer, B. & Peacock, S. M. (2002). High-resolution models of subduction zones: Implications for mineral dehydration reactions and the transport of water into the deep mantle. *Geochemistry Geophysics Geosystems* **3**, doi:10.1029/2001GC000256.
- Vielzeuf, D. & Schmidt, M. W. (2001). Melting relations in hydrous systems revisited: Application to metapelites, metagreywackes, and metabasalts. *Contributions to Mineralogy and Petrology* **141**, 251-267.

Williams, R. W. & Gill, J. B. (1989). Effects of partial melting on the uranium decay series. *Geochimica et Cosmochimica Acta* **53**, 1607-1619.

## **Chapter 4: Crustal modification of mantle-derived U-series isotope signatures: A case study from the central Oregon Cascades**

### **Abstract**

Postglacial mafic eruptions in the vicinity of the arc-defining Three Sisters volcanic cluster, and rear-arc Newberry volcano, in the central Oregon Cascades range in composition from primitive basalt to evolved andesite ( $\text{SiO}_2$  49-59 wt.%,  $\text{MgO}$  9-3 wt.%,  $\text{K}_2\text{O}$  0.62-1.74 wt.%). Erupted lavas define restricted ranges in  $^{87}\text{Sr}/^{86}\text{Sr}$  and  $^{143}\text{Nd}/^{144}\text{Nd}$  (0.70317-0.70391 and  $\epsilon_{\text{Nd}}$  3.67-5.97) but large ranges in ( $^{230}\text{Th}/^{238}\text{U}$ ) (1.016-1.350) and ( $^{231}\text{Pa}/^{235}\text{U}$ ) (1.178-9.143). Samples from Nash Crater and Belknap volcano near the Three Sisters define linear major and trace element arrays that are distinct from those defined by the Newberry samples. The two sample sets also display distinct U-series variations as lavas become more evolved. These observations suggest that differentiation of primitive magmas occurs via different processes in the two areas, controlled by the thermal and structural state of the arc crust. Extension along the axis of the arc in the vicinity of the Three Sisters results in a large flux of mantle-derived basalt to the mafic lower crust. Mixing between primitive magmas and  $\text{H}_2\text{O}$ -rich lower crustal liquids is the main control on differentiation in the Three Sisters region, with residence in, and interaction with, felsic upper crust being limited as a consequence of rifting. The construction of a large volcanic edifice in the rear-arc at Newberry, where extension is less focused, slows the passage of magmas through the upper crust and results in extensive interaction between primitive magmas and felsic upper crust.

At Newberry the effect of differentiation is to drive U-series isotope activity ratios towards secular equilibrium. In contrast, interaction with lower crustal melts beneath the

Three Sisters can both decrease and increase activity ratios, with implications for U-series-based interpretations of mantle metasomatism and melting processes in the Cascades sub-arc mantle. The trace element and traditional radiogenic isotope signature of crustal interaction is especially cryptic beneath the Three Sisters, as a consequence of the similarity of primitive magma and assimilant, suggesting that lower crustal interaction may be a more prevalent, but largely unrecognized, process than commonly thought. This highlights the importance of detailed studies of individual volcanic centers for identifying the effects of differentiation and constraining truly primitive compositions. Linear arrays of U-series isotope activity ratios could be an important indicator of crustal interaction. The potential interaction of mantle-derived magmas with hydrous lower crustal melts has implications not only for the correct interpretation of arc U-series data, but for the extrapolation of melt inclusion volatile contents also.

#### 4.1. Introduction

Uranium-series (U-series) isotopes ( $^{238}\text{U}$ - $^{230}\text{Th}$ - $^{226}\text{Ra}$ ,  $^{235}\text{U}$ - $^{231}\text{Pa}$ ) have become an increasingly popular tool with which to probe the genesis of convergent margin magmas. Disequilibrium between various parent-daughter isotope pairs has been interpreted to provide constraints on the mechanisms and timescales of mantle metasomatism, magma transport rates, and mantle melting (see reviews by Gill and Williams (1990), McDermott and Hawkesworth (1991), Condomines and Sigmarsson (1993), and Turner et al. (2003)).

The characteristic enrichment of  $^{238}\text{U}$  relative to  $^{230}\text{Th}$  in arc lavas (i.e.  $(^{230}\text{Th}/^{238}\text{U}) < 1$ ), as well as larger  $^{226}\text{Ra}$ -excesses ( $(^{226}\text{Ra}/^{230}\text{Th}) > 1$ ) relative to those in MORB and OIB lavas, are commonly interpreted to reflect the addition of U- and Ra-bearing aqueous fluids derived from the subducting slab to the mantle wedge (e.g., Gill, 1981; Allegre and Condomines, 1982; Newman et al., 1984; Gill and Williams, 1990; Hawkesworth et al., 1993; Elliott et al., 1997; Elliott, 2003; Turner et al., 2003). This interpretation is supported by correlations between  $^{238}\text{U}$ - and  $^{226}\text{Ra}$ -excesses and ratios of fluid mobile to fluid immobile trace elements (e.g., Ba/Th or Sr/Th) (e.g., Reagan et al., 1994; Chabaux et al., 1999; Turner et al., 2000; 2001; 2003; Sigmarsson et al., 2002; Thomas et al., 2002; Huang et al., 2011).

Linear arrays on  $(^{238}\text{U}/^{232}\text{Th})$  vs.  $(^{230}\text{Th}/^{232}\text{Th})$  equiline diagrams have been interpreted to reflect the time elapsed between fluid addition and eruption (e.g., Turner et al., 1996; Elliott et al., 1997; Hawkesworth et al., 1997; Turner and Hawkesworth, 1997; Turner et al., 2003), although they also may reflect ingrowth during melting or mixing trajectories with Th-bearing fluids (e.g., DuFrane et al., 2006). The preservation of  $^{226}\text{Ra}$ -excesses has been used to argue for very rapid ( $< 8$  k.y.) melting and melt transport through the

mantle wedge and overlying crust (e.g., Reagan et al., 1994; Chabaux et al., 1999; Turner et al., 2001; Sigmarsson et al., 2002), although this interpretation has been challenged (e.g., Feineman and DePaolo, 2003; Saal and Van Orman, 2004). Furthermore, the Ra-Th pair is more likely to be affected by open-system processes during differentiation (e.g., Asmerom et al., 2005), as a result of the high diffusivity and fluid mobility of Ra (e.g., Cooper, 2001).

Although ( $^{231}\text{Pa}/^{235}\text{U}$ ) data are scarcer than ( $^{230}\text{Th}/^{238}\text{U}$ ) and ( $^{226}\text{Ra}/^{230}\text{Th}$ ) data, mainly due to analytical difficulties, an excess of  $^{231}\text{Pa}$  over  $^{235}\text{U}$  appears to be an almost ubiquitous feature of arc lavas, in contrast to the expected  $^{235}\text{U}$ -excess generated by fluid addition (e.g., Pickett and Murrell, 1997; Thomas et al., 2002; Dosseto et al., 2003; Turner et al., 2006; Huang and Lundstrom, 2007; Huang et al., 2011). This has led to the recognition that partial melting in the mantle wedge following fluid addition can substantially modify U-series disequilibria (e.g., Thomas et al., 2002; Bourdon et al., 2003; Dosseto et al., 2003; Turner et al., 2006). Finally, the stability and role of various accessory phases in the slab during dehydration and melting, reflecting slab thermal state, has started to be recognized as a strong control on U-series disequilibria (Avanzinelli et al., 2012; Chapter 3).

Interpretations such as these are typically based on activity ratio (i.e. ( $^{230}\text{Th}/^{238}\text{U}$ ), ( $^{226}\text{Ra}/^{230}\text{Th}$ ), and ( $^{231}\text{Pa}/^{235}\text{U}$ )) variations in regional (arc scale) or global datasets. However, recent studies have revealed that individual volcanoes can exhibit similarly broad ranges in U-series isotope disequilibria (e.g., Yokoyama et al., 2006; Turner et al., 2007; Hora et al., 2009; Reubi et al., 2011). Clearly such variable disequilibria measured in lavas erupted in close spatial and temporal proximity cannot be related to regional

variations in fluid addition or melting parameters, but instead must reflect more localized, second-order processes occurring during passage through, and residence in, the overlying crust, such as aging, assimilation, and fractional crystallization (e.g., Bourdon et al., 2000; Hawkesworth et al., 2000; Davidson et al., 2005; Garrison et al., 2006; Jicha et al., 2007; Price et al., 2007; Handley et al., 2008; Huang et al., 2008; Reubi et al., 2011). Huang et al. (2008) demonstrated that correlations between ( $^{226}\text{Ra}/^{230}\text{Th}$ ) and Sr/Th or Ba/Th can be produced during differentiation as well as by fluid addition. Others have highlighted that assimilation of the plutonic roots of arc volcanoes can be difficult to discern using traditional indicators of crustal assimilation, such as Sr, Nd, Pb, or Hf isotopes, due to the isotopic similarity of melt and assimilant (e.g., Yokoyama et al., 2006; Jicha et al., 2009a; Reubi et al., 2011). Os isotopes have been suggested as a sensitive isotopic tracer for the involvement of young crust due to the greater degree of parent-daughter fractionation (Hart et al., 2003; Jicha et al., 2009a; 2009b), although interpretations have been hindered by uncertainty in the flux of slab-derived Os (Borg et al., 2000). Linear mixing arrays defined by U-series nuclides with contrasting half-lives, as opposed to curved arrays produced by time-dependent differentiation, could be the most effective indicators of plutonic assimilation (Reubi et al., 2011).

Correct interpretation of U-series disequilibria measured in arc lavas, with all the attendant implications for subduction zone geodynamics, is dependent critically upon the ability to discern the frequently subtle effects of crustal interaction. Only consideration of truly primitive (ideally primary) melts, and their U-series activity ratios, can inform our knowledge of slab and mantle processes. Furthermore, recognition of modification of

mantle-derived signatures can advance understanding of the processes via which arc magmas differentiate and continental crust is formed.

In this chapter I use major/trace element and isotopic data to constrain the differentiation processes that control evolution from primitive basalts to basaltic andesite and andesitic compositions in central Oregon, and the effect on U-series disequilibria recorded in erupted lavas. The results suggest different processes operating at different locations across the arc, most likely related to the thermal and structural state of the arc crust. These results have implications for the application of U-series data to constrain melting processes and fluid/melt involvement in the sub-arc mantle wedge beneath the Cascades. In particular, it is stressed that crustal interaction and magmatic differentiation can both decrease *and* increase mantle-derived activity ratios, and it cannot be assumed that differentiation processes will drive a system closer to secular equilibrium.

## **4.2. Background**

The Cascade arc is an end member in the global suite of convergent margins with respect to both the age (< 10 Ma at the trench) and velocity ( $\sim 3.5 \text{ cm a}^{-1}$ ) of the subducting slab (Wilson, 2002). These factors create an unusually warm subduction environment, with recent thermal models suggesting slab surface temperatures of 850 to 950°C (Syracuse et al., 2010), and a lower thermal gradient within the subducting basaltic crust and lithospheric mantle than in cooler subduction zones (i.e. higher within-slab temperatures) (van Keken et al., 2002). The temperature in the mantle wedge also is predicted to be unusually high, with transient temperatures at the base of the crust as high as 1300 to 1450°C beneath the northern California segment of the arc (Elkins Tanton et al., 2001)

and similar inferred temperatures beneath northern Oregon and southern Washington (Leeman et al., 2005).

The arc crust in central Oregon is inferred to be ~ 40 to 45 km thick (Eagar et al., 2011) and composed of mafic amphibolites and granulites in the middle and lower crust respectively (Stanley et al., 1990; Conrey et al., 2001). Underplating of voluminous quantities of mafic magma to the base of the crust in this part of the arc is responsible in part for the presence of mafic granulite in the lower crust (Conrey et al., 2001). The eruption of high-Sr andesite at Mt. Jefferson (just to the north of the study area) is interpreted to be a consequence of melting this MORB-like lower crustal granulite (Conrey et al., 2001).

This chapter focuses on small volume, often monogenetic, mafic centers that volumetrically dominate the magmatic output of the arc, and are more abundant in central Oregon since the end of the last glaciation than in any other part of the arc (Hildreth, 2007). This is interpreted to be a consequence of the tectonic regime imposed on the arc (Hildreth, 2007). A combination of oblique Juan de Fuca plate convergence (Wilson, 2002), dextral shear between the Pacific and North American plates (Atwater, 1970), and impingement of Basin and Range extension (Lawrence, 1976; Jones et al., 1996), has resulted in clockwise rotation of the Oregon forearc block and east-west intra-arc extension since at least 5 Ma (Wells et al., 1998; McCaffrey et al., 2007; Hildreth, 2007). The Three Sisters region lies within this zone of intra-arc extension, delineated by the High Cascades graben and numerous north-south trending vent alignments (e.g., Sand Mountain chain of vents, Four-in-One cone, Devils Hill chain of vents) (Fig. 4.1). The rear-arc Newberry center appears to occupy a unique tectonic location, where the eastern

boundary of the High Cascades graben is intersected by a northwest trending crustal-melting anomaly that has propagated across the High Lava Plains since the middle Miocene (10-15 Ma) (MacLeod et al., 1975; Jordan et al., 2004), generating a bimodal basalt-rhyolite volcanic field (Jordan et al., 2004).

These tectonic factors appear to control the location and composition of postglacial eruptions in the Three Sisters and Newberry regions. Along the axis of the arc in the vicinity of the Three Sisters, postglacial eruptions are almost entirely mafic, unusually primitive, and distributed around the periphery of the Three Sisters volcanic cluster, with the only activity from the Three Sisters themselves being the rhyolitic Rock Mesa and Devils Hill episodes on the south flank of South Sister (Sherrod et al., 2004; Hildreth et al., 2012). At Newberry, in contrast, mafic lavas are basaltic andesites to andesites, and mafic eruptions are confined to the flanks, most prominently along the northwest rift zone (McKay et al., 2009). Contemporaneous eruption of obsidian within the central caldera has been commonplace throughout the Holocene (MacLeod et al., 1995). These observations suggest that interaction of mantle-derived melts with middle and upper crust is likely to be limited within the intra-arc graben as a result of rifting (Schmidt and Grunder, 2011) and also that mafic magmas are prevented from erupting within Newberry caldera. However, there is evidence that interaction of mantle-derived melts with mafic lower crust in central Oregon and elsewhere within the arc (Conrey et al., 2001; Jicha et al., 2009b; Mitchell and Asmerom, 2011; Schmidt and Grunder, 2011; Schmidt et al., 2013) has influenced the composition of erupted lavas, including U-series disequilibria (Jicha et al., 2009b; Mitchell and Asmerom, 2011).

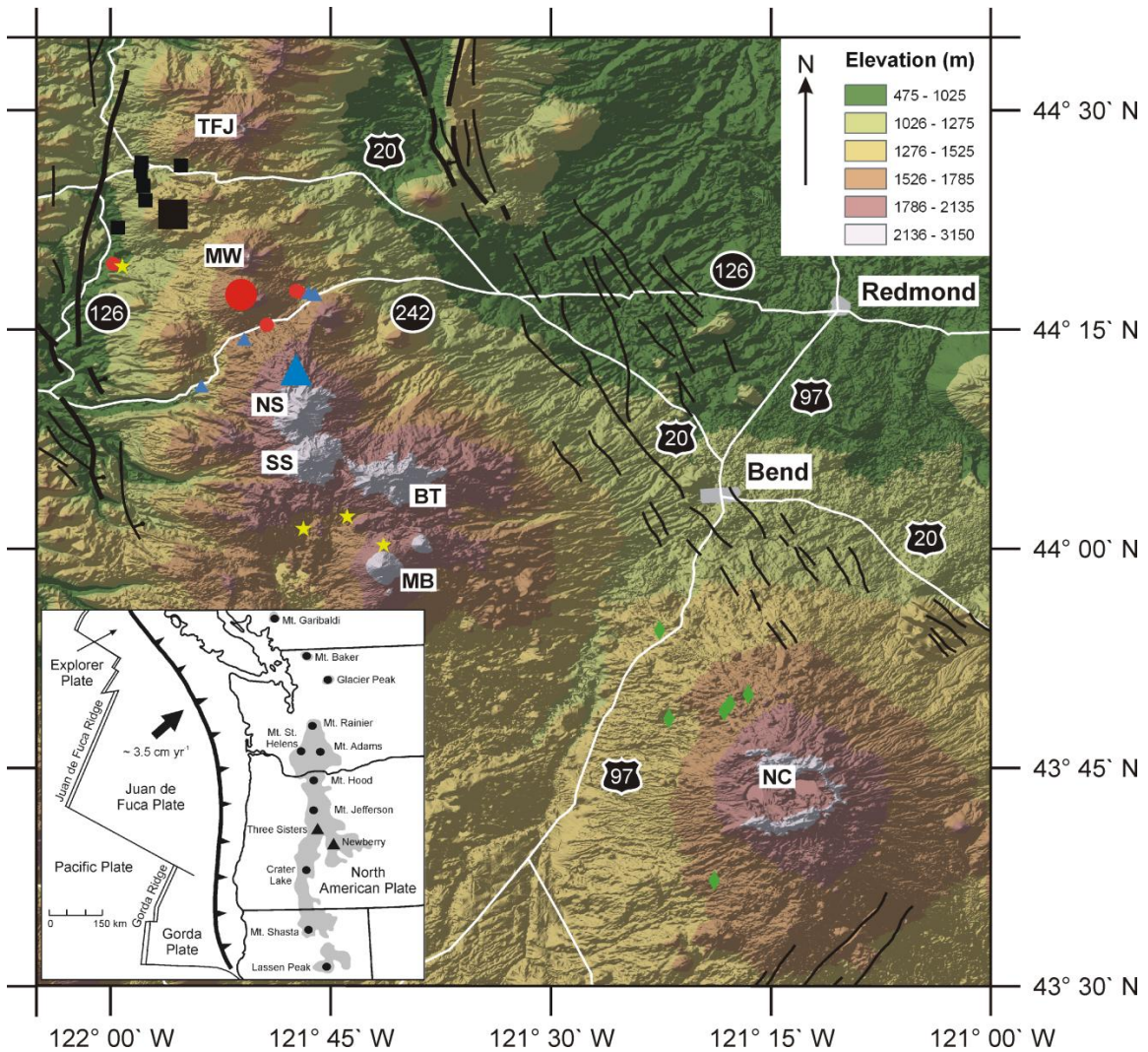


**Figure 4.1:** Shaded relief map of the study area in central Oregon. Sample localities, grouped on the basis of vent location, are indicated with small symbols (see main text for discussion of groups and sub-groups). Black squares = Santiam group; red circles = Belknap group; blue triangles = Yapoah group; green diamonds = Newberry group; yellow stars = pre-Mazama group. Larger symbols (in this figure only) mark approximate vent locations for the first three groups. Prominent stratovolcanoes are labeled: TFJ = Three Fingered Jack, MW = Mt. Washington, NS = North Sister, SS = South Sister, BT = Broken Top, MB = Mt. Bachelor, NC = Newberry caldera. Black lines are faults, ball and bar on downthrown side. Thin lines are faults with displacement < 300 m, thick lines are faults with displacement > 300 m. Major towns and roads in the area are marked. Inset shows general tectonic setting of the Cascadia margin (after Luedke & Smith, 1982). Thick black line is the trench, teeth on overriding plate. Shaded area shows the extent of the Quaternary High Cascades. Prominent volcanoes are indicated with circles and labeled. The study area lies in central Oregon in the vicinity of the Three Sisters and Newberry volcano, marked with triangles.

Many of the numerous previous studies in the Cascades have focused, understandably, on the typically andesitic to dacitic stratovolcanoes that define the volcanic arc (e.g., Mt. Jefferson (Conrey et al., 2001) and the Three Sisters (Gardner, 1994; Brophy and Dreher, 2000; Mercer and Johnston, 2008; Schmidt and Grunder, 2009; 2011; Fierstein et al., 2011;) in central Oregon, and Mt. Adams (Jicha et al., 2009a) in Washington, among many others). These are large, long-lived volcanic centers, where extensive crustal processing of primary mantle-derived melts would be expected. In contrast, the focus here is on the eruptive products of the smaller mafic centers, which are important because they have been the subject of recent attempts to further understanding of magma generation in the Oregon Cascades, in particular the role of slab-derived components in such a warm arc (Ruscitto et al., 2010; Mitchell and Asmerom, 2011; Chapter 3). These lavas should be more representative of primary mantle-derived melts, but they still must traverse 40 to 45 km thick arc crust, much of it composed of compositionally similar, young, mafic rocks, assimilation of which can be difficult to discern with traditional indicators of crustal contamination such as Sr, Nd, Pb, and Hf isotopes (e.g., Jicha et al., 2009a). Not only could U-series isotopes be a useful tool for identifying this crustal interaction (Reubi et al., 2011), but the effects of this interaction could have implications for the identification of the U-series signature of slab and mantle processes, and thus understanding of magma generation processes, in the Cascades.

### **4.3. Samples and Methods**

#### *4.3.1. Samples*

A total of eighteen samples were collected from sixteen separate mafic flows in the Sisters reach (named for the prominent Three Sisters volcanoes) along the Oregon

segment of the Cascade arc axis, and a further six samples from six separate flows were collected from the flanks of Newberry volcano, a rear-arc volcanic field straddling the Sisters and Wickiup reaches (Hildreth, 2007) (Fig. 4.1). The samples are divided into five groups: the Three Sisters samples were initially divided into three groups on the basis of vent location (the Santiam, Belknap, and Yapoah groups), with four older samples grouped separately (the pre-Mazama group). The Newberry samples comprise the fifth group (Fig. 4.1). The Santiam group subsequently was divided further into two sub-groups (Sand Mountain and Nash Crater) on the basis of geochemistry (Section 4.4.). [N.B. For clarity the name Santiam is used here for the group of six samples previously referred to as the Sand Mountain group (Chapter 2), and usage of the name Sand Mountain is restricted to the sub-group of three samples erupted from the Sand Mountain chain of vents.]

The Santiam group (07-LN-01, 07-NC-01, 08-LL-01, 08-NCSW-01, 08-SM-01, and 08-SMCL-01) consists of six samples erupted from at least four separate vents near Santiam Junction in the NW part of the field area (Fig. 4.1). The most prominent feature here is the Sand Mountain Volcanic Field (SMVF), one of many conspicuous north-south trending vent alignments in this part of the arc (Hildreth, 2007). At the northern end of the SMVF lie another three Holocene vents - Nash Crater, Little Nash Crater, and Lost Lake. The age of the Sand Mountain episode has been revised recently and constrained to ~ 2800 to 2900 yr b.p. (Ruscitto, 2011; N. Deligne, pers. comm., 2011). The Little Nash Crater flow is known only to be younger than  $2590 \pm 150$   $^{14}\text{C}$  yr b.p., and the Lost Lake chain of cones have a radiocarbon age of  $1950 \pm 150$   $^{14}\text{C}$  yr b.p. (Sherrod et al., 2004).

The Belknap group (07-BCB-01, 07-BCB-02, 07-LB-01, and 08-WBB-01) consists of four samples from three separate flows erupted from Belknap and Little Belknap craters, summit and satellite vents respectively, on the larger Belknap shield volcano (Fig. 4.1). Ages range from  $1400 \pm 100$  to  $> 2883 \pm 175$   $^{14}\text{C}$  yr b.p. (Sherrod et al., 2004).

The Yapoah group (07-CC-01, 07-FCA-01, 07-YC-01, and 07-YC-02) contains four samples from three separate flows erupted from a cluster of three closely spaced, but likely genetically unrelated, vents (Collier Cone, Four-in-One 'cone', and Yapoah Crater respectively) on the north flank of North Sister volcano (Fig. 4.1). Sample 07-FCA-01 was collected from an early erupted flow, now forming a mafic levee surrounding the main andesitic unit, at the most distal northern limit of the flow. The source is part of another series of north-south trending vents. North Sister is the oldest and most mafic of the Three Sisters volcanoes, and has erupted a compositionally monotonous low-K basaltic andesite since  $\sim 400$  ka (Schmidt and Grunder, 2009; 2011). Ages of Yapoah group samples range from  $1600 \pm 100$  to  $> 1980 \pm 160$  but  $< 2883 \pm 175$   $^{14}\text{C}$  yr b.p. (Sherrod et al., 2004).

The final group from the Three Sisters region, the pre-Mazama group, consists of four geographically widespread samples (08-CYC-01, 08-EC-01, 08-LC-01, and 08-WIC-01) that are all older than the Mazama ash bed, produced during the climactic eruption of Mt. Mazama (Crater Lake)  $\sim 7650$  yr b.p. and 120 km to the south (Sherrod et al., 2004).

The Newberry group samples (08-FRF-01, 08-LBF-01, 08-LCFF-01, 08-MBF-02, 08-SF-01, and 08-SPBF-01) represent mid-Holocene ( $\sim 7000$  yr b.p.) basaltic andesites and

andesites, chiefly erupted from a rift zone on the northwest flank of Newberry volcano (Fig. 4.1).

#### 4.3.2. *Methods*

Samples (~ 1-2 kg) were crushed with a Bico rock crusher, and hand-picked chips, visually identified to be free of hammer/crusher marks or obvious contamination, were powdered in a ceramic shatterbox. Whole-rock major and trace element concentrations were determined by X-ray fluorescence (XRF) and inductively coupled plasma mass spectrometry (ICP-MS) at the University of New Mexico. XRF analysis was conducted in the Analytical Chemistry Laboratory on fused glass disks comprised of a 9:1  $\text{Li}_2\text{B}_4\text{O}_7$  flux:sample mixture, using a Rigaku ZSX Primus II wavelength dispersive spectrometer. Analytical accuracy, based on analysis of known standards (Table 4.1), is estimated at  $\pm \leq 1\%$  for most elements. ICP-MS analysis was conducted in the Radiogenic Isotope Laboratory using a Thermo X-Series II quadrupole instrument. A known amount (~ 0.25 g) of powder was thoroughly mixed with ~ 1.25g of ultra pure  $\text{LiBO}_2$  flux, fused for 10 minutes at  $1100^\circ\text{C}$ , poured directly into ~ 150 mL of 3%  $\text{HNO}_3$  (~ 600x dilution) containing a 10 ppb In internal standard and stirred continuously with a magnetic stirrer until complete dissolution had been achieved (typically < 10 minutes). An ~ 1 g aliquot of this solution was subsequently diluted a further 100x (~ 60,000x) for analysis of high concentration trace elements (e.g., Sr, Ba, Zr, V, Cr, Ni). Analytical accuracy, based on analysis of known standards (Table 4.1), is estimated at  $\pm \leq 3\%$  for most elements.

U-Th-Ra and Sr-Nd isotope analysis was performed in the Radiogenic Isotope Laboratory, University of New Mexico, on a single powder batch following the dissolution and U-Th separation procedure described in Asmerom and Edwards (1995)

**Table 4.1**

Major and trace element data for central Oregon lavas.

Sample ID	08-LL-01	07-LN-01	08-NCSW-01	08-SM-01	08-SMCL-01	07-NC-01	08-WBB-01
Latitude (N)	44° 26.259'	44° 26.474'	44° 24.869'	44° 23.867'	44° 22.014'	44° 25.842'	44° 19.526'
Longitude (W)	121° 54.924'	121° 57.589'	121° 57.457'	121° 57.318'	121° 59.179'	121° 57.648'	121° 59.506'
Group	Nash Crater	Nash Crater	Nash Crater	Sand Mtn.	Sand Mtn.	Sand Mtn.	Belknap
SiO <sub>2</sub>	49.56	52.30	52.60	51.60	52.87	53.21	51.02
Al <sub>2</sub> O <sub>3</sub>	16.58	17.52	17.76	16.86	17.34	17.88	16.72
Fe <sub>2</sub> O <sub>3T</sub>	9.83	9.18	8.91	8.91	8.50	8.28	9.59
MgO	8.99	6.25	5.70	6.99	6.00	5.57	8.09
CaO	9.33	8.44	8.52	9.56	9.07	8.75	8.66
Na <sub>2</sub> O	3.13	3.70	3.86	3.27	3.58	3.80	3.43
K <sub>2</sub> O	0.75	0.80	0.83	0.99	0.86	0.82	0.70
TiO <sub>2</sub>	1.37	1.27	1.28	1.32	1.27	1.22	1.34
P <sub>2</sub> O <sub>5</sub>	0.31	0.39	0.39	0.37	0.37	0.35	0.30
MnO	0.15	0.14	0.13	0.14	0.13	0.13	0.15
Measured Total	99.98	99.77	100.00	99.88	99.64	99.00	100.33
Mg#	63.23	55.97	54.36	59.50	56.87	55.67	61.27
Sc	27.03	24.88	19.88	27.05	22.87	23.62	23.73
V	195.2	173.0	170.0	186.7	170.0	166.7	195.1
Cr	356.5	124.5	101.0	192.4	133.5	92.86	302.60
Co	90.89	36.40	33.48	67.63	54.87	30.57	47.82
Ni	206.3	150.5	102.4	121.6	100.7	118.4	180.8
Cu	58.46	55.38	51.50	58.98	56.81	55.24	67.99
Zn	74.25	83.54	80.90	74.47	76.82	76.78	77.28
Rb	8.76	9.59	9.70	9.88	9.21	8.32	10.13
Sr	648.5	722.1	761.5	1002	1046	982.1	508.1
Y	22.75	23.59	23.24	23.65	22.50	20.68	23.09
Zr	136.6	177.2	173.6	164.8	168.3	162.5	135.8
Nb	10.62	12.60	12.20	12.51	11.11	10.47	12.48
Cs	0.18	0.22	0.22	0.20	0.20	0.17	0.22
Ba	288.9	326.0	326.9	381.4	332.5	314.6	246.0
La	14.03	17.69	18.00	19.04	20.41	18.46	13.83
Ce	33.39	42.02	43.03	45.56	48.05	43.13	31.65
Pr	4.45	5.45	5.61	5.89	6.14	5.51	4.14
Nd	19.81	23.83	24.53	25.31	26.09	23.57	18.06
Sm	4.44	5.05	5.18	5.12	5.25	4.80	4.37
Eu	1.34	1.49	1.50	1.52	1.53	1.43	1.23
Gd	4.01	4.53	4.64	4.50	4.57	4.21	4.52
Tb	0.685	0.749	0.750	0.723	0.726	0.679	0.745
Dy	3.90	4.08	4.19	4.05	3.97	3.66	4.24
Ho	0.832	0.824	0.834	0.852	0.802	0.752	0.905
Er	2.27	2.30	2.36	2.37	2.27	2.08	2.45
Tm	0.318	0.315	0.325	0.329	0.306	0.282	0.343
Yb	2.12	2.12	2.16	2.21	2.12	1.90	2.28
Lu	0.313	0.311	0.317	0.328	0.308	0.281	0.336
Hf	2.69	3.32	3.31	3.27	3.33	3.20	3.01
Ta	0.60	0.66	0.67	0.69	0.59	0.57	0.73
Th	1.29	1.15	1.24	1.41	1.41	1.36	1.15
U	0.43	0.44	0.46	0.48	0.48	0.46	0.45

**Table 4.1**

Continued.

Sample ID	07-LB-01	07-BCB-01	07-BCB-02	07-FCA-01	07-YC-01	07-YC-02	07-CC-01
Latitude (N)	44° 15.337'	44° 17.675'	44° 17.620'	44° 14.389'	44° 17.569'	44° 17.431'	44° 11.167'
Longitude (W)	121° 49.101'	121° 47.108'	121° 46.963'	121° 50.622'	121° 46.251'	121° 45.835'	121° 53.529'
Group	Belknap	Belknap	Belknap	Yapoah	Yapoah	Yapoah	Yapoah
SiO <sub>2</sub>	53.22	53.43	53.37	53.45	55.66	55.96	58.55
Al <sub>2</sub> O <sub>3</sub>	17.94	17.95	17.91	16.86	18.90	18.80	17.43
Fe <sub>2</sub> O <sub>3T</sub>	8.47	8.40	8.45	9.17	6.83	6.71	7.48
MgO	5.30	4.86	4.91	6.22	4.78	4.60	3.22
CaO	8.81	8.82	8.88	7.86	8.22	8.15	6.48
Na <sub>2</sub> O	3.73	3.90	3.83	3.65	3.66	3.80	4.41
K <sub>2</sub> O	0.81	0.86	0.86	1.02	0.92	0.95	1.14
TiO <sub>2</sub>	1.22	1.27	1.28	1.32	0.77	0.77	1.04
P <sub>2</sub> O <sub>5</sub>	0.36	0.38	0.38	0.31	0.15	0.15	0.14
MnO	0.13	0.13	0.13	0.14	0.11	0.11	0.12
Measured Total	100.16	100.13	99.43	99.53	99.54	99.87	99.48
Mg#	53.89	51.87	52.01	55.83	56.78	56.24	44.39
Sc	26.34	27.38	26.49	25.46	21.27	21.44	22.22
V	179.4	180.2	179.2	171.6	142.6	143.9	190.9
Cr	88.88	81.97	77.85	172.0	71.30	68.94	22.25
Co	28.33	41.84	39.61	50.71	43.14	24.84	34.21
Ni	48.22	40.82	42.02	116.3	70.85	58.84	20.94
Cu	66.67	69.03	67.16	61.44	64.89	63.36	47.97
Zn	75.76	75.37	72.03	75.20	57.58	56.38	66.47
Rb	11.21	12.07	11.60	17.53	16.45	16.62	20.36
Sr	623.8	595.8	589.8	413.1	635.0	622.9	493.2
Y	23.42	24.01	24.53	26.84	14.06	14.62	17.99
Zr	171.0	175.0	167.6	163.6	102.1	99.31	113.9
Nb	12.52	13.00	12.30	10.57	5.19	5.09	5.34
Cs	0.26	0.28	0.25	0.47	0.54	0.55	0.66
Ba	323.0	327.5	323.3	358.9	288.5	300.5	355.2
La	17.77	17.91	18.32	15.79	10.40	10.67	11.17
Ce	40.77	41.20	42.74	36.26	22.66	23.68	25.06
Pr	5.27	5.36	5.56	4.75	2.87	3.01	3.21
Nd	22.51	22.82	23.61	20.48	12.15	12.55	13.74
Sm	5.00	5.13	5.23	4.85	2.83	2.88	3.32
Eu	1.38	1.41	1.45	1.36	0.86	0.88	1.01
Gd	5.07	5.14	5.25	5.09	2.84	2.94	3.41
Tb	0.785	0.808	0.834	0.834	0.455	0.467	0.558
Dy	4.33	4.44	4.62	4.82	2.57	2.60	3.21
Ho	0.878	0.907	0.937	0.998	0.550	0.548	0.680
Er	2.47	2.54	2.64	2.87	1.47	1.54	1.89
Tm	0.336	0.353	0.361	0.405	0.215	0.218	0.266
Yb	2.26	2.36	2.43	2.72	1.45	1.48	1.80
Lu	0.334	0.347	0.364	0.406	0.216	0.220	0.269
Hf	3.64	3.65	3.76	3.55	2.31	2.45	2.82
Ta	0.72	0.74	0.75	0.66	0.34	0.36	0.37
Th	1.22	1.28	1.30	1.81	1.63	1.69	2.09
U	0.48	0.51	0.51	0.69	0.63	0.66	0.87

**Table 4.1**

Continued.

Sample ID	08-SPBF-01	08-FRF-01	08-LCFF-01	08-SF-01	08-LBF-01	08-MBF-02	08-WIC-01
Latitude (N)	43° 48.360'	43° 49.375'	43° 48.856'	43° 37.275'	43° 54.416'	43° 50.017'	44° 19.368'
Longitude (W)	121° 21.820'	121° 17.681'	121° 18.085'	121° 18.748'	121° 22.466'	121° 16.447'	121° 58.871'
Group	Newberry	Newberry	Newberry	Newberry	Newberry	Newberry	Pre-Mazama
SiO <sub>2</sub>	52.12	53.35	53.62	54.66	55.55	57.74	49.55
Al <sub>2</sub> O <sub>3</sub>	16.83	17.05	16.96	16.75	16.95	15.73	16.98
Fe <sub>2</sub> O <sub>3T</sub>	9.60	8.96	8.90	8.49	7.89	8.31	10.17
MgO	5.74	5.40	5.26	5.15	5.02	4.01	8.00
CaO	9.58	9.04	8.88	8.44	8.04	6.93	9.51
Na <sub>2</sub> O	3.55	3.64	3.74	3.71	3.81	3.98	3.20
K <sub>2</sub> O	0.77	0.92	0.98	1.19	1.33	1.74	0.63
TiO <sub>2</sub>	1.37	1.24	1.23	1.19	1.06	1.20	1.47
P <sub>2</sub> O <sub>5</sub>	0.28	0.27	0.27	0.26	0.23	0.21	0.32
MnO	0.16	0.15	0.14	0.14	0.13	0.14	0.16
Measured Total	99.67	99.86	100.08	99.79	99.55	99.51	99.73
Mg#	52.77	52.97	52.47	53.07	54.25	47.16	59.64
Sc	32.36	26.45	28.00	26.85	24.03	23.69	28.60
V	228.6	210.7	206.7	180.2	171.0	185.2	216.2
Cr	113.1	109.1	101.5	106.6	103.8	40.0	272.0
Co	34.95	55.65	104.3	29.73	37.93	112.9	49.65
Ni	44.42	52.19	72.47	46.51	59.05	60.14	139.3
Cu	76.79	72.19	70.01	64.96	63.01	53.25	59.93
Zn	75.66	74.97	73.08	71.66	69.54	70.41	74.11
Rb	14.31	18.96	21.46	28.88	33.80	48.65	8.74
Sr	404.9	427.2	408.9	367.2	386.4	272.0	427.2
Y	23.14	23.02	23.04	24.51	24.33	29.70	23.99
Zr	125.9	135.8	137.8	156.3	167.0	193.2	137.9
Nb	10.30	10.04	10.06	11.44	11.03	12.48	14.25
Cs	0.45	0.65	0.74	1.01	1.17	1.73	0.21
Ba	245.0	292.2	292.1	325.7	354.4	398.1	196.1
La	11.55	12.56	12.71	13.90	14.66	16.36	12.43
Ce	26.29	28.35	28.54	30.76	32.26	35.85	28.86
Pr	3.56	3.77	3.80	4.01	4.14	4.52	3.84
Nd	15.67	16.32	16.31	17.23	17.21	18.73	16.28
Sm	3.97	4.03	4.06	4.16	4.08	4.57	4.24
Eu	1.23	1.22	1.19	1.18	1.15	1.18	1.33
Gd	4.35	4.35	4.40	4.67	4.57	5.13	4.06
Tb	0.710	0.706	0.713	0.740	0.735	0.842	0.686
Dy	4.14	4.15	4.17	4.35	4.31	5.09	4.23
Ho	0.873	0.874	0.865	0.898	0.900	1.064	0.891
Er	2.46	2.49	2.50	2.62	2.65	3.18	2.48
Tm	0.343	0.345	0.351	0.371	0.377	0.461	0.342
Yb	2.32	2.40	2.42	2.53	2.62	3.18	2.33
Lu	0.343	0.346	0.351	0.377	0.384	0.473	0.341
Hf	2.73	3.01	3.07	3.48	3.66	4.40	2.80
Ta	0.61	0.60	0.59	0.69	0.68	0.83	0.87
Th	1.55	2.06	2.17	2.89	3.16	4.68	1.14
U	0.59	0.78	0.83	1.10	1.21	1.74	0.43

**Table 4.1**

Continued.

Sample ID	08-CYC-01	08-EC-01	08-LC-01	BHVO-2 Standard (n = 6)			
Latitude (N)	44° 02.224'	44° 00.280'	44° 01.400'	Measured	St. Dev.	Certified	±
Longitude (W)	121° 43.638'	121° 41.157'	121° 46.598'				
Group	Pre-Mazama	Pre-Mazama	Pre-Mazama				
SiO <sub>2</sub>	51.19	51.96	55.44	49.71	0.026	49.9	0.6
Al <sub>2</sub> O <sub>3</sub>	16.47	17.42	16.41	13.47	0.009	13.5	0.2
Fe <sub>2</sub> O <sub>3T</sub>	9.32	10.72	8.33	12.27	0.051	12.3	0.2
MgO	8.76	5.01	5.88	7.19	0.016	7.23	0.12
CaO	9.27	8.11	7.21	11.48	0.030	11.4	0.2
Na <sub>2</sub> O	2.98	3.70	3.66	2.20	0.011	2.22	0.08
K <sub>2</sub> O	0.62	0.72	1.35	0.53	0.007	0.52	0.01
TiO <sub>2</sub>	1.03	1.64	1.28	2.72	0.006	2.73	0.04
P <sub>2</sub> O <sub>5</sub>	0.21	0.54	0.30	0.26	0.002	0.27	0.02
MnO	0.15	0.17	0.13	0.17	0.001	0.17	0.01
Measured Total	98.96	99.61	99.44				
Mg#	64.00	46.47	56.77				
Sc	27.37	21.76	20.46	30.9	0.544	32	1
V	196.3	182.9	165.8	320.9	6.709	317	11
Cr	453.2	54.53	179.8	286.7	8.540	280	19
Co	42.71	94.85	77.93	45.7	1.274	45	3
Ni	155.1	78.09	131.5	117.6	5.229	119	7
Cu	58.43	44.58	42.77	126.5	4.485	127	7
Zn	71.21	93.35	70.47	102.8	3.538	103	6
Rb	10.25	9.76	27.19	9.64	0.096	9.8	1.0
Sr	439.4	482.40	409.0	392.6	8.661	389	23
Y	18.25	32.26	22.38	25.3	0.856	26	2
Zr	101.2	148.9	178.3	177.9	2.970	172	11
Nb	6.95	9.23	12.20	18.3	0.229	18	2
Cs	0.34	0.35	0.89	0.102	0.003		
Ba	212.0	327.90	403.7	127.2	4.748	130	13
La	9.67	14.87	15.61	15.3	0.478	15	1
Ce	21.57	36.43	34.44	38.1	1.095	38	2
Pr	2.90	5.11	4.39	5.32	0.166		
Nd	12.74	23.30	18.38	24.51	0.580	25.0	1.8
Sm	3.15	5.91	4.23	6.11	0.160	6.2	0.4
Eu	1.00	1.78	1.25	1.71	0.030		
Gd	3.50	5.58	4.58	6.25	0.115	6.3	0.2
Tb	0.565	0.932	0.707	0.97	0.025	0.9	
Dy	3.31	5.68	4.06	5.21	0.123		
Ho	0.713	1.181	0.846	1.00	0.038	1.04	0.04
Er	2.01	3.31	2.41	2.54	0.047		
Tm	0.279	0.457	0.330	0.328	0.010		
Yb	1.93	3.07	2.31	2.04	0.037	2.0	0.2
Lu	0.280	0.448	0.341	0.285	0.014	0.28	0.01
Hf	2.34	3.35	3.79	4.17	0.172	4.1	0.3
Ta	0.39	0.56	0.76	1.16	0.024	1.4	
Th	1.28	1.00	2.68				
U	0.48	0.44	1.03				

Group refers to the sample groups identified in Figure 4.1 and subsequent plots. Major elements (wt.%) were determined by XRF on fused glass disks. Analyses are normalized to 100% on an anhydrous basis. Measured analytical totals are given for reference. Total Fe is reported as Fe<sub>2</sub>O<sub>3</sub>. Mg# = molar (MgO/(MgO+FeO))\*100. Trace element concentrations (ppm) were determined by ICP-MS, except Th and U concentrations which were determined from Neptune MC-ICP-MS analyses. Measured values for the USGS standard BHVO-2 are the mean of six separate analyses.

and Asmerom (1999) (Appendix A4). Elemental separation and purification of Ra, Sr, and Nd followed a procedure modified from Chabaux et al. (1994) and Turner et al. (2000). Approximately 200-250 mg of whole rock powder was weighed into a PVA bomb containing an HF-HNO<sub>3</sub> mixture and dissolved at 110°C for ~ 48 hours. Following dissolution the solution was transferred to a 30 mL PFA beaker containing ~ 1 g of a mixed <sup>228</sup>Ra-<sup>229</sup>Th-<sup>233</sup>U-<sup>236</sup>U spike and fluxed with perchloric and boric acids to ensure breakdown of fluoride compounds and complete spike-sample equilibration. A co-precipitation step with iron hydroxides was employed before the sample was dissolved in 7N HNO<sub>3</sub> for element separation and purification. U and Th were separated using 1.2 mL columns of Biorad AG 1-X8 anion exchange resin, eluting with H<sub>2</sub>O/HBr and HCl respectively. The load solution and 7N HNO<sub>3</sub> washes from this column were dried and dissolved in 2.5N HCl and passed through Biorad AG 50W-X8 cation exchange resin to separate Ra, Sr, and the REEs. U and Th were further purified by sequential passes through 0.5 mL columns of anion resin. Ra was purified with one further pass through 0.5 mL columns of cation resin, and Ra-Ba separation was achieved using a 0.5 mL column of Eichrom Sr resin. Sr was purified by passing through 0.25 mL columns of Eichrom Sr resin and Nd was chromatographically separated from the REEs with 2 mL columns of Eichrom LN resin (Appendix A4). U, Th, Sr, and Nd were dissolved in 1 mL of 3% HNO<sub>3</sub> for ICP-MS analysis, and Ra was dissolved in ~ 4 μL 6N HCl and loaded onto zone refined, sintered Re filaments with a Ta-HF-H<sub>3</sub>PO<sub>4</sub> activator solution for TIMS analysis.

Protactinium isotope analysis was performed in the Radiogenic Isotope Laboratory at the University of New Mexico following the general Pa separation procedure described in

Thomas et al. (2002). Sample dissolution procedures were similar to those described above but a larger aliquot, approximately 450 to 500 mg, of the same powders used for earlier elemental and isotopic analyses was weighed into a PVA bomb containing 25 drops (~ 0.5 mL) of 15N HNO<sub>3</sub>, to which 4.5 to 5 mL of concentrated HF was added. The mixture was disaggregated and dissolved at 120°C for ~ 48 hours. The resultant solution was evaporated to dryness in the presence of perchloric acid in a 30 mL PFA beaker and dissolved twice in 15N HNO<sub>3</sub> before dissolution in 6N HCl. Final dissolution and fluxing of the samples was achieved in 15 mL of 2N HCl and 0.5 mL boric acid. After fluxing, this solution was split in half by weight into two clean PFA beakers, one of which contained a <sup>233</sup>Pa spike solution (the remaining half was either spiked with a mixed <sup>229</sup>Th-<sup>233</sup>U-<sup>236</sup>U spike for U-Th analysis or kept for subsequent <sup>233</sup>Pa-spiking and replicate Pa analysis). The <sup>233</sup>Pa-spiked aliquot was dried down and subsequently re-dissolved and fluxed in 10 mL 2N HCl before pH neutralization with NH<sub>4</sub>OH and co-precipitation with iron hydroxides. Initial Pa separation was achieved by loading in 7N HNO<sub>3</sub> into a 1.2 mL column of Biorad AG 1-X8 anion exchange resin and eluting in 9.8N HCl + 0.05N HF after Th removal in 9.8N HCl. Further separation of Th and Pa was achieved by three passes through separate 0.5 mL columns containing Biorad AG 1-X8 anion exchange resin (Appendix A4). Samples were loaded between thin layers of graphite in ~ 0.5 to 1 µL of 1N HNO<sub>3</sub> + 0.4N HF onto zone refined, sintered Re filaments within 24 hours of final Th-Pa separation.

U, Th, Sr, and Nd isotope ratios were measured on a Neptune MC-ICP-MS. Sr and Nd isotopes were analyzed in Faraday cups, monitoring <sup>83</sup>Kr and <sup>85</sup>Rb for interference during Sr runs and <sup>147</sup>Sm during Nd runs. NBS-987 Sr standard and the La Jolla Nd standard

were run at the beginning and end of each analytical session, yielding average values (n = 8) of  $0.71026 \pm 2$  and  $0.511830 \pm 6$  ( $2\sigma$ ) respectively. Sr ratios are normalized to  $^{86}\text{Sr}/^{88}\text{Sr} = 0.1194$  and Nd ratios are normalized to  $^{146}\text{Nd}/^{144}\text{Nd} = 0.7219$ . U and Th were analyzed in static mode using a combination of Faraday cups ( $^{229}\text{Th}$ ,  $^{232}\text{Th}$ ,  $^{233}\text{U}$ ,  $^{235}\text{U}$ ,  $^{236}\text{U}$  and  $^{238}\text{U}$ ) with  $10^{10}$ - $10^{12}$   $\Omega$  resistors, and a secondary electron multiplier (SEM) for  $^{230}\text{Th}$  and  $^{234}\text{U}$ . SEM-Faraday gain was monitored using NBL-112 U standard for U and an in-house Th standard for Th. Mass fractionation was corrected for using the spike  $^{233}\text{U}$ - $^{236}\text{U}$  ratio of 1.00046. Repeat analyses of spiked NBL-112 U standard yielded average  $\delta^{234}\text{U} = -37.16 \pm 0.74\%$  (n = 9) in agreement with published values (Edwards et al., 1993; Cheng et al., 2000) ( $\delta^{234}\text{U}$  is the per mil deviation of the  $^{234}\text{U}/^{238}\text{U}$  from the secular equilibrium ratio).

Radium and protactinium analyses were conducted on a Micromass Sector 54 thermal ionization mass spectrometer (TIMS) equipped with a Daly ion counter and WARP energy filter. Due to decay of the short-lived  $^{233}\text{Pa}$  spike isotope to  $^{233}\text{U}$  (half-life ~ 27 days), Pa analyses were conducted as soon as possible (typically within a week) after final column separation. Additionally, slow sample warm-up and ionization of uranium at lower temperature (~ 1700°C) is essential to prevent isobaric interference.

The  $^{233}\text{Pa}$  spike was produced by neutron irradiation of a 10 mg/g  $^{232}\text{Th}$  solution (NIST 3159) in HDPE vials at the USGS TRIGA reactor facility outside Denver, CO. The irradiated vials were subsequently fluxed in 7N  $\text{HNO}_3$ , which was then dried down, dissolved twice in 15N  $\text{HNO}_3$ , and subjected to the same column separation procedure as the samples. A volume of  $^{232}\text{Th}$  solution sufficient to generate a 1 pg/g  $^{233}\text{Pa}$  spike solution was irradiated approximately every four months over the course of one year to

produce three separate spike solutions. The  $^{233}\text{Pa}$  concentration of each spike was calibrated by at least two analyses of a high-U (~ 450 ppm) stalagmite from cave C-322 in Grand Canyon National Park, AZ, with a U-Pb age of  $0.663 \pm 0.029$  Ma (V. Polyak, pers. comm., 2013).

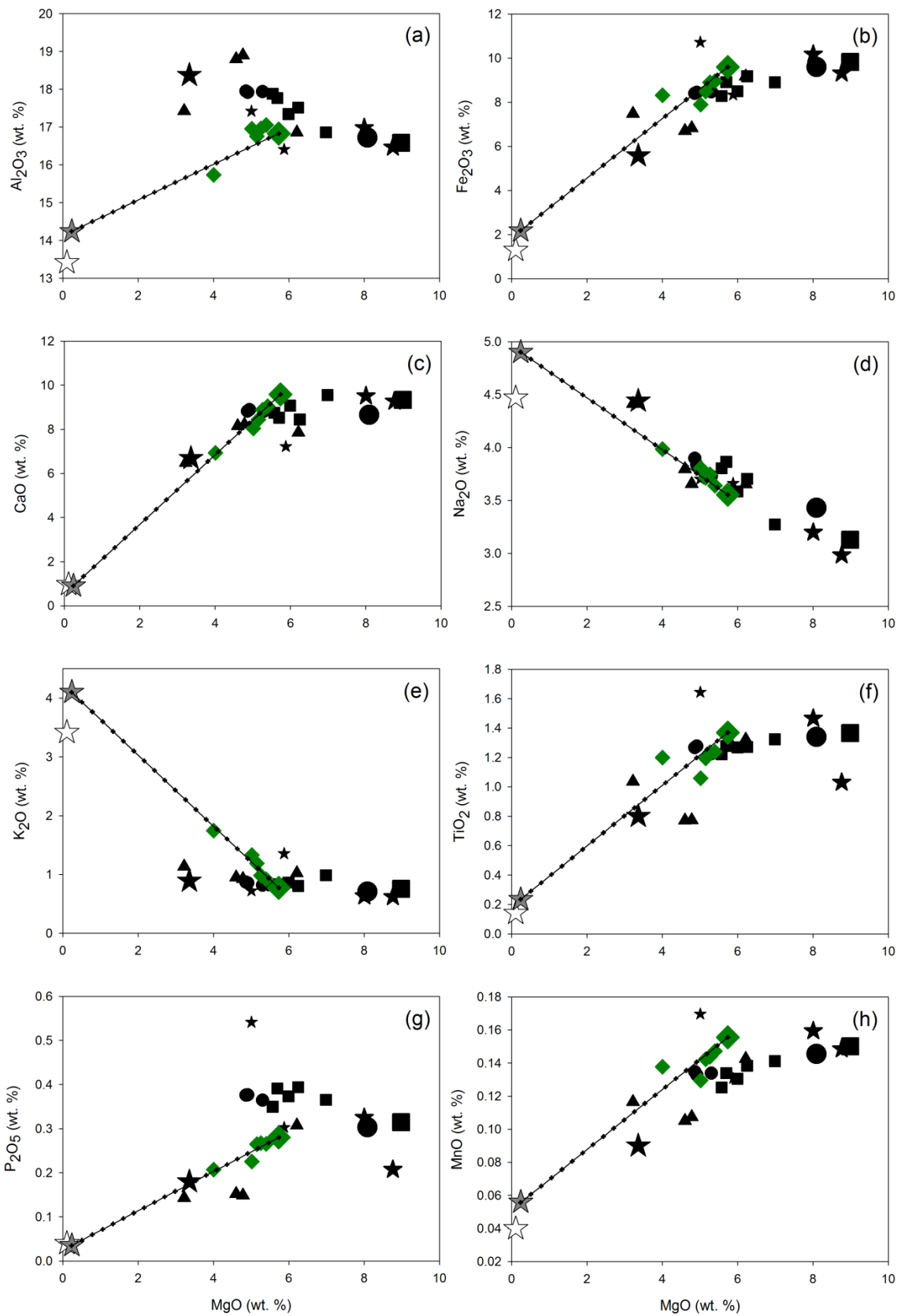
## 4.4. Results

### 4.4.1. Major and Trace Elements

Major and trace element data for all samples are presented in Table 4.1 and Figures 4.2, 4.3, 4.4, and 4.5. The samples range in composition from basalt to andesite according to IUGS silica vs. total alkali classification, with most samples falling in the basaltic andesite field (Fig. 4.2a). All samples plot in the calc-alkaline field on a plot of  $\text{SiO}_2$  vs.  $\text{K}_2\text{O}$  (Fig. 4.2b). The low  $\text{SiO}_2$  samples plot at the low  $\text{K}_2\text{O}$  end of the fields for Group I Intraplate and Group II CAB lavas from the Cascades (Fig. 4.2b) (Leeman et al., 2005).

Figure 4.3 presents Harker-type major element variation diagrams with MgO used as an index of differentiation. MgO varies from ~ 9 to 3 wt.% and varies linearly and inversely with  $\text{SiO}_2$ , which ranges from ~ 49 to 59 wt.% (Fig. 4.2). The salient feature of the major element data is that the Newberry samples (green diamonds) define a coherent linear array in most plots, trending toward the average composition of Holocene obsidians (large gray stars). Arrays involving  $\text{Fe}_2\text{O}_3$ ,  $\text{TiO}_2$ , and MnO diverge from this trend in a consistent fashion (see Section 4.5.3.). Although there is more scatter within the Three Sisters data, these samples also define generally coherent arrays, which are distinct from the Newberry arrays and do not trend towards any upper crustal felsic composition. The most notable differences between the Newberry and Three Sisters trends are a greater increase in  $\text{K}_2\text{O}$  with decreasing MgO in the Newberry samples (Fig.





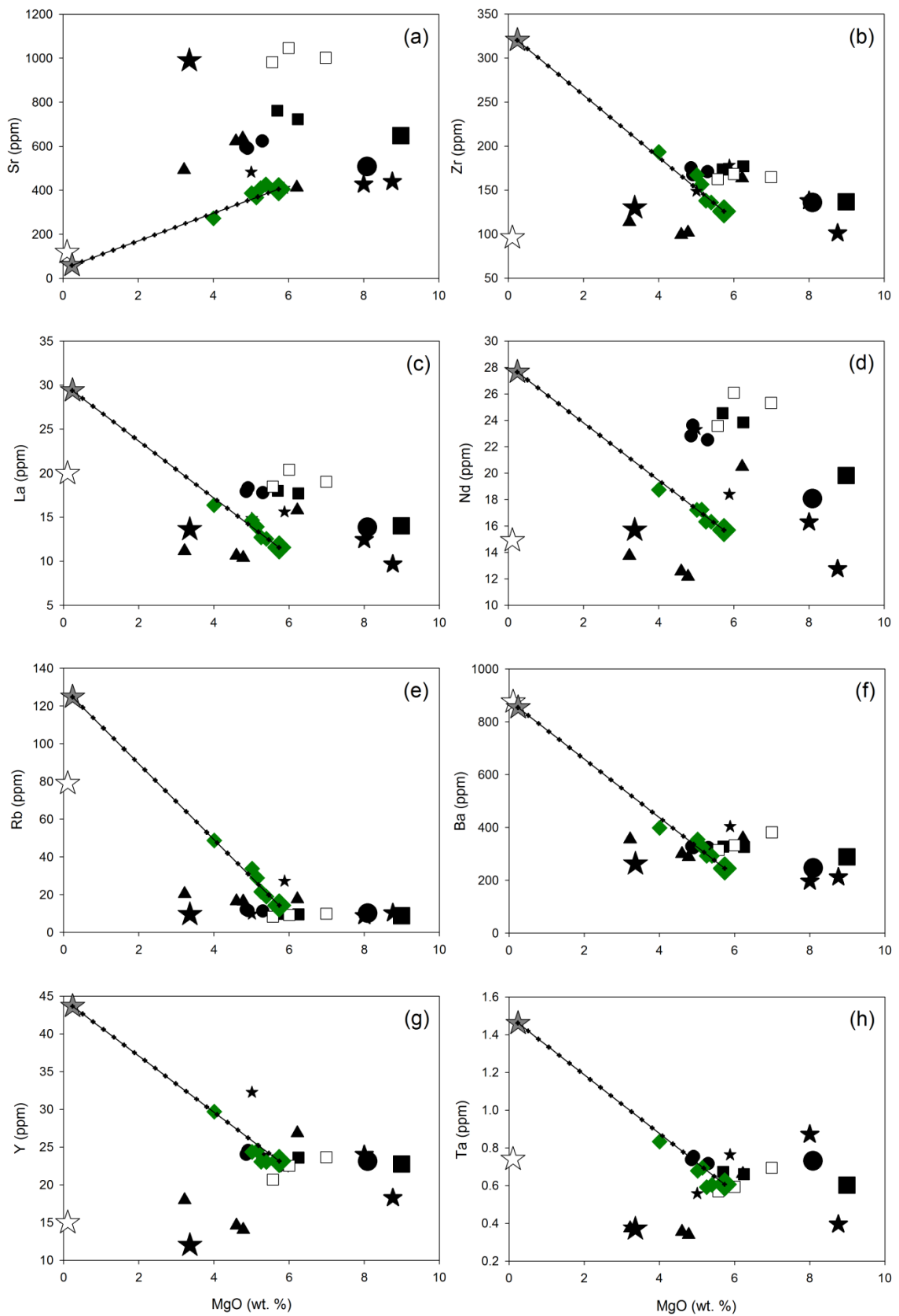
would be expected from samples that are likely genetically unrelated (Section 4.3.1.). This scatter is especially noticeable in plots involving  $\text{TiO}_2$ ,  $\text{P}_2\text{O}_5$ , and  $\text{MnO}$ .

Figure 4.4 shows a variety of Harker-type trace element variation diagrams, again plotted against  $\text{MgO}$  as an index of differentiation. The Newberry samples again define a linear array trending toward the average composition of Holocene obsidians. The scatter within the Three Sisters samples is more apparent in the trace element dataset. However, the Santiam (squares) and Belknap (circles) group samples again define linear arrays, although in some instances they are parallel but displaced from one another (e.g., 4.4d). A distinction within the Santiam group samples between a high-Sr cluster (those from Sand Mountain) and a low-Sr cluster (those from Nash Crater) is apparent in Figure 4.4a, and these two sub-groups are plotted with open and filled symbols, respectively, in these, and subsequent, plots.

An important observation is that there exists significant variability among elements within the Santiam and Belknap groups with respect to the relative concentration change with decreasing  $\text{MgO}$  abundance. For example, panels (g) and (h) in Figure 4.4 are representative of two elements that display little variation within the Santiam and Belknap groups, and thus the samples in these groups define essentially flat arrays in

---

**Figure 4.3:** Harker-type major element variation diagrams for central Oregon lavas plotted against  $\text{MgO}$ , symbols as Figure 4.2. Newberry and Three Sisters samples define distinct trends. White star is the composition of the Pleistocene Obsidian Cliffs rhyolite (3S139 from Sherrod et al., 2004), thought to be representative of the upper crust in much of the Three Sisters region. Gray star is the average composition of Holocene Newberry obsidians (Chapter 5). Black star is the average composition of Mt. Jefferson Sr-rich andesites (from Conrey et al., 2001), interpreted as melts of lower crustal MORB-like mafic granulite. Also shown are mixing lines between the most primitive Newberry sample (08-SPBF-01) and the average Holocene obsidian, tick marks are 5% increments.



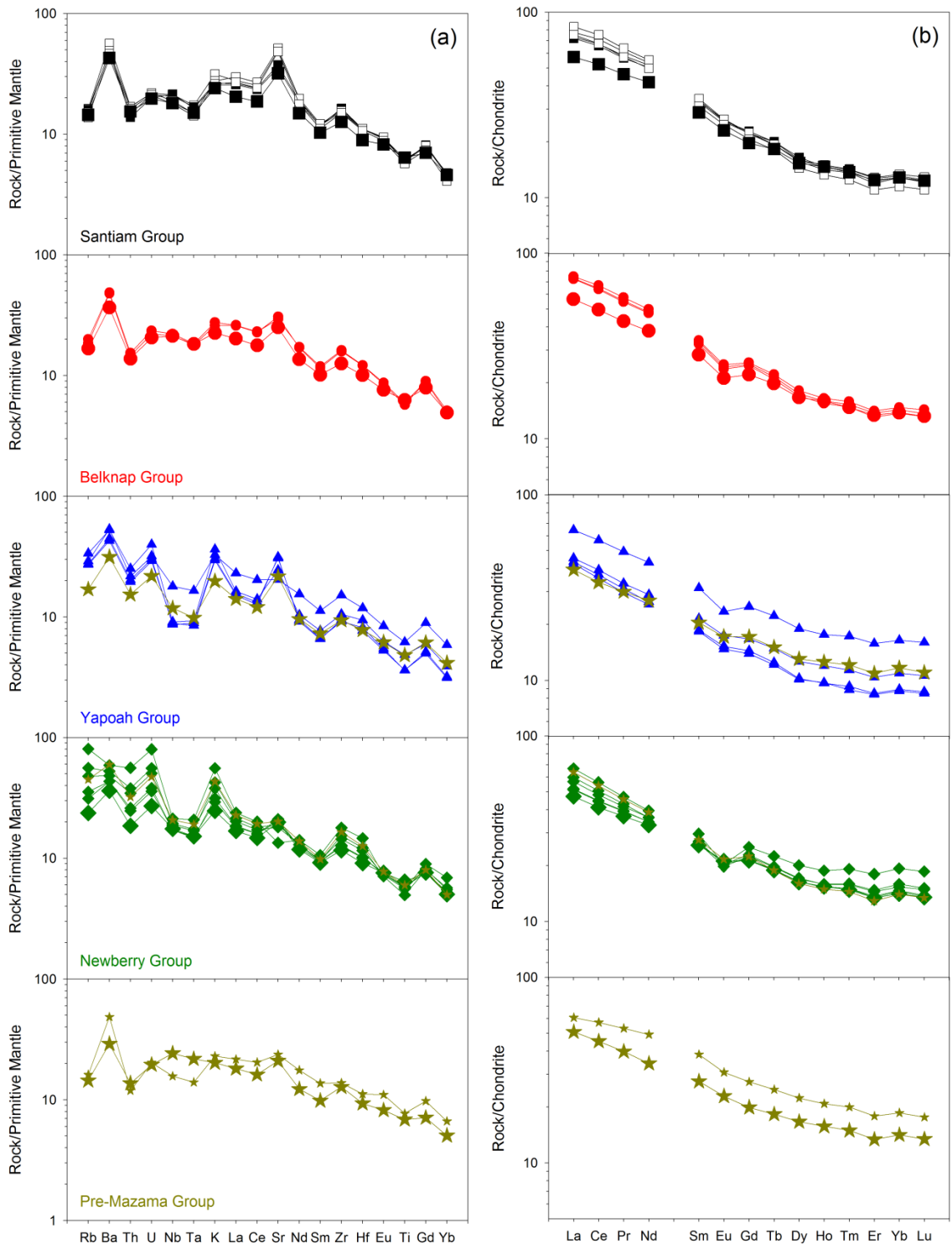
these plots (although in the case of Ta this is more apparent in the Belknap group). The concentrations of elements that follow this trend (the HREE (Tb-Lu), Y, Nb, and Ta) vary by less than 10%, and frequently less than 5%, within the Santiam and Belknap groups. In contrast, the concentrations of most elements within these two groups increase significantly as MgO decreases, by up to 30% in the case of Ba, Zr, and the LREE (La-Nd) (Fig. 4.5a-f).

Figure 4.5 displays primitive mantle-normalized trace element ‘spidergram’ and chondrite-normalized REE diagrams, plotted by group. Once again, the most primitive samples are plotted with larger symbols. The most primitive Newberry sample (08-SPBF-01) displays a ‘spidergram’ pattern that is similar to the most primitive Santiam and Belknap group samples, although the absolute concentration of most elements is lower. Exceptions are higher Rb, Th, U, and K in the Newberry sample, which give the Newberry pattern a more pronounced Nb-Ta anomaly. The REE pattern of the most primitive Newberry sample is similar also to the most primitive Santiam and Belknap samples, although the Newberry sample has lower LREE concentrations.

Within the Newberry group, REE concentrations increase from most primitive to most evolved lava, with the exception of Eu (Eu/Eu\* decreases from 0.90 to 0.74 from most primitive to most evolved lava) (Fig. 4.5). The concentrations of most elements in the

---

**Figure 4.4:** Harker-type trace element variation diagrams for central Oregon lavas plotted against MgO, symbols and lines as Figure 4.3. The samples from the Santiam group in the Three Sisters region have been sub-divided into a high-Sr sub-group (those from Sand Mountain, open squares) and a low-Sr sub-group (those from the Nash Crater area, filled squares). Newberry samples define the same mixing trend with the average obsidian composition as defined by the major elements. South Sister samples are more variable, but Santiam (squares) and Belknap (circles) samples again define trends that are distinct from those of the Newberry samples.



‘spidergram’ plot increase also, with the largest increases for the most highly incompatible elements (i.e. Rb, Th, U, and K) (Fig. 4.5). The concentrations of Sr and Ti decrease also from most primitive to most evolved lava. Negative Nb-Ta anomalies, and positive Zr-Hf anomalies, increase with increasing differentiation in the Newberry group. Pre-Mazama group sample 08-LC-01, plotted with the Newberry group in Figure 4.5, displays similar ‘spidergram’ and REE patterns as the more evolved Newberry samples.

The most primitive Santiam and Belknap group samples display similar ‘spidergram’ patterns, having lower concentrations of most elements than the more evolved lavas within their respective groups (Fig. 4.5). The Santiam group samples generally have slightly lower concentrations for most elements than the Belknap group samples. All samples in these two groups display modest Ba, Sr, and to a lesser extent K and Zr spikes. Very moderate Nb-Ta troughs are present also.

REE profiles for the Belknap samples display LREE enrichments and relatively flat HREE patterns, with increasing concentrations from most primitive to most evolved lava (Fig. 4.5). Small and constant negative Eu anomalies ( $\text{Eu}/\text{Eu}^* = 0.84\text{-}0.83$ ) are present. The REE patterns for Nash Crater sub-group samples (filled squares in the Santiam plot) are similar to the Belknap samples and display an increase in concentration with increasing differentiation, although Eu anomalies are smaller in the Nash Crater samples (0.95-0.92). The Sand Mountain sub-group samples (open squares in the Santiam plot)

---

**Figure 4.5:** Primitive mantle-normalized incompatible element ‘spidergrams’ (panel a) and chondrite-normalized REE profiles (panel b) for central Oregon lavas plotted by geographic groupings identified in Figure 4.1. Normalizing values for primitive mantle and chondrites are from Palme and O’Neill (2003) and Palme and Jones (2003) respectively. Pre-Mazama group samples 08-CYC-01 and 08-LC-01 are plotted with the Yapoh and Newberry groups respectively.

have higher LREE concentrations and more variable (both higher and lower) HREE concentrations than the Nash Crater sub-group samples.

Within the Yapoah group, sample 07-FCA-01 has noticeably higher concentrations of most trace elements, including REEs, than the other samples. The other samples in the group display ‘spidergram’ patterns that are broadly similar to the Newberry group, but with prominent Sr spikes. The absolute concentrations of many trace elements in samples within this group are the lowest in the entire suite. This characteristic is shared with primitive pre-Mazama group sample 08-CYC-01 (plotted with the Yapoah group in Figure 4.5), which has lower concentrations of the most incompatible elements than the Yapoah samples. Apart from sample 07-FCA-01, REE concentrations are low, and Eu anomalies are small ( $\text{Eu}/\text{Eu}^* = 0.92\text{-}0.91$ ), in the Yapoah group samples and 08-CYC-01.

Pre-Mazama group sample 08-WIC-01 displays characteristics typical of Group I intraplate lavas in the Cascades, most notably elevated Nb and Ta concentrations and minor or absent Sr and K spikes. Sample 08-EC-01 is broadly similar to the Belknap samples but with a more pronounced Nb-Ta anomaly.

#### 4.4.2. *U-series, Sr, and Nd Isotopes*

Table 4.2 contains the complete  $^{238}\text{U}$ - $^{230}\text{Th}$ - $^{226}\text{Ra}$ ,  $^{235}\text{U}$ - $^{231}\text{Pa}$ ,  $^{87}\text{Sr}/^{86}\text{Sr}$ , and  $^{143}\text{Nd}/^{144}\text{Nd}$  dataset, and the data are presented in Figure 4.6. Sr and Nd isotope ratios exhibit little variation, with the exception of sample 08-EC-01 (yellow star), and are within the range of values previously measured in the Cascades (Schmidt et al., 2008).  $^{87}\text{Sr}/^{86}\text{Sr}$  is in general inversely correlated with Sr concentration, although the Belknap (circles) intra-group trend departs from this correlation (Fig. 4.6a). Likewise, there is a rough positive

**Table 4.2**

U-Th-Ra-Pa-Sr-Nd isotope data for central Oregon lavas.

Sample ID	Age ( $^{14}\text{C}$ yr B.P.)	U (ppm)	Th (ppm)	$^{232}\text{Th}/^{238}\text{U}$	$(^{230}\text{Th}/^{232}\text{Th})$	$(^{238}\text{U}/^{232}\text{Th})$	$(^{234}\text{U}/^{238}\text{U})$	$(^{230}\text{Th}/^{238}\text{U})$
08-LL-01	1950 ± 150	0.432 ± 1	1.305 ± 3	3.119 ± 11	1.287 ± 5	1.005 ± 3	1.003 ± 1	1.280 ± 5
07-LN-01	<2590 ± 150	0.439 ± 1	1.151 ± 3	2.708 ± 9	1.411 ± 5	1.158 ± 4	1.002 ± 1	1.219 ± 5
08-NCSW-01	2850 ± 50	0.462 ± 1	1.241 ± 3	2.772 ± 10	1.393 ± 6	1.131 ± 4	1.001 ± 1	1.231 ± 5
08-SM-01	2850 ± 50	0.471 ± 1	1.403 ± 4	3.079 ± 11	1.339 ± 5	1.018 ± 4	1.001 ± 1	1.315 ± 5
08-SMCL-01	2850 ± 50	0.479 ± 1	1.409 ± 4	3.039 ± 11	1.340 ± 6	1.032 ± 4	0.996 ± 1	1.299 ± 5
07-NC-01	2850 ± 50	0.460 ± 1	1.360 ± 3	3.058 ± 10	1.384 ± 6	1.025 ± 3	1.001 ± 1	1.350 ± 5
08-WBB-01	1400 ± 100	0.445 ± 1	1.150 ± 3	2.670 ± 9	1.294 ± 5	1.174 ± 4	1.002 ± 1	1.102 ± 4
07-LB-01	2883 ± 175	0.483 ± 1	1.236 ± 3	2.646 ± 9	1.329 ± 5	1.185 ± 4	1.001 ± 1	1.121 ± 4
07-BCB-01	>2883 ± 175	0.511 ± 1	1.284 ± 5	2.598 ± 11	1.342 ± 8	1.207 ± 5	1.003 ± 1	1.112 ± 6
07-BCB-02	>2883 ± 175	0.512 ± 1	1.300 ± 3	2.626 ± 9	1.346 ± 6	1.194 ± 4	1.000 ± 1	1.127 ± 5
07-FCA-01	1980 ± 160	0.694 ± 2	1.811 ± 5	2.696 ± 15	1.204 ± 6	1.163 ± 5	1.000 ± 2	1.035 ± 5
07-YC-01	>1980 ± 160 <2883 ± 175	0.634 ± 1	1.626 ± 4	2.650 ± 9	1.263 ± 6	1.183 ± 4	1.001 ± 1	1.067 ± 4
07-YC-02	>1980 ± 160 <2883 ± 175	0.650 ± 1	1.660 ± 4	2.639 ± 9	1.278 ± 5	1.188 ± 4	1.004 ± 1	1.076 ± 4
07-CC-01	1600 ± 100	0.866 ± 3	2.094 ± 5	2.498 ± 11	1.292 ± 6	1.255 ± 5	1.002 ± 2	1.029 ± 5
08-SPBF-01	5870 ± 60	0.585 ± 1	1.545 ± 4	2.730 ± 9	1.271 ± 5	1.149 ± 4	1.002 ± 1	1.106 ± 4
08-FRF-01	5960 ± 100	0.777 ± 2	2.058 ± 5	2.739 ± 9	1.243 ± 5	1.145 ± 5	1.000 ± 1	1.085 ± 4
08-LCFF-01	6320 ± 110	0.833 ± 2	2.165 ± 5	2.687 ± 9	1.238 ± 5	1.167 ± 4	1.001 ± 1	1.061 ± 4
08-SF-01	6030 ± 90	1.097 ± 3	2.887 ± 7	2.718 ± 9	1.222 ± 5	1.153 ± 4	1.001 ± 1	1.059 ± 4
08-LBF-01	6160 ± 70	1.191 ± 3	3.158 ± 8	2.739 ± 9	1.218 ± 5	1.145 ± 5	1.000 ± 1	1.064 ± 4
08-MBF-02	n.d.	1.739 ± 4	4.684 ± 11	2.783 ± 9	1.195 ± 5	1.126 ± 4	1.001 ± 1	1.060 ± 4
08-WIC-01	> MMA	0.425 ± 1	1.142 ± 3	2.780 ± 9	1.322 ± 8	1.128 ± 4	0.998 ± 1	1.172 ± 7
08-CYC-01	> MMA	0.475 ± 1	1.279 ± 4	2.782 ± 11	1.215 ± 6	1.127 ± 4	1.000 ± 1	1.078 ± 5
08-EC-01	> MMA	0.442 ± 1	0.996 ± 3	2.329 ± 9	1.368 ± 6	1.346 ± 5	1.001 ± 1	1.016 ± 4
08-LC-01	> MMA	1.033 ± 2	2.682 ± 6	2.682 ± 9	1.191 ± 5	1.169 ± 4	1.001 ± 1	1.019 ± 4
Ryan-1 Std.		1.262 ± 3	7.348 ± 18	6.015 ± 21	0.522 ± 2	0.521 ± 2	1.004 ± 1	1.002 ± 4
Ryan-2 Std.		1.261 ± 1	7.196 ± 31	5.895 ± 26	0.530 ± 2	0.532 ± 2	0.997 ± 1	0.996 ± 2
TML-2 Std.		10.73 ± 2	29.42 ± 12	2.834 ± 12	1.037 ± 4	1.106 ± 5	0.997 ± 1	0.937 ± 2
TML-3 Std.		n.m.	n.m.	n.m.	n.m.	n.m.	n.m.	n.m.
TML-4 Std.		10.39 ± 1	28.45 ± 10	2.829 ± 11	1.108 ± 6	1.108 ± 4	1.000 ± 1	1.000 ± 4

**Table 4.2**

Continued.

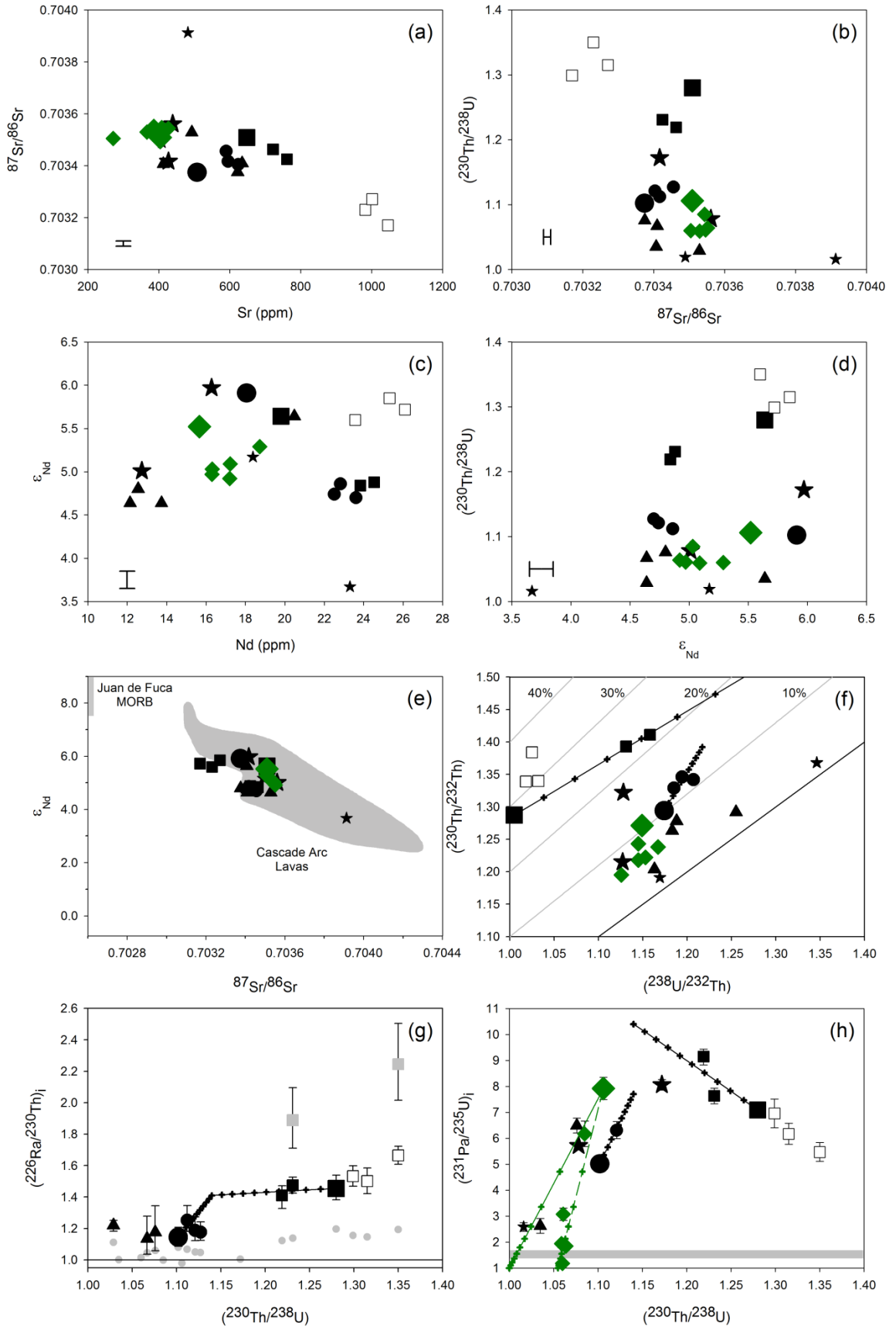
$^{226}\text{Ra}$ (pg/g)	$(^{226}\text{Ra}/^{230}\text{Th})$	$(^{226}\text{Ra}/^{230}\text{Th})_i$	$^{231}\text{Pa}$ (pg/g)	$(^{231}\text{Pa}/^{235}\text{U})$	$(^{231}\text{Pa}/^{235}\text{U})_i$	$^{87}\text{Sr}/^{86}\text{Sr}$	$^{143}\text{Nd}/^{144}\text{Nd}$	$\epsilon_{\text{Nd}}$
0.224 ± 4	1.197 ± 19	1.455 <sup>+84</sup> <sub>-73</sub>	0.974 ± 37	6.850 ± 261	7.094 <sup>+296</sup> <sub>-292</sub>	0.703509 ± 6	0.512927 ± 3	5.64 ± 0.06
0.199 ± 2	1.122 ± 12	1.411 <sup>+61</sup> <sub>-84</sub>	1.254 ± 37	8.673 ± 259	9.143 <sup>+294</sup> <sub>-322</sub>	0.703463 ± 7	0.512886 ± 4	4.84 ± 0.08
0.219 ± 2	1.138 ± 12	1.475 <sup>+52</sup> <sub>-50</sub>	1.098 ± 42	7.243 ± 276	7.631 <sup>+300</sup> <sub>-300</sub>	0.703425 ± 6	0.512888 ± 4	4.88 ± 0.08
0.240 ± 4	1.146 ± 20	1.501 <sup>+83</sup> <sub>-79</sub>	0.911 ± 58	5.869 ± 376	6.171 <sup>+406</sup> <sub>-404</sub>	0.703271 ± 9	0.512938 ± 4	5.85 ± 0.08
0.243 ± 3	1.155 ± 15	1.533 <sup>+65</sup> <sub>-64</sub>	1.039 ± 80	6.608 ± 512	6.956 <sup>+551</sup> <sub>-549</sub>	0.70317 ± 2	0.512931 ± 5	5.72 ± 0.10
0.250 ± 3	1.193 ± 13	1.665 <sup>+58</sup> <sub>-56</sub>	0.787 ± 51	5.206 ± 336	5.467 <sup>+362</sup> <sub>-360</sub>	0.70323 ± 1	0.512925 ± 2	5.60 ± 0.04
0.179 ± 5	1.080 ± 32	1.145 <sup>+63</sup> <sub>-59</sub>	0.716 ± 18	4.902 ± 123	5.016 <sup>+132</sup> <sub>-130</sub>	0.703374 ± 1	0.512941 ± 4	5.91 ± 0.08
0.192 ± 3	1.050 ± 14	1.187 <sup>+86</sup> <sub>-64</sub>	0.946 ± 44	5.977 ± 281	6.307 <sup>+334</sup> <sub>-321</sub>	0.703404 ± 5	0.512881 ± 3	4.74 ± 0.06
0.205 ± 3	1.067 ± 15	1.251 <sup>+95</sup> <sub>-70</sub>	n.m.	n.m.	n.d.	0.703417 ± 5	0.512887 ± 4	4.86 ± 0.08
0.204 ± 2	1.047 ± 10	1.176 <sup>+67</sup> <sub>-51</sub>	n.m.	n.m.	n.d.	0.703456 ± 4	0.512879 ± 3	4.70 ± 0.06
0.237 ± 2	1.001 ± 10	n.d.	0.558 ± 59	2.555 ± 270	2.621 <sup>+289</sup> <sub>-286</sub>	0.703407 ± 6	0.512927 ± 2	5.64 ± 0.04
0.239 ± 7	1.046 ± 30	1.135 <sup>+143</sup> <sub>-99</sub>	n.m.	n.m.	n.d.	0.70341 ± 1	0.512876 ± 4	4.64 ± 0.08
0.250 ± 8	1.059 ± 35	1.176 <sup>+169</sup> <sub>-118</sub>	1.325 ± 45	6.205 ± 213	6.488 <sup>+285</sup> <sub>-280</sub>	0.703375 ± 8	0.512884 ± 5	4.80 ± 0.10
0.301 ± 3	1.112 ± 13	1.220 <sup>+32</sup> <sub>-38</sub>	n.m.	n.m.	n.d.	0.703529 ± 5	0.512876 ± 5	4.64 ± 0.10
0.214 ± 12	0.980 ± 53	n.d.	1.348 ± 68	7.000 ± 355	7.917 <sup>+434</sup> <sub>-420</sub>	0.703509 ± 5	0.512921 ± 4	5.52 ± 0.08
0.284 ± 3	0.999 ± 11	n.d.	1.345 ± 101	5.475 ± 412	6.168 <sup>+492</sup> <sub>-488</sub>	0.703544 ± 7	0.512896 ± 4	5.03 ± 0.08
n.m.	n.m.	n.d.	0.730 ± 52	2.778 ± 198	3.071 <sup>+238</sup> <sub>-236</sub>	0.703547 ± 5	0.512893 ± 4	4.97 ± 0.08
n.m.	n.m.	n.d.	0.624 ± 45	1.806 ± 130	1.932 <sup>+153</sup> <sub>-152</sub>	0.703530 ± 4	0.512899 ± 4	5.09 ± 0.08
n.m.	n.m.	n.d.	0.671 ± 22	1.726 ± 57	1.842 <sup>+69</sup> <sub>-68</sub>	0.703552 ± 7	0.512890 ± 5	4.92 ± 0.10
0.631 ± 15	1.014 ± 24	n.d.	0.655 ± 55	1.154 ± 97	1.178 <sup>+114</sup> <sub>-112</sub>	0.703505 ± 6	0.512909 ± 4	5.29 ± 0.08
0.169 ± 2	1.004 ± 11	n.d.	0.976 ± 24	6.997 ± 172	8.058 <sup>+202</sup> <sub>-202</sub>	0.703417 ± 9	0.512944 ± 4	5.97 ± 0.08
n.m.	n.m.	n.d.	0.775 ± 17	5.003 ± 109	5.711 <sup>+128</sup> <sub>-128</sub>	0.703561 ± 5	0.512895 ± 4	5.01 ± 0.08
n.m.	n.m.	n.d.	0.329 ± 20	2.347 ± 143	2.585 <sup>+169</sup> <sub>-169</sub>	0.703913 ± 5	0.512826 ± 5	3.67 ± 0.10
n.m.	n.m.	n.d.	n.m.	n.m.	n.d.	0.703489 ± 4	0.512903 ± 4	5.17 ± 0.08
0.433 ± 5	1.010 ± 13	n.d.	n.m.	n.m.	n.d.	n.m.	n.m.	n.d.
n.m.	n.m.	n.d.	0.426 ± 21	1.038 ± 51	n.d.	n.m.	n.m.	n.d.
n.m.	n.m.	n.d.	3.539 ± 166	1.013 ± 48	n.d.	n.m.	n.m.	n.d.
n.m.	n.m.	n.d.	3.641 ± 186	1.042 ± 53	n.d.	n.m.	n.m.	n.d.
n.m.	n.m.	n.d.	n.m.	n.m.	n.d.	n.m.	n.m.	n.d.

Ratios in parentheses represent activity ratios (the number of atoms times the decay constant,  $\lambda$ ). Decay constants used are as follows:  $\lambda_{226} = 4.33 \times 10^{-4} \text{ yr}^{-1}$ ,  $\lambda_{230} = 9.1577 \times 10^{-6} \text{ yr}^{-1}$ ,  $\lambda_{231} = 2.1158 \times 10^{-5} \text{ yr}^{-1}$ ,  $\lambda_{232} = 4.9475 \times 10^{-11} \text{ yr}^{-1}$ ,  $\lambda_{233} = 9.386925 \text{ yr}^{-1}$ ,  $\lambda_{234} = 2.8263 \times 10^{-6} \text{ yr}^{-1}$ ,  $\lambda_{238} = 1.5513 \times 10^{-10} \text{ yr}^{-1}$ . All uncertainties are  $2\sigma$  measurement errors. Spikes were prepared from pure metals (U and Th),  $^{228}\text{Ra}$  was milked from NIST 3159  $^{232}\text{Th}$  Standard, and  $^{233}\text{Pa}$  was produced by neutron irradiation of NIST 3159  $^{232}\text{Th}$  Standard. A secular equilibrium standard (Ryan or TML) was processed and measured with each batch of samples. An additional correction for interference of  $^{232}\text{Th}$  on  $^{229}\text{Th}$  was applied to TML-4. U standard NBL-112 was also measured during each analytical session yielding a mean  $\delta^{234}\text{U}$  value of  $-37.16 \pm 0.74\%$  ( $n = 9$ ) in agreement with published values of  $-37.1 \pm 1.2\%$  (Edwards et al., 1993) and  $-36.9 \pm 2.1\%$  (Cheng et al., 2000).  $(^{226}\text{Ra}/^{230}\text{Th})_i$  and  $(^{231}\text{Pa}/^{235}\text{U})_i$  ratios are initial values corrected back to the time of eruption using calibrated ages in sidereal years based on  $^{14}\text{C}$  ages (" $> \text{MMA}$ " = older than the Mt. Mazama ash horizon, approx. 7.65 ka). Samples 07-NC-01, 08-NCSW-01, 08-SM-01, and 08-SMCL-01 are corrected using new estimate for the age of the Nash Crater-Sand Mountain eruptive episode of 2.8-2.9 ka (Ruscitto, 2011). Sr standard NBS-987 and the La Jolla Nd standard were analyzed at the beginning and end of each analytical session, yielding average values ( $n = 8$ ) of  $0.71026 \pm 2$  and  $0.511830 \pm 6$  ( $2\sigma$ ) respectively.  $\epsilon_{\text{Nd}} = [((^{143}\text{Nd}/^{144}\text{Nd})_{\text{sample}} - (^{143}\text{Nd}/^{144}\text{Nd})_{\text{CHUR}}) / (^{143}\text{Nd}/^{144}\text{Nd})_{\text{CHUR}}] * 10,000$ , where  $(^{143}\text{Nd}/^{144}\text{Nd})_{\text{CHUR}} = 0.512638$ , relative to  $^{146}\text{Nd}/^{144}\text{Nd} = 0.7219$ . n.m. = not measured, n.d. = not determined.

correlation of  $^{143}\text{Nd}/^{144}\text{Nd}$  with Nd concentration, although the Nash Crater (filled squares) and Belknap (circles) groups display inverse correlations (Fig 4.6c). The Santiam group data, particularly  $^{87}\text{Sr}/^{86}\text{Sr}$ , confirm the presence of two distinct compositions within this group, with the Sand Mountain sub-group samples (open squares) having the lowest  $^{87}\text{Sr}/^{86}\text{Sr}$  ratios and highest Sr concentrations. Neither  $^{87}\text{Sr}/^{86}\text{Sr}$  nor  $^{143}\text{Nd}/^{144}\text{Nd}$  is correlated with ( $^{230}\text{Th}/^{238}\text{U}$ ) within the sample suite as a whole, although correlations are apparent within certain groups, especially the Nash Crater and Belknap groups (Fig. 4.6b & 4.6d).

All samples display  $^{230}\text{Th}$ -enrichment, up to a maximum of 35%, with the degree of  $^{230}\text{Th}$ -enrichment generally correlating with different groups (Fig. 4.6f). The Santiam group samples (squares) display the largest and most variable  $^{230}\text{Th}$ -enrichments (~ 20-35%), followed by the Belknap group samples (circles) (10-13%). Pre-Mazama group sample 08-WIC-01 also has significant  $^{230}\text{Th}$ -enrichment (17%). The remaining pre-Mazama, Yapoah, and Newberry group samples have the least  $^{230}\text{Th}$ -enrichment (< 10%).

Of the samples from the three groups (Santiam, Belknap, and Yapoah) young enough to have maintained  $^{226}\text{Ra}$ -enrichments since eruption, only one (07-FCA-01) is in secular equilibrium. The degree of  $^{226}\text{Ra}$ -enrichment varies by group, with the Santiam samples (squares) having the largest ( $^{226}\text{Ra}/^{230}\text{Th}$ )<sub>i</sub>, followed by the Belknap (circles) and Yapoah groups (triangles), which overlap. Within the Santiam group, a slight increase in ( $^{226}\text{Ra}/^{230}\text{Th}$ ) is observed with increasing ( $^{230}\text{Th}/^{238}\text{U}$ ) (Fig. 4.6g). The three Newberry group samples analyzed for ( $^{226}\text{Ra}/^{230}\text{Th}$ ) are within analytical error of secular equilibrium, but the age of the samples (~ 7 ka) is close to the age limit (~ 8 ka) beyond which any initial  $^{226}\text{Ra}$ -excesses present upon eruption will have decayed away. As a



result it is difficult to know whether the lack of measured  $^{226}\text{Ra}$ -enrichment reflects eruption of a ( $^{226}\text{Ra}/^{230}\text{Th}$ ) secular equilibrium magma or post-eruption decay of (likely small) initial  $^{226}\text{Ra}$ -excesses.

Plots of MgO vs. ( $^{230}\text{Th}/^{238}\text{U}$ ) and ( $^{226}\text{Ra}/^{230}\text{Th}$ )<sub>i</sub> do not display simple time-dependent differentiation trends (Fig. 4.7). With decreasing MgO, ( $^{230}\text{Th}/^{238}\text{U}$ ) decreases slightly in the Nash Crater sub-group samples (filled squares) but ( $^{226}\text{Ra}/^{230}\text{Th}$ )<sub>i</sub> is constant. In the Belknap group samples (circles) both ( $^{230}\text{Th}/^{238}\text{U}$ ) and ( $^{226}\text{Ra}/^{230}\text{Th}$ )<sub>i</sub> increase slightly. Newberry group samples display a possible time-dependent decrease in ( $^{230}\text{Th}/^{238}\text{U}$ ) with decreasing MgO (see Section 4.5.3.).

---

**Figure 4.6:** Isotopic data for central Oregon lavas, symbols as Figure 4.4. Panel (a): Sr vs.  $^{87}\text{Sr}/^{86}\text{Sr}$ . Panel (b):  $^{87}\text{Sr}/^{86}\text{Sr}$  vs. ( $^{230}\text{Th}/^{238}\text{U}$ ). Panel (c): Nd vs.  $\epsilon_{\text{Nd}}$ . Panel (d):  $\epsilon_{\text{Nd}}$  vs. ( $^{230}\text{Th}/^{238}\text{U}$ ). Maximum  $^{87}\text{Sr}/^{86}\text{Sr}$  and  $^{143}\text{Nd}/^{144}\text{Nd}$  error bar size is shown in panels (a) to (d). Panel (e):  $^{87}\text{Sr}/^{86}\text{Sr}$  vs.  $\epsilon_{\text{Nd}}$ . Also shown are fields for Juan de Fuca ridge MORB (field extends to  $^{87}\text{Sr}/^{86}\text{Sr} = 0.7023$  &  $\epsilon_{\text{Nd}} = 11.94$ ) and Cascade CAB lavas (from White et al., 1987 and Schmidt et al., 2008 respectively). Panel (f): ( $^{238}\text{U}/^{232}\text{Th}$ ) vs. ( $^{230}\text{Th}/^{232}\text{Th}$ ) ‘equiline’ diagram. Black line is the secular equilibrium ‘equiline’, and gray lines are 10, 20, 30, and 40%  $^{230}\text{Th}$ -excess lines as labeled. Mixing lines between primitive Nash Crater (large square) and Belknap (large circle) group samples and the calculated lower crustal components (Table 4.3) are shown with ticks at 10% increments. Estimated composition of the Nash Crater end member is: ( $^{230}\text{Th}/^{238}\text{U}$ ) = 1.145 and ( $^{238}\text{U}/^{232}\text{Th}$ ) = 1.429. Estimated composition of the Belknap end member is: ( $^{230}\text{Th}/^{238}\text{U}$ ) = 1.144 and ( $^{238}\text{U}/^{232}\text{Th}$ ) = 1.217. Panel (g): ( $^{230}\text{Th}/^{238}\text{U}$ ) vs. ( $^{226}\text{Ra}/^{230}\text{Th}$ )<sub>i</sub>. Large gray symbols are data for samples 07-NC-01 and 08-NCSW-01 corrected with old ages used in Mitchell and Asmerom (2011). Age of the Nash Crater-Sand Mountain eruptive episode has been revised recently to 2.8-2.9 ka (Ruscitto, 2011). Small gray symbols in panel (g) are measured (uncorrected) data, error bars are approximately symbol size. Mixing lines as in panel (f) with end member ( $^{226}\text{Ra}/^{230}\text{Th}$ ) = 1.41. Panel (h): ( $^{230}\text{Th}/^{238}\text{U}$ ) vs. ( $^{231}\text{Pa}/^{235}\text{U}$ )<sub>i</sub>. Gray band is the range in ( $^{231}\text{Pa}/^{235}\text{U}$ ) measured in Holocene Newberry obsidians (Chapter 5). Mixing lines as in panel (f), with Nash Crater end member having ( $^{231}\text{Pa}/^{235}\text{U}$ ) = 10.4 and Belknap end member having ( $^{231}\text{Pa}/^{235}\text{U}$ ) = 7.7. Green mixing lines are between the most primitive Newberry sample (08-SPBF-01) and ( $^{231}\text{Pa}/^{235}\text{U}$ ) secular equilibrium assimilants, with ( $^{230}\text{Th}/^{238}\text{U}$ ) = 1.000 (solid line) and ( $^{230}\text{Th}/^{238}\text{U}$ ) = 1.055 (dashed line). Ticks marks are 10% increments.

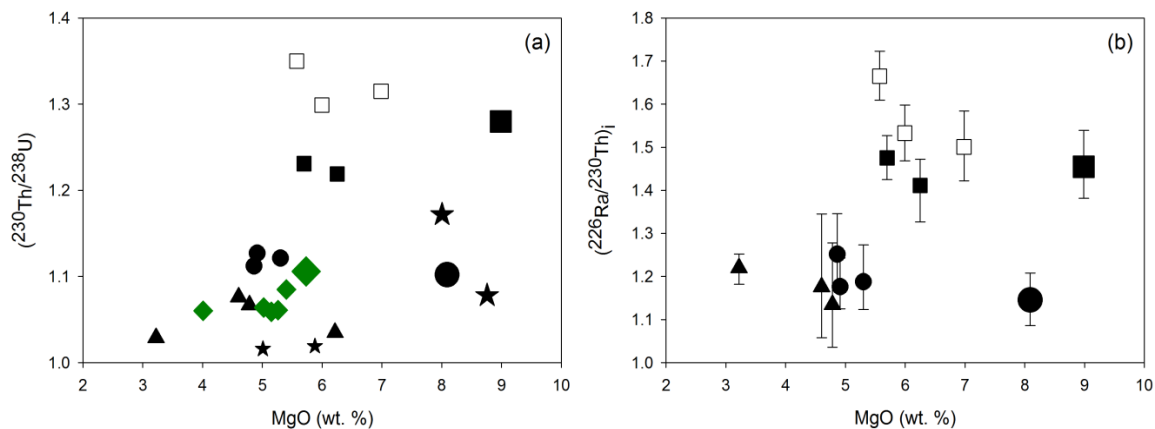


**Figure 4.7:** MgO vs.  $(^{230}\text{Th}/^{238}\text{U})$  and  $(^{226}\text{Ra}/^{230}\text{Th})_i$  plots for central Oregon lavas, symbols as Figure 4.4. Samples define both decreasing and increasing trends with increasing differentiation.

All of the subset of 19 samples analyzed for  $(^{231}\text{Pa}/^{235}\text{U})$  display  $^{231}\text{Pa}$ -enrichment, with maximum  $(^{231}\text{Pa}/^{235}\text{U})_i$  ratios of  $\sim 9$  (Fig. 4.6h). A broad positive correlation exists between  $(^{230}\text{Th}/^{238}\text{U})$  and  $(^{231}\text{Pa}/^{235}\text{U})$ , although the Santiam group samples define a separate inverse trend at higher  $(^{230}\text{Th}/^{238}\text{U})$  (Fig. 4.6h).

## 4.5. Discussion

### 4.5.1. Identification of Primitive Magmas and Parental Compositions

The aims of this chapter are twofold: (i) to identify the process(es) by which primary mantle-derived melts are modified by passage through, and residence in, the overlying arc crust; and (ii) to identify the effects of this modification on mantle-derived U-series isotope ratios. By definition, these aims first require identification of those primitive lavas that have compositions closest to primary, mantle-derived melts. [N.B. A primary magma is one that remains unmodified from the composition of the mantle-melt. Few, if any, erupted compositions anywhere meet this criterion, hence the use of the more

subjective term primitive magma for one that is least modified from the primary composition. A parental composition is one (ideally, but not necessarily, primitive) that could have given rise to a genetically related suite of more evolved lavas.]

The criteria used for identifying primitive compositions are  $\text{SiO}_2 < 55 \text{ wt.}\%$ ,  $\text{MgO} > 6 \text{ wt.}\%$ ,  $\text{Mg\# (molar MgO/(MgO+FeO)*100)} > 55$ ,  $\text{Ni} > 100 \text{ ppm}$ , and  $\text{Cr} > 200 \text{ ppm}$  (Leeman et al., 2005). Four samples representing three separate groups (08-LL-01, Nash Crater; 08-WBB-01, Belknap; and 08-CYC-01/08-WIC-01, pre-Mazama) meet all these criteria. These four samples, along with the most primitive Newberry sample (08-SPBF-01), are plotted in Figures 4.2 to 4.7 with larger symbols. Sand Mountain group sample 08-SM-01, and Yapoah group sample 07-FCA-01, meet all the criteria for being primitive compositions except for Cr concentration.

The coherent major and trace element trends within the Nash Crater, Belknap, and Newberry groups noted above suggest that each group is a genetically related suite, and the most primitive sample in each group (08-LL-01-Nash Crater-large square, 08-WBB-01-Belknap-large circle, and 08-SPBF-01-Newberry-large diamond) is interpreted as a possible parental composition for the group in the following discussion. Furthermore, the similarity of the Nash Crater and Belknap group trends suggests a common process, or combination of processes, is controlling their evolution; however, the distinct trends among the Newberry group samples indicate that a different process, or set of processes, is operating there.

The pre-Mazama samples are geographically distributed and grouped solely on the basis of age, thus no genetic relationship would be expected within this group. The

Yapoah group samples were all erupted from vents on the north flank of North Sister but do not appear related to one another in any simple fashion.

#### *4.5.2. Previous Studies*

As noted earlier, previous work in the central Oregon Cascades has focused largely on the eruptive products of the arc-defining stratovolcanoes, such as Mt. Jefferson (Conrey et al., 2001), North Sister (Mercer and Johnston, 2008; Schmidt and Grunder, 2009; 2011), South Sister (Brophy and Dreher, 2000; Fierstein et al., 2011), and Mt. Bachelor (Gardner, 1994). Detailed studies of the smaller, but far more numerous, mafic volcanoes are scarcer, but deserve a brief review here.

Schick (1994) studied in detail the compositional variations in Collier Cone lavas (Yapoah group) and concluded that the variability was the result of a combination of fractional crystallization, wallrock assimilation, and magma mixing at shallow depths. Ruscitto (2011) investigated the compositional variability of Collier Cone, as well as Four-in-One 'cone' (both Yapoah group), from the perspective of olivine-hosted melt inclusion compositions. Fractional crystallization of olivine + spinel  $\pm$  clinopyroxene  $\pm$  plagioclase was interpreted to be the main cause of melt inclusion compositional variability, with bulk rock compositions trending toward those of silicic xenoliths, which have compositions similar to the nearby Pleistocene Obsidian Cliffs rhyolite. The Collier (and potentially Yapoah crater) lavas likely originated from a parental magma similar to the low-K basaltic andesite erupted from North Sister (Schmidt and Grunder, 2009). Sample 07-FCA-01 may represent a near-primitive composition that is parental to the more evolved basaltic andesite and andesite that comprises most of the erupted unit, but not the Yapoah group as a whole.

Ruscitto (2011) also studied melt inclusions from Sand Mountain tephra deposits and concluded that interaction with silicic crust was not an important process there, and that melt inclusion compositional variability was dominated by fractional crystallization of olivine. In light of the discussion to follow it is important to note that this study only addressed shallow crustal processes, and conceded that bulk rock compositions, which are similar to melt inclusion compositions, likely indicate the operation of additional processes.

Clark (1983) interpreted the Le Conte crater flow (08-LC-01, pre-Mazama group) to represent mixing between basalt and rhyodacite in a stratified magma chamber, which is consistent with its broad similarity to the Newberry samples. The remaining pre-Mazama group sample (08-EC-01) was erupted on the north flank of Mt. Bachelor at the very southern end of the study area (Fig. 4.1). The Mt. Bachelor chain is distinct from, and older than, the mafic lavas considered here (Scott and Gardner, 1992; Gardner, 1994).

#### *4.5.3. Origin of the Newberry Group Trend*

The Newberry group samples define linear major element arrays that are distinct from those of the other groups, suggesting that a different process, or set of processes, is controlling their evolution. This idea is supported by the trace element data (Fig. 4.4), where the Newberry samples do not define arrays like those displayed by the Sand Mountain and Belknap group samples (Section 4.4.1.).

On the basis of the linear arrays in Figures 4.3 and 4.4 that trend toward the average composition of Holocene obsidians, the most likely explanation for these trends is simple assimilation of a felsic upper crustal component that is compositionally similar to the

obsidians erupted within Newberry caldera. Mixing lines between the most primitive Newberry sample (08-SPBF-01) and the average Holocene obsidian composition in these figures support this interpretation, with most samples requiring 5 to 15% assimilation and the most evolved sample (08-MBF-02) ~ 30%. In greater detail, with increasing differentiation the sample suite falls progressively further below the mixing curves for  $\text{Fe}_2\text{O}_3$ ,  $\text{TiO}_2$ , and  $\text{MnO}$ , with the exception of the most evolved sample (08-MBF-02), which is displaced above the curves (Fig. 4.3). This is interpreted to reflect fractional crystallization of an Fe-Ti oxide accompanying assimilation of the felsic component, and Fe-Ti oxide accumulation in the most evolved sample. Trace element 'spidergram' and REE profile mixing plots confirm the interpretation that differentiation dominantly is driven by assimilation of felsic crust, and imply that the intra-group trends observed in Figure 4.5, such as the increase in the magnitude of negative Nb-Ta and Eu anomalies, simply reflect the composition of the assimilant (Fig. 4.8 and 4.9). The degree of assimilation required to match the trace element data in these plots agrees with the major element arrays, 5% for the samples (08-FRF-01 and 08-LCFF-01) least evolved from the primitive composition, 15% for the next most evolved samples (08-SF-01 and 08-LBF-01), and 30% in the most evolved sample (08-MBF-02).

The minor variation in  $^{87}\text{Sr}/^{86}\text{Sr}$  and  $^{143}\text{Nd}/^{144}\text{Nd}$  within the Newberry group is consistent with simple assimilation of a component with only a slightly more radiogenic composition, which also is consistent with the Holocene obsidians (Chapter 5). This interpretation contrasts with that of Linneman (1990), who proposed the requirement of a second crustal assimilant with a highly radiogenic Sr isotope composition.

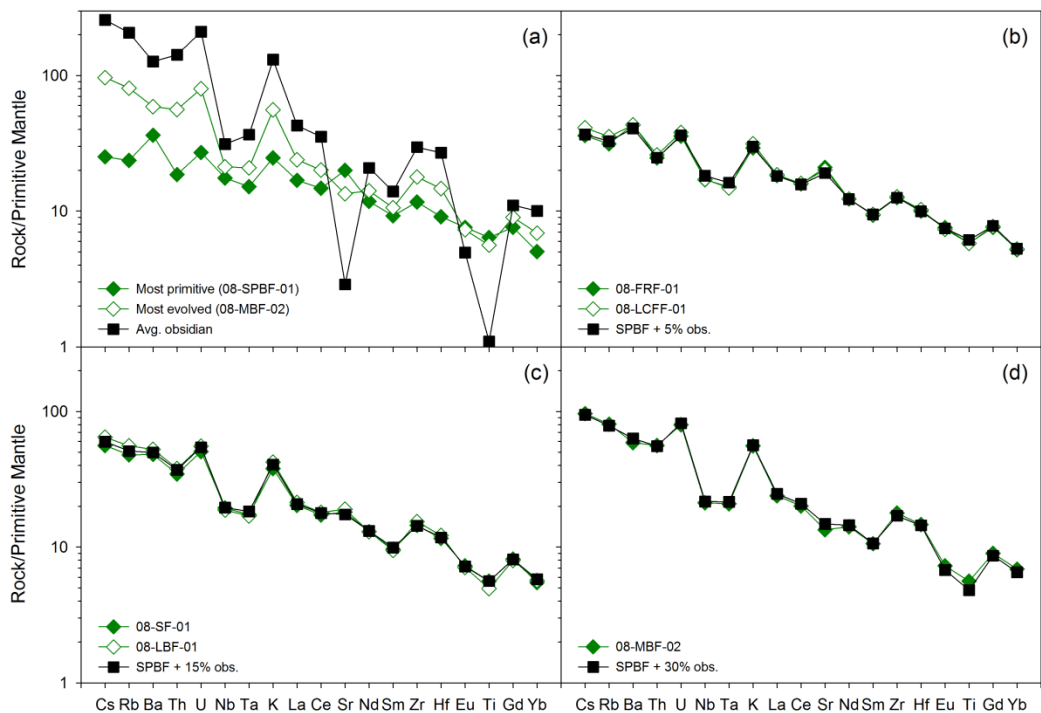


**Figure 4.8:** Trace element ‘spidergram’ mixing plots for Newberry group samples. Panel (a): Composition of the most primitive Newberry sample (08-SPBF-01), most evolved Newberry sample (08-MBF-02), and the average Holocene obsidian composition. Panel (b): Newberry samples 08-FRF-01 and 08-LCFF-01, and the composition produced by 5% mixing between the most primitive Newberry sample and the average obsidian composition. Panel (c): Newberry group samples 08-SF-01 and 08-LBF-01, and 15% mixing composition. Panel (d): Most evolved Newberry group sample (08-MBF-02) and 30% mixing composition.

While the interpretation presented above is consistent with that of Linneman (1990), except as noted, he was unable to differentiate between bulk assimilation of felsic crust and mixing with a felsic melt. The new U-series data potentially allow discrimination between these two possibilities, as well as the prospect of constraining the timescale over which this assimilation/mixing occurred.

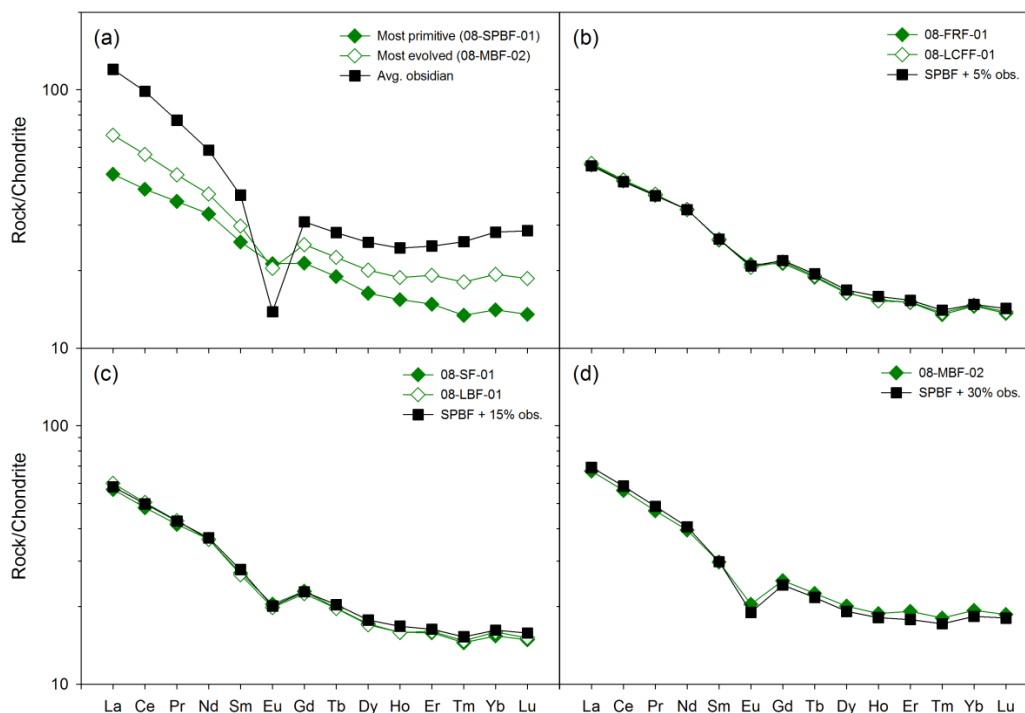


**Figure 4.9:** REE mixing plots for Newberry group samples. All panels and symbols as Figure 4.8.

Thus far the average composition of two Holocene obsidians erupted within Newberry caldera has been assumed to be representative of shallow crustal rocks beneath the volcanic edifice. However, in light of the upcoming discussion of time-sensitive U-series data, it is important to note that these obsidians were erupted *after* the basaltic andesites in question. Compositionally similar obsidians, however, were erupted in the caldera earlier in the Holocene (including in a pulse contemporaneous with the mafic northwest rift zone eruption) and around the Pleistocene-Holocene boundary (Linneman, 1990; MacLeod et al., 1995). These Holocene obsidians have been interpreted as isolated, small-volume melts of the plutonic equivalents of even earlier Pleistocene rhyolites (Linneman, 1990; Chapter 5). Thus a variety of plutonic felsic rocks, the un-erupted

counterparts to the Pleistocene and Holocene units, with broadly similar bulk chemistry but variable U-series activity ratios, could reasonably be assumed to be present beneath Newberry volcano.

The samples define a broadly vertical, or slightly positively sloped, trend on a U-Th ‘equiline’ diagram (Fig. 4.6f), which is consistent with bulk assimilation of a component that is in, or close to, secular equilibrium. Consideration of the ( $^{231}\text{Pa}/^{235}\text{U}$ ) data allows for further interpretation. The best-fit to the combined ( $^{230}\text{Th}/^{238}\text{U}$ ) and ( $^{231}\text{Pa}/^{235}\text{U}$ ) data is mixing with a component with 5 to 6%  $^{230}\text{Th}$ -excess that is in ( $^{231}\text{Pa}/^{235}\text{U}$ ) secular equilibrium (dashed green line in Fig. 4.6h). The degree of assimilation of this component required to match the more evolved samples (~ 40-80%), far exceeds that implied from the major and trace element data (max. ~ 30%; Figs. 4.3, 4.4, 4.8, and 4.9). Assimilation of a lower  $^{230}\text{Th}$ -excess component, coupled with aging, could potentially explain the data, but the required timescale is 10s to 100s of thousands of years and a decay curve is inconsistent with the data trend (cf. Huang et al., 2008). A more compelling alternative is derivation of the four most evolved (lowest ( $^{230}\text{Th}/^{238}\text{U}$ ) and ( $^{231}\text{Pa}/^{235}\text{U}$ )) samples from a separate parental magma, which had a similar elemental composition but lower initial ( $^{231}\text{Pa}/^{235}\text{U}$ ). This is consistent with age constraints and closer consideration of the linear ( $^{238}\text{U}/^{232}\text{Th}$ ) vs. ( $^{230}\text{Th}/^{232}\text{Th}$ ) array parallel to the ‘equiline’ defined by these four samples (Fig. 4.6f).

In light of the relatively large measured  $^{231}\text{Pa}$ -excesses in the late Holocene Newberry obsidians (Chapter 5), and the apparent requirement that the mafic lavas assimilated a felsic crustal component in ( $^{231}\text{Pa}/^{235}\text{U}$ ) secular equilibrium but with slight  $^{230}\text{Th}$ -excess,

the most likely scenario is bulk assimilation of a young, upper crustal felsic intrusive rock that has decayed into ( $^{231}\text{Pa}/^{235}\text{U}$ ), but not ( $^{230}\text{Th}/^{238}\text{U}$ ), secular equilibrium.

#### *4.5.4. Origin of the Nash Crater and Belknap Group Trends*

It is apparent from the trends in Figures 4.3 and 4.4 that a different process, or set of processes, is controlling the compositional evolution of the Nash Crater and Belknap group samples. This is further illustrated in Figure 4.10, which shows a number of ‘H vs. H/M’ plots. On the abscissa in these plots is an H (hypermagmatophile or highly incompatible) element, and on the ordinate is the ratio of H to an M (magmatophile or moderately incompatible) element (Allegre and Minster, 1978; Schiano et al., 2010). On such a diagram a suite of lavas related by fractional crystallization will plot along a nearly horizontal line, while a suite of lavas generated by two component mixing will define a hyperbolic curve (Allegre and Minster, 1978; Schiano et al., 2010).

The very restricted range in both H element concentration (e.g., Th) and H/M ratio (e.g., Th/Nd) in the Nash Crater and Belknap groups (black squares and red circles), and the observation that H/M ratios typically decrease within the group as H element concentrations increase, suggests that fractional crystallization, or assimilation-fractional crystallization, of any normal mineral assemblage is not controlling the evolution of these samples. The data do not define a mixing trend with a felsic component similar to that invoked at Newberry either. Therefore, assimilation of a component with very different characteristics to the felsic Newberry assimilant is assumed to be the dominant process. The major element arrays in Figure 4.3 trend toward a component with higher  $\text{Al}_2\text{O}_3$ ,  $\text{Fe}_2\text{O}_3$ , CaO,  $\text{TiO}_2$ ,  $\text{P}_2\text{O}_5$ , and MnO than the felsic Newberry assimilant, but lower  $\text{K}_2\text{O}$  and similar  $\text{Na}_2\text{O}$ , suggesting a relatively mafic assimilant. This is supported by the trace

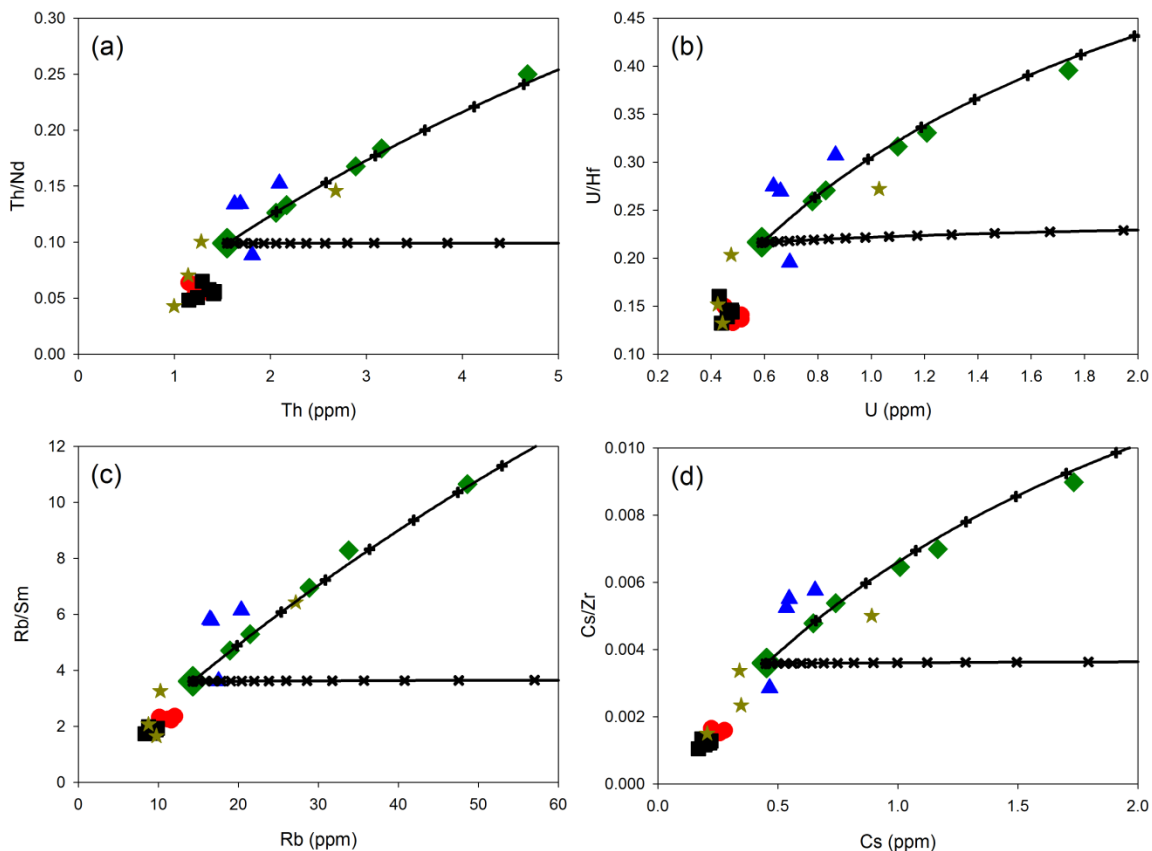


**Figure 4.10:** H vs. H/M plots for central Oregon lavas, symbols as Figure 4.5. Lines with pluses are mixing curves between the most primitive Newberry sample (08-SPBF-01) and the average composition of Holocene Newberry obsidians. Horizontal lines with crosses are fractional crystallization curves for an olivine and plagioclase-dominated assemblage (D values from Claeson and Meurer, 2004). Tick marks on both curves are 5% increments. Newberry mixing arrays indicate that the most primitive sample could have been modified from a truly primitive magma by ~ 5% assimilation of felsic upper crust, although the arrays in Figure 4.3 are suggestive of mixing with a lower crustal component prior to this.

element arrays in Figure 4.4 and the ‘spidergram’ patterns in Figure 4.5, which suggest that the Three Sisters assimilant is enriched in trace elements relative to the primitive samples, but less so than the trace element-rich felsic Newberry assimilant. The notable exception to this is the Sr-rich nature of the Three Sisters assimilant. The composition of Sr-rich andesite erupted at Mt. Jefferson (~ 35-40 km north of Belknap/Sand Mountain),

interpreted as a melt of MORB-like mafic lower crust (Conrey et al., 2001), is a closer fit to this inferred mafic composition than either of the estimates of silicic upper crust in the region ( large black stars in Figs. 4.3 and 4.4).

The Sr and Nd data require the involvement of a component that is isotopically similar to the primitive lavas, with very similar  $^{87}\text{Sr}/^{86}\text{Sr}$  and slightly lower  $^{143}\text{Nd}/^{144}\text{Nd}$  (Fig. 4.6a-e). The  $^{87}\text{Sr}/^{86}\text{Sr}$  data also require slightly different assimilants mixing with the primitive Nash Crater (filled squares) and Belknap (circles) magmas, as do the U-series data (see below). More significantly, the arrays in the U-series data do not trend toward secular equilibrium values, implying that the assimilant is out of secular equilibrium for all three parent-daughter pairs ( $(^{230}\text{Th}/^{238}\text{U})$ ,  $(^{226}\text{Ra}/^{230}\text{Th})$ , and  $(^{231}\text{Pa}/^{235}\text{U})$ ) (Fig. 4.6f-h). The  $(^{226}\text{Ra}/^{230}\text{Th})$  data in particular require that the disequilibrium in this component was created very shortly before assimilation by the primitive magmas, and that subsequent ascent and eruption was essentially instantaneous with respect to the half-life of  $^{226}\text{Ra}$  (1599 yrs).

These observations can be used to estimate the composition of the assimilant that appears to be controlling differentiation of these magmas. Several observations are critical in this regard: (i) the Nash Crater (black squares) and Belknap (red circles) samples define the same mixing arrays on trace element ratio vs.  $(^{230}\text{Th}/^{238}\text{U})$  plots (Fig. 4.11); (ii) in each of these plots the inferred degree of mixing is similar within each group; and (iii) in each of these plots the denominator in the trace element ratio (i.e. Y, Yb, Nb, Ta) is one of the elements that displays limited variation within these groups as a function of MgO (see Section 4.4.1.). This allows the absolute concentration of these four elements in the mixing end member to be estimated with a high degree of confidence, and

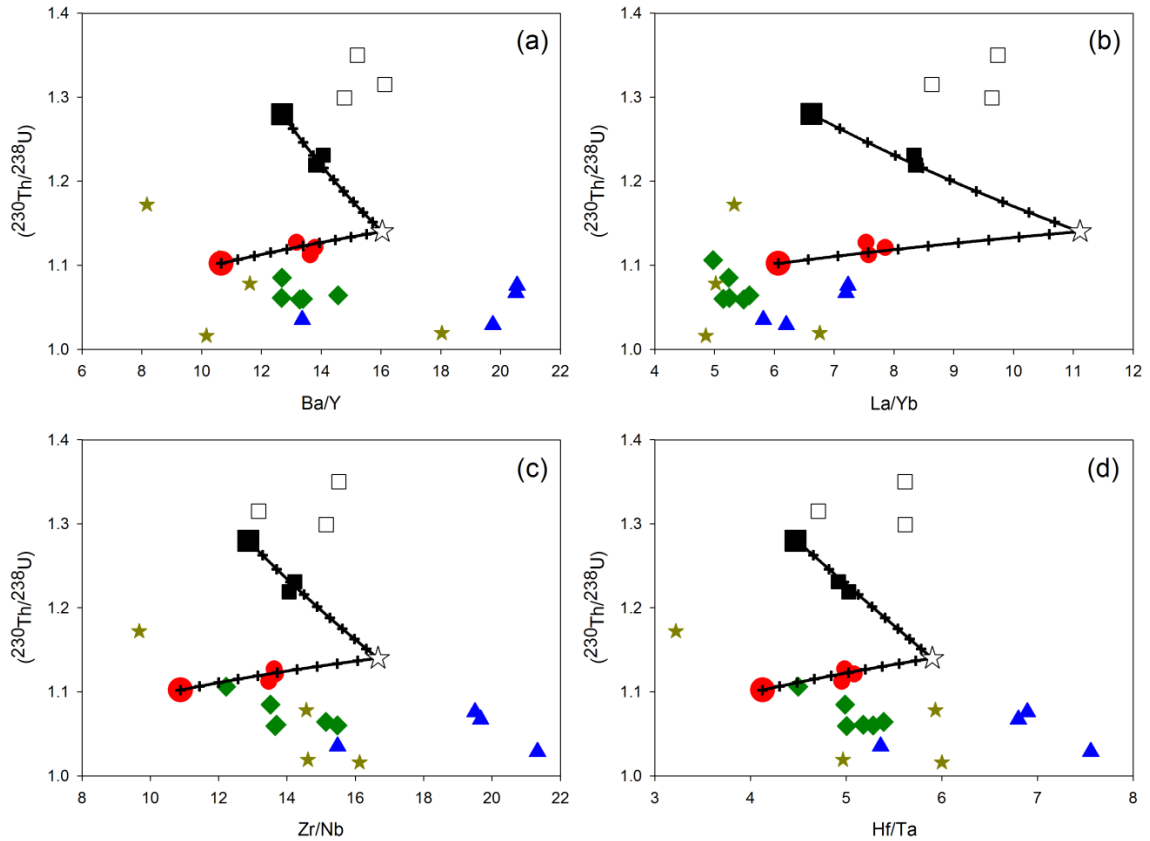


**Figure 4.11:** Plots of various trace element ratios vs.  $(^{230}\text{Th}/^{238}\text{U})$  for central Oregon lavas, symbols as Figure 4.5. Lines are mixing curves (tick marks are 10% increments) between the most primitive Nash Crater (08-LL-01, large square) and Belknap (08-WBB-01, large circle) lavas and a hypothetical crustal component (indicated with a white star, see main text for discussion) inferred from trends in Figure 4.4. The inferred/calculated composition (ppm) of the component is: Y = 24, Zr = 200, Nb = 12, Ba = 385, La = 25, Yb = 2.25, Hf = 4.425, Ta = 0.75.

by extension, on the basis of the mixing arrays in Figure 4.11, allows the concentration of the more variable numerator element in the mixing end member to be estimated. The mixing curves in these plots consistently return the same assimilant composition; 0.5 ppm U and  $(^{230}\text{Th}/^{238}\text{U}) = 1.14$ , lending support to the validity of this approach.

On the basis of this approach, the concentration in the mixing end member of the eight trace elements plotted in Figure 4.11 can be estimated. However, the extent of mixing

required by the data is similar in each instance, allowing the complete elemental composition of this end member to be estimated by solving a simple mass balance equation. The more evolved samples in the Belknap group (red circles) consistently can be explained by mixing between ~ 40 to 45% of this end member and the most primitive Belknap composition, and the more evolved samples in the Nash Crater group (black squares) consistently can be explained by mixing between ~ 35 to 40% of this end member and the most primitive Nash Crater composition (Fig. 4.11). From these extents of mixing we can calculate elemental abundances in the mixing end member for each of the four evolved samples in these two groups, assuming that mixing is the sole process involved (see below). The compositions of the four end members calculated in this fashion, and the average for the two groups, are shown in Table 4.3.

Certain elements (e.g., Cr, Co, Ni) have negative concentrations in some or all of the calculated end members, indicating that processes other than simple mixing are occurring. Considering that these three elements are compatible in olivine and spinel, and that olivine + spinel fractionation has been invoked as the dominant control on melt inclusion compositional variability in Sand Mountain tephras (Ruscitto, 2011), this is the most likely additional process in operation. Addition of 5 wt.% olivine (Fo<sub>83</sub>) to the calculated end member compositions raises the MgO contents to ~ 3 wt.%, similar to the Mt. Jefferson Sr-rich andesite (Conrey et al., 2001), with minimal impact on most of the other major or trace elements.

The calculated end members have basaltic andesite to andesitic compositions that are broadly similar to the composition of Sr-rich andesite from Mt. Jefferson (Conrey et al., 2001), as noted earlier. The calculated trace element and REE compositions of the

**Table 4.3**

Estimated composition of crustal melt components beneath the Three Sisters.

	LL-LN	LL-NCSW	WBB-BCB	WBB-LB	Assim. 1	Assim. 2	Sr And.
SiO <sub>2</sub>	57.39	57.16	56.88	55.90	57.27	56.39	59.61
Al <sub>2</sub> O <sub>3</sub>	19.25	19.54	19.71	19.42	19.39	19.57	18.37
Fe <sub>2</sub> O <sub>3T</sub>	7.98	7.54	6.74	7.10	7.76	6.92	5.58
MgO	1.17	0.77	0.15	1.89	0.97	1.02	3.36
CaO	6.79	7.31	9.22	9.00	7.05	9.11	6.69
Na <sub>2</sub> O	4.77	4.97	4.44	4.09	4.87	4.27	4.44
K <sub>2</sub> O	0.89	0.95	1.08	0.95	0.92	1.01	0.89
TiO <sub>2</sub>	1.10	1.15	1.18	1.08	1.12	1.13	0.80
P <sub>2</sub> O <sub>5</sub>	0.54	0.51	0.49	0.44	0.52	0.46	0.18
MnO	0.12	0.11	0.11	0.12	0.11	0.12	0.09
Sc	20.89	9.16	30.63	29.53	15.02	30.08	14.7
V	131.8	132.2	155.4	160.2	132.0	157.8	117.5
Cr	(-306.36)	(-282.25)	(-259.28)	(-172.33)	(-294.3)	(-215.8)	36.5
Co	(-64.80)	(-52.64)	27.30	4.51	(-58.72)	15.90	n.m.
Ni	46.87	(-53.45)	(-166.15)	(-113.82)	(-3.29)	(-140.0)	32.3
Cu	49.66	41.06	65.92	65.06	45.36	65.49	59.0
Zn	100.79	90.88	64.16	73.90	95.83	69.03	55.5
Rb	11.14	11.10	13.81	12.53	11.12	13.17	9.50
Sr	858.8	931.0	712.4	765.2	894.9	738.8	991.0
Y	25.16	23.97	26.69	23.82	24.57	25.26	12.0
Zr	252.6	229.1	215.3	214.0	240.9	214.7	129.3
Nb	16.28	14.57	12.03	12.57	15.42	12.30	5.45
Cs	0.280	0.282	0.301	0.301	0.281	0.301	0.157
Ba	394.9	383.9	439.3	417.1	389.4	428.2	261.8
La	24.49	23.96	25.06	22.59	24.22	23.82	13.62
Ce	58.05	57.49	59.38	51.92	57.77	55.65	28.65
Pr	7.31	7.35	7.69	6.65	7.33	7.17	3.76
Nd	31.30	31.61	31.94	27.95	31.45	29.94	15.69
Sm	6.18	6.30	6.51	5.76	6.24	6.14	3.03
Eu	1.77	1.75	1.79	1.56	1.76	1.67	1.08
Gd	5.50	5.60	6.35	5.74	5.55	6.05	2.62
Tb	0.868	0.847	0.966	0.834	0.858	0.900	0.370
Dy	4.41	4.61	5.19	4.43	4.51	4.81	2.19
Ho	0.811	0.837	0.984	0.845	0.824	0.915	0.415
Er	2.36	2.48	2.91	2.48	2.42	2.70	1.21
Tm	0.310	0.335	0.388	0.326	0.322	0.357	0.180
Yb	2.11	2.22	2.66	2.24	2.16	2.45	1.11
Lu	0.308	0.321	0.407	0.332	0.315	0.369	0.155
Hf	4.48	4.24	4.87	4.40	4.36	4.64	2.72
Ta	0.769	0.780	0.789	0.698	0.774	0.744	0.365
Th	0.89	1.17	1.53	1.30	1.03	1.41	1.80
U	0.456	0.505	0.605	0.521	0.480	0.563	0.607

First four columns are crustal components calculated on the basis of individual samples, assuming 07-LN-01 and 08-NCSW-01 are generated from 08-LL-01 by 35% and 40% assimilation respectively, and 07-BCB-02 and 07-LB-01 are generated from 08-WBB-01 by 40% and 45% assimilation respectively. 'Assim. 1' is the average composition of the two Nash Crater group sample assimilants, and 'Assim. 2' is the average composition of the two Belknap group sample assimilants (see main text for details). Negative values in parentheses likely reflect olivine fractionation. 'Sr And.' is the average composition of Sr-rich andesite from Mt. Jefferson (Conrey et al., 2001).

average Nash Crater and Belknap end members, along with the average Mt. Jefferson Sr-rich andesite composition, are plotted in Figure 4.12. The REE patterns are broadly similar, but the Mt. Jefferson andesite has significantly lower concentrations of all elements. The ‘spidergram’ patterns share some common features (similar Rb, U, K, Sr concentrations) but the Mt. Jefferson andesite again has lower concentrations for many elements, including a Nb-Ta anomaly that is absent from the calculated end members (Fig. 4.12). The large positive Sr anomaly in the Mt. Jefferson andesite, which is less prominent in the Three Sisters end members, as well as the small positive Eu anomaly in the Mt. Jefferson andesite, which is a small negative anomaly in the Three Sisters (esp. Belknap) end members, suggest either that plagioclase, in addition to olivine + spinel, was a shallow fractionating phase in the Three Sisters region and/or that plagioclase was a greater constituent of the original source lithology beneath Mt. Jefferson. This comparison between the Mt. Jefferson andesite and the calculated components suggests that the Nash Crater/Belknap end members could be derived from smaller extents of partial melting of a MORB-like lithology similar to that invoked at Mt. Jefferson, and/or similar extents of melting of a more trace element-enriched, arc-like lithology.

Annen et al. (2006) recently proposed that the generation of intermediate and silicic magmas in the lower crust is a consequence of repeated intrusion and incomplete crystallization of hydrous basalt, coupled with crustal melting, and subsequent mixing of these two H<sub>2</sub>O-rich components. Re-Os isotope data for North Sister basaltic andesites suggest interaction with young mafic crust via a similar process (Schmidt et al., 2013). The differences between the Mt. Jefferson andesite and the calculated end members beneath the Three Sisters could, therefore, result also from different extents of mixing

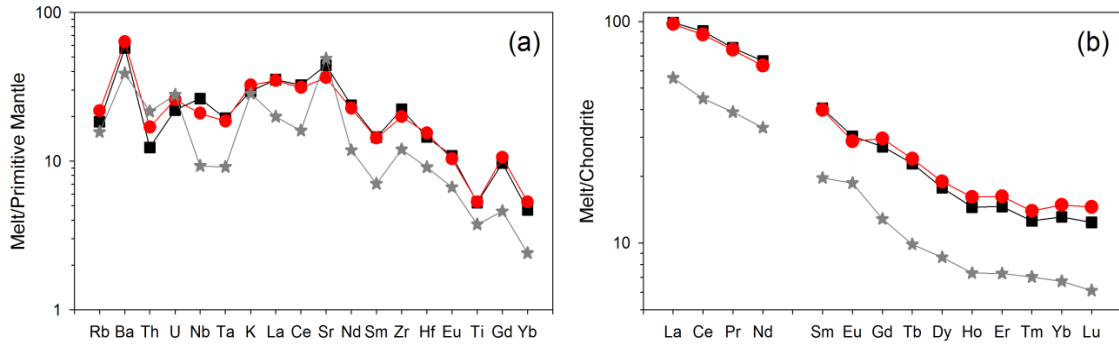


**Figure 4.12:** Trace element ‘spidergram’ and REE profiles for the average Nash Crater and Belknap crustal melt end members (‘Assim. 1’ (black squares) and ‘Assim. 2’ (red circles) respectively from Table 4.3). Shown for comparison is the average composition of Sr-rich andesite from Mt. Jefferson (gray stars) (Conrey et al., 2001).

between different liquids in the lower crust (i.e. the erupted lavas could be three component mixtures involving a primitive magma, a crustal melt, and a residual liquid from fractional crystallization). The existence of such a deep crustal hot zone seems especially likely beneath the Three Sisters as a result of intra-arc rifting and abundant mafic magmatism in the region (Hildreth, 2007).

As noted earlier the  $^{87}\text{Sr}/^{86}\text{Sr}$  data require that the primitive Nash Crater and Belknap group magmas mixed with slightly different components. This is true also of the U-series data (Fig. 4.6). Mixing lines (not shown) between the primitive lavas and a single end member reproduce the linear U-Th-Pa arrays, but the required extents of mixing are significantly different from those inferred from the trace element data (Fig. 4.10). The best-fit mixing lines, which also are consistent with the trace element data, require that the end member mixing with the primitive Nash Crater magma has higher ( $^{238}\text{U}/^{232}\text{Th}$ ) and ( $^{231}\text{Pa}/^{235}\text{U}$ ) than the end member mixing with the Belknap magma (Fig. 4.6f & 4.6h). Large error bars on the ( $^{226}\text{Ra}/^{230}\text{Th}$ ) data, a consequence of age uncertainties, preclude

drawing any definitive conclusions about the ( $^{226}\text{Ra}/^{230}\text{Th}$ ) of the end members, but a single end member with ( $^{226}\text{Ra}/^{230}\text{Th}$ )  $\approx 1.4$  is consistent with the data. Slight differences in the degree of mixing between crustal melts and residual liquids, or heterogeneities in the crustal material experiencing melting, in a crustal hot zone could generate these U-series variations while keeping bulk chemistry broadly similar (Annen et al., 2006).

If the end members are indeed lower crustal melts, or mixtures of lower crustal melts and residual liquids from fractional crystallization, then the large  $^{230}\text{Th}$ ,  $^{226}\text{Ra}$ , and  $^{231}\text{Pa}$ -excesses inferred for these end members require residual/fractionating phases capable of retaining U over Th, and especially U over Pa, as well as Th over Ra. Ra is a highly incompatible element in nearly all phases (Blundy and Wood, 2003) and thus provides few constraints. However, the generation of a liquid with modest ( $^{230}\text{Th}/^{238}\text{U}$ ), yet simultaneously large ( $^{231}\text{Pa}/^{235}\text{U}$ ), should place tight constraints on the phases present. Small amounts of accessory phases such as apatite and/or rutile could plausibly generate a liquid with the requisite characteristics. Such accessory phases commonly have large partition coefficients for U and Th (Klemme et al., 2005; Prowatke and Klemme, 2006) and have been invoked to explain  $^{230}\text{Th}$  and  $^{231}\text{Pa}$ -excesses in felsic magmas, interpreted as crustal melts, in this part of the arc (Chapter 5). Apatite is also a significant host for Sr (Prowatke and Klemme, 2006), which may be another explanation for the apparent relative lack of Sr-enrichment in comparison to the Mt. Jefferson andesite. Finally, if the crustal rocks that are undergoing partial melting are young, they may have yet to decay to secular equilibrium prior to the next episode of intrusion and crystallization/melting.

#### 4.5.5. *Implications for Arc Magmatism and Cascades U-Series Data*

The preceding discussion suggests that assimilation/mixing is the dominant process via which magmas beneath both the Three Sisters and Newberry volcanoes are differentiating. However, there appears to be a significant difference in the depth at which this differentiation is occurring, with the assimilant being a lower crustal melt and/or residual liquid, and presumably mixing occurring in the lower crust, beneath the Three Sisters. In contrast, bulk assimilation of an upper crustal lithology at shallow depths beneath Newberry is the best explanation. This may reflect a hotter lower crust along the axis of the arc beneath the Three Sisters in response to a greater flux of mantle-derived melt, as well as differences in shallow crustal structure. The vents for the Santiam group samples in particular are close to the intra-arc graben-defining Horse Creek fault zone, which is a major structure with several 100s of meters, and possibly as much as a kilometer, of offset (Sherrod et al., 2004). The presence of large faults could allow rapid ascent and eruption of magma from the lower crust, with only minor fractionation of olivine  $\pm$  plagioclase at shallow depths (c.f. Ruscitto, 2011). In contrast, the large edifice that is Newberry volcano may slow the passage of magmas through the upper crust, allowing more extensive interaction with that felsic crust.

The lavas erupted in the Three Sisters region and at Newberry cover a remarkably large range in U-series isotope activity ratios, with ( $^{230}\text{Th}/^{238}\text{U}$ ) ranging from 1.016 to 1.350 and ( $^{231}\text{Pa}/^{235}\text{U}$ ) ranging from 1.178 to 9.143. The range in the primitive lavas, however, is considerably smaller, only 1.078 to 1.280 (1.315 incl. 08-SM-01) in ( $^{230}\text{Th}/^{238}\text{U}$ ) and 5.016 to 8.058 in ( $^{231}\text{Pa}/^{235}\text{U}$ ), indicating the effects of crustal interaction. The effect of assimilating a  $^{230}\text{Th}$ -enriched crustal component, as suggested

here and at Mt. Adams (Jicha et al., 2009b), is likely to be relatively minor in the central and northern Cascades, where  $^{230}\text{Th}$ -enriched mantle melts appear to be the norm as a result of the unusual arc thermal regime (Jicha et al., 2009b; Mitchell and Asmerom, 2011). However, the composition of more typical  $^{238}\text{U}$ -enriched arc magmas, either in the southern Cascades or elsewhere, would be more strongly influenced by a  $^{230}\text{Th}$ -enriched crustal component. Eruptive products from single volcanoes with ( $^{230}\text{Th}/^{238}\text{U}$ ) data falling on both sides of the equiline (e.g., Ramos, 2000; Garrison et al., 2006) cannot reflect bulk assimilation of secular equilibrium crust by, or simple aging of, initially homogeneous magmas, and are unlikely to reflect source variations (Davidson et al., 2005). Variable assimilation of  $^{230}\text{Th}$ -enriched assimilants by initially  $^{238}\text{U}$ -enriched melts, however, could generate such variability (e.g., Garrison et al., 2006; Hora et al. 2009), although recognition of the potential prevalence of this process could be hampered by the elemental and isotopic similarity of crustal, subducted sedimentary, and adakitic components (Davidson et al., 2005; Zellmer et al., 2012). This highlights the critical importance for studying slab and mantle processes of identifying cryptic crustal interaction, and thus truly primitive compositions, through detailed studies of individual volcanoes (Davidson et al., 2005).

Finally, the interpretation presented here, of interaction of mantle-derived magmas with  $\text{H}_2\text{O}$ -rich crustal melts/residual liquids in the lower crust, implies an additional process that could generate  $\text{H}_2\text{O}$ -rich magmas, and therefore melt inclusions (c.f. Plank et al., 2013). This has significant implications for the origin of inferred primary magma  $\text{H}_2\text{O}$  contents,  $\text{H}_2\text{O}$  mass balance at subduction zones (Plank et al., 2013), and interpretations

of slab contributions and slab surface temperatures in the warm Cascadia subduction zone (Ruscitto et al., 2010; Cooper et al., 2012).

#### **4.6. Conclusions**

Different processes are controlling the compositional evolution of mafic lavas erupted from the Three Sisters region of the Oregon Cascades and from the rear-arc Newberry volcano. In the Three Sisters region, along the axis of the volcanic arc, interaction with a mafic lower crustal component is the main driver of compositional variability among lavas erupted from the Sand Mountain Volcanic Field and nearby Nash Crater vents, as well as from the Belknap shield volcano. In contrast, at the rear-arc Newberry volcano compositional evolution is driven by assimilation of a felsic component in the upper crust. The  $^{87}\text{Sr}/^{86}\text{Sr}$  and  $^{143}\text{Nd}/^{144}\text{Nd}$  ratios of both upper and lower crustal components are almost indistinguishable from those of the more primitive lavas, and the mafic nature of the crustal assimilant in the Three Sisters region in particular makes the trace element and isotopic signature of crustal interaction especially cryptic.

Interaction of primitive magmas with crustal rocks at Newberry volcano drives U-series activity ratios closer to secular equilibrium. Beneath the Three Sisters, however, interaction of primitive magmas with a non-equilibrium crustal component leads to both decreases *and* increases in U-series activity ratios during differentiation. As a result, the highest measured activity ratios in a suite of lavas cannot a priori be assumed to represent the most primitive composition. Furthermore, the elemental and isotopic similarity of potential crustal assimilants and primitive magmas in volcanic arcs means that such a process could be more widespread than commonly thought, with implications for interpretations of arc U-series data, particularly at continental margins. Detailed

investigations of suites of rocks from individual volcanoes, where the effects of differentiation can be recognized and accounted for, are the best means of identifying true variations in primary magma compositions and, by extension, source processes. Finally, the interaction of primitive magmas with water-rich lower crustal liquids is a process that must be considered when extrapolating primary arc magma water contents from melt inclusion data.

### **Acknowledgements**

Victor Polyak provided assistance with the lab work and sample analysis. Funding was provided by the National Science Foundation (EAR-0948703 to YA).

## References

- Allegre, C. J. & Minster, J. F. (1978). Quantitative models of trace element behavior in magmatic processes. *Earth and Planetary Science Letters* **38**, 1-25.
- Allegre, C. J. & Condomines, M. (1982). Basalt genesis and mantle structure studied through Th-isotopic geochemistry. *Nature* **299**, 21-24.
- Annen, C., Blundy, J. D. & Sparks, R. S. J. (2006). The genesis of intermediate and silicic magmas in deep crustal hot zones. *Journal of Petrology* **47**, 505-539.
- Asmerom, Y. (1999). Th-U fractionation and mantle structure. *Earth and Planetary Science Letters* **166**, 163-175.
- Asmerom, Y. & Edwards, R. L. (1995). U-series isotope evidence for the origin of continental basalts. *Earth and Planetary Science Letters* **134**, 1-7.
- Asmerom, Y., DuFrane, S. A., Mukasa, S. B., Cheng, H. & Edwards, R. L. (2005). Time scale of magma differentiation in arcs from protactinium-radium isotopic data. *Geology* **33**, 633-636.
- Atwater, T. (1970). Implications of plate tectonics for the Cenozoic evolution of western North America. *Geological Society of America Bulletin* **81**, 3513-3536.
- Avanzinelli, R., Prytulak, J., Skora, S., Heumann, A., Koetsier, G. & Elliott, T. (2012). Combined  $^{238}\text{U}$ - $^{230}\text{Th}$  and  $^{235}\text{U}$ - $^{231}\text{Pa}$  constraints on the transport of slab-derived material beneath the Mariana Islands. *Geochimica et Cosmochimica Acta* **92**, 308-328.
- Blundy, J. & Wood, B. (2003). Mineral-melt partitioning of uranium, thorium and their daughters. *Reviews in Mineralogy and Geochemistry* **52**, 59-123.
- Borg, L. E., Brandon, A. D., Clyne, M. A. & Walker, R. J. (2000). Re-Os isotopic systematics of primitive lavas from the Lassen region of the Cascade arc, California. *Earth and Planetary Science Letters* **177**, 301-317.
- Bourdon, B., Worner, G. & Zindler, A. (2000). U-series evidence for crustal involvement and magma residence times in the petrogenesis of Parinacota volcano, Chile. *Contributions to Mineralogy and Petrology* **139**, 458-469.

- Bourdon, B., Turner, S. & Dosseto, A. (2003). Dehydration and partial melting in subduction zones: Constraints from U-series disequilibria. *Journal of Geophysical Research* **108**, doi:10.1029/2002JB001839.
- Brophy, J. G. & Dreher, S. T. (2000). The origin of composition gaps at South Sister volcano, central Oregon: implications for fractional crystallization processes beneath active calc-alkaline volcanoes. *Journal of Volcanology and Geothermal Research* **102**, 287-307.
- Chabaux, F., Othman, D. B. & Birck, J. L. (1994). A new Ra-Ba chromatographic separation and its application to Ra mass-spectrometric measurement in volcanic rocks. *Chemical Geology* **114**, 191-197.
- Chabaux, F., Hemond, C. & Allegre, C. J. (1999).  $^{238}\text{U}$ - $^{230}\text{Th}$ - $^{226}\text{Ra}$  disequilibria in the Lesser Antilles arc: Implications for mantle metasomatism. *Chemical Geology* **153**, 171-185.
- Cheng, H., Edwards, R. L., Hoff, J., Gallup, C. D., Richards, D. A. & Asmerom, Y. (2000). The half lives of uranium-234 and thorium-230. *Chemical Geology* **169**, 17-33.
- Claeson, D. & Meurer, W. (2004). Fractional crystallization of hydrous basaltic “arc-type” magmas and the formation of amphibole-bearing gabbroic cumulates. *Contributions to Mineralogy and Petrology* **147**, 288-304.
- Clark, J. G. (1983). Geology and petrology of South Sister Volcano, High Cascade Range, Oregon. *Ph.D. Dissertation*, University of Oregon.
- Condomines, M. & Sigmarsson, O. (1993). Why are so many arc magmas close to  $^{238}\text{U}$ - $^{230}\text{Th}$  radioactive equilibrium? *Geochimica et Cosmochimica Acta* **57**, 4491-4497.
- Conrey, R. M., Hooper, P. R., Larson, P. B., Chesley, J. & Ruiz, J. (2001). Trace element and isotopic evidence for two types of crustal melting beneath a High Cascade volcanic center, Mt. Jefferson, Oregon. *Contributions to Mineralogy and Petrology* **141**, 710-732.
- Conrey, R. M., Taylor, E. M., Donnelly-Nolan, J. J. & Sherrod, D. (2002). North-Central Oregon Cascades: exploring petrologic and tectonic intimacy in a propagating intra-

- arc rift. In: Moore, G. (Ed.) Field Guide to Geologic Processes in Cascadia. *Oregon Department of Geology and Mineral Industries Special Paper* **36**, 47-90.
- Cooper, K. M. (2001). Time scales of magma generation, differentiation, and storage: Constraints from uranium-238-thorium-230-radium-226 disequilibria. *Ph.D. Dissertation*, University of California, Los Angeles.
- Cooper, L. B., Ruscitto, D. M., Plank, T., Wallace, P. J., Syracuse, E. M. & Manning, C. E. (2012). Global variations in H<sub>2</sub>O/Ce: 1. Slab surface temperatures beneath volcanic arcs. *Geochemistry Geophysics Geosystems* **13**, doi:10.1029/2011gc003902.
- Davidson, J. P., Hora, J. M., Garrison, J. M. & Dungan, M. A. (2005). Crustal forensics in arc magmas. *Journal of Volcanology and Geothermal Research* **140**, 157-170.
- Dosseto, A., Bourdon, B., Joron, J. L. & Dupre, B. (2003). U-Th-Pa-Ra study of the Kamchatka arc: new constraints on the genesis of arc lavas. *Geochimica et Cosmochimica Acta* **67**, 2857-2877.
- DuFrane, S. A., Asmerom, Y., Mukasa, S. B., Morris, J. D. & Dreyer, B. M. (2006). Subduction and melting processes inferred from U-Series, Sr-Nd-Pb isotope, and trace element data, Bicol and Bataan arcs, Philippines. *Geochimica et Cosmochimica Acta* **70**, 3401-3420.
- Eagar, K. C., Fouch, M. J., James, D. E. & Carlson, R. W. (2011). Crustal structure beneath the High Lava Plains of eastern Oregon and surrounding regions from receiver function analysis. *Journal of Geophysical Research* **116**, B02313, doi:10.1029/2010JB007795.
- Edwards, R. L., Beck, J. W., Burr, G. S., Donahue, D. J., Chapell, J. M. A., Bloom, A. L., Druffel, E. R. M. & Taylor, F. W. (1993). A large drop in atmospheric <sup>14</sup>C/<sup>12</sup>C and reduced melting in the Younger Dryas documented with <sup>230</sup>Th ages of corals. *Science* **260**, 962-968.
- Elkins Tanton, L. T., Grove, T. L. & Donnelly-Nolan, J. (2001) Hot, shallow mantle melting under the Cascades volcanic arc. *Geology* **29**, 631-634.
- Elliott, T. (2003). Tracers of the slab. In: Eiler, J. (Ed.), Inside the Subduction Factory. *American Geophysical Union Geophysical Monograph* **138**, 23-45.

- Elliott, T., Plank, T., Zindler, A., White, W. & Bourdon, B. (1997). Element transport from slab to volcanic front at the Mariana arc. *Journal of Geophysical Research* **102**, 14,991-15,019.
- Feineman, M. D. & DePaolo, D. J. (2003). Steady-state  $^{226}\text{Ra}/^{230}\text{Th}$  disequilibrium in mantle minerals: Implications for melt transport rates in island arcs. *Earth and Planetary Science Letters* **215**, 339-355.
- Fierstein, J., Hildreth, W. & Calvert, A. T. (2011). Eruptive history of South Sister, Oregon Cascades. *Journal of Volcanology and Geothermal Research* **207**, 145-179.
- Gardner, C. A. (1994). Temporal, spatial and petrologic variations of lava flows from the Mount Bachelor volcanic chain, central Oregon High Cascades. *U.S. Geological Survey Open-File Report* **94-261**.
- Garrison, J., Davidson, J., Reid, M. & Turner, S. (2006). Source versus differentiation controls on U-series disequilibria: Insights from Cotopaxi volcano, Ecuador. *Earth and Planetary Science Letters* **244**, 548-565.
- Gill, J. B. (1981). *Orogenic Andesites and Plate Tectonics*. Springer Verlag, Berlin.
- Gill, J. B. & Williams, R. W. (1990). Th isotope and U-series studies of subduction-related volcanic rocks. *Geochimica et Cosmochimica Acta* **54**, 1427-1442.
- Handley, H. K., Turner, S. P., Smith, I. E. M., Stewart, R. B. & Cronin, S. J. (2008). Rapid timescales of differentiation and evidence for crustal contamination at intra-oceanic arcs: Geochemical and U-Th-Ra-Sr-Nd isotopic constraints from Lopevi volcano, Vanuatu, SW Pacific. *Earth and Planetary Science Letters* **273**, 184-194.
- Hart, G. L., Johnson, C. M., Hildreth, W. & Shirey, S. B. (2003). New osmium isotope evidence for intracrustal recycling of crustal domains with discrete ages. *Geology* **31**, 427-430.
- Hawkesworth, C. J., Gallagher, K., Hergt, J. M. & McDermott, F. (1993). Mantle and slab contributions in arc magmas. *Annual Review of Earth and Planetary Sciences* **21**, 175-204.

- Hawkesworth, C. J., Turner, S. P., McDermott, F., Peate, D. W. & van Calsteren, P. (1997). U-Th isotopes in arc magmas: Implications for element transfer from the subducted crust. *Science* **276**, 551-555.
- Hawkesworth, C. J., Blake, S., Evans, P., Hughes, R., Macdonald, R., Thomas, L. E., Turner, S. P. & Zellmer, G. (2000). Time scales of crystal fractionation in magma chambers - Integrating physical, isotopic and geochemical perspectives. *Journal of Petrology* **41**, 991-1006.
- Hildreth, W. (2007). Quaternary Magmatism in the Cascades - Geologic Perspectives. *U.S. Geological Survey Professional Paper* **1744**.
- Hildreth, W., Fierstein, J. & Calvert, A. T. (2012). Geologic map of Three Sisters volcanic cluster, Cascade Range, Oregon. *U.S. Geological Survey Scientific Investigations Map* **3186**, scale 1:24,000.
- Hora, J. M., Singer, B. S., Worner, G., Beard, B. L., Jicha, B. R. & Johnson, C. M. (2009). Shallow and deep crustal control on differentiation of calc-alkaline and tholeiitic magma. *Earth and Planetary Science Letters* **285**, 75-86.
- Huang, F. & Lundstrom, C. C. (2007).  $^{231}\text{Pa}$  excesses in arc volcanic rocks: Constraint on melting rates at convergent margins. *Geology* **35**, 1007-1010.
- Huang, F., Gao, L. & Lundstrom, C. C. (2008). The effect of assimilation, fractional crystallization, and ageing on U-series disequilibria in subduction zone lavas. *Geochimica et Cosmochimica Acta* **72**, 4136-4145.
- Huang, F., Lundstrom, C. C., Sigurdsson, H. & Zhang, Z. (2011). U-series disequilibria in Kick'em Jenny submarine volcano lavas: A new view of time-scales of magmatism in convergent margins. *Geochimica et Cosmochimica Acta* **75**, 195-212.
- Jicha, B. R., Singer, B. S., Beard, B. L., Johnson, C. M., Moreno-Roa, H. & Naranjo, J. A. (2007). Rapid magma ascent and generation of  $^{230}\text{Th}$  excesses in the lower crust at Puyehue-Cordon Caulle, Southern Volcanic Zone, Chile. *Earth and Planetary Science Letters* **255**, 229-242.
- Jicha, B., Hart, G., Johnson, C., Hildreth, W., Beard, B., Shirey, S. & Valley, J. (2009a). Isotopic and trace element constraints on the petrogenesis of lavas from the Mount

- Adams volcanic field, Washington. *Contributions to Mineralogy and Petrology* **157**, 189-207.
- Jicha, B. R., Johnson, C. M., Hildreth, W., Beard, B. L., Hart, G. L., Shirey, S. B. & Singer, B. S. (2009b). Discriminating assimilants and decoupling deep- vs. shallow-level crystal records at Mount Adams using  $^{238}\text{U}$ - $^{230}\text{Th}$  disequilibria and Os isotopes. *Earth and Planetary Science Letters* **277**, 38-49.
- Jones, C. H., Unruh, J. R. & Sonder, L. J. (1996). The role of gravitational potential energy in active deformation in the southwestern United States. *Nature* **381**, 37-41.
- Jordan, B. T., Grunder, A. L., Duncan, R. A. & Deino, A. L. (2004). Geochronology of age-progressive volcanism of the Oregon High Lava Plains: Implications for the plume interpretation of Yellowstone. *Journal of Geophysical Research* **109**, doi:10.1029/2003JB002776.
- Klemme, S., Prowatke, S., Hametner, K. & Gunther, D. (2005). Partitioning of trace elements between rutile and silicate melts: Implications for subduction zones. *Geochimica et Cosmochimica Acta* **69**, 2361-2371.
- Lawrence, R. D. (1976). Strike-slip faulting terminates the Basin and Range province in Oregon. *Geological Society of America Bulletin* **87**, 846-850.
- Le Bas, M. J., LeMaitre, R. W., Streckeisen, A. L. & Zanettin, B. (1986). A chemical classification of volcanic rocks based on the total alkali-silica diagram. *Journal of Petrology* **27**, 745-750.
- Leeman, W. P., Lewis, J. F., Evarts, R. C., Conrey, R. M. & Streck, M. J. (2005). Petrologic constraints on the thermal structure of the Cascades arc. *Journal of Volcanology and Geothermal Research* **140**, 67-105.
- Linneman, S. R. (1990). The petrologic evolution of the Holocene magmatic system of Newberry Volcano, central Oregon. *Ph.D. Dissertation*, University of Wyoming.
- Luedke, R. G. & Smith, R. L. (1982). Map showing distribution, composition, and age of Late Cenozoic volcanic centers in Oregon and Washington. *U.S. Geological Survey Miscellaneous Investigations Series I-1091 D*, scale 1:500,000.

- MacLeod, N. S., Walker, G. W. & McKee, E. H. (1975). Geothermal significance of eastward increase in age of Upper Cenozoic rhyolitic domes in southeastern Oregon. *U.S. Geological Survey Open-File Report* **75-348**.
- MacLeod, N. S., Sherrod, D. R., Chitwood, L. A. & Jensen, R. A. (1995). Geologic map of Newberry volcano, Deschutes, Klamath, and Lake Counties, Oregon. *U.S. Geological Survey Miscellaneous Investigations Series* **I-2455**, scale 1:62,500.
- McCaffrey, R., Qamar, A. I., King, R. W., Wells, R., Khazaradze, G., Williams, C. A., Stevens, C. W., Vollick, J. J. & Zwick, P. C. (2007). Fault locking, block rotation and crustal deformation in the Pacific Northwest. *Geophysical Journal International* **169**, 1315-1340.
- McDermott, F. & Hawkesworth, C. (1991). Th, Pb, and Sr isotope variations in young island arc volcanics and oceanic sediments. *Earth and Planetary Science Letters* **104**, 1-15.
- McKay, D., Donnelly-Nolan, J. M., Jensen, R. A. & Champion, D. E. (2009). The post-Mazama northwest rift zone eruption at Newberry Volcano, Oregon. In: O'Connor, J. E., Dorsey, R. J. & Madin, I. P. (Eds.) *Volcanoes to Vineyards: Geologic Field Trips through the Dynamic Landscape of the Pacific Northwest. Geological Society of America Field Guide* **15**, 91-110.
- Mercer, C. N. & Johnston, A. D. (2008). Experimental studies of the *P-T-H<sub>2</sub>O* near-liquidus phase relations of basaltic andesite from North Sister Volcano, High Oregon Cascades: Constraints on lower-crustal mineral assemblages. *Contributions To Mineralogy and Petrology* **155**, 571-592.
- Mitchell, E. C. & Asmerom, Y. (2011). U-series isotope systematics of mafic magmas from central Oregon: Implications for fluid involvement and melting processes in the Cascade arc. *Earth and Planetary Science Letters* **312**, 378-389.
- Newman, S., Macdougall, J. D. & Finkel, R. C. (1984). <sup>230</sup>Th-<sup>238</sup>U disequilibrium in island arcs: evidence from the Aleutians and the Marianas. *Nature* **308**, 268-270.

- Palme, H. & Jones, A. (2003). Solar system abundances of the elements. *In: Davis, A. M. (Ed.), Meteorites, Comets, and Planets. Treatise on Geochemistry 1*, Elsevier-Pergamon, 41-61.
- Palme, H. & O'Neill, H. S. C. (2003). Cosmochemical estimates of mantle composition. *In: Carlson, R. W. (Ed.), The Mantle and Core. Treatise on Geochemistry 2*, Elsevier-Pergamon, 1-38.
- Peacock, S. M. (2003). Thermal structure and metamorphic evolution of subducting slabs. *In: Eiler, J. (Ed.), Inside the Subduction Factory. American Geophysical Union Geophysical Monograph 138*, 7-22.
- Pickett, D. A. & Murrell, M. T. (1997). Observations of  $^{231}\text{Pa}/^{235}\text{U}$  disequilibrium in volcanic rocks. *Earth and Planetary Science Letters 148*, 259-271.
- Plank, T., Kelley, K. A., Zimmer, M. M., Hauri, E. H. & Wallace, P. J. (2013). Why do mafic arc magmas contain ~ 4 wt% water on average? *Earth and Planetary Science Letters 364*, 168-179.
- Price, R. C., George, R., Gamble, J. A., Turner, S., Smith, I. E. M., Cook, C., Hobden, B. & Dosseto, A. (2007). U-Th-Ra fractionation during crustal-level andesite formation at Ruapehu volcano, New Zealand. *Chemical Geology 244*, 437-451.
- Prowatke, S. & Klemme, S. (2006). Trace element partitioning between apatite and silicate melts. *Geochimica et Cosmochimica Acta 70*, 4513-4527.
- Ramos, F. C. (2000). Processes and mantle sources generating basaltic volcanism: Insights from Th isotopes. *Ph.D. Dissertation*, University of California, Los Angeles.
- Reagan, M. K., Morris, J. D., Herrstrom, E. A. & Murrell, M. T. (1994). Uranium series and beryllium isotope evidence for an extended history of subduction modification of the mantle below Nicaragua. *Geochimica et Cosmochimica Acta 58*, 4199-4212.
- Reubi, O., Bourdon, B., Dungan, M. A., Koornneef, J. M., Selles, D., Langmuir, C. H. & Aciego, S. (2011). Assimilation of the plutonic roots of the Andean arc controls variations in U-series disequilibria at Volcan Llaima, Chile. *Earth and Planetary Science Letters 303*, 37-47.

- Ruscitto, D. (2011). Magmatic volatile contents and explosive cinder cone eruptions in the High Cascades: Recent volcanism in central Oregon and northern California. *Ph.D. Dissertation*, University of Oregon.
- Ruscitto, D. M., Wallace, P. J., Johnson, E. R., Kent, A. J. R. & Bindeman, I. N. (2010). Volatile contents of mafic magmas from cinder cones in the Central Oregon High Cascades: Implications for magma formation and mantle conditions in a hot arc. *Earth and Planetary Science Letters* **298**, 153-161.
- Saal, A. E. & Van Orman, J. A. (2004). The  $^{226}\text{Ra}$  enrichment in oceanic basalts: Evidence for melt-cumulate diffusive interaction processes within the oceanic lithosphere. *Geochemistry Geophysics Geosystems* **5**, doi:10.1029/2003GC000620.
- Schiano, P., Monzier, M., Eissen, J. P., Martin, H. & Koga, K. (2010). Simple mixing as the major control of the evolution of volcanic suites in the Ecuadorian Andes. *Contributions to Mineralogy and Petrology* **160**, 297-312.
- Schick, J. D. (1994). Origin of compositional variability of the lavas at Collier Cone, High Cascades, Oregon. *M.S. Thesis*, University of Oregon.
- Schmidt, M. E. & Grunder, A. L. (2009). The evolution of North Sister: A volcano shaped by extension and ice in the central Oregon Cascade Arc. *Geological Society of America Bulletin* **121**, 643-662.
- Schmidt, M. E. & Grunder, A. L. (2011). Deep mafic roots to arc volcanoes: Mafic recharge and differentiation of basaltic andesite at North Sister volcano, Oregon Cascades. *Journal of Petrology* **52**, 603-641.
- Schmidt, M. E., Grunder, A. L. & Rowe, M. C. (2008). Segmentation of the Cascade Arc as indicated by Sr and Nd isotopic variation among diverse primitive basalts. *Earth and Planetary Science Letters* **266**, 166-181.
- Schmidt, M. E., Grunder, A. L., Rowe, M. C. & Chesley, J. T. (2013). Re and Os isotopes of the central Oregon Cascades and along the arc indicate variable homogenization and mafic growth in the deep crust. *Geochimica et Cosmochimica Acta* **109**, 345-364.

- Scott, W. E. & Gardner, C. A. (1992). Geologic map of the Mount Bachelor volcanic chain and surrounding area, Cascade Range, Oregon. *U.S. Geological Survey Geologic Miscellaneous Investigations Series I-1967*, scale 1:50,000.
- Sherrod, D. R. & Smith, J. G. (1990). Quaternary extrusion rates of the Cascade Range, northwestern United States and southern British Columbia. *Journal of Geophysical Research* **95**, 19,465-19,474.
- Sherrod, D. R., Taylor, E. M., Ferns, M. L., Scott, W. E., Conrey, R. M. & Smith, G. A. (2004). Geologic map of the Bend 30- x 60-minute quadrangle, central Oregon. *U.S. Geological Survey Geologic Investigations Series I-2683*, scale 1:100,000.
- Sigmarsson, O., Chmeleff, J., Morris, J. & Lopez-Escobar, L. (2002). Origin of  $^{226}\text{Ra}$ - $^{230}\text{Th}$  disequilibria in arc lavas from southern Chile and implications for magma transfer time. *Earth and Planetary Science Letters* **196**, 189-196.
- Stanley, W. D., Mooney, W. D. & Fuis, G. S. (1990). Deep crustal structure of the Cascade Range and surrounding regions from seismic refraction and magnetotelluric data. *Journal of Geophysical Research* **95**, 19,419-19,438.
- Thomas, R. B., Hirschmann, M. M., Cheng, H., Reagan, M. K. & Edwards, R. L. (2002). ( $^{231}\text{Pa}/^{235}\text{U}$ )-( $^{230}\text{Th}/^{238}\text{U}$ ) of young mafic volcanic rocks from Nicaragua and Costa Rica and the influence of flux melting on U-series systematics of arc lavas. *Geochimica et Cosmochimica Acta* **66**, 4287-4309.
- Turner, S. & Hawkesworth, C. (1997). Constraints on flux rates and mantle dynamics beneath island arcs from Tonga-Kermadec lava geochemistry. *Nature* **389**, 568-573.
- Turner, S., Hawkesworth, C., van Calsteren, P., Heath, E., Macdonald, R. & Black, S. (1996). U-series isotopes and destructive plate margin magma genesis in the Lesser Antilles. *Earth and Planetary Science Letters* **142**, 191-207.
- Turner, S., Bourdon, B., Hawkesworth, C. & Evans, P. (2000).  $^{226}\text{Ra}$ - $^{230}\text{Th}$  evidence for multiple dehydration events, rapid melt ascent and the time scales of differentiation beneath the Tonga-Kermadec island arc. *Earth and Planetary Science Letters* **179**, 581-593.

- Turner, S., Evans, P. & Hawkesworth, C. (2001). Ultrafast source-to-surface movement of melt at island arcs from  $^{226}\text{Ra}$ - $^{230}\text{Th}$  systematics. *Science* **292**, 1363-1366.
- Turner, S., Bourdon, B. & Gill, J. (2003). Insights into magma genesis at convergent margins from U-series isotopes. *Reviews in Mineralogy and Geochemistry* **52**, 255-315.
- Turner, S., Regelous, M., Hawkesworth, C. & Rostami, K. (2006). Partial melting processes above subducting plates: Constraints from  $^{231}\text{Pa}$ - $^{235}\text{U}$  disequilibria. *Geochimica et Cosmochimica Acta* **70**, 480-503.
- Turner, S., Sims, K. W. W., Reagan, M. & Cook, C. (2007). A  $^{210}\text{Pb}$ - $^{226}\text{Ra}$ - $^{230}\text{Th}$ - $^{238}\text{U}$  study of Klyuchevskoy and Bezymianny volcanoes Kamchatka. *Geochimica et Cosmochimica Acta* **71**, 4771-4785.
- van Keken, P. E., Kiefer, B. & Peacock, S. M. (2002). High-resolution models of subduction zones: Implications for mineral dehydration reactions and the transport of water into the deep mantle. *Geochemistry Geophysics Geosystems* **3**, doi:10.1029/2001GC000256.
- Wells, R. E., Weaver, C. S. & Blakely, R. J. (1998). Fore-arc migration in Cascadia and its neotectonic significance. *Geology* **26**, 759-762.
- White, W. M., Hofmann, A. W. & Puchelt, H. (1987). Isotope geochemistry of Pacific mid-ocean ridge basalt. *Journal of Geophysical Research* **92**, 4881-4893.
- Wilson, D. S. (2002). The Juan de Fuca plate and slab - isochron structure and Cenozoic plate motions. *U.S. Geological Survey Open-File Report* **02-328**, 9-12.
- Yokoyama, T., Kuritani, T., Kobayashi, K. & Nakamura, E. (2006). Geochemical evolution of a shallow magma plumbing system during the last 500 years, Miyakejima volcano, Japan: Constraints from  $^{238}\text{U}$ - $^{230}\text{Th}$ - $^{226}\text{Ra}$  systematics. *Geochimica et Cosmochimica Acta* **70**, 2885-2901.
- Zellmer, G. F., Iizuka, Y., Miyoshi, M., Tamura, Y. & Tatsumi, Y. (2012). Lower crustal  $\text{H}_2\text{O}$  controls on the formation of adakitic melts. *Geology* **40**, 487-490.

## **Appendix A4**

This appendix contains:

Appendix A4.1. Silicate U-Th-Ra-Sr-Nd Chemistry Procedure

Table A4.1 - U-Th-Ra-Sr-Nd column separation procedure.

Table A4.2 - Pa column separation procedure.

#### **A4.1. Silicate U-Th-Ra-Sr-Nd Chemistry Procedure**

##### Sample Dissolution:

1. Weigh sample (typically ~ 0.25 g) into a Teflon bomb containing 10 drops 15N HNO<sub>3</sub> and wet powder to prevent dispersal.
2. Add enough concentrated HF (~ 2 mL) to just cover the bottom of the bomb and swirl gently to disaggregate powder.
3. Seal bomb securely and place into pre-heated oven at 125°C for 24 to 48 hours.

##### Spike-Sample Equilibration:

4. Remove bomb from oven and let cool.
5. Weigh ~ 1 g mixed <sup>228</sup>Ra-<sup>229</sup>Th-<sup>233</sup>U-<sup>236</sup>U spike to a clean 30 mL beaker.
6. Transfer contents of bomb to the spiked beaker and rinse inside of bomb with 7N HNO<sub>3</sub> if necessary to ensure complete sample removal.
7. Add 10 drops perchloric acid to sample beaker and dry down hard on hot plate - make sure no fumes or droplets on the walls of the beaker remain.
8. Add 10 to 20 drops 15N HNO<sub>3</sub> and dry hard again.
9. Repeat until sample is a uniform dark brown color.
10. Add ~ 2 mL 6N HCl and disaggregate sample.
11. Dry slowly (hot plate setting 1).
12. Add 10 mL 2N HCl, 0.5 mL boric acid (~ 20 drops), and disaggregate.
13. Flux overnight with cap loosely on beaker.

##### Co-Precipitation:

14. Check that sample has fully dissolved (solution should be yellow).

15. Transfer solution to large (50 mL) centrifuge tube and clean 30 mL beaker with 18 M $\Omega$  DI.
16. Carefully adjust solution to pH 7 by drop-wise addition of Na<sub>4</sub>OH solution: orange iron hydroxides will start to precipitate as pH nears 7 - do not overshoot and check pH by adding a single drop to litmus paper with clean tubing.
17. Centrifuge sample (centrifuge should already be set to correct settings - 4 minutes @ 2700 rpm).
18. Carefully pour out liquid, fill CF tube with 18 M $\Omega$  DI, empty, and repeat.
19. Add 10 to 15 mL 18 M $\Omega$  DI and one drop Na<sub>4</sub>OH, disaggregate, and centrifuge.
20. Repeat steps 18 and 19.
21. Carefully pour out liquid and dissolve precipitate in 10 to 20 drops 15N HNO<sub>3</sub>.
22. Return to cleaned 30 mL beaker and dry easy.
23. Dissolve in 1.5 CV (1.8 mL) 7N HNO<sub>3</sub> and centrifuge in small (15 mL) CF tube.
24. Load to column 1 (Table A4.1) if solution is yellow and not cloudy.

**Table A4.1**

U-Th-Ra-Sr-Nd column separation procedure.

Column 1: U-Th Separation		Column 2: U-Th Purification		Column 3: Ra-Sr-Nd Separation		Column 4: Ra Purification	
1.2 mL AG 1-X8 Resin		500 µL AG 1-X8 Resin		8 mL AG 50W-X8 Resin		500 µL AG 50W-X8 Resin	
Reusable Columns	Disposable Columns	Reusable Columns	Disposable Columns	Reusable Columns & Resin	Reusable Columns	Disposable Columns	Reusable Columns
Clean	6 CV 6N HCl	Clean	6 CV 6N HCl	Clean (new resin only)	8 mL 7N HNO <sub>3</sub>	Clean	2 mL 7N HNO <sub>3</sub>
Clean	H <sub>2</sub> O	Clean	H <sub>2</sub> O	Clean (new resin only)	24 mL 6N HCl	Clean	2 mL 6N HCl
Rinse Reservoir	H <sub>2</sub> O	Condition	7N HNO <sub>3</sub>	Clean (new resin only)	8 mL H <sub>2</sub> O	Clean	2 mL H <sub>2</sub> O
Condition	7N HNO <sub>3</sub>	Load Th	7N HNO <sub>3</sub>	Condition	6 mL 2.5N HCl	Condition	1.5 mL 2.5N HCl
Load & Collect Ra	1 CV 7N HNO <sub>3</sub>	Wash	7N HNO <sub>3</sub>	Condition	6 mL 2.5N HCl	Load Ra (4 x 125 µL)	0.5 mL 2.5N HCl
Wash & Collect Ra	1 CV 7N HNO <sub>3</sub>	Wash	7N HNO <sub>3</sub>	Load (4 x 1 mL)	4 mL 2.5N HCl	Wash (from beaker)	1 mL 2.5N HCl
Wash & Collect Ra	1 CV 7N HNO <sub>3</sub>	Wash	7N HNO <sub>3</sub>	Wash (from beaker)	2 mL 2.5N HCl	Wash	2 mL 2.5N HCl
Wash & Collect Ra	1 CV 7N HNO <sub>3</sub>	Collect Th	6N HCl	Wash	28 mL 2.5N HCl	Wash	2 mL 2.5N HCl
Collect Th	1 CV 6N HCl	Collect Th	6N HCl	Collect Sr	12 mL 2.5N HCl	Wash	1 mL 2.5N HCl
Collect Th	3 CV 6N HCl	Clean	H <sub>2</sub> O	Collect Sr	7 mL 3.75N HNO <sub>3</sub>	Wash	1 mL 3.75N HNO <sub>3</sub>
Collect U	1 CV H <sub>2</sub> O	Condition	7N HNO <sub>3</sub>	Collect Sr	2 mL 3.75N HNO <sub>3</sub>	Collect Ra	2 mL 3.75N HNO <sub>3</sub>
Collect U	3 CV 1N HBr	Load U	7N HNO <sub>3</sub>	Collect Ra	7 mL 3.75N HNO <sub>3</sub>	Collect Ra	2 mL 3.75N HNO <sub>3</sub>
		Wash	7N HNO <sub>3</sub>	Collect Nd	8 mL 3.75N HNO <sub>3</sub>		
		Wash	6N HCl	Clean	8 mL 7N HNO <sub>3</sub>		
		Collect U	H <sub>2</sub> O	Clean	24 mL 6N HCl		
		Collect U	1N HBr	Clean	8 mL H <sub>2</sub> O		

Column 5: Ra-Ba Separation		Column 6: Sr Purification		Column 7: Nd Purification	
500 µL Sr Spec Resin		250 µL Sr Spec Resin		2 mL LN Resin	
Reusable Columns	Disposable Columns	Reusable Columns	Disposable Columns	Reusable Columns & Resin	Reusable Columns
Clean	6 CV 3N HNO <sub>3</sub>	Clean	2 mL H <sub>2</sub> O	Clean	10 mL 6N HCl
Clean	10 CV H <sub>2</sub> O	Clean	3 mL 0.1% HNO <sub>3</sub>	Condition	3 mL 0.18N HCl
Condition	20 CV 3N HNO <sub>3</sub>	Condition	1 mL 1N HNO <sub>3</sub>	Condition	2 mL 0.18N HCl
Load Ra	1 CV 3N HNO <sub>3</sub>	Load Sr	2 mL 1N HNO <sub>3</sub>	Load Nd	0.2 mL 0.18N HCl
Wash	0.5 CV 3N HNO <sub>3</sub>	Wash	3 mL 7N HNO <sub>3</sub>	Wash	0.2 mL 0.18N HCl
Collect Ra	1 CV 3N HNO <sub>3</sub>	Collect Sr	2 mL 0.1% HNO <sub>3</sub>	Wash	0.2 mL 0.18N HCl
Collect Ra	1.5 CV 3N HNO <sub>3</sub>	Dry Sr and re-dissolve	Clean	Wash	0.5 mL 0.18N HCl
			3 mL 0.1% HNO <sub>3</sub>	Wash	1 mL 0.18N HCl
			2 mL 1N HNO <sub>3</sub>	Wash	16 mL 0.18N HCl
			3 mL 7N HNO <sub>3</sub>	Collect Nd	8 mL 0.18N HCl
			2 mL 0.1% HNO <sub>3</sub>	Clean	6 mL 0.5N HCl
			Clean	Clean	10 mL 6N HCl

**Table A4.2**

Pa column separation procedure.

Column 1: U-Th Separation 1.2 mL AG 1-X8 Resin	Column 2: Pa Purification 500 µL AG 1-X8 Resin	Column 3: Pa Purification 500 µL AG 1-X8 Resin	Column 4: Pa Purification 500 µL AG 1-X8 Resin
Reusable Columns	Disposable Columns	Disposable Columns	Disposable Columns
Clean 6 CV 6N HCl			
Clean 6 CV H <sub>2</sub> O			
Rinse Reservoir H <sub>2</sub> O	Condition 6 CV 7N HNO <sub>3</sub>	Condition 6 CV 7N HNO <sub>3</sub>	Condition 6 CV 7N HNO <sub>3</sub>
Condition 6 CV 7N HNO <sub>3</sub>	Load Pa 1 CV 7N HNO <sub>3</sub>	Load Pa 1 CV 7N HNO <sub>3</sub>	Load Pa 1 CV 7N HNO <sub>3</sub>
Load 2-3 CV 7N HNO <sub>3</sub>	Wash 1 CV 7N HNO <sub>3</sub>	Wash 1 CV 7N HNO <sub>3</sub>	Wash 1 CV 7N HNO <sub>3</sub>
Wash 1 CV 7N HNO <sub>3</sub>			
Wash 1 CV 7N HNO <sub>3</sub>			
Wash 1 CV 7N HNO <sub>3</sub>	Clean Th 1 CV 9.8N HCl	Clean Th 1 CV 9.8N HCl	Clean Th 1 CV 9.8N HCl
Clean Th 1 CV 9.8N HCl	Clean Th 1.5 CV 9.8N HCl	Clean Th 1.5 CV 9.8N HCl	Clean Th 1.5 CV 9.8N HCl
Clean Th 1.5 CV 9.8N HCl	Collect Pa 1 CV 9.8N HCl + 0.05N HF	Collect Pa 1 CV 9.8N HCl + 0.05N HF	Collect Pa 1 CV 9.8N HCl + 0.05N HF
Collect Pa 1 CV 9.8N HCl + 0.05N HF	Collect Pa 1.5 CV 9.8N HCl + 0.05N HF	Collect Pa 1.5 CV 9.8N HCl + 0.05N HF	Collect Pa 1.5 CV 9.8N HCl + 0.05N HF
Collect Pa 1.5 CV 9.8N HCl + 0.05N HF			

**Chapter 5:  $^{238}\text{U}$ - $^{230}\text{Th}$ - $^{226}\text{Ra}$  and  $^{235}\text{U}$ - $^{231}\text{Pa}$  constraints on rhyolite generation at South Sister and Newberry volcanoes, central Oregon Cascades**

**Abstract**

The origins of granitic and rhyolitic magmas, along with the timescales over which such silicic bodies are assembled and stored prior to eruption, remain the subject of considerable debate and study. Felsic magma generation within the Cascade arc has been attributed to both melting and basalt fractionation scenarios, as well as combinations of these end members. A spatial and temporal correlation between areas of active intra-arc extension and the eruption of both unusually high and low  $\text{SiO}_2$  magmas suggests a causal relationship between production of large volumes of mantle-derived basalt and rhyolitic volcanism. Elemental and isotopic variations between Holocene rhyolites erupted from South Sister and Newberry volcanoes in central Oregon reflect melting of different crustal lithologies at different depths. Greater extension around South Sister is interpreted to allow ascent and eruption of lower crustal melts, while re-melting of upper crustal granitic intrusive at Newberry generates the Holocene obsidians there.

## 5.1. Introduction

More than 50 years after Tuttle and Bowen (1958) demonstrated conclusively the magmatic nature of granite, the origin of granitic batholiths, and associated rhyolitic lavas, is still a matter of extensive debate and study, as are the timescales over which such bodies are generated and stored within the crust (e.g., Davies et al., 1994; Reid et al., 1997; Hawkesworth et al., 2000; Reagan et al., 2003; Eppich et al., 2012; Simakin and Bindeman, 2012; Stelten and Cooper, 2012). Resolution of this problem has many implications, including hazard assessment and the origin and evolution of the continental crust, which is estimated to have an andesitic bulk composition, with a more mafic lower crust and granite-dominated upper crust (Taylor and McLennan, 1985; Ruddick and Fountain, 1995; Rudnick and Gao, 2003). End member models for the origin of felsic magmas fall into two categories: (i) fractional crystallization of mafic magmas in either the upper or lower crust (e.g., Bowen, 1928; Grove and Donnelly-Nolan, 1986; Bacon and Druitt, 1988; Grove et al., 2003; Prouteau and Scaillet, 2003); and (ii) partial melting of mafic crustal lithologies (e.g., Beard and Lofgren, 1991; Tepper et al., 1993; Wolf and Wyllie, 1994; Rapp and Watson, 1995; Petford and Gallagher, 2001; Sisson et al., 2005). These scenarios are end members, and both processes may occur simultaneously (e.g., Grove et al., 1997; Annen and Sparks, 2002; Annen et al., 2006). Felsic magma generation within the Cascade arc has been ascribed variously to both of these scenarios, as well as to combinations of these end members (Grove and Donnelly-Nolan, 1986; Smith and Leeman, 1987; Bacon and Druitt, 1988; Bullen and Clynne, 1990; Hill, 1991; Smith and Leeman, 1993; Tepper et al., 1993; Guffanti et al., 1996; Cribb and Barton,

1997; Grove et al., 1997; Borg and Clynne, 1998; Brophy and Dreher, 2000; Kinzler et al., 2000; Conrey et al., 2001; Grove et al., 2005; Eppich et al., 2012).

Within the Cascade arc eruption of true rhyolite ( $> 72$  wt.%  $\text{SiO}_2$ ) is common at rear-arc centers (i.e. the Simcoe Mountains Volcanic Field, Newberry Volcanic Field, and Medicine Lake Volcanic Field, all of which occupy unique tectonic niches (Hildreth, 2007)), but rare along the axis of the arc, where dacite (63-68 wt.%  $\text{SiO}_2$ ) and rhyodacite (68-72 wt.%  $\text{SiO}_2$ ) are more common (Hildreth, 2007). Exceptions are the Lassen segment of northern California and the Sisters reach of central Oregon, both locations where Basin and Range extension and/or intra-arc rifting exert a strong control on magmatism (Hildreth, 2007). Additionally, the Lassen segment and Sisters reach are the two locations within the arc where eruption of true basalt ( $< 52$  wt.%  $\text{SiO}_2$ ), rather than basaltic andesite, is common too (Hildreth, 2007). The large rear-arc volcanic centers are dominantly mafic also (Hildreth, 2007). These observations strongly suggest that eruption of rhyolite within the Cascades is facilitated by greater than normal fluxes of basaltic magma beneath the arc in areas of active extension. However, the exact nature of the relationship is unclear. Grove et al. (1997) interpreted the rhyolite of Glass Mountain at Medicine Lake to be the product of mixing between two silica-rich liquids, generated via fractional crystallization and melting of granitic crustal rocks. Felsic rocks in the Lassen region have been interpreted as melts of basaltic lower crust under variable  $f(\text{H}_2\text{O})$  and temperature conditions (Borg and Clynne, 1998).

The Three Sisters region of central Oregon (Fig. A5.1) is the location of recent ( $< 5$  Ma) intra-arc extension and rifting, a consequence of dextral shear between the Pacific and North American plates (Atwater, 1970), and impingement of Basin and Range

extension (Jones et al., 1996). This region also is the locus of intersection with the arc of a NW-trending, age-progressive crustal-melting anomaly, which has generated a bimodal basalt-rhyolite volcanic field in southeastern Oregon that arrived at Newberry < 1 Ma (Jordan et al., 2004; Hildreth, 2007). Postglacial eruptive suites at both South Sister and Newberry volcanoes are strongly bimodal, with compositional gaps from 56 to 72 wt.% SiO<sub>2</sub> and 57 to 73 wt.% SiO<sub>2</sub> respectively (Clark, 1983; Linneman, 1990).

Previous studies of South Sister volcano typically invoke crustal melting, of either lower crustal mafic amphibolite (Hill, 1991) or upper crustal granitoids (Clark, 1983; Price, 1993), as the source for the Holocene rhyolites. Crystal fractionation from a basaltic parent also has been proposed (Hughes, 1983; Brophy and Dreher, 2000), although the large compositional gap and high magmatic temperatures in the postglacial suite (Hill, 1991) argue against this interpretation (Simakin and Bindeman, 2012). The Newberry obsidians have received considerably less attention, although Linneman (1990) interpreted them as melts of upper crustal granitic rocks. U-series isotopes can provide additional constraints on these proposed melting scenarios, as well as post-melting crustal residence times (e.g., Davies et al., 1994; Reagan et al., 2003; Eppich et al., 2012).

The aim of this chapter is to utilize new U-series isotope (<sup>238</sup>U-<sup>230</sup>Th-<sup>226</sup>Ra and <sup>235</sup>U-<sup>231</sup>Pa) and trace element data for Holocene rhyolites from South Sister and Newberry to test the hypothesis that the South Sister rhyolites are lower crustal melts and the Newberry obsidians are melts of upper crustal granitic rocks. The results support these interpretations and suggest that local tectonic factors may be the main driving force controlling melting at different depths within the crust.

## 5.2. Samples and Methods

Samples were collected from three rhyolite flows at South Sister volcano and two obsidian flows within Newberry caldera (Fig. A5.1). Eruption of the Holocene rhyolites at South Sister produced  $\sim 0.9 \text{ km}^3$  (dense-rock equivalent) of tephra, lava domes, and lava flows between  $\sim 2.3$  and  $2.0 \text{ ka}$  in two distinct episodes, separated by a repose period of as long as several centuries. The earlier eruption produced the  $\sim 0.5 \text{ km}^3$  Rock Mesa lava flow and associated pyroclastic deposits (Scott, 1987). The second eruptive episode produced the slightly less evolved Devils Hill chain of vents and the  $0.2 \text{ km}^3$  Newberry lava flow, leading to the suggestion that the eruptions were tapping the same compositionally zoned magma chamber (Scott, 1987). Samples were collected from the SE side of the Rock Mesa (08-RM-01) and Newberry (08-NF-01) flows, as well as from the southern edge of the Devils Hill chain of vents (07-DH-01) (Fig. A5.1). All samples are glassy rhyolites with common flow banding and  $< 10\%$  phenocrysts. Plagioclase ( $\text{An}_{53-21}$ ) is the most abundant phenocryst phase, with minor orthopyroxene and oxides, and traces of hornblende, apatite, zircon, and clinopyroxene (Clark, 1983; Hill, 1991; Fierstein et al., 2011; Hildreth et al., 2012). The majority of the plagioclase phenocrysts are strongly resorbed, complexly zoned, and contain abundant glass inclusions (Clark, 1983; Hill, 1991). Small biotite grains are occasionally found with glomerocrystic plagioclase (Hill, 1991).

A number of obsidian flows have been erupted within Newberry caldera at regular intervals of  $\sim 2$  to  $4 \text{ k.y.}$  during the Holocene, starting with the Southeastern Obsidian Flow at  $\sim 10 \text{ ka}$  and culminating with the Big Obsidian Flow at  $\sim 1.3 \text{ ka}$  (Linneman, 1990). Samples were collected from the small East Lake Flow (08-ELO-01), erupted  $\sim$

3.5 ka, and from the Big Obsidian Flow (08-BOF-01) (Linneman, 1990) (Fig. A5.1). The obsidians are flow banded and crystal-poor, although the BOF is more crystal-rich than the ELO, with ~ 1.5% phenocrysts (Linneman, 1990). Plagioclase is the most abundant phase, with minor orthopyroxene and oxides, and rare hornblende (Linneman, 1990). Partially melted silicic inclusions have been found in the BOF, including biotite granites and plagioclase-rich granophyres, along with quenched andesitic inclusions that have similar compositions to the Holocene mafic lavas (Linneman, 1990).

Whole-rock major and trace element concentrations were determined by XRF and ICP-MS at the University of New Mexico (UNM) following the procedure described in Mitchell and Asmerom (2011). Analytical accuracy, based on analysis of known standards, is estimated at  $\pm 2\%$  for most major elements and  $\pm 5\%$  for most trace elements.

U-Th-Ra and Sr-Nd isotopic analyses were performed on ~ 100 mg powder aliquots in the Radiogenic Isotope Laboratory at UNM following the fusion method of Ulfbeck et al. (2003). Following dissolution of the quenched melt the samples were spiked with ~ 1 g of a mixed  $^{228}\text{Ra}$ - $^{229}\text{Th}$ - $^{233}\text{U}$ - $^{236}\text{U}$  spike. Elemental separation-purification and mass spectrometric analysis followed procedures described in Mitchell and Asmerom (2011).

Subsequent U-Th-Pa analyses were performed on ~ 400 to 500 mg aliquots of the same powders employing the same fusion procedure used for trace element analysis. The dissolved melt solution was split into separate aliquots for U-Th and Pa analyses and spiked with the appropriate  $^{229}\text{Th}$ - $^{233}\text{U}$ - $^{236}\text{U}$  or  $^{233}\text{Pa}$  spike. U-Th elemental separation and analysis followed standard procedures (Mitchell and Asmerom, 2011) and is the data

reported in Table 5.2. Pa separation and analysis followed the procedure described in Chapter 3. More details of the Pa analytical procedures are given in Appendix A5.

### 5.3. Results

The three South Sister samples display very similar major element abundances, although systematic differences between the earlier erupted RM (higher SiO<sub>2</sub> and K<sub>2</sub>O) and later erupted DH/NF samples are apparent (Table 5.1 and Fig. A5.2). These observations agree with previous major element analyses (e.g., Scott, 1987; Price, 1993; Brophy and Dreher, 2000; Stelten and Cooper, 2012). The Newberry samples are distinct from the South Sister samples, having higher Na<sub>2</sub>O and K<sub>2</sub>O, and lower MgO, CaO, TiO<sub>2</sub>, and P<sub>2</sub>O<sub>5</sub>, at similar SiO<sub>2</sub> (Table 5.1 and Fig. A5.2). Subtle, but less systematic, variations are apparent also between the Newberry samples, with the earlier erupted ELO flow having higher SiO<sub>2</sub>, MgO, K<sub>2</sub>O, TiO<sub>2</sub> and P<sub>2</sub>O<sub>5</sub> than the later erupted BOF (Table 5.1 and Fig. A5.2). These variations agree with the data of Laidley and McKay (1971) and Linneman (1990), but contrast slightly with those of MacLeod and Sherrod (1988).

The trace element data display more variation between the South Sister and Newberry samples, with the Newberry flows being enriched in most trace elements (Fig. 5.1). A notable exception is the very low Sr concentrations in both Newberry samples (Fig. 5.1a). Greater trace element variability is apparent also between the Newberry samples than between the South Sister samples (Fig. 5.1b).

All five samples define a very restricted range of <sup>87</sup>Sr/<sup>86</sup>Sr and <sup>143</sup>Nd/<sup>144</sup>Nd that is slightly higher and lower, respectively, than values for most mafic rocks from the region (Table 5.2 and Fig. 5.2a). The South Sister samples define a narrower range of both

**Table 5.1**

Major and trace element data for South Sister and Newberry rhyolites.

Sample ID	07-DH-01	08-NF-01	08-RM-01	08-BOF-01	08-ELO-01	RGM-1 Standard (n=3)			
	Latitude (N)	44° 01.978'	44° 04.363'	44° 03.520'	43° 42.371'	43° 43.024'	Meas.	St. Dev.	Cert.
Longitude (W)	121° 45.340'	121° 43.947'	121° 47.298'	121° 14.278'	121° 11.998'				
SiO <sub>2</sub>	72.58	72.58	73.56	72.97	73.28	73.84	0.028	73.4	0.53
Al <sub>2</sub> O <sub>3</sub>	14.56	14.55	14.18	14.31	14.16	14.00	0.017	13.7	0.19
Fe <sub>2</sub> O <sub>3T</sub>	2.30	2.34	2.05	2.27	2.09	1.90	0.006	1.86	0.03
MgO	0.58	0.57	0.50	0.19	0.28	0.30	0.007	0.28	0.03
CaO	1.94	1.92	1.69	0.82	0.97	1.18	0.001	1.15	0.07
Na <sub>2</sub> O	4.41	4.40	4.22	5.10	4.71	4.04	0.009	4.07	0.15
K <sub>2</sub> O	3.17	3.17	3.40	4.02	4.17	4.38	0.003	4.30	0.10
TiO <sub>2</sub>	0.326	0.328	0.285	0.225	0.243	0.270	0.002	0.27	0.02
P <sub>2</sub> O <sub>5</sub>	0.083	0.085	0.071	0.030	0.039	0.049	0.000	n.d.	n.d.
MnO	0.053	0.053	0.046	0.062	0.050	0.036	0.001	0.036	0.004
Measured Total	98.63	98.81	98.81	98.82	98.90				
V	25.13	25.14	21.34	4.46	9.87	15.96	15.48	13	2
Cr	1.70	1.82	1.84	0.51	0.97	3.75	3.67	3.7	
Co	2.96	2.97	2.58	0.87	1.33	1.97	1.95	2.0	0.2
Ni	1.51	2.14	3.17	1.06	1.53	5.07	8.70		
Cu	8.03	7.19	6.42	6.15	5.46	11.70	11.76	12	1.4
Zn	35.35	35.08	30.84	45.40	37.75	30.66	29.75	32	
Rb	75.1	74.1	82.7	118.6	131.0	159.3	154.7	150	8
Sr	238.8	232.9	198.0	52.98	63.92	113.5	109.7	110	10
Y	17.44	17.45	17.31	45.48	41.81	25.12	24.88	25	
Zr	185.0	182.0	176.6	354.3	286.1	228.7	223.6	220	20
Nb	8.92	8.99	8.68	20.45	16.24	8.88	8.71	8.9	0.6
Cs	2.58	2.61	2.96	4.32	4.92	9.46	9.53	9.6	0.6
Ba	770.9	780.6	813.6	843.1	865.2	833.4	836.2	810	46
La	19.25	19.31	19.67	29.82	28.96	23.08	22.93	24	1.1
Ce	38.23	38.66	39.10	64.35	61.60	47.37	47.28	47	4
Pr	4.25	4.33	4.33	7.54	7.16	5.39	5.41	5.32	
Nd	15.29	15.56	15.53	28.52	26.77	19.56	19.80	19	1
Sm	2.99	3.03	3.00	6.29	5.75	4.17	4.10	4.3	0.3
Eu	0.665	0.681	0.640	0.827	0.778	0.660	0.658	0.66	0.08
Gd	3.03	3.08	3.02	6.58	6.00	4.10	4.15	3.7	0.4
Tb	0.451	0.462	0.456	1.10	1.00	0.656	0.649	0.605	
Dy	2.57	2.62	2.59	6.82	6.22	3.77	3.80	4.1	0.1
Ho	0.538	0.549	0.569	1.46	1.31	0.788	0.794	0.769	
Er	1.56	1.60	1.59	4.30	3.94	2.29	2.34	2.33	
Tm	0.250	0.252	0.249	0.696	0.627	0.365	0.365	0.36	0.02
Yb	1.80	1.80	1.80	4.85	4.43	2.62	2.64	2.6	0.3
Lu	0.283	0.285	0.280	0.759	0.689	0.402	0.404	0.4	0.03
Hf	4.56	4.71	4.66	8.66	7.53	5.94	6.03		
Ta	0.85	0.86	0.89	1.57	1.36	1.00	1.01	0.95	0.1
Th	7.73	7.87	8.77	12.09	12.82	15.02	15.79	15	1.3
U	2.82	2.84	3.15	4.23	4.51	5.96	6.33	5.8	0.5

Major elements (wt.%) were determined by XRF on fused glass disks. Analyses are normalized to 100% on an anhydrous basis with all Fe reported as Fe<sub>2</sub>O<sub>3</sub>. Original analytical totals are given for reference. Trace element concentrations (ppm) were determined by ICP-MS, except U and Th concentrations, which were determined from isotope ratio analyses. USGS standard RGM-1 was analyzed as an external standard. Major element values are the average of three separate analyses of the same glass disk, standard deviation is quoted. Trace element values are for two separate analyses of the same solution.

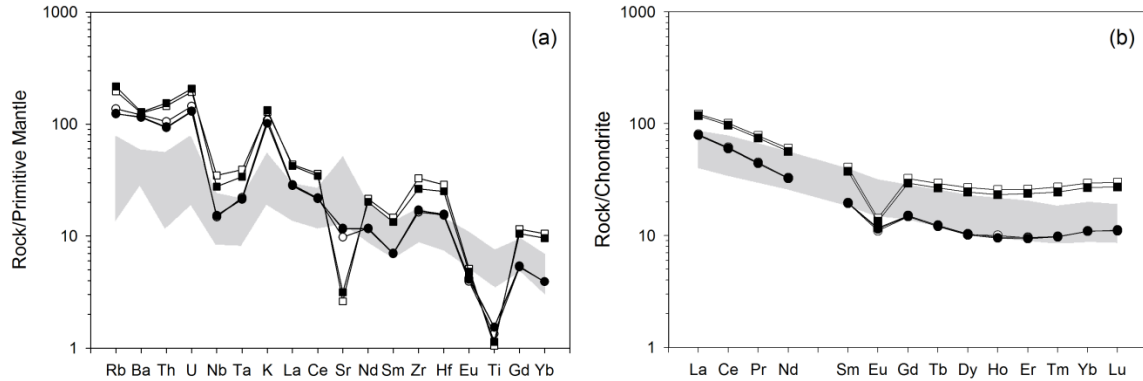


**Figure 5.1:** Trace element data for Holocene felsic rocks from South Sister and Newberry and fields for regional mafic rocks (gray shaded fields; Mitchell and Asmerom, 2011). Panel (a): Primitive mantle-normalized trace element ‘spidergrams’, normalizing values from Palme and O’Neill (2003). South Sister samples are shown with circles (DH & NF filled circles, RM open circles) and Newberry samples with squares (BOF open squares, ELO filled squares). Panel (b): Chondrite-normalized rare earth element plot, normalizing values from Palme and Jones (2003). Note the concave-upward MREE pattern and pronounced negative Eu anomaly in all samples.

$^{87}\text{Sr}/^{86}\text{Sr}$  and  $^{143}\text{Nd}/^{144}\text{Nd}$  than do the Newberry samples. The sample from the more evolved, earlier erupted Rock Mesa episode has slightly higher  $^{87}\text{Sr}/^{86}\text{Sr}$  than the less evolved samples from the Devils Hill episode.

The U-series data indicate further some interesting similarities and differences between the samples (Fig. 5.2). The South Sister samples are all within 5% of ( $^{230}\text{Th}/^{238}\text{U}$ ) secular equilibrium, and have similar  $^{231}\text{Pa}$ -excesses of ~ 40% (Fig. 5.2c). The Newberry flows are more variable, having similar and small  $^{230}\text{Th}$ -excesses (~ 7%), but more variable  $^{231}\text{Pa}$ -excesses of ~ 59 and 42% (Fig. 5.2c). All five samples are within error of ( $^{226}\text{Ra}/^{230}\text{Th}$ ) secular equilibrium (Fig. 5.2d).

**Table 5.2**  
U-Th-Ra-Pa-Sr-Nd isotope data for South Sister and Newberry rhyolites.

Sample ID	07-DH-01	08-NF-01	08-RM-01	08-BOF-01	08-ELO-01	Ryan Std. A	Ryan Std. B	TML Std.
U (ppm)	2.823 ± 2	2.835 ± 2	3.148 ± 3	4.226 ± 4	4.514 ± 5	1.261 ± 1	1.271 ± 2	10.73 ± 2
Th (ppm)	7.728 ± 42	7.867 ± 79	8.765 ± 92	12.090 ± 26	12.815 ± 98	7.196 ± 31	7.248 ± 2	29.42 ± 12
$^{232}\text{Th}/^{238}\text{U}$	2.829 ± 16	2.868 ± 29	2.877 ± 30	2.957 ± 7	2.934 ± 23	5.895 ± 26	5.891 ± 9	2.834 ± 12
$(^{230}\text{Th}/^{232}\text{Th})$	1.114 ± 7	1.099 ± 12	1.093 ± 12	1.138 ± 3	1.138 ± 9	0.530 ± 2	0.529 ± 1	1.037 ± 4
$(^{238}\text{U}/^{232}\text{Th})$	1.108 ± 6	1.093 ± 11	1.090 ± 11	1.060 ± 2	1.069 ± 8	0.532 ± 2	0.532 ± 1	1.106 ± 5
$(^{234}\text{U}/^{238}\text{U})$	1.000 ± 1	1.001 ± 1	0.997 ± 1	0.998 ± 1	0.999 ± 1	0.997 ± 1	0.996 ± 1	0.997 ± 1
$(^{230}\text{Th}/^{238}\text{U})$	1.005 ± 3	1.005 ± 3	1.003 ± 3	1.073 ± 2	1.065 ± 3	0.996 ± 2	0.994 ± 2	0.937 ± 2
$^{226}\text{Ra}$ (pg/g)	0.913 ± 46	0.934 ± 23	0.992 ± 49	1.469 ± 43	1.482 ± 103	n.m.	0.417 ± 17	n.m.
$(^{226}\text{Ra}/^{230}\text{Th})$	0.985 ± 50	1.009 ± 25	0.962 ± 48	1.029 ± 31	1.014 ± 71	n.m.	0.988 ± 41	n.m.
$(^{226}\text{Ra}/^{230}\text{Th})_i$	0.965 ± 118	1.022 ± 58	0.896 ± 129	1.050 ± 54	1.065 ± 322	n.d.	n.d.	n.d.
$^{231}\text{Pa}$ (pg/g)	1.323 ± 55	1.337 ± 30	1.388 ± 38	2.171 ± 48	2.039 ± 32	0.426 ± 21	0.390 ± 39	3.539 ± 166
$(^{231}\text{Pa}/^{235}\text{U})$	1.440 ± 59	1.448 ± 33	1.354 ± 37	1.578 ± 35	1.387 ± 22	1.038 ± 51	0.937 ± 95	1.013 ± 48
$(^{231}\text{Pa}/^{235}\text{U})_i$	1.460 ± 63	1.469 ± 36	1.371 ± 40	1.594 ± 39	1.417 ± 25	n.d.	n.d.	n.d.
$^{87}\text{Sr}/^{86}\text{Sr}$	0.703584 ± 5	0.703585 ± 3	0.703652 ± 4	0.703663 ± 4	0.703845 ± 3	n.m.	n.m.	n.m.
$^{143}\text{Nd}/^{144}\text{Nd}$	0.512858 ± 8	0.512862 ± 5	0.512863 ± 6	0.512879 ± 3	0.512848 ± 7	n.m.	n.m.	n.m.
$\epsilon_{\text{Nd}}$	4.29 ± 0.16	4.37 ± 0.10	4.39 ± 0.12	4.70 ± 0.06	4.10 ± 0.14	n.m.	n.m.	n.m.

Ratios in parentheses represent activity ratios (the number of atoms times the decay constant,  $\lambda$ ). Decay constants used are as follows:  $\lambda_{226} = 4.33 \times 10^{-4} \text{ yr}^{-1}$ ,  $\lambda_{230} = 9.1577 \times 10^{-6} \text{ yr}^{-1}$ ,  $\lambda_{231} = 2.1158 \times 10^{-5} \text{ yr}^{-1}$ ,  $\lambda_{232} = 4.9475 \times 10^{-11} \text{ yr}^{-1}$ ,  $\lambda_{233} = 9.386925 \text{ yr}^{-1}$ ,  $\lambda_{234} = 2.8263 \times 10^{-6} \text{ yr}^{-1}$ ,  $\lambda_{238} = 1.5513 \times 10^{-10} \text{ yr}^{-1}$ . All uncertainties are  $2\sigma$  measurement errors. Spikes were prepared from pure metals (U and Th), Ra was milked from NIST 3159  $^{232}\text{Th}$  Standard and  $^{233}\text{Pa}$  was produced by neutron irradiation of NIST 3159  $^{232}\text{Th}$  Standard. "Ryan A" is an in-house secular equilibrium basalt standard prepared using a standard HF-HNO<sub>3</sub> digestion. "Ryan B" is the same in-house standard prepared following the fusion procedure described in the text and used for the samples - U-Th-Pa data were generated from fusion of a single batch of powder and Ra-Th data were generated from a separate batch of powder. TML is the Table Mountain Latite standard prepared using a standard HF-HNO<sub>3</sub> digestion. U standard NBL-112 was also analyzed yielding a  $\delta^{234}\text{U}$  value of  $-38.8 \pm 0.96\%$  in agreement with published values of  $-37.1 \pm 1.2\%$  (Edwards et al., 1993) and  $-36.9 \pm 2.1\%$  (Cheng et al., 2000). Sr standard NBS-987 and the La Jolla Nd standard were analyzed at the beginning and end of the analytical session, yielding values of 0.710269 and 0.710268 for NBS-987, and 0.511832 and 0.511833 for La Jolla.  $\epsilon_{\text{Nd}} = [({}^{143}\text{Nd}/{}^{144}\text{Nd})_{\text{sample}} - ({}^{143}\text{Nd}/{}^{144}\text{Nd})_{\text{CHUR}}] / ({}^{143}\text{Nd}/{}^{144}\text{Nd})_{\text{CHUR}} * 10,000$ , where  $({}^{143}\text{Nd}/{}^{144}\text{Nd})_{\text{CHUR}} = 0.512638$ , relative to  ${}^{146}\text{Nd}/{}^{144}\text{Nd} = 0.7219$ .

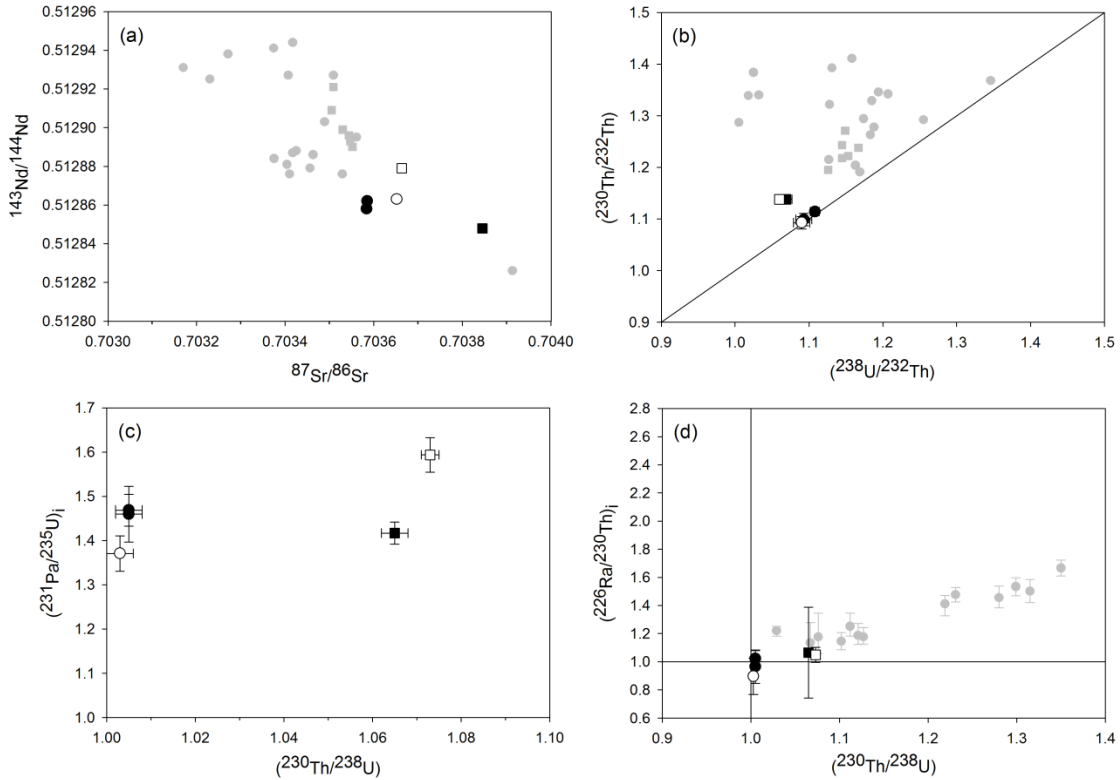


**Figure 5.2:** U-Th-Pa-Sr-Nd isotope data for Holocene felsic rocks from South Sister and Newberry, symbols as in Figure 5.1. Data for mafic rocks from Three Sisters and Newberry regions shown in panels (a) and (b) as gray circles and squares respectively (Mitchell and Asmerom, 2011). Panel (a):  $^{87}\text{Sr}/^{86}\text{Sr}$  vs.  $^{143}\text{Nd}/^{144}\text{Nd}$  plot. The felsic rocks have only slightly higher  $^{87}\text{Sr}/^{86}\text{Sr}$  and lower  $^{143}\text{Nd}/^{144}\text{Nd}$  than the mafic rocks, suggesting limited contribution from old continental crust. Panel (b):  $(^{230}\text{Th}/^{232}\text{Th})$  vs.  $(^{238}\text{U}/^{232}\text{Th})$  ‘equiline’ plot. The South Sister samples are within error of secular equilibrium, Newberry samples have ~ 6 to 7%  $^{230}\text{Th}$ -enrichment. Panel (c):  $(^{230}\text{Th}/^{238}\text{U})$  vs.  $(^{231}\text{Pa}/^{235}\text{U})_i$  plot. South Sister and Newberry samples define similar ranges in  $(^{231}\text{Pa}/^{235}\text{U})_i$  despite  $(^{230}\text{Th}/^{238}\text{U})$  differences. Mafic data extend to  $(^{230}\text{Th}/^{238}\text{U}) = 1.350$  and  $(^{231}\text{Pa}/^{235}\text{U})_i = 9.143$  (Mitchell and Asmerom, 2011). Panel (d):  $(^{230}\text{Th}/^{238}\text{U})$  vs.  $(^{226}\text{Ra}/^{230}\text{Th})_i$  plot. All samples are within error of secular equilibrium. Error bars show permissible range of eruption-age values.

#### 5.4. Discussion and Conclusions

The concave-upward chondrite-normalized REE patterns of South Sister and Newberry rhyolites are similar to those observed by Tepper et al. (1993), in northern Cascades leucocratic granitoids, and in northern California by Borg and Clynne (1998), in their

group 2 felsic rocks. These authors interpreted such REE patterns as the result of lower crustal melting under relatively hydrous (high  $f(\text{H}_2\text{O})$ ) conditions, where amphibole remains in the restite. The major element compositions of the South Sister and Newberry rhyolites are consistent with such an interpretation (Appendix A5). The new  $^{87}\text{Sr}/^{86}\text{Sr}$  and  $^{143}\text{Nd}/^{144}\text{Nd}$  data are similar to mafic rocks from the region, which also is consistent with derivation of the rhyolites from a young crustal source.

The new REE data can be used to test this interpretation of melting of lower crustal amphibolite. The best-fit model to the South Sister data uses a primitive arc basalt source, 25% melting, and has a residual mineralogy dominated by plagioclase, amphibole, and orthopyroxene, with minor garnet, apatite, clinopyroxene, and magnetite (Fig. 5.3). The Newberry REE data can be reproduced with such a model also, but the data require an evolved andesitic protolith, 45% melting, and an apatite- and garnet-free source (Fig. 5.3). Such a high degree of melting is unlikely to result in a rhyolitic composition (e.g., Sisson et al., 2005).

Neither the South Sister nor the Newberry REE models are able to reproduce the magnitude of the negative Eu anomaly, or the low Sr concentrations in the samples, indicating subsequent modification of any lower crustal melt is required. The limited major element variation among the Holocene South Sister rhyolites has been modeled as the result of 5% fractional crystallization (FC) of a plagioclase-dominated assemblage, with subordinate orthopyroxene, amphibole, Fe-Ti oxides, and apatite (Hill, 1991).

The new ( $^{230}\text{Th}/^{238}\text{U}$ ) and ( $^{231}\text{Pa}/^{235}\text{U}$ ) data can place further constraints on this crustal melting-fractional crystallization scenario. The presence of  $^{231}\text{Pa}$ -excesses, coupled with

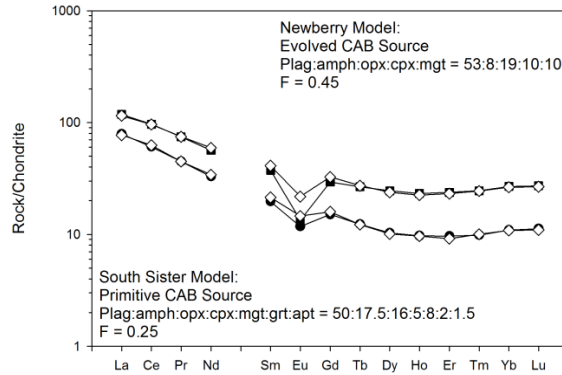


**Figure 5.3:** Results of lower crustal partial melting models for South Sister and Newberry. Black circles are South Sister sample 08-NF-01 and squares are Newberry sample 08-ELO-01. White diamonds are melting model results. Best-fit South Sister model uses a primitive CAB source (sample 08-CYC-01), 25% melting, and a residual mineralogy of plag:amph:opx:cpx:mgt:grt:apt = 50:17.5:16:5:8:2:1.5. Best-fit Newberry model uses a basaltic andesite source (08-MBF-02), 45% melting, and a residual mineralogy of plag:amph:opx:cpx:mgt = 53:8:19:10:10. D values from Borg and Clynne (1998), except apatite data from Prowatke and Klemme (2006) and garnet data from (Dufek and Cooper, 2005). Note that neither model is able to reproduce the magnitude of the negative Eu anomaly in the erupted lavas.

an absence of  $^{230}\text{Th}$ -excesses, require that the ( $^{230}\text{Th}/^{238}\text{U}$ ) secular equilibrium values are a consequence of the melting/fractionation process, not simply prolonged post-melting residence in an upper crustal magma chamber. Recent experimental work has demonstrated that apatite  $D_{\text{U}}$  and  $D_{\text{Th}}$  values are  $\sim 1$  (Prowatke and Klemme, 2006), at least one or two orders of magnitude higher than in any of the other phases considered. As a consequence, the behavior of U and Th will largely be controlled by the presence of apatite in the melting restite and fractionating assemblage. Partition coefficients are largely unknown for protactinium, which is assumed to be highly incompatible in most phases, and low apatite D values for other pentavalent elements (e.g., Nb and Ta; Prowatke and Klemme, 2006) suggest Pa should not partition readily into apatite either.

The results of a coupled partial melting-fractional crystallization model are shown in Figure 5.4. The best-fit to the South Sister ( $^{231}\text{Pa}/^{235}\text{U}$ ) and U-Pa concentration data is 20% lower crustal melting followed by 40% FC, assuming bulk  $D_{\text{U}} = 0.09$  and bulk  $D_{\text{Pa}} = 10^{-5}$  (Fig. 5.4). This model will generate ( $^{230}\text{Th}/^{238}\text{U}$ ) values within 2% of secular equilibrium as long as bulk  $D_{\text{Th}}$  is within 5% of bulk  $D_{\text{U}}$  (i.e.  $\sim 0.085\text{-}0.095$ ).

This extent of FC (40%) is significantly higher than inferred by Hill (1991) (5% FC between RM and DH/NF compositions) and would significantly affect the bulk rock composition. An alternative is coupled assimilation-fractional crystallization (AFC), with an assimilant of similar felsic composition. This interpretation is supported by several lines of evidence, including higher  $^{87}\text{Sr}/^{86}\text{Sr}$  in the more evolved Rock Mesa flow (Fig. 5.2a), which cannot be generated solely through FC, mineral separate U-Th-Ra U-series data suggesting that a significant fraction of the crystal cargo in both flows is antecrystic and formed in an older, compositionally distinct magma (Stelten and Cooper, 2010), and the apparent slight decrease in ( $^{231}\text{Pa}/^{235}\text{U}$ ) in the more evolved Rock Mesa flow (Fig. 5.2c). If AFC processes do lower initial melt ( $^{231}\text{Pa}/^{235}\text{U}$ ), which would depend on the composition and age of the assimilant as well as the assimilation to fractional crystallization ratio, then melting of the lower crust must generate a melt with ( $^{231}\text{Pa}/^{235}\text{U}$ ) greater than  $\sim 1.5$ . This can be easily achieved in the original lower crustal melting model, where ( $^{231}\text{Pa}/^{235}\text{U}$ ) increases significantly at small degrees of melting (Fig. 5.4a). For example, lowering the extent of melting from 20 to 15% would raise the ( $^{231}\text{Pa}/^{235}\text{U}$ ) of the melt from 1.36 to 1.51. Approximately 15 to 20% assimilation by this melt of a secular equilibrium component with similar U concentration to the South Sister samples could then explain the range in ( $^{231}\text{Pa}/^{235}\text{U}$ ).

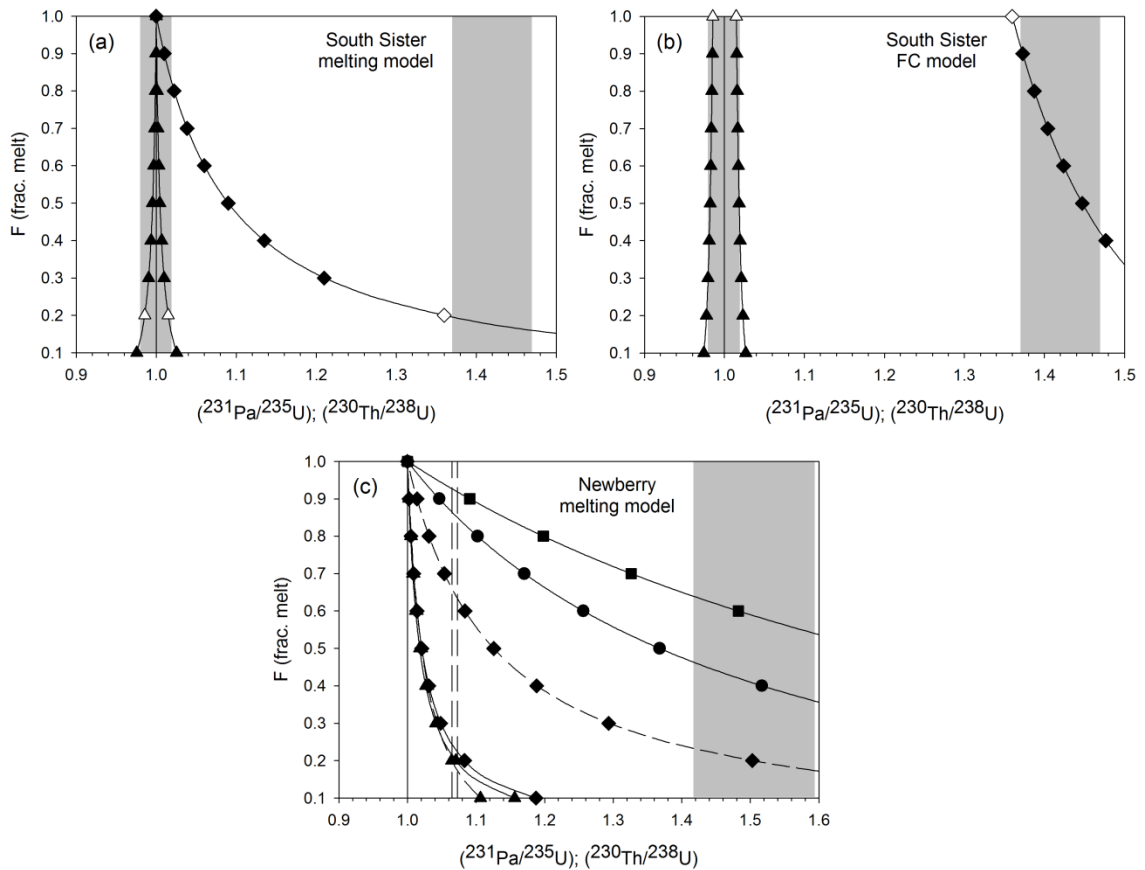


**Figure 5.4:**  $(^{231}\text{Pa}/^{235}\text{U})$  and  $(^{230}\text{Th}/^{238}\text{U})$  modeling plots for South Sister and Newberry Holocene felsic rocks. Panel (a): Results of lower crustal batch melting models, assuming a secular equilibrium source. F is the degree of melting. Narrow gray rectangle is an activity ratio of  $1.000 \pm 0.02$ . Wide gray rectangle is the range in  $(^{231}\text{Pa}/^{235}\text{U})_i$  in the South Sister samples. Solid line with diamonds is the  $(^{231}\text{Pa}/^{235}\text{U})$  output of the best-fit South Sister melting model from Figure 5.3, assuming bulk  $D_{\text{U}} = 0.09$  and  $D_{\text{Pa}} = 10^{-5}$ . Solid lines with triangles are the  $(^{230}\text{Th}/^{238}\text{U})$  output for the same model assuming two different values of bulk  $D_{\text{Th}}$ , 0.085 and 0.095. These bulk D values require apatite  $D_{\text{U}} \sim 6$  and  $D_{\text{Th}} \sim 5$ , consistent with experimental data and natural samples (Bea et al., 1994; Prowatke and Klemme, 2006). Open symbols are the starting compositions in panel (b). Panel (b): Results of a fractional crystallization model using the output from panel (a) as a starting composition and the same D values. F is the amount of residual melt (i.e. 1 - degree of crystallization). Gray rectangles are as in panel (a). Fractionating assemblage is the observed modal assemblage (Hill, 1991), dominated by plagioclase (84%) with 0.5% apatite. Panel (c): Results of upper crustal batch melting models, assuming a secular equilibrium source and a plagioclase-dominated restite (after Patino Douce, 1997). F is the degree of melting. Vertical dashed lines are the range in  $(^{230}\text{Th}/^{238}\text{U})$  measured in the Newberry samples and gray rectangle is the range of  $(^{231}\text{Pa}/^{235}\text{U})_i$  measured in the Newberry samples. Solid lines with squares and circles are the  $(^{230}\text{Th}/^{238}\text{U})$  results of melting with 1% and 0.5% zircon in the restite. Solid lines with triangles and diamonds

The simple batch melting model generates 13 to 18%  $^{226}\text{Ra}$ -excess at 15 to 20% melting, although this is sensitive to the plagioclase  $D_{\text{Ra}}$  value (estimates of which differ by an order of magnitude; Berlo et al., 2004; Dufek and Cooper, 2005). The high proportion of plagioclase in the fractionating assemblage, with relatively high  $D_{\text{Ra}}$ , limits the increase in  $(^{226}\text{Ra}/^{230}\text{Th})$  during FC. Instantaneous assimilation of 15 to 20% of a secular equilibrium component, by a 15% lower crustal melt with  $(^{226}\text{Ra}/^{230}\text{Th}) = 1.177$ , would generate a magma that still had 13 to 14%  $^{226}\text{Ra}$ -excess. The maximum  $^{226}\text{Ra}$ -excess for the DH and NF samples at the time of eruption is  $\sim 8\%$  (Table 5.2). This places a lower limit on the time from lower crustal melting to eruption of  $\sim 1600$  years (i.e.  $\sim$  one  $^{226}\text{Ra}$  half-life). The secular equilibrium  $(^{226}\text{Ra}/^{230}\text{Th})$  values are, of course, permissible of a much more protracted timescale for ascent and eruption, which would be required if incongruent lower crustal melting generated much larger  $(^{226}\text{Ra}/^{230}\text{Th})$  (Dufek and Cooper, 2005) than calculated here for the simple case of batch melting (Berlo et al., 2004). Alternatively, if the upper crustal assimilant is  $^{231}\text{Pa}$ -enriched, but in  $(^{226}\text{Ra}/^{230}\text{Th})$  secular equilibrium, then the degree of assimilation could be increased and melt ascent and eruption could be essentially instantaneous. In light of the high diffusivity and fluid mobility of Ra (Cooper, 2001), and evidence for open-system behavior during differentiation (Asmerom et al., 2005), the lack of observed  $(^{226}\text{Ra}/^{230}\text{Th})$  disequilibrium is surprising, and may be evidence for rapid post-melting ascent and eruption.

In summary, the South Sister rhyolites are interpreted as  $\sim 15$  to 20% melts of lower

---

are the  $(^{230}\text{Th}/^{238}\text{U})$  and  $(^{231}\text{Pa}/^{235}\text{U})$  results, respectively, of a model with 1.5% rutile and 1.5% ilmenite in the restite. Dashed lines with the same symbols are the same output for a model with 2% apatite and 1% ilmenite in the restite. Zircon, apatite, and rutile D values from Garrison et al. (2006), Prowatke and Klemme (2006), and Klemme et al. (2005) respectively.

crustal mafic amphibolite with minor apatite in the restite. The very slight compositional differences between the two eruptive episodes, including U-series variations, reflect a small amount of assimilation and fractional crystallization in the same compositionally zoned upper crustal magma chamber. The preceding discussion demonstrates that the elemental and isotopic compositions of the South Sister rhyolites are consistent with a relatively simple model of melting followed by AFC. However, if basalt intrusion into the lower crust occurs repeatedly, and in geologically rapid succession, a complex and dynamic environment can be created, where mixing between liquids generated by a number of different processes, with different U-series signatures, could be expected, adding significant complexity to interpretation of U-series ratios in erupted lavas (Annen et al., 2006).

The lack of any phases in the Newberry melting model restite capable of retaining U over Th, and especially over Pa, eliminates the possibility of generating the observed  $^{230}\text{Th}$ - and  $^{231}\text{Pa}$ -excesses during lower crustal melting. Several independent lines of evidence led Linneman (1990) to propose that the Holocene obsidians at Newberry represent near-total re-melting of the intrusive equivalents of Pleistocene felsic eruptives, a process he termed “crustal distillation”. Thermal models demonstrate that such a process is possible, and capable of rapidly producing superheated, crystal-poor, rhyolitic melts with granite eutectic compositions, like the Newberry obsidians (Appendix A5), and has been invoked to explain the presence of large and small, low- $\delta^{18}\text{O}$  rhyolites at Yellowstone caldera, within the Snake River Plain, and elsewhere (Huppert and Sparks, 1988; Simakin and Bindeman, 2012). To generate the observed  $^{230}\text{Th}$ -excesses in this manner still requires a phase in the unmelted felsic rock capable of preferentially

retaining U over Th. None of the major phases present in granitic rocks are capable of this at high melt fractions, and of the typical accessory phases in granites, zircon is the most likely candidate. Figure 5.4c illustrates the results of melting a felsic protolith with variable amounts of zircon in the residue. The observed range in ( $^{230}\text{Th}/^{238}\text{U}$ ) can be generated by 85 to 95% melting with 0.5% to 1% zircon in the residue. However, this would be expected to generate a negative Zr anomaly in the trace element pattern, which is not observed (Fig. 5.1).

Melting of non-eutectic compositions would result in lower melt fractions (Huppert and Sparks, 1988), and experimental work has demonstrated that A-type granites, which have compositional similarities with the Newberry obsidians (Appendix A5), can be generated by ~ 20% melting of calc-alkaline granitoids at low pressures (Patino Douce, 1997). At this significantly lower melt fraction zircon is not required to generate the observed  $^{230}\text{Th}$ -excesses, which can be produced in the presence of small amounts of residual rutile  $\pm$  ilmenite (Fig. 5.4c). In this scenario the large  $^{231}\text{Pa}$ -excesses observed would have to be at least partially inherited from earlier processes as rutile ( $\pm$  ilmenite) cannot simultaneously reproduce the ( $^{230}\text{Th}/^{238}\text{U}$ ) and ( $^{231}\text{Pa}/^{235}\text{U}$ ) data. However, incorporating small amounts of apatite into the restite could achieve this (Fig. 5.4c).

Estimated timescales for melting, crystallization, and re-melting in silicic systems are on the order of  $10^2$  to  $10^4$  years (Huppert and Sparks, 1988; Bindeman et al., 2008; Simakin and Bindeman, 2008; Bindeman et al., 2012), more than sufficient to preserve U-series disequilibria from earlier events. The requirement of generating all of the observed ( $^{231}\text{Pa}/^{235}\text{U}$ ) disequilibrium during upper crustal melting could be obviated if lower crustal melting occurs beneath Newberry in a similar fashion as beneath South

Sister, generating  $^{231}\text{Pa}$ -enriched, but ( $^{230}\text{Th}/^{238}\text{U}$ ) secular equilibrium, felsic melts. Subsequent crystallization of these melts in the upper crust could generate the granitic protoliths that are the direct parents of the Newberry obsidians. Melting of these granites in response to further intrusion of hot magma, generates A-type rhyolitic melts, which now possess both  $^{231}\text{Pa}$ - and  $^{230}\text{Th}$ -enrichment. This interpretation is consistent with recent seismic studies of Newberry, which resolve a high-velocity intrusive complex at 3 to 6 km depth and a low-velocity zone below 3 km (Beachly et al., 2012). This low-velocity zone is consistent with a thin melt layer overlying a solidifying mush region (Beachly et al., 2012). Further study of the Pleistocene rhyolites at Newberry could help constrain if they are lower or upper crustal melts, and whether their intrusive equivalents could be the  $^{231}\text{Pa}$ -enriched parental material to the Holocene obsidians.

Despite many striking similarities (Linneman, 1990), the Glass Mountain rhyolite at Medicine Lake volcano has been interpreted somewhat differently, as a mixture of partial melts of granodioritic crust and residual liquid from andesite crystallization (Grove et al., 1997). U-series isotope data from the Glass Mountain rhyolite may help to distinguish between these two different interpretations of very similar lavas.

If shallow crystallization of lower crustal melts and subsequent re-melting in response to further magma intrusion occur on a timescale of  $10^2$  to  $10^4$  years, then successive episodes of melting will gradually increase, or at a minimum maintain, melt ( $^{231}\text{Pa}/^{235}\text{U}$ ) and ( $^{230}\text{Th}/^{238}\text{U}$ ), potentially maintaining non-equilibrium ratios for far longer than the 5 to 7 half-lives required for decay to secular equilibrium in an undisturbed system. In such a scenario measured U-series disequilibria in felsic magmas would be a time-integrated

average of potentially numerous melting and crystallization events, with no chronologic significance.

In summary, the Holocene obsidians at Newberry are interpreted to reflect melting of upper crustal granitic rocks, which in turn are the products of lower crustal melting. The ( $^{230}\text{Th}/^{238}\text{U}$ ) disequilibrium in these rocks is interpreted to be a consequence of upper crustal melting in the presence of residual Fe-Ti oxides. The ( $^{231}\text{Pa}/^{235}\text{U}$ ) disequilibrium could be generated by upper crustal melting in the presence of residual apatite, or could be inherited largely from the lower crustal melting process and enhanced during subsequent re-melting.

The geochemical and isotopic differences between young rhyolitic rocks at South Sister and Newberry are interpreted to reflect crustal melting of different protoliths occurring at different depths. It is suggested that ascent and eruption of lower crustal melts at South Sister is facilitated by active intra-arc extension, while the large volcanic edifice at Newberry, and position farther from the locus of extension, stalls lower crustal and/or mantle melts at shallow depths, promoting crystallization and subsequent re-melting of granitic lithologies (cf. Clark, 1983).

### **Acknowledgements**

Victor Polyak provided assistance with the lab work and sample analysis. Funding was provided by the National Science Foundation (EAR-0948703 to YA).

## References

- Annen, C. & Sparks, R. S. J. (2002). Effects of repetitive emplacement of basaltic intrusions on thermal evolution and melt generation in the crust. *Earth and Planetary Science Letters* **203**, 937-955.
- Annen, C., Blundy, J. D. & Sparks, R. S. J. (2006). The genesis of intermediate and silicic magmas in deep crustal hot zones. *Journal of Petrology* **47**, 505-539.
- Asmerom, Y., DuFrane, S. A., Mukasa, S. B., Cheng, H. & Edwards, R. L. (2005). Time scale of magma differentiation in arcs from protactinium-radium isotopic data. *Geology* **33**, 633-636.
- Atwater, T. (1970). Implications of plate tectonics for the Cenozoic evolution of western North America. *Geological Society of America Bulletin* **81**, 3513-3536.
- Bacon, C. R. & Druitt, T. H. (1988). Compositional evolution of the zoned calcalkaline magma chamber of Mount Mazama, Crater Lake, Oregon. *Contributions To Mineralogy and Petrology* **98**, 224-256.
- Bea, F., Pereira, M. D. & Stroh, A. (1994). Mineral/leucosome trace-element partitioning in a peraluminous migmatite (a laser ablation-ICP-MS study). *Chemical Geology* **117**, 291-312.
- Beachly, M. W., Hooft, E. E. E., Toomey, D. R. & Waite, G. P. (2012). Upper crustal structure of Newberry Volcano from P-wave tomography and finite difference waveform modeling. *Journal of Geophysical Research* **117**, doi:10.1029/2012JB009458.
- Beard, J. S. & Lofgren, G. E. (1991). Dehydration melting and water-saturated melting of basaltic and andesitic greenstones and amphibolites at 1, 3, and 6.9 kb. *Journal of Petrology* **32**, 365-401.
- Bergantz, G. W. (1989). Underplating and partial melting implications for melt generation and extraction. *Science* **245**, 1093-1095.
- Berlo, K., Turner, S., Blundy, J. & Hawkesworth, C. J. (2004). The extent of U-series disequilibria produced during partial melting of the lower crust with implications for

- the formation of the Mount St. Helens dacites. *Contributions to Mineralogy and Petrology* **148**, 122-130.
- Bindeman, I. N., Fu, B., Kita, N. T. & Valley, J. W. (2008). Origin and evolution of silicic magmatism at Yellowstone based on ion microprobe analysis of isotopically zoned zircons. *Journal of Petrology* **49**, 163-193.
- Bindeman, I., Gurenko, A., Carley, T., Miller, C., Martin, E. & Sigmarsson, O. (2012). Silicic magma petrogenesis in Iceland by remelting of hydrothermally altered crust based on oxygen isotope diversity and disequilibria between zircon and magma with implications for MORB. *Terra Nova* **24**, 227-232.
- Borg, L. E. & Clyne, M. A. (1998). The petrogenesis of felsic calc-alkaline magmas from the southernmost Cascades, California: Origin by partial melting of basaltic lower crust. *Journal of Petrology* **39**, 1197-1222.
- Bowen, N. L. (1928). *The Evolution of the Igneous Rocks*. Princeton University Press.
- Brophy, J. G. & Dreher, S. T. (2000). The origin of composition gaps at South Sister volcano, central Oregon: implications for fractional crystallization processes beneath active calc-alkaline volcanoes. *Journal of Volcanology and Geothermal Research* **102**, 287-307.
- Bullen, T. D. & Clyne, M. A. (1990). Trace element and isotopic constraints on magmatic evolution at Lassen Volcanic Center. *Journal of Geophysical Research* **95**, 19,671-19,691.
- Cheng, H., Edwards, R. L., Hoff, J., Gallup, C. D., Richards, D. A. & Asmerom, Y. (2000). The half lives of uranium-234 and thorium-230. *Chemical Geology* **169**, 17-33.
- Clark, J. G. (1983). Geology and petrology of South Sister Volcano, High Cascade Range, Oregon. *Ph.D. Dissertation*, University of Oregon.
- Conrey, R. M., Hooper, P. R., Larson, P. B., Chesley, J. & Ruiz, J. (2001). Trace element and isotopic evidence for two types of crustal melting beneath a High Cascade volcanic center, Mt. Jefferson, Oregon. *Contributions to Mineralogy and Petrology* **141**, 710-732.

- Cooper, K. M. (2001). Time scales of magma generation, differentiation, and storage: Constraints from uranium-238-thorium-230-radium-226 disequilibria. *Ph.D. Dissertation*, University of California, Los Angeles.
- Cribb, J. W. & Barton, M. (1997). Significance of crustal and source region processes on the evolution of compositionally similar calc-alkaline lavas, Mt. Hood, Oregon. *Journal of Volcanology and Geothermal Research* **76**, 229-249.
- Davies, G. R., Halliday, A. N., Mahood, G. A. & Hall, C. M. (1994). Isotopic constraints on the production rates, crystallization histories and residence times of pre-caldera silicic magmas, Long Valley, California. *Earth and Planetary Science Letters* **125**, 17-37.
- Dufek, J. & Cooper, K. M. (2005).  $^{226}\text{Ra}/^{230}\text{Th}$  excess generated in the lower crust: Implications for magma transport and storage time scales. *Geology* **33**, 833-836.
- Edwards, R. L., Beck, J. W., Burr, G. S., Donahue, D. J., Chapell, J. M. A., Bloom, A. L., Druffel, E. R. M. & Taylor, F. W. (1993). A large drop in atmospheric  $^{14}\text{C}/^{12}\text{C}$  and reduced melting in the Younger Dryas documented with  $^{230}\text{Th}$  ages of corals. *Science* **260**, 962-968.
- Eppich, G. R., Cooper, K. M., Kent, A. J. R. & Koleszar, A. (2012). Constraints on crystal storage timescales in mixed magmas: Uranium-series disequilibria in plagioclase from Holocene magmas at Mount Hood, Oregon. *Earth and Planetary Science Letters* **317-318**, 319-330.
- Fierstein, J., Hildreth, W. & Calvert, A. T. (2011). Eruptive history of South Sister, Oregon Cascades. *Journal of Volcanology and Geothermal Research* **207**, 145-179.
- Fountain, J. C., Hodge, D. S. & Shaw, R. P. (1989). Melt segregation in anatectic granites: A thermomechanical model. *Journal of Volcanology and Geothermal Research* **39**, 279-296.
- Garrison, J., Davidson, J., Reid, M. & Turner, S. (2006). Source versus differentiation controls on U-series disequilibria: Insights from Cotopaxi Volcano, Ecuador. *Earth and Planetary Science Letters* **244**, 548-565.

- Grove, T. L. & Donnelly-Nolan, J. M. (1986). The evolution of young silicic lavas at Medicine Lake Volcano, California: Implications for the origin of compositional gaps in calc-alkaline series lavas. *Contributions to Mineralogy and Petrology* **92**, 281-302.
- Grove, T. L., Donnelly-Nolan, J. M. & Housh, T. (1997). Magmatic processes that generated the rhyolite of Glass Mountain, Medicine Lake volcano, N. California. *Contributions To Mineralogy and Petrology* **127**, 205-223.
- Grove, T. L., Elkins-Tanton, L. T., Parman, S. W., Chatterjee, N., Müntener, O. & Gaetani, G. A. (2003). Fractional crystallization and mantle-melting controls on calc-alkaline differentiation trends. *Contributions To Mineralogy and Petrology* **145**, 515-533.
- Grove, T. L., Baker, M. B., Price, R. C., Parman, S. W., Elkins-Tanton, L. T., Chatterjee, N. & Muntener, O. (2005). Magnesian andesite and dacite lavas from Mt. Shasta, northern California: Products of fractional crystallization of H<sub>2</sub>O-rich mantle melts. *Contributions To Mineralogy and Petrology* **148**, 542-565.
- Guffanti, M., Clyne, M. A. & Muffler, L. J. P. (1996). Thermal and mass implications of magmatic evolution in the Lassen volcanic region, California, and minimum constraints on basalt influx to the lower crust. *Journal of Geophysical Research* **101**, 3003-3013.
- Hawkesworth, C. J., Blake, S., Evans, P., Hughes, R., Macdonald, R., Thomas, L. E., Turner, S. P. & Zellmer, G. (2000). Time scales of crystal fractionation in magma chambers-Integrating physical, isotopic and geochemical perspectives. *Journal of Petrology* **41**, 991-1006.
- Hildreth, W., Fierstein, J. & Calvert, A. T. (2012). Geologic map of Three Sisters volcanic cluster, Cascade Range, Oregon. *U.S. Geological Survey Scientific Investigations Map* **3186**, scale 1:24,000.
- Hill, B. E. (1991). Petrogenesis of compositionally distinct silicic volcanoes in the Three Sisters region of the Oregon Cascade range: The effects of crustal extension on the

- development of continental arc silicic magmatism. *Ph.D. Dissertation*, Oregon State University.
- Hughes, S. S. (1983). Petrochemical evolution of the High Cascade volcanic rocks in the Three Sisters region, Oregon. *Ph.D. Dissertation*, Oregon State University.
- Huppert, H. E. & Sparks, R. S. J. (1988). The generation of granitic magmas by intrusion of basalt into continental crust. *Journal of Petrology* **29**, 599-624.
- Jones, C. H., Unruh, J. R. & Sonder, L. J. (1996). The role of gravitational potential energy in active deformation in the southwestern United States. *Nature* **381**, 37-41.
- Kinzler, R. J., Donnelly-Nolan, J. M. & Grove, T. L. (2000). Late Holocene hydrous mafic magmatism at the Paint Pot Crater and Callahan flows, Medicine Lake Volcano, N. California and the influence of H<sub>2</sub>O in the generation of silicic magmas. *Contributions To Mineralogy and Petrology* **138**, 1-16.
- Klemme, S., Gunther, D., Hametner, K., Prowatke, S. & Zack, T. (2006). The partitioning of trace elements between ilmenite, ulvospinel, armalcolite and silicate melts with implications for the early differentiation of the moon. *Chemical Geology* **234**, 251-263.
- Laidley, R. A. & McKay, D. S. (1971). Geochemical examination of obsidians from Newberry Caldera, Oregon. *Contributions To Mineralogy and Petrology* **30**, 336-342.
- Linneman, S. R. (1990). The petrologic evolution of the Holocene magmatic system of Newberry Volcano, central Oregon. *Ph.D. Dissertation*, University of Wyoming.
- Linneman, S. R. & Myers, J. D. (1990). Magmatic inclusions in the Holocene rhyolites of Newberry volcano, central Oregon. *Journal of Geophysical Research* **95**, 17,677-17,691.
- Luedke, R. G. & Smith, R. L. (1982). Map showing distribution, composition, and age of Late Cenozoic volcanic centers in Oregon and Washington. *U.S. Geological Survey Miscellaneous Investigations Series I-1091 D*, scale 1:500,000.

- MacLeod, N. S. & Sherrod, D. R. (1988). Geologic evidence for a magma chamber beneath Newberry Volcano, Oregon. *Journal of Geophysical Research* **93**, 10,067-10,079.
- Mitchell, E. C. & Asmerom, Y. (2011). U-series isotope systematics of mafic magmas from central Oregon: Implications for fluid involvement and melting processes in the Cascade arc. *Earth and Planetary Science Letters* **312**, 378-389.
- Palme, H. & Jones, A. (2003). Solar system abundances of the elements. In: Davis, A. M. (Ed.), *Meteorites, Comets, and Planets. Treatise on Geochemistry* **1**, Elsevier-Pergamon, 41-61.
- Palme, H. & O'Neill, H. S. C. (2003). Cosmochemical estimates of mantle composition. In: Carlson, R. W. (Ed.), *The Mantle and Core. Treatise on Geochemistry* **2**, Elsevier-Pergamon, 1-38.
- Patino Douce, A. E. (1997). Generation of metaluminous A-type granites by low-pressure melting of calc-alkaline granitoids. *Geology* **25**, 743-746.
- Pedersen, T., Heeremans, N. & vanderBeek, P. (1998). Models of crustal anatexis on volcanic rifts: Applications to southern Finland and the Oslo Graben, southeast Norway. *Geophysical Journal International* **132**, 239-255.
- Petford, N. & Gallagher, K. (2001). Partial melting of mafic (amphibolitic) lower crust by periodic influx of basaltic magma. *Earth and Planetary Science Letters* **193**, 483-499.
- Price, J. D. (1993). The nature and origin of the intermediate and silicic rocks, and their mafic inclusions, at South Sister Volcano, central High Cascades. *M.S. Thesis*, Baylor University.
- Prouteau, G. L. & Scaillet, B. (2003). Experimental constraints on the origin of the 1991 Pinatubo dacite. *Journal of Petrology* **44**, 2203-2241.
- Prowatke, S. & Klemme, S. (2006). Trace element partitioning between apatite and silicate melts. *Geochimica et Cosmochimica Acta* **70**, 4513-4527.

- Rapp, R. P. & Watson, E. B. (1995). Dehydration melting of metabasalt at 8-32 kbar: Implications for continental growth and crust-mantle recycling. *Journal of Petrology* **36**, 891-931.
- Reagan, M. K., Sims, K. W. W., Erich, J., Thomas, R. B., Cheng, H., Edwards, R. L., Layne, G. & Ball, L. (2003). Time-scales of differentiation from mafic parents to rhyolite in North American continental arcs. *Journal of Petrology* **44**, 1703-1726.
- Reid, M. R., Coath, C. D., Mark Harrison, T. & McKeegan, K. D. (1997). Prolonged residence times for the youngest rhyolites associated with Long Valley Caldera:  $^{230}\text{Th}$ - $^{238}\text{U}$  ion microprobe dating of young zircons. *Earth and Planetary Science Letters* **150**, 27-39.
- Rudnick, R. L. & Fountain, D. M. (1995). Nature and composition of the continental crust: a lower crustal perspective. *Reviews of Geophysics* **33**, 267-309.
- Rudnick, R. L. & Gao, S. (2003). Composition of the continental crust. *In*: Rudnick, R. L. (Ed.), *The Crust. Treatise on Geochemistry* **3**, Elsevier-Pergamon, 1-64.
- Scott, W. E. (1987). Holocene rhyodacite eruptions on the flanks of South Sister volcano, Oregon. *In*: Fink, J. H. (Ed.) *The Emplacement of Silicic Domes and Lava Flows. Geological Society of America Special Paper* **212**, 35-53.
- Sherrod, D. R., Taylor, E. M., Ferns, M. L., Scott, W. E., Conrey, R. M. & Smith, G. A. (2004). Geologic map of the Bend 30- x 60-minute quadrangle, central Oregon. *U.S. Geological Survey Geologic Investigations Series* **I-2683**, scale 1:100,000.
- Simakin, A. G. & Bindeman, I. N. (2008). Evolution of crystal sizes in the series of dissolution and precipitation events in open magma systems. *Journal of Volcanology and Geothermal Research* **177**, 997-1010.
- Simakin, A. G. & Bindeman, I. N. (2012). Remelting in caldera and rift environments and the genesis of hot, "recycled" rhyolites. *Earth and Planetary Science Letters* **337-338**, 224-235.
- Sisson, T. W., Ratajeski, K., Hankins, W. B. & Glazner, A. F. (2005). Voluminous granitic magmas from common basaltic sources. *Contributions to Mineralogy and Petrology* **148**, 635-661.

- Smith, D. R. & Leeman, W. P. (1987). Petrogenesis of Mount St. Helens dacitic magmas. *Journal of Geophysical Research* **92**, 10,313-10,334.
- Smith, D. R. & Leeman, W. P. (1993). The origin of Mount St. Helens andesites. *Journal of Volcanology and Geothermal Research* **55**, 271-303.
- Stelten, M. E. & Cooper, K. M. (2012). Constraints on the nature of the subvolcanic reservoir at South Sister volcano, Oregon from U-series dating combined with sub-crystal trace-element analysis of plagioclase and zircon. *Earth and Planetary Science Letters* **313-314**, 1-11.
- Taylor, S. R. & McLennan, S. M. (1985). *The Continental Crust: Its Composition and Evolution*. Blackwell.
- Tepper, J. H., Nelson, B. K., Bergantz, G. W. & Irving, A. J. (1993). Petrology of the Chilliwack batholith, North Cascades, Washington: Generation of calc-alkaline granitoids by melting of mafic lower crust with variable water fugacity. *Contributions to Mineralogy and Petrology* **113**, 333-351.
- Tuttle, O. F. & Bowen, N L. (1958). Origin of granite in the light of experimental studies in the system NaAlSi<sub>3</sub>O<sub>8</sub>-KAlSi<sub>3</sub>O<sub>8</sub>-SiO<sub>2</sub>-H<sub>2</sub>O. *Geological Society of America Memoir* **74**.
- Ulfbeck, D., Baker, J., Waight, T. & Krogstad, E. (2003). Rapid sample digestion by fusion and chemical separation of Hf for isotopic analysis by MC-ICPMS. *Talanta* **59**, 365-373.
- Wolf, M. B. & Wyllie, P. J. (1994). Dehydration-melting of amphibolite at 10 kbar: the effects of temperature and time. *Contributions to Mineralogy and Petrology* **115**, 369-383.

## Appendix A5

This appendix contains:

Appendix A5.1. U-Series Analytical Methods

Appendix A5.2. Major Element Constraints on Crustal Melting Scenarios

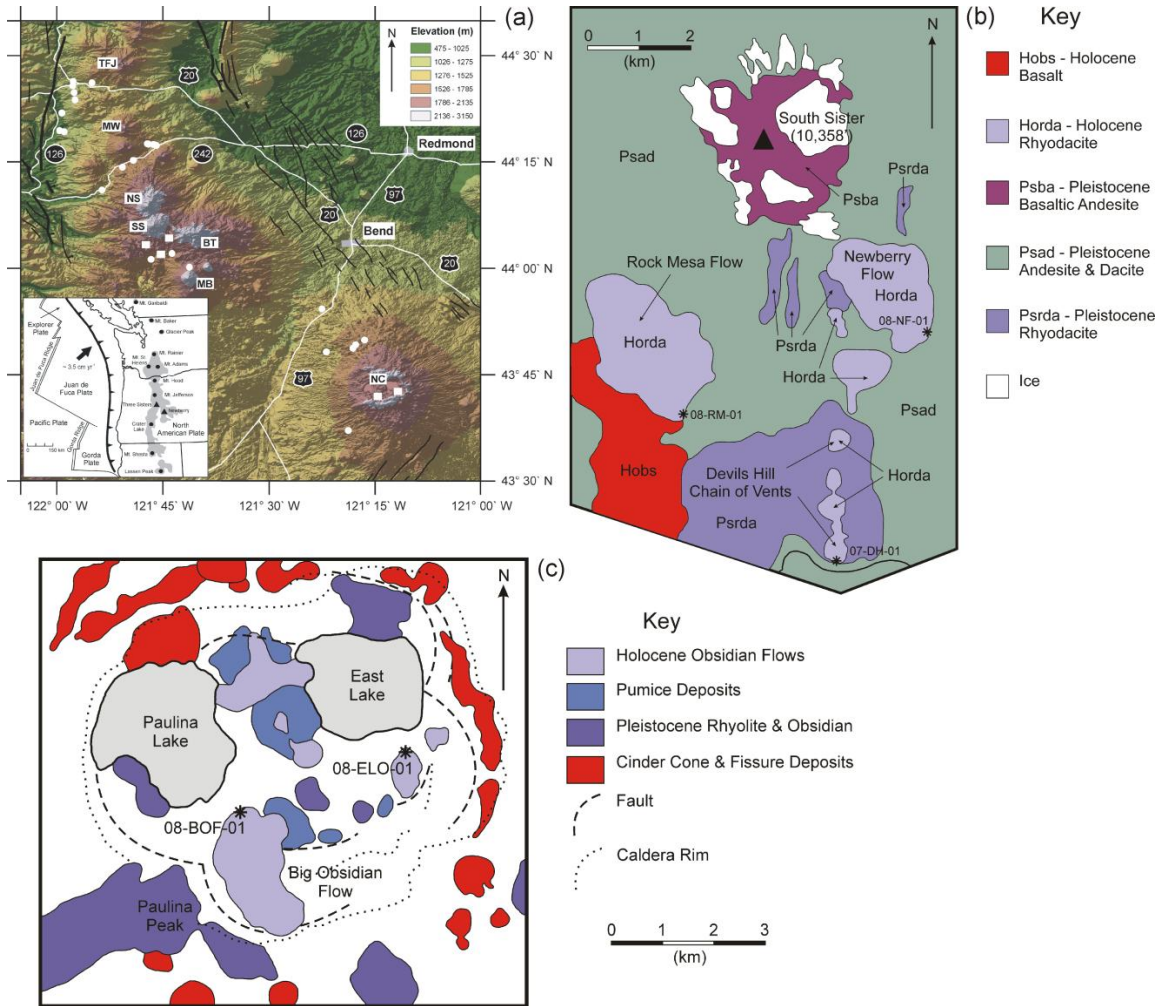
Figure A5.1: Location maps of the study area in central Oregon.

Figure A5.2: Harker variation diagrams for Holocene felsic rocks from South Sister and Newberry.

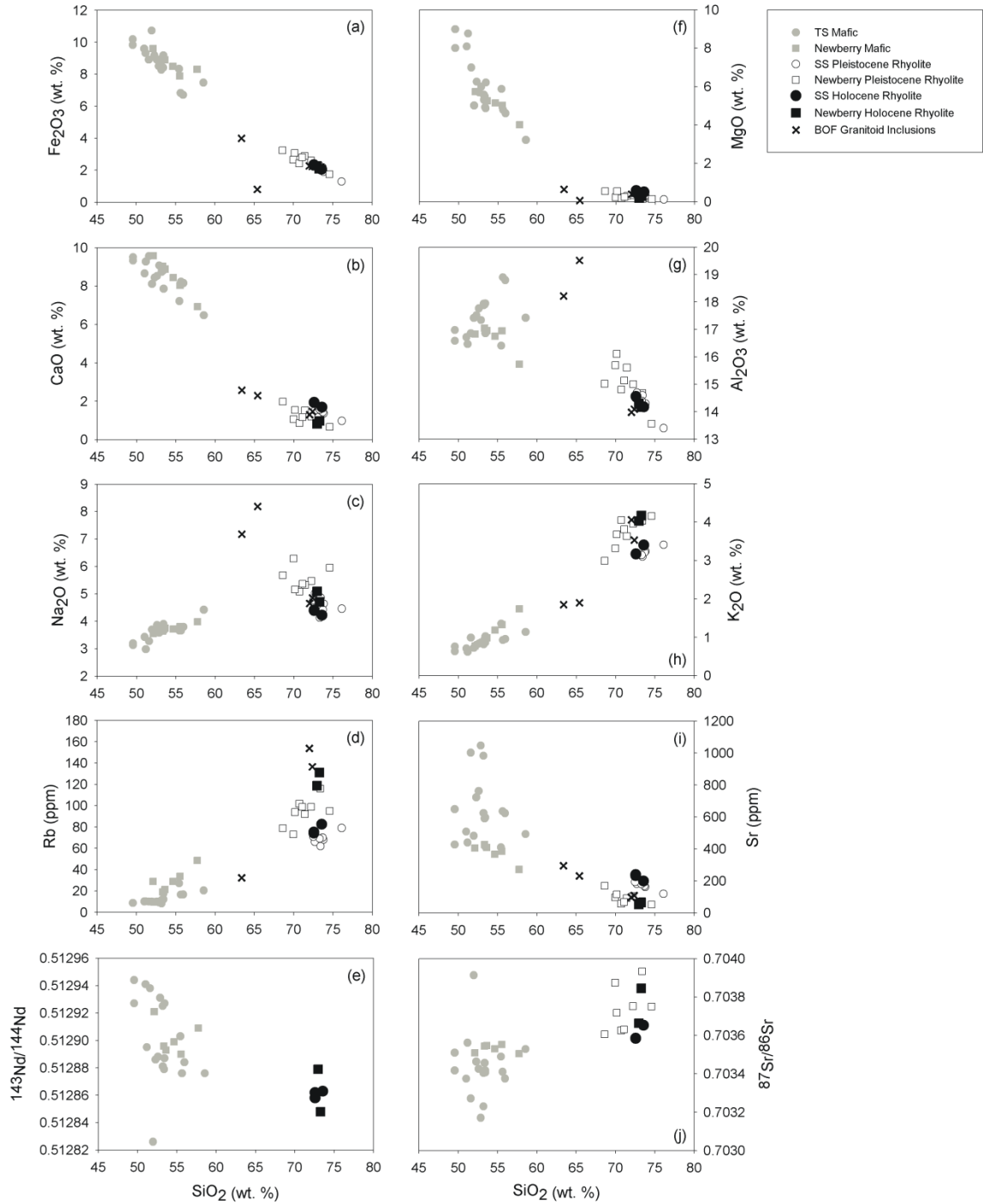
Figure A5.3: Plots of  $\text{SiO}_2$  vs.  $\text{Al}_2\text{O}_3$ , FeO, CaO, and MgO for South Sister and Newberry Holocene rhyolites and the fields for experimentally produced glasses from Sisson et al. (2005).

Figure A5.4: Qtz-Ab-Or ternary plot for Holocene felsic rocks from South Sister and Newberry, symbols as in Figure 5.1.

References



**Figure A5.1:** Location maps of the study area in central Oregon. Panel (a): Shaded relief map of the study area. Felsic samples are marked with white squares. White circles show the sample localities for mafic samples (Mitchell and Asmerom, 2011). Major stratovolcanoes are labeled: TFJ = Three Fingered Jack, MW = Mount Washington, NS = North Sister, SS = South Sister, BT = Broken Top, MB = Mount Bachelor, and NC = Newberry Caldera. Black lines are faults, ball and bar on the downthrown side. Thin lines mark faults with displacement < 300 m, thick lines mark faults with displacement > 500 m (after Sherrod et al., 2004). Inset shows the general tectonic setting of the Cascade arc (after Luedke and Smith, 1982). Thick black line is the trench, teeth on the overriding plate. Single thin lines are transform faults, double thin lines are spreading ridges. Shaded area shows the extent of the Quaternary High Cascades. Prominent volcanoes are marked and labeled. Panel (b): Geologic sketch map of South Sister volcano and vicinity (after Clark, 1983). Panel (c): Geologic sketch map of Newberry caldera (after MacLeod and Sherrod, 1988).



**Figure A5.2:** Harker variation diagrams for Holocene felsic rocks from South Sister and Newberry. Also shown are the composition of Holocene mafic rocks in the region (Mitchell and Asmerom, 2011), Pleistocene felsic rocks (Linneman, 1990; Hill, 1991) and granitoid inclusions within the Big Obsidian Flow (BOF) at Newberry (Linneman, 1990). TS = Three Sisters, SS = South Sister.

### **A5.1. U-Series Analytical Methods**

The U-Th-Pa data were acquired on 400 to 500 mg powder aliquots fused with ultra-pure  $\text{LiBO}_2$  flux following the method described for trace element analysis in Mitchell and Asmerom (2011). The melt was poured directly into a 150 mL solution of 3%  $\text{HNO}_3$ , which was subsequently stirred until complete dissolution of the quenched glass had been observed. Two aliquots of this liquid, containing  $\sim 0.1$  g powder, were separated and spiked with the appropriate spike solution for U-Th or Pa analysis. U-Th separation and purification followed the method described in Mitchell and Asmerom (2011), with addition of Fe solution prior to co-precipitation. A gel-like substance was observed in the samples during chemistry but was centrifuged out of the solution loaded into the first columns and did not affect the known standard concentrations or activity ratios (cf. 'Ryan Std. A' and 'Ryan Std. B' in Table 5.2).

Pa separation and purification also followed previously described methods (Chapter 3), which only slightly modify the U-Th column procedure. The gel-like substance was again observed but appears to have removed all the Pa from solution as no analyses were possible on these aliquots. The remaining aliquot of 3%  $\text{HNO}_3$ , containing 0.2 to 0.3 g powder, was subsequently spiked and the chemistry was repeated. Despite repeated and thorough washing of the precipitate formed during co-precipitation, extensive gel formation was observed while the samples sat for several days following this step. This gel is interpreted to be a slowly polymerizing silicic acid, which is scavenging Pa from solution. The gel-containing solutions were dried down, dissolved in 15N  $\text{HNO}_3$ , and subsequently centrifuged in 7N  $\text{HNO}_3$ . The undissolved residue was separated, dried to a powder in 15N  $\text{HNO}_3$ , and was found to dissolve readily in a few drops of concentrated

HF. This HF solution was dried, and repeatedly dissolved and dried in 15N HNO<sub>3</sub> with boric acid to remove excess F, before dissolving in 7N HNO<sub>3</sub> for column separation as previously described (Chapter 3).

A separate <sup>233</sup>Pa spike solution was used for the felsic rocks than was previously used for the mafic samples. This spike was prepared and calibrated in the same fashion as the three earlier spikes described in Chapters 3 and 4.

### **A5.2. Major Element Constraints on Crustal Melting Scenarios**

It is well established that crystallization of basaltic magma can provide sufficient heat to melt surrounding country rocks (e.g., Huppert and Sparks, 1988; Bergantz, 1989; Fountain et al., 1989; Pedersen et al., 1998) and more recent thermal models have stressed the effects of repeated intrusion over geologically short time periods (Petford and Gallagher, 2001; Annen and Sparks, 2002; Annen et al., 2006).

Likewise, numerous experimental studies have demonstrated the potential for melting of mafic lower crust to produce melts of a felsic composition. Sisson et al. (2005) stressed that partial melting of medium-to-high K mafic protoliths (unlike the low-K protoliths investigated by most studies) would generate high-K felsic rocks, more similar to true granites and rhyolites. Compositions produced under lower temperature and/or higher *f*O<sub>2</sub> conditions in particular could reproduce very well the composition of granite and rhyolite commonly found in many continental arcs and the western US. The composition of the Holocene rhyolites investigated here, especially those from South Sister, are very close matches for the lower temperature/higher *f*O<sub>2</sub> run products in terms

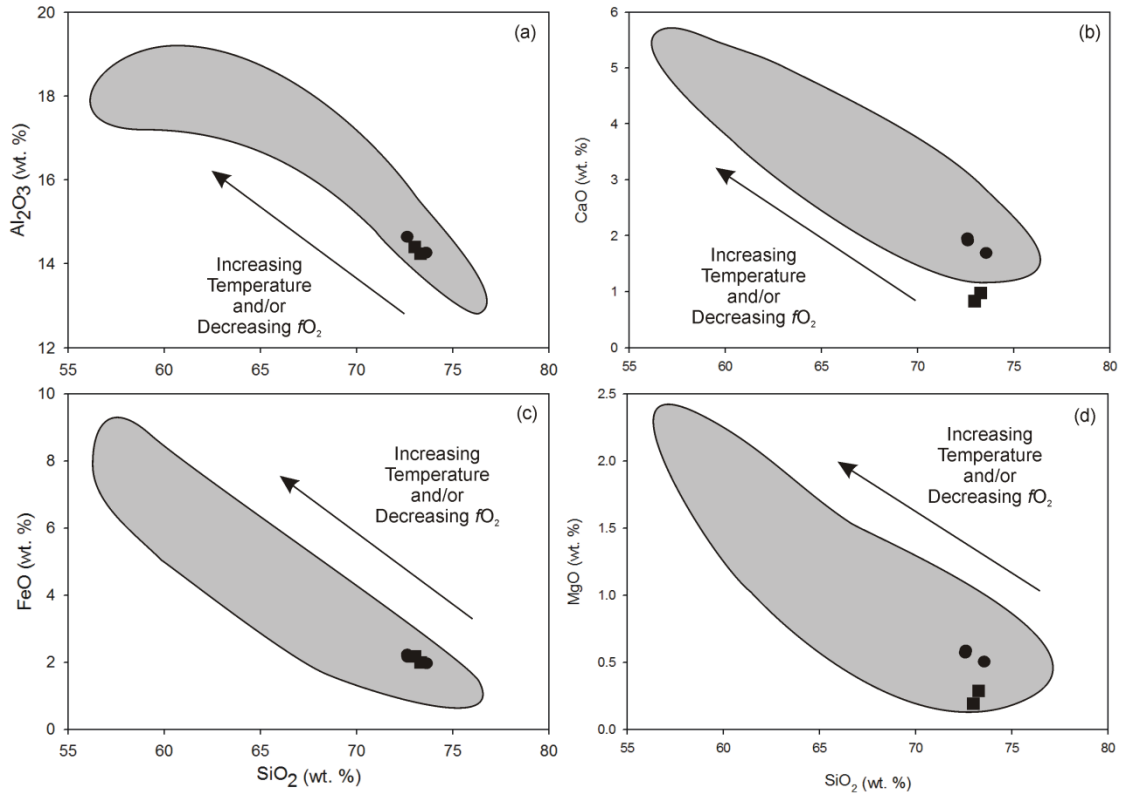


**Figure A5.3:** Plots of  $\text{SiO}_2$  vs.  $\text{Al}_2\text{O}_3$ ,  $\text{FeO}$ ,  $\text{CaO}$ , and  $\text{MgO}$  for South Sister and Newberry Holocene rhyolites and the fields for experimentally produced glasses from Sisson et al. (2005). Glasses are the products of dehydration melting experiments on medium- to high-K basaltic compositions at 825-975°C, 7 kbar, and  $f\text{O}_2$  ranging from Ni-NiO -1.3 to +4. Restite mineralogy is dominated by approximately subequal amounts of plagioclase and amphibole, coexisting with up to 30-35% melt (Sisson et al., 2005).

of major element abundances (Fig. A5.3) and normative quartz, orthoclase, and plagioclase compositions (Fig. A5.4).

While the Newberry obsidians and South Sister rhyolites share broad major element similarities, there are important differences. Features in the Newberry obsidians such as lower  $\text{CaO}$  and  $\text{Sr}$ , as well as higher  $\text{FeO}/\text{MgO}$ ,  $\text{TiO}_2/\text{MgO}$ , and  $(\text{Na}_2\text{O}+\text{K}_2\text{O})/\text{Al}_2\text{O}_3$ , are consistent with the A-type granite-composition experimental run products produced by melting calc-alkaline granitoids, such as the South Sister rhyolite compositions, at low

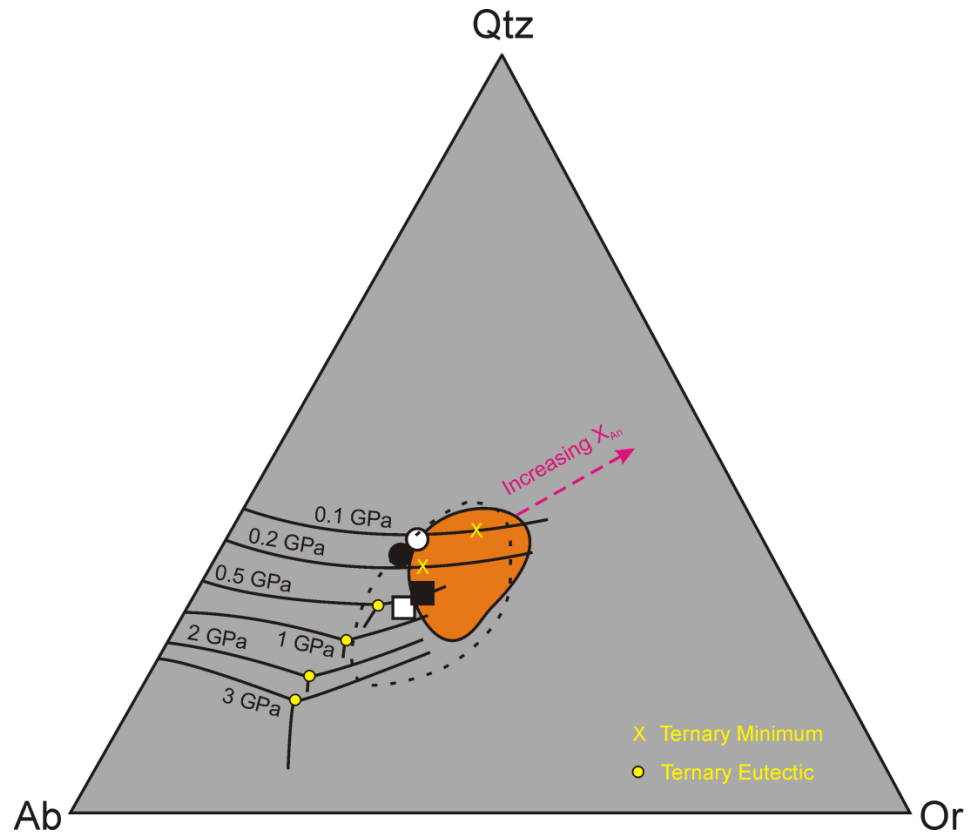


**Figure A5.4:** Qtz-Ab-Or ternary plot for Holocene felsic rocks from South Sister and Newberry, symbols as in Figure 5.1. Also shown are the cotectic curves and field (in orange) for most granite compositions (after Winter, 2001). Dashed field shows the range of compositions in experimental products of Sisson et al. (2005).

pressure (Patino Douce, 1997). This suggests that the Newberry obsidians, or their parental plutonic rocks, could have been generated by shallow melting of calc-alkaline granitoids, which themselves could have been generated by lower crustal melting under conditions similar to those that generated the South Sister magmas. Repeated magma intrusion and re-melting of the crust in this fashion will generate several of the features observed at Newberry, such as eutectic-like major element compositions (Fig. A5.4), nearly crystal-free melts, and a temporal increase in Rb/Sr (Linneman, 1990).

## References

- Annen, C. & Sparks, R. S. J. (2002). Effects of repetitive emplacement of basaltic intrusions on thermal evolution and melt generation in the crust. *Earth and Planetary Science Letters* **203**, 937-955.
- Annen, C., Blundy, J. D. & Sparks, R. S. J. (2006). The genesis of intermediate and silicic magmas in deep crustal hot zones. *Journal of Petrology* **47**, 505-539.
- Bergantz, G. W. (1989). Underplating and partial melting implications for melt generation and extraction. *Science* **245**, 1093-1095.
- Fountain, J. C., Hodge, D. S. & Shaw, R. P. (1989). Melt segregation in anatectic granites: A thermomechanical model. *Journal of Volcanology and Geothermal Research* **39**, 279-296.
- Huppert, H. E. & Sparks, R. S. J. (1988). The generation of granitic magmas by intrusion of basalt into continental crust. *Journal of Petrology* **29**, 599-624.
- Linneman, S. R. (1990). The petrologic evolution of the Holocene magmatic system of Newberry Volcano, central Oregon. *Ph.D. Dissertation*, University of Wyoming.
- Mitchell, E. C. & Asmerom, Y. (2011). U-series isotope systematics of mafic magmas from central Oregon: Implications for fluid involvement and melting processes in the Cascade arc. *Earth and Planetary Science Letters* **312**, 378-389.
- Patino Douce, A. E. (1997). Generation of metaluminous A-type granites by low-pressure melting of calc-alkaline granitoids. *Geology* **25**, 743-746.
- Pedersen, T., Heeremans, N. & vanderBeek, P. (1998). Models of crustal anatexis on volcanic rifts: Applications to southern Finland and the Oslo Graben, southeast Norway. *Geophysical Journal International* **132**, 239-255.
- Petford, N. & Gallagher, K. (2001). Partial melting of mafic (amphibolitic) lower crust by periodic influx of basaltic magma. *Earth and Planetary Science Letters* **193**, 483-499.

Sisson, T. W., Ratajeski, K., Hankins, W. B. & Glazner, A. F. (2005). Voluminous granitic magmas from common basaltic sources. *Contributions to Mineralogy and Petrology* **148**, 635-661.

Winter, J. D. (2001). *An Introduction to Igneous and Metamorphic Petrology*. Prentice Hall, London.